ACTA TECHNICA

ACADEMIAE SCIENTIARUM HUNGARICAE

EDITOR: M. MAJOR

VOLUME 97
NUMBERS 1—4

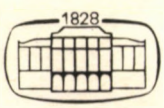

AKADÉMIAI KIADÓ, BUDAPEST 1984

ACTA TECHNICA

A JOURNAL OF THE HUNGARIAN ACADEMY OF SCIENCES

Acta Technica publishes original papers, preliminary reports and reviews in English, which contribute to the advancement of engineering sciences.
Acta Technica is published by

AKADÉMIAI KIADÓ
Publishing House of the Hungarian Academy of Sciences
H-1450 Budapest, Alkotmány u. 21.

Subscription information

Orders should be addressed to

KULTURA Foreign Trading Company
H-1389 Budapest P.O. Box 149

or to its representatives abroad

Acta Technica is indexed in Current Contents

ACTA TECHNICA

VOLUME 97 NOS 1—4

ACTA TECHNICA

ACADEMIAE SCIENTIARUM HUNGARICAE

VOLUME 97
NUMBERS 1—4

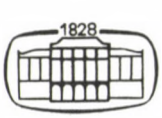

AKADÉMIAI KIADÓ, BUDAPEST 1984

ACTA TECHNICA

ACADEMIAE SCIENTIARUM HUNGARICAE

VOLUME 97

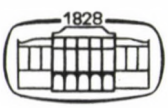

AKADÉMIAI KIADÓ, BUDAPEST 1984

Acta Technica Academiae Scientiarum Hungaricae, 97 (1—4), pp. 5—9 (1984)

EFFECT OF CONCRETE SHRINKAGE ON THE STABILITY OF REINFORCED CONCRETE SHELLS

E. DULÁCSKA*

[Received: 15 July, 1983]

The effect of concrete shrinkage on the stability of reinforced concrete shells, and the possibility of how to reckon with this effect has been investigated. Geometry alteration due to shrinkage was found to be significant for very shallow shells, while the increase of imperfection due to shrinkage may generally be omitted in stability analyses of reinforced concrete shells.

1. Introduction

Deviation of the shell form from the designed one is known to impair the stability behaviour of shells [1], and to significantly reduce the critical load. Shrinkage of concrete in reinforced concrete structures is an effect likely to affect the critical load by deforming the shell. Shrinkage will be seen to involve two possibilities of affecting stability characteristics of reinforced concrete shells: partly by modifying the shell form, and partly, by increasing the initial imperfection amplitude of the shell. In the following, effects of these phenomena will be considered.

2. Alteration of the shell form

The shrinkage effect will be analysed on a bar cut by two parallel planes of the shell. The originally straight bar of symmetric reinforcement is shortened by shrinkage but it remains straight. Shortening decreases if counteracted by increasing reinforcement percentage. (For slighter reinforcement percentages usual in shells, this effect may be neglected, on the safety side.)

The effect of shrinkage on the curved bar depends on boundary conditions.

For a shell edge with sidesway (exempt from lateral pressure) shrinkage produces no bending moment but the bar keeps its form, though at a reduced curvature radius, due to shortening.

This is the characteristic behaviour of free-edge shells, shells supported on shear diaphragms, and closed annular shell strips. Decrease of the curvature radius increases the critical force by less than 1%. Thus, in this case, shrinkage somewhat increases the safety.

* Dr. E. Dulácska, H-1022 Budapest, Kitaibel Pál u. 12, Hungary

If curved bar ends are restrained from displacement, a constraint force arises, causing a bending moment to develop, keeping, in turn, bar ends in place. In this process the curvature changes, with an increase of the curvature radius, as can be seen in Fig. 1.

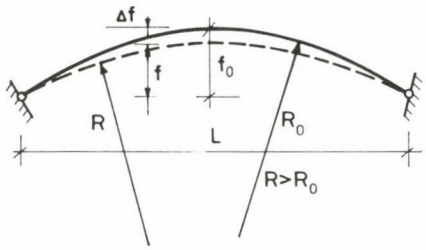

Fig. 1. Curvature radius variation due to shrinkage

Let both the original and the deformed bar shapes be shallow second-order parabolae. Assume the length change due to shrinkage to be fully equalized by curvature change, neglecting the bar elongation or compression due to shrinkage constraint (a neglect on the safety side).

With symbols in Fig. 1, the original bar arc length is fairly approximated by:

$$S_0 = L\left[1 + \frac{8}{3}\left(\frac{f_0^2}{L^2}\right)\right] \tag{1}$$

and the reduced arc length of the bar, due to specific shrinkage

$$S = L\left[1 + \frac{8}{3}\left(\frac{f_0^2}{L^2}\right)\right]\cdot(1-\varepsilon_{sh}) = \left[1 + \frac{8}{3}\left(\frac{f^2}{L^2}\right)\right]. \tag{2}$$

Expressing quotient f/f_0 after simplification and arrangement:

$$f/f_0 = \sqrt{1-\varepsilon_{sh}\left[1 + \frac{3}{8}\cdot\left(\frac{L^2}{f_0^2}\right)\right]}. \tag{3}$$

Substituting the usual specific concrete shrinkage coefficient $\varepsilon_{sh} = 0.0003$ into (3), it yields for some f_0/L ratios in the range of validity of the theory of shallow shells:

f_0/L	0.05	0.10	0.15	0.20	0.25
f/f_0	0.977	0.994	0.997	0.998	0.999
R/R_0	1.024	1.006	1.003	1.002	1.001

The Table shows the maximum increase of curvature radius, 2.4%, to result for ratio $f_0/L = 0.05$, the lower limit of shallow shells with fixed edges, reducing the critical shell load by about 4.6%.

This reduction being rather slight, it is considered to be negligible. For very shallow shells it is advisable to calculate curvature radii with regard to shrinkage effects, and to calculate the critical loads with increased curvature radii.

3. Increase of initial imperfections

Deflection of the originally straight r.c. bar in bending is increased by shrinkage. To our knowledge there being no research result on shell structures available, as to indicate the imperfection increment due to shrinkage, its assessment will start from the deflection increment of the straight bar.

Approximate deflection increment of the cracked r.c. bar in bending due to shrinkage [2]:

$$w_{sh} \approx \frac{K}{10} \cdot \frac{\varepsilon_{sh}}{h} l^2 , \tag{4}$$

where h is the shell thickness.

Concerning length l, let imperfection wavelength equal the wavelength of the linear critical load. As an unfavourable case, let us consider a spherical shell with two-way identical wavelengths $l_x = l_y = l$. In this case [1]:

$$l = 2.38 \sqrt{hR} . \tag{5}$$

According to [2], K is obtained from

$$K = 1{,}3 \frac{2 + \varphi_c}{6} (1 - \sqrt{n\mu'}) . \tag{6}$$

where φ_c is a creep factor, and μ' the compressed reinforcement to concrete cross section ratio. The worst value $\mu' = 0$ occurs in plain concrete shells and in shells with a single mesh of reinforcement in the middle of the cross section. In the case $\mu' = 0$, for $\varphi_c = 2$, $K = 0.87$, and for $\varphi_c = 3$, $K = 1.08$. Practically, $\varphi_c < 3$, hence $K = 1$ is a good approximation.

Substituting the mean concrete shrinkage $\varepsilon_{sh} = 0.0003$ into (4):

$$w_{sh} = \frac{1}{10} \frac{0.0003 \cdot 2.38^2 \cdot hR}{h} = \frac{R}{5884} \approx \frac{R}{6000} \tag{7}$$

Shells, however, differ from straight bars. For instance, shrinkage deformation produces membrane forces, moderating, in turn, shrinkage curvature.

Derivation of the critical load for linear elastic shells is known to show the linear critical load to result where the load is evenly shared between bending stiffnesses and membrane rigidities [1]. In other words, in the case of deflection corresponding to the buckling curve the shell undergoes half the bending deformation of that in the bar. Applying this analogy on shrinkage deformation, the w_{sh} value may be multiplied by 0.5.

Besides as a rule, the shell cross section is subject to eccentric compression rather than to pure bending. Shrinkage curvature of the r.c. cross section under eccentric compression is, however, less than that of the flexural one, since it has to pass into an axially compressed cross section without a shrinkage curvature. Besides, in a part of the imperfection wavelengths, both cross section edges are compressed, with no shrinkage curvature.

In conformity with previous research results [3], cross-sectional rigidities of shell plates under eccentric compression approximate those in bending for $e_0/h \geq 0.5$. Accordingly the full shrinkage curvature may be assumed to arise for $e_0/h = 0.50$. Reckoning with this value, transition from the state of no shrinkage curvature and axial compression without eccentricity in range $e_0/h < 0.5$ is approximated by

$$\chi_{sh} = \frac{\varepsilon_{sh}}{h} \cdot \frac{1}{2}\left(1 - \cos \pi \frac{e_0}{h}\right), \tag{8}$$

where χ is the shrinkage curvature (Fig. 2.).

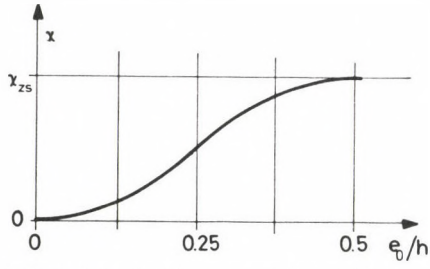

Fig. 2. Variation of shrinkage curvature with eccentricity

Neglecting longitudinal variation of shrinkage curvature, on the safety side, and applying values of the cross section with a maximum ordinate, shrinkage imperfection $w_{0,sh}$ becomes, also taking shell effect factor 0.5 into consideration:

$$w_{0,sh} \approx 0.5 \cdot \frac{R}{6000} \cdot \frac{1}{2}\left(1 - \cos \pi \frac{e_0}{h}\right). \tag{9}$$

Obtained $R/w_{0,sh}$ values rounded out have been compiled as:

$e_0/h =$	0	0.1	0.2	0.3	0.4	0.5
$R/w_{0,sh}$	∞	490 000	125 000	58 200	34 700	24 000

Initial imperfection w_0 is about $R/3000$ [3]. Hence, for the usual $e_0/h < 0.3$ values, shrinkage imperfection increment is at most one twentieth of the accidental imper-

fection. Since also the random imperfection values has been assumed by assessment, shrinkage imperfection increment is deemed to be negligible in practical cases.

References

1. Kollár, L., Dulácska, E.: Schalenbeulung. Theorie und Ergebnisse der Stabilität gekrümmter Flächentragwerke. Werner V, Düsseldorf 1975
2. Leonhard, F.: Vorlesungen über Massivbau. Springer V, Berlin–Heidelberg–New York 1978
3. Dulácska, E.: Die Beulung von Stahlbetonschalen. Acta Techn. Hung. 86 (1978), 33–115

Acta Technica Academiae Scientiarum Hungaricae, 97 (1—4), pp. 11—22 (1984)

RELATION BETWEEN THE INITIAL IMPERFECTION AND THE ECCENTRICITY OF NORMAL FORCES OF SHELL STRUCTURES

E. DULÁCSKA*

[Received: 27 September 1983]

For the dimensioning of the cross section and stability analysis of shell structures the knowledge of the eccentricity of the normal forces of the shell is necessary. Eccentricity may also be caused by a random imperfection but its value and the value of the amplitude of imperfection are not the same. The purpose of this paper is to evaluate the eccentricity mentioned above. The evaluation is presented for cases of shell structures of different types of surfaces, supports and loadings, and eventually also suggests an approximate assumption of the eccentricity.

1. Introduction

It is known that the critical load of shell structures decreases by the increase of the random imperfection amplitude [1].

It is also known that the values of the stiffness and load carrying capacity of the cross section made of non-elastic materials or reinforced concrete structures decrease by the increase of the eccentricity of cross sectional forces [2], [3].

The decrease of the values of the characteristics mentioned above is connected with the preliminary effect whereby an accentuated reduction of the critical loading takes place. That is why the value of the eccentricity of the cross sectional force is to be known for the dimensioning of the shell structure. The eccentricity originated from the calculated loading is obtained by the analysis carried out by making use of the theory of bending. However, no procedure of analysis exists for the evaluation of the eccentricity associated with an imperfection of random character. This paper is intended to analyse this problem.

2. Basic relations

In connection with the following calculations it is assumed that the theory of bending of shallow shells might be applied to the shell structure analysed. The problem is to find the initial eccentricity, so it can be assumed that the deformations are of low value, and the shell structure may be considered elastic. The loading applied to the shell

* E. Dulácska, H-1022 Budapest, Kitaibel P. u. 12, Hungary

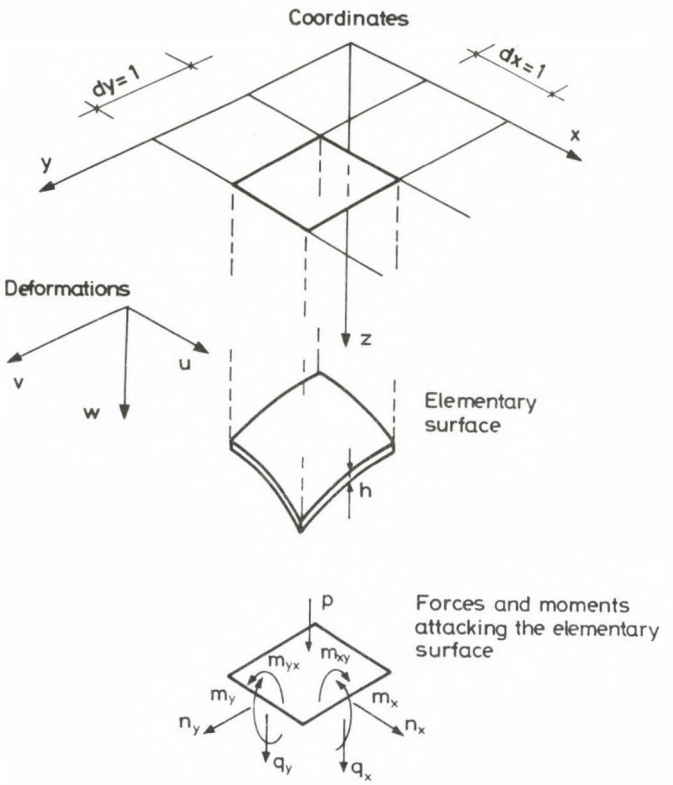

Fig. 1

structure, the forces on the cross section and its deformations are considered positive in the case represented in Fig. 1. In the calculation the derivation with respect to x and y is designated with a prime and overpoint respectively.

The equations of equilibrium of the shells are as follows:

$$n_x^{\mathrm{I}} + \dot{n}_{yx} = 0\,, \tag{1a}$$

$$\dot{n}_y + n'_{xy} = 0\,. \tag{1b}$$

Making use of $n_{xy} = n_{yx}$,

$$\ddot{z} n_y + 2\dot{z}^{\mathrm{I}} n_{xy} + z^{\mathrm{II}} n_x + q_x^{\mathrm{I}} + \dot{q}_y + p = 0\,, \tag{1c}$$

$$m_x^{\mathrm{I}} + \dot{m}_{yx} + q_x = 0\,, \tag{1d}$$

$$\dot{m}_y + m_{xy}^{\mathrm{I}} + q_y = 0\,, \tag{1e}$$

$$z^{\mathrm{II}} m_{xy} - \dot{z}^{\mathrm{I}} m_x + \dot{z}^{\mathrm{I}} m_y - \ddot{z} m_{yx} = 0\,. \tag{1f}$$

Neglecting the cross contraction, the equations of deformation of the shell assume the form:

$$n_x = D(u^{\mathrm{I}} + w^{\mathrm{I}} z^{\mathrm{I}}), \tag{2a}$$

$$n_y = D(v^{\cdot} + w^{\cdot} z^{\cdot}), \tag{2b}$$

$$n_{xy} = \frac{D}{2}(u^{\cdot} + v^{\mathrm{I}} + w^{\cdot} z^{\mathrm{I}} + w^{\mathrm{I}} z^{\cdot}), \tag{2c}$$

$$m_x = -Bw^{\mathrm{II}}, \tag{2d}$$

$$m_y = -Bw^{\cdot\cdot}, \tag{2e}$$

$$m_{xy} = -Bw^{\mathrm{I}\cdot}. \tag{2f}$$

In the above equations, besides the notation used in Fig. 1, B means the bending or torsional stiffness, while D designates the strain or compression stiffness.

Let us introduce the stress function F. The relationship between F and the normal forces is expressed as follows:

$$n_x = F^{\cdot\cdot}, \tag{3a}$$

$$n_y = F^{\mathrm{II}}, \tag{3b}$$

$$n_{xy} = -F^{\mathrm{I}\cdot}. \tag{3c}$$

Taking Eqs (3) into account, it can be seen that Eqs (1a) and (1b) are satisfied. By replacing (1d) and (1e) into Eq. (1c) and by taking into consideration Eqs (3), we arrive at

$$z^{\cdot\cdot} F^{\mathrm{II}} - 2z^{\mathrm{I}\cdot} F^{\mathrm{I}\cdot} + z^{\mathrm{II}} F^{\cdot\cdot} + m_x^{\mathrm{II}} + 2m_{xy}^{\mathrm{I}\cdot} + m_y^{\cdot\cdot} + p = 0. \tag{4}$$

As is customary, in applying the theory of shallow shells neglects Eq. (1f) and makes use of the approximation $m_{xy} = m_{yx}$.

Substituting Eqs (2d), (2e) and (2f) into Eq. (4) we obtain

$$-B(w^{\mathrm{IV}} + 2w^{\mathrm{II}\cdot\cdot} + w^{\cdot\cdot\cdot\cdot}) + z^{\cdot\cdot} F^{\mathrm{II}} - 2z^{\mathrm{I}\cdot} F^{\mathrm{I}\cdot} + z^{\mathrm{II}} F^{\cdot\cdot} + p = 0. \tag{5}$$

Hereafter let us differentiate twice Eq. (2a) with respect to y and Eq. (2b) with respect to x and extract from the sum of them the double value of Eq. (2c) differentiated only once with respect to both x and y. Carrying out the above operations we arrive at the compatibility equation of the shell:

$$F^{\mathrm{IV}} + 2F^{\mathrm{II}\cdot\cdot} + F^{\cdot\cdot\cdot\cdot} = -D(w^{\cdot\cdot} z^{\mathrm{II}} - 2w^{\mathrm{I}\cdot} z^{\mathrm{I}\cdot} + w^{\mathrm{II}} z^{\cdot\cdot}) \tag{6}$$

In Eqs (4) and (6) z designates the deformed surface, i.e.,

$$z = z_0 + w_0 + w. \tag{7}$$

we assume that expressions

$$z_0^{\mathrm{II}} \gg w_0^{\mathrm{II}} \gg w^{\mathrm{II}} \tag{8a}$$

and

$$z_0'' \gg w_0'' \gg w'' \tag{8b}$$

and

$$F = F_0 + \Phi \tag{9}$$

hold.

Here z_0 is the designed perfect surface, w_0 the amplitude of the imperfection, w the vertical deformation component to the surface, F_0 the stress function of the membrane state of the perfect shell, and Φ is the stress function associated with the deformation w.

Introducing the relationships (7) and (9) into Eq. (5), we find the equilibrium equation of the shell

$$\begin{aligned} &B(w^{IV} + 2w^{II\cdot\cdot} + w'''') \quad \boxed{+F_0^{II} z_0''} \quad + F_0^{II}(w_0'' + w'') + \\ &+ \Phi^{II}(z_0'' + w_0'' + w'') \quad \boxed{-2F_0^{I\cdot} z_0^{I\cdot}} \quad - 2F_0^{I\cdot}(w_0^{I\cdot} + w^{I\cdot}) - \\ &- 2\Phi^{I\cdot}(z_0^{I\cdot} + w_0^{I\cdot} + w^{I\cdot}) \quad \boxed{+F_0'' z_0''} \quad + F_0^{II}(w_0^{II} + w^{II}) + \\ &+ \Phi''(z_0^{II} + w_0^{II} + w^{II}) \quad \boxed{+p} \quad = 0 \end{aligned} \tag{10}$$

In the above equation the terms in rectangles are the equations of the membrane equilibrium. Provided a membrane solution exists in the case in question, these terms express automatically equilibrium, therefore they can be omitted, and the residual terms also should express equilibrium.

Thus we arrive at the following equation:

$$\begin{aligned} &- B(w^{IV} + 2w^{II\cdot\cdot} + w'''') + F_0^{II}(w_0'' + w'') + \Phi^{II}(z_0'' + w_0'' + w'') - \\ &- 2F_0^{I\cdot}(w_0^{I\cdot} + w^{I\cdot}) - 2\Phi^{I\cdot}(z_0^{I\cdot} + w_0^{I\cdot} + w^{I\cdot}) + F_0''(w_0^{II} + w^{II}) + \\ &+ \Phi''(z_0^{II} + w_0^{II} + w^{II}) = 0\,. \end{aligned} \tag{11}$$

In consequence of the assumption expressed by inequality (8) the second derivatives of w may be neglected besides the second derivatives w_0^{II}, likewise the second derivatives w_0 and w besides the second derivatives of z_0.

Carrying out the neglects in Eq. (11) and concentrating the analyses on the case $z_0^{I\cdot} = 0$ and $F_0^{I\cdot} = 0$, we obtain

$$- B(w^{IV} + 2w^{II\cdot\cdot} + w'''') + F_0^{II} w_0'' + \Phi^{II} z_0'' + F_0'' w_0^{II} + \Phi'' z_0^{II} = 0\,. \tag{12}$$

In the following let us have $z_0^{II} = \alpha$; $z_0'' = \beta$; $F_0'' = n_{x0}$ and $F_0^{II} = n_{y0}$. Using this notation, Eq. (12) takes the form

$$- B(w^{IV} + 2w^{II\cdot\cdot} + w'''') + \alpha\Phi'' + \beta\Phi^{II} + n_{x0} w_0^{II} + n_{y0} w_0'' = 0\,. \tag{13}$$

The analysis will be continued by making use of Eq. (13).

3. Relationship between the imperfection of the shell surface and the eccentricity of the force acting on the cross section of that surface

For evaluating the eccentricity e of a cross-sectional force associated with a given imperfection w_0, a deformation w should be applied to the shell, and the eccentricity is obtained as the ratio of the bending moment incited by the deformation and the sum of the membrane force augmented by the primary cross-sectional force. The analyses are concentrated on shells wherewith $z_0^{\prime}=0$, while $z_0^{\prime\prime}$ and $z_0^{\cdot\cdot}$ are constant. Besides, it is assumed that the shape and extent of the imperfection is conform with the waves of buckling, because, in general, the critical load is in this case the lowest. Under such circumstances the solution may be found in the form of sine function product while the variable part of the function disappears from the equations.

As with what was said above, the compatibility equation can be written in the following form:

$$\Phi_0 a^4 + 2\Phi_0 a^2 b^2 + \Phi_0 b^4 = D(b^2\alpha + a^2\beta)W. \tag{14}$$

Herein

$a^2=\pi^2/l_x^2$, $b^2=\pi^2/l_y^2$, $\alpha=1/R_x$, $\beta=1/R_y$,
W_0 and W = amplitude of imperfection and buckling deformation, respectively,
D = strain or compressive stiffness,
Φ_0 = constant of the stress function
and
l_x and l_y = wave-length of buckling in directions x and y, respectively
R_x and R_y = radius of curvature projected to planes x, z and y, z, respectively.

From equation (14)

$$\Phi_0 = D\frac{\alpha b^2 + \beta a^2}{(a^2+b^2)^2}W \tag{15}$$

can be expressed.

Dropping the sine members and making use of Eq. (15), the equilibrium Eq. (13) of the shell takes the form

$$-BW(a^4+2a^2b^2+b^4)+DW\frac{\alpha b^2+\beta a^2}{(a^2+b^2)^2}(\alpha b^2+\beta a^2)=$$

$$=\pi^2 W_0\left(\frac{n_{x0}}{l_x^2}+\frac{n_{y0}}{l_y^2}\right). \tag{16}$$

In the above equation

B = bending stiffness,
n_{x0}, n_{y0} = membrane forces in directions x and y respectively (prior to deformation).

The value of amplitude of W can be expressed from Eq. (16):

$$W = W_0\frac{n_{x0}a^2+n_{y0}b^2}{B(a^2+b^2)^2+D\left(\frac{\alpha b^2+\beta a^2}{a^2+b^2}\right)^2}. \tag{17}$$

The values of e_x and e_y i.e. the eccentricities defined on planes x, z and y, z, respectively are as follows:

$$e_x = \frac{Bw^{II}}{n_{x0} + F^{\cdot\cdot}}, \qquad e_y = \frac{Bw^{\cdot\cdot}}{n_y^0 + F^{II}}. \tag{18), (19}$$

And for the sine deformation we have

$$w^{II} = Wa^2, \tag{20}$$

$$w^{\cdot\cdot} = Wb^2, \tag{21}$$

$$F^{\cdot\cdot} = \Phi_0 b^2, \tag{22}$$

$$F^{II} = \Phi_0 a^2. \tag{23}$$

Let us introduce the notations:

$$\rho = \frac{a^2}{b^2} = \frac{l_y^2}{l_x^2}, \qquad \eta = \frac{n_{y0}}{n_{x0}}, \qquad k = \frac{\alpha}{\beta} = \frac{R_y}{R_x},$$

$$M = \eta + \rho, \qquad N = k + \rho, \qquad P = 1 + \rho. \tag{24}$$

Using the above abbreviations in Eq. (15) yields:

$$\Phi_0 b^2 = \frac{DW}{R_y} \cdot \frac{N}{P^2}, \tag{25}$$

and in Eq. (17):

$$W = W_0 n_{x0} b^2 \frac{M}{Bb^4 P^2 + \frac{D}{R_y^2} \cdot \frac{N^2}{P^2}}. \tag{26}$$

Substituting the values of (25) and (26) into the relationships (18) and (19) and using expressions (20) to (23) we obtain

$$e_x = \frac{B\rho b^4 W_0 n_{x0} \left(\frac{M}{Bb^4 P^2 + DN^2/R_y^2 P^2} \right)}{n_{x0} + \frac{DW_0 n_{x0} b^2}{R_y} \left(\frac{NM}{Bb^4 P^4 + DN^2/R_y^2} \right)}. \tag{27}$$

The value of e_y may similarly be calculated. Let us introduce $R = R_y$, $B = Eh^3/12$ and $D = Eh$, wherein E is the modulus of elasticity and h is the thickness of the shell. By using also the designation $\gamma = b^2 Rh$, we obtain the following simpler forms:

$$\frac{e_x}{W_0} = \frac{\frac{\rho M}{P^2 + 12N^2/\gamma^2 P^2}}{1 + \frac{W_0}{h} \left(\frac{NM}{P^4 \gamma/12 + N^2/\gamma} \right)}, \tag{28}$$

$$\frac{e_y}{W_0} = \frac{1}{\eta} \cdot \frac{\dfrac{M}{\sqrt{P^2 + 12N^2/\gamma^2 P^2}}}{1 + \dfrac{\rho W_0}{\eta h}\left(\dfrac{NM}{P^4\gamma/12 + N^2/\gamma}\right)}. \tag{29}$$

Knowing both of these expressions, the relative eccentricity $c = e/W$ can be evaluated for each type of shells.

4. Examples to initial eccentricity

In the following, the relative eccentricity will be evaluated for several types of shells as well as for different loadings and shapes of buckling. In the case of a square-shaped buckling form, the mean value of the bidirectional eccentricity, in the case of a buckling of oblong shape, the eccentricity coinciding with the shorter wave-length of the buckling may be considered critical. The results are presented in tables, without the detailed calculations. We have to take the values in the thick rectangles to the analysis into account.

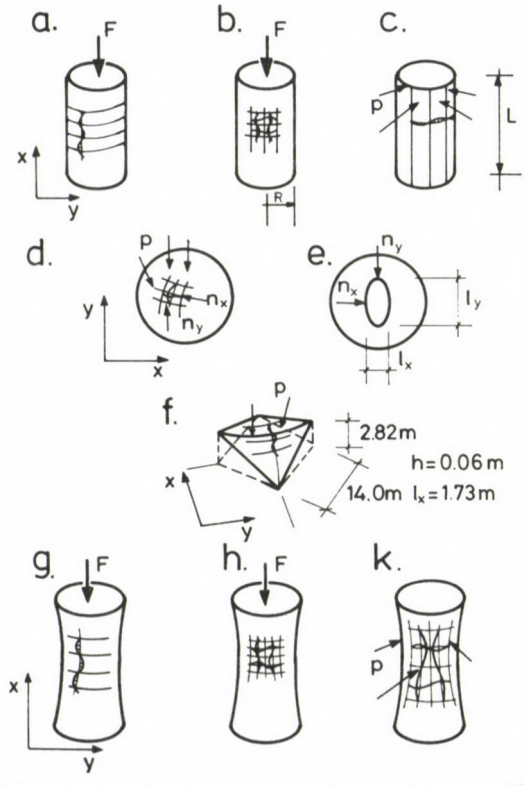

Fig. 2. Waviness of imperfections for the evaluation of eccentricity caused by the imperfection

4.1. Axially compressed cylinder, ring buckling (Fig. 2a)

$$\rho \to \infty\,, \qquad \eta = k = 0\,, \qquad \gamma = \frac{a^2}{\rho}\, Rh = \frac{\pi^2}{1.69^2 \rho}\,,$$

$$a^2 = (\pi/l)^2 = \pi^2/1.69^2\, Rh\,.$$

W_0/h	e_x/W_0	e_y/W_0
0	0.5	0
0.1	0.5	0
0.25	0.5	0
0.50	0.5	0

4.2. Axially compressed cylinder

$l_x/l_y = 1$, buckling of reticulated pattern (Fig. 2b)

$$\rho = 1\,, \qquad k = 0\,,$$

$$\eta \to \infty\,,$$

$$\gamma = \frac{\sqrt{3}}{2} = 0.87.$$

W_0/h	e_x/W_0	e_y/W_0	$\frac{e_x + e_y}{2W_0}$
0	0.125	∞	∞
0.1	0.124	2.900	1.512
0.25	0.113	1.155	0.634
0.50	0.103	0.577	0.340

4.3. Cylinder subjected to radial pressure (Fig. 2c)

$L/R = 6$, number of waves of waves along the ring direction

$$n = 4\,, \qquad R/h = 200\,, \qquad p = 0.017\,, \qquad \eta = 10\,000\,,$$

$$k = 0\,, \qquad R = 1\,, \qquad l_y = 0.785\,, \qquad \gamma = \frac{\pi^2 Rh}{l_y^2} = 0.080\,.$$

W_0/h	e_x/W_0	e_y/W_0
0	∞	0.642
0.1	0.685	0.642
0.25	0.028	0.637
0.50	0.014	0.633

4.4. Sphere subjected to radial pressure (Fig. 2d)

$$\rho = 1\,, \qquad \eta = 1\,, \qquad k = 1\,, \qquad \gamma = \sqrt{3}$$

$$n_x/n_y = 1.0\,.$$

W_0/h	e_x/W_0	e_y/W_0	$\frac{e_x+e_y}{2W_0}$
0	0.25	0.25	0.25
0.1	0.23	0.23	0.23
0.25	0.21	0.21	0.21
0.50	0.174	0.174	0.174

4.5a. Sphere with non-symmetrical stress pattern (Fig. 2e) (for example, dome shells)

$$l_y/l_x = 2\,, \qquad n_x/n_y = 2\,,$$

$$\rho = 4\,, \qquad \eta = 0.5\,, \qquad k = 1.00\,, \qquad \gamma = 2.77\,.$$

W_0/h	e_x/W_0	e_y/W_0
0	0.678	0.339
0.1	0.668	0.303
0.25	0.654	0.262
0.50	0.631	0.213

4.5b. Sphere with the same buckling pattern like in the case above (Fig. 2e)

but $n_x/n_y = 10\,, \qquad \eta = 0.1\,.$

W_0/h	e_x/W_0	e_y/W_0
0	0.617	1.543
0.1	0.609	1.006
0.25	0.597	0.660
0.50	0.579	0.420

4.5c. Sphere with the same buckling pattern as under the above points (Fig. 2e)

but $n_x/n_y = 1.0 \qquad \eta = 1.0\,.$

W_0/h	e_x/W_0	e_y/W_0
0	0.753	0.188
0.1	0.741	0.177
0.25	0.723	0.162
0.50	0.696	0.142

4.6. Hypar shell over a rectangular ground plan supported along its generatrices (Fig. 2f) (data of an actual shell)

$$\rho = 66\,, \qquad \eta = 1\,, \qquad k = -1\,, \qquad \gamma = 0.053$$

W_0/h	e_x/W_0	e_y/W_0
0	0.504	0
0.01	0.503	0
0.10	0.501	0
0.25	0.498	0

4.7a. Hyperboloid shell of revolution (Fig. 2g) subjected to axial pressure with a ring buckling

$$\rho \to \infty\,, \qquad \eta = 0.2\,, \qquad k = -0.2\,, \qquad \gamma = \pi^2/1.69^2\rho$$

W_0/h	e_x/W_0	e_y/W_0
0	0.50	0.002
0.1	0.50	0.001
0.25	0.50	0.001
0.50	0.50	0

4.7b. The same hyperboloid of revolution (Fig. 2g) as above, however with a buckling of reticulated pattern (Fig. 2h)

$l_x/l_y = 1$, $\rho = 1$, $\eta = 0.2$, $k = -0.2$, $\gamma \approx 0.87$.

W_0/h	e_x/W_0	e_y/W_0	$\frac{e_x + e_y}{2W_0}$
0	0.184	0.918	0.551
0.1	0.175	0.732	0.454
0.25	0.163	0.562	0.363
0.50	0.146	0.405	0.276

4.7c. The same hyperboloid of revolution as above, however, subjected to radial pressure (Fig. 2k)

$\rho = 0.052$, $\eta = 10\,000$, $k = -0.2$, $\gamma = 0.350$

W_0/h	e_x/W_0	e_y/W_0
0	170	0.328
0.01	−1.14	0.329
0.10	−0.113	0.331
0.25	−0.045	0.335
0.50	−0.023	0.342

4.8. Hyperboloid of revolution subjected to axial pressure (data of an actual shell)

$R_0 = 35.0$ m, $h = 0.19$ m, number of waves along x-axis: $n = 7$.

$l_y = 13.7$ m, $l_x = 60$ m, $\rho = 0.052$, $\eta = 0.2$,

$$k = -0.2, \qquad \gamma = \frac{35 \cdot 0.19 \cdot \pi^2}{13.7^2} = 0.350$$

W_0/h	e_x/W_0	e_y/W_0
0	0.004	0.413
0.1	0.004	0.418
0.25	0.005	0.424
0.50	0.005	0.435

4.9. Approximate upper bounds

On the basis of what was said above, within the limiting values $0.167 < W_0/h < 0.5$, the following values of relative eccentricity $c = e_0/W_0$ might be suggested for good approximate upper bounds:

Type of shell	Suggested value of c
Cylinder	1.00
Sphere	0.25
Dome-shell	0.67
Saddle-shaped shell	0.50
Hyperboloid of revolution	0.50
With safety to all types of shell	1.00

References

1. Kollár, L., Dulácska, E.: Buckling of Shells for Engineers. John Wiley and Sons Chichester, New York, Brisbane, Toronto 1984
2. Dulácska, E.: Buckling of elastic-plastic shells. IASS Bulletin 68 (1978), 15–20.
3. Dulácska, E.: Buckling of reinforced concrete shells. Journal of Structural Div. ASCE. Dec. 1981.

Acta Technica Academiae Scientiarum Hungaricae, 97 (1—4), pp. 23—38 (1984)

ON THE TORSION OF THIN-WALLED BARS WITH AN ANNULUS CROSS-SECTION OF VARIABLE SIZE

I. ECSEDI*

[Received: 29 March 1983]

The paper deals with the torsion of thin-walled elastic bars with an annulus cross-section of variable size. The intensity of the continuous load acting on the surface of the bar elastically supported along its entire length is proportional to the displacement of the points of the surface. The boundary value problem of torsion and also inequalities for the torsional rigidity of the bar are presented. The demonstration of these inequalities is based on Schwarz's inequality. Numerical examples show the practical application of the inequalities.

Symbols

r, φ, z	polar co-ordinates,
$\mathbf{e}_r, \mathbf{e}_\varphi, \mathbf{e}_z$	unit vectors in the polar co-ordinate system,
$\mathbf{u} = v(r, z)\mathbf{e}_\varphi$	displacement vector,
ϑ	the angle of rotation of the cross-section defined by $z = l$.
l	the length of the bar,
$\psi = \psi(r, z)$	auxiliary function,
T	the planar domain xy defined by the meridian section of the bar (Fig. 2),
$\partial T = \partial T_1 \cup \partial T_2 \cup \partial T_3 \cup \partial T_4$	the boundary of domain T (Fig. 2),
$\mathbf{p}_3 = \mathbf{p}_3\mathbf{e}_\varphi, \quad \mathbf{p}_4 = \mathbf{p}_4\mathbf{e}_\varphi$	surface load,
G	shearing rigidity of the bar,
k	constant characterizing the elastic support,
$R_3 = R_3(z) \quad (0 \leqq z \leqq l)$	the equation of curve ∂T_3,
$R_4 = R_4(z) \quad (0 \leqq z \leqq l)$	the equation of curve ∂T_4,
$\partial/\partial n$	the sign of derivation in the direction of the external normal to curve ∂T,
$h = R_4(z) - R_3(z)$	the thickness of the bar measured in the direction of the radius of the cross-section,
$R = R(z) \quad (0 \leqq z \leqq l)$	the equation of curve γ (Fig. 3),
$\mathbf{t} = t_r\mathbf{e}_r + t_z\mathbf{e}_z$	the unit vector of the tangent to curve γ (Fig. 3),
s	arc co-ordinate measured along curve γ (Fig. 3),
$\tau_{r\varphi}, \tau_{z\varphi}, \tau_{s\varphi}, \tau_{n\varphi}$	shearing stresses,
M	torque acting on the cross-section defined by $z = l$,
$m = m(z)$	torque acting on the cross-section defined by z,
$f = f(z) \quad (0 \leqq z \leqq l)$	auxiliary function,
S	torsional rigidity,
$\mathbf{b} = \mathbf{b}(z) = [b_1(z), b_2(z)]$	two dimensional vector,

* I. Ecsedi, H-3524 Miskolc, Hungary, Klapka Gy. u. 36, IX/2

$\mathbf{c} = \mathbf{c}(z) = [c_1(z), c_2(z)]$ two dimensional vector,
$\mathbf{q} = \mathbf{q}(z) = [q_1(z), q_2(z)]$ two dimensional vector,
$g = g(z),\ b = b(z),\ F = F(z)\quad (0 \leq z \leq l)$ auxiliary functions

and

$A(z) = R^3(z)/\{1 + [R'(z)]^2\}$,
$B(z) = R^3(z)\sqrt{1 + [R'(z)]^2}$,

Further symbols and variables are defined in the text.

1. Introduction, basic relations

Figure 1 shows a bar with an annulus cross-section of variable size. The volume of the bar and its cross-section defined by $z = 0$ are unloaded. The displacement vector of the points of the cross-section defined by $z = l$ is prescribed as

$$\mathbf{u}_2 = \vartheta r \mathbf{e}_\varphi\,, \qquad z = l\,. \tag{1.1}$$

The bar is subjected to distributed loads of intensity

$$\mathbf{p}_3 = p_3(r, z)\mathbf{e}_\varphi; \qquad \mathbf{p}_4 = p_4(r, z)\mathbf{e}_\varphi$$

both in its internal and external surfaces. The loads acting on the internal and external surfaces and on the cross-section defined by $z = l$ are in equilibrium.

The usual assumptions of elasticity are applied, i.e.:

— deformations and displacements are small,

— no initial stresses and deformation exist,

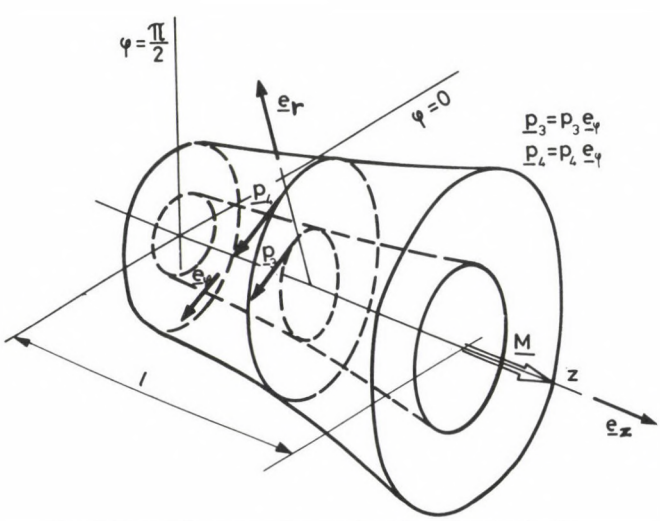

Fig. 1. Bar with an annulus cross-section of variable size

— the effect of heat is negligible,
— the material of the bar is homogeneous, isotropic and linearly elastic,
— the problem is a quasistatic one, etc.

The general solution to the problem of torsion of bars with an annulus cross-section of variable size was presented by I. H. Michell [1], A. Föppl [2], Fr. Willers [3] and A. Timpe [4]. According to their results, the scalar co-ordinates of the stress tensor, not identically equal to zero, can be presented as

$$\tau_{r\varphi} = Gr\frac{\partial \psi}{\partial r}, \qquad \tau_{z\varphi} = G\frac{\partial \psi}{\partial z} \tag{1.2), (1.3}$$

and the displacement vector field $\mathbf{u}$ can be obtained from

$$\mathbf{u} = \mathbf{u}(r, \varphi, z) = v(r, z)\mathbf{e}_\varphi = r\psi(r, z)\mathbf{e}_\varphi . \tag{1.4}$$

The function of two variables $\psi = \psi(r, z)$ in the above formulas satisfies the partial differential equation

$$\frac{\partial^2 \psi}{\partial r^2} + \frac{3}{r}\frac{\partial \psi}{\partial r} + \frac{\partial^2 \psi}{\partial z^2} = 0, \qquad (r, z) \in T. \tag{1.5}$$

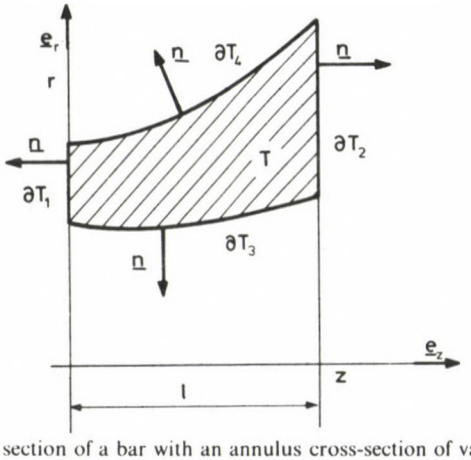

Fig. 2. Meridian section of a bar with an annulus cross-section of variable size

The load of the bar and the kinematic restriction related to the cross-section defined by $z = l$ are given by the following boundary conditions (Fig. 2):

$$Gr\frac{\partial \psi}{\partial n} = p_3, \qquad (r, z) \in \partial T_3 , \tag{1.6}$$

$$Gr\frac{\partial \psi}{\partial n} = p_4, \qquad (r, z) \in T_4 , \tag{1.7}$$

$$\frac{\partial \psi}{\partial n} = 0 \qquad (r, z) \in T_1 , \tag{1.8}$$

$$\psi = \vartheta \qquad (r, z) \in T_2 . \tag{1.9}$$

In the case of a bar subjected to continuous elastic supports, the load on the external surface of the bar is proportional to the displacement of the points of the surface, i.e. we have

$$p_3 = -kv = -kr\psi, \qquad (r, z) \in \partial T_3 , \tag{1.10}$$

$$p_4 = -kv = -kr\psi, \qquad (r, z) \in \partial T_4 . \tag{1.11}$$

2. Approximate solution for thin-walled bars

Figure 3 shows the meridional section of a thin-walled bar. We shall only deal with the case where the wall thickness is constant:

$$h = R_4(z) - R_3(z) = \text{constant}, \quad (0 \leqq z \leqq l) . \tag{2.1}$$

Let us consider curve γ defined by the equation

$$R = R(z) = 0.5(R_3(z) + R_4(z)) . \tag{2.2}$$

Denoting the unit vector of the tangent to γ by t and the arc co-ordinate measured along γ by s, we have

$$\mathbf{t} = t_r \mathbf{e}_r + t_z \mathbf{e}_z = \frac{\mathrm{d}R}{\mathrm{d}s} \mathbf{e}_r + \frac{\mathrm{d}z}{\mathrm{d}s} \mathbf{e}_z . \tag{2.3}$$

The shearing stress $\tau_{s\varphi}$ parallel to the tangent to curve γ is obtained from the following formula [5]:

$$\tau_{s\varphi} = \tau_{r\varphi} t_r + \tau_{z\varphi} t_z = GR \left(\frac{\partial \psi}{\partial r} \frac{\mathrm{d}R}{\mathrm{d}s} + \frac{\partial \psi}{\partial z} \frac{\mathrm{d}z}{\mathrm{d}s} \right) = GR \frac{\partial \psi}{\partial s} . \tag{2.4}$$

Domain T and its boundary

$$\partial T = \partial T_1 \, U \partial T_2 \, U \partial T_3 \, U \partial T_4$$

are represented in Fig. 2.

We assume that formulas

$$\mathbf{u}(r, \varphi, z) = R\psi(s) \mathbf{e}_\varphi , \tag{2.5}$$

$$\tau_{s\varphi} = \tau_{s\varphi}(s) , \tag{2.6}$$

$$\tau_{n\varphi} = 0 \tag{2.7}$$

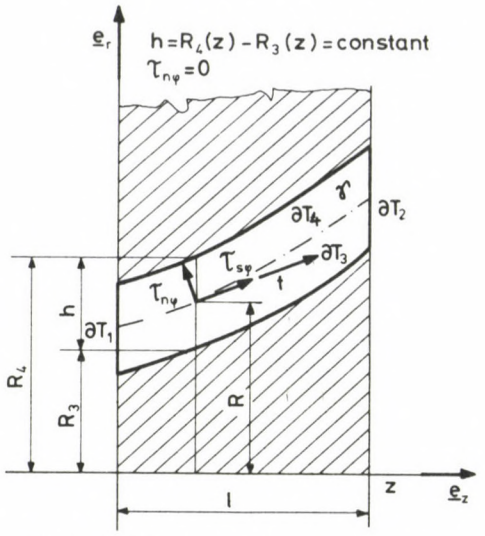

Fig. 3. Meridian section of a thin-walled bar

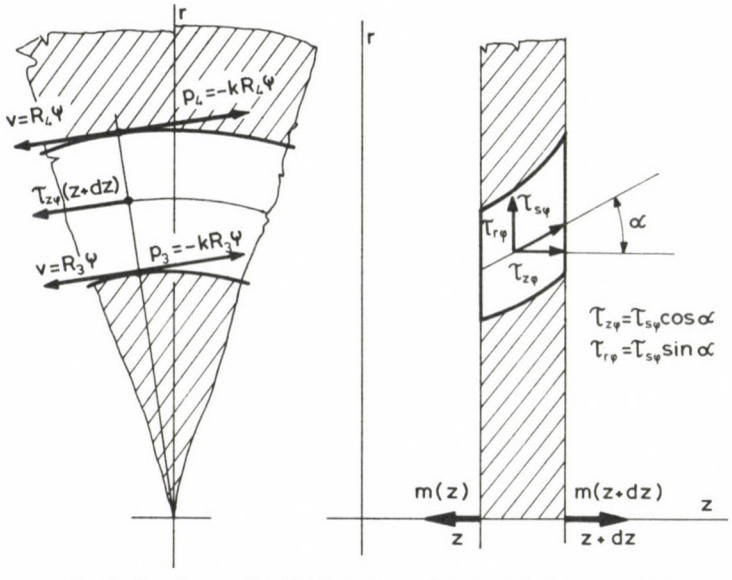

Fig. 4. Bar element for the derivation of the equilibrium equations

hold (Fig. 3) and, for the derivation of the equilibrium equations, we shall apply the following approximation:

$$R_3 = R - 0.05h \cong R\,, \tag{2.8}$$

$$R_4 = R + 0.5h \cong R\,. \tag{2.9}$$

The equilibrium condition of the bar element limited by z and $z+\mathrm{d}z$ (Fig. 4) is expressed by

$$\frac{\mathrm{d}m}{\mathrm{d}z}+2\pi(p_3+p_4)R^2\frac{\mathrm{d}s}{\mathrm{d}z}=0\,, \tag{2.10}$$

where we have

$$p_3=p_4=-kR\psi\,, \tag{2.11}$$

$$\cos\alpha=\frac{1}{\sqrt{1+(R'(z))^2}}\,, \tag{2.12}$$

$$\frac{\mathrm{d}s}{\mathrm{d}z}=\sqrt{1+(R'(z))^2}\,, \tag{2.13}$$

$$\tau_{s\varphi}=GR\frac{\mathrm{d}\psi}{\mathrm{d}s}=GR\frac{\mathrm{d}\psi}{\mathrm{d}z}\frac{\mathrm{d}z}{\mathrm{d}s}=G\frac{R(z)}{\sqrt{1+(R'(z))^2}}\frac{\mathrm{d}\psi}{\mathrm{d}z} \tag{2.14}$$

and

$$m(z)=2\pi R^2h\,\tau_{s\varphi}\cos\alpha \tag{2.15}$$

is the torque acting on the cross-section defined by z.

We should point out that the relation

$$\tau_{z\varphi}=\tau_{s\varphi}\cos\alpha=G\frac{R(z)}{1+(R'(z))^2}\frac{\mathrm{d}\psi}{\mathrm{d}z} \tag{2.16}$$

also holds.

Combining Eqs (2.10)...(2.15), we arrive at

$$Gh\frac{\mathrm{d}}{\mathrm{d}z}\left(\frac{R^3}{1+(R')^2}\frac{\mathrm{d}\psi}{\mathrm{d}z}\right)-2kR^3\sqrt{1+(R')^2}\psi=0,\qquad 0<z<l\,. \tag{2.17}$$

The cross-section defined by $z=0$ is unloaded, i.e.

$$\tau_{z\varphi}(0)=G\left[\frac{R}{1+(R')^2}\frac{\mathrm{d}\psi}{\mathrm{d}z}\right]_{z=0}=0\,, \tag{2.18}$$

so that condition

$$\left[\frac{\mathrm{d}\psi}{\mathrm{d}z}\right]_{z=0}=0 \tag{2.19}$$

must hold.

Since the displacement of the points of the cross-section $z=l$ is prescribed, i.e. $v_2=\vartheta R$, the boundary condition for $z=l$ emerges as

$$\psi(l)=\vartheta\,. \tag{2.20}$$

Let function f be taken as

$$f=f(z)=\frac{\psi(z)}{\vartheta}. \tag{2.21}$$

Making use of Eqs (2.17), (2.19) and (2.20), the torsional problem of an elastic bar with a thin-walled annulus section of variable size, subjected to an elastic support along its entire length, is characterized by the following boundary value problem:

$$Gh\frac{\mathrm{d}}{\mathrm{d}z}\left(A\frac{\mathrm{d}f}{\mathrm{d}z}\right)-2kBf=0, \qquad 0<z<l, \tag{2.22}$$

$$\frac{\mathrm{d}f}{\mathrm{d}z}=0 \qquad z=0, \tag{2.23}$$

$$f=1, \qquad z=l. \tag{2.24}$$

In Eq. (2.22) the notation

$$A(z)=\frac{(R(z))^3}{1+(R'(z))^2}, \tag{2.25}$$

$$B(z)=(R(z))^3\sqrt{1+(R'(z))^2} \tag{2.26}$$

was introduced. Functions $A(z)$ and $B(z)$ fulfil the conditions

$$A(z)>0, \qquad B(z)>0. \qquad (0\leq z\leq l).$$

Knowing function $f=f(z)$, the shearing stresses $\tau_{s\varphi}=\tau_{s\varphi}(z)$ and $\tau_{z\varphi}=\tau_{z\varphi}(z)$ can be determined from

$$\tau_{s\varphi}(z)=G\vartheta\frac{R}{\sqrt{1+(R')^2}}\frac{\mathrm{d}f}{\mathrm{d}z}, \tag{2.27}$$

$$\tau_{z\varphi}(z)=G\vartheta\frac{R}{1+(R')^2}\frac{\mathrm{d}f}{\mathrm{d}z}. \tag{2.28}$$

The cross-section defined by $z=l$ is subjected to the torque

$$M=2\pi GhR^2\tau_{z\varphi}(l)=\vartheta\left\{2\pi Gh\left[\frac{R^3}{1+R'^2}\frac{\mathrm{d}f}{\mathrm{d}z}\right]_{z=l}\right\}=$$

$$=\vartheta 2\pi GhA(l)\left[\frac{\mathrm{d}f}{\mathrm{d}z}\right]_{z=l}. \tag{2.29}$$

Defining the torsional rigidity of the thin-walled elastic bar with an annulus cross-section of variable size subjected to an elastic support as

$$S=\frac{M}{\vartheta}, \tag{2.30}$$

formulas (2.29) and (2.30) result in

$$S=2\pi GhA(l)\left[\frac{\mathrm{d}f}{\mathrm{d}z}\right]_{z=l} \tag{2.31}$$

for the torsional rigidity S.

In the following, two more formulas will be derived for the calculation of the torsional rigidity. Integrating Eq. (2.22), we obtain

$$Gh\int_0^l \frac{\mathrm{d}}{\mathrm{d}z}\left(A\frac{\mathrm{d}f}{\mathrm{d}z}\right)\mathrm{d}z-2k\int_0^l Bf\,\mathrm{d}z=$$

$$=GhA(l)\left[\frac{\mathrm{d}f}{\mathrm{d}z}\right]_{z=l}-GhA(0)\left[\frac{\mathrm{d}f}{\mathrm{d}z}\right]_{z=l}-2k\int_0^l Bf\,\mathrm{d}z\,. \tag{2.32}$$

Making use of Eqs. (2.23), (2.32) and formula (2.31), we arrive at

$$S=4\pi k\int_0^l Bf\,\mathrm{d}z\,. \tag{2.33}$$

Integrating the equation

$$Ghf\frac{\mathrm{d}}{\mathrm{d}z}\left(A\frac{\mathrm{d}f}{\mathrm{d}z}\right)-2kBf^2=0 \tag{2.34}$$

by parts, we find

$$Gh\int_0^l f\frac{\mathrm{d}}{\mathrm{d}z}\left(A\frac{\mathrm{d}f}{\mathrm{d}z}\right)\mathrm{d}z-2k\int_0^l Bf^2\mathrm{d}z=Gh\left[Af\frac{\mathrm{d}f}{\mathrm{d}z}\right]_{z=l}-$$

$$-Gh\left[Af\frac{\mathrm{d}f}{\mathrm{d}z}\right]_{z=0}-Gh\int_0^l A\left(\frac{\mathrm{d}f}{\mathrm{d}z}\right)^2\mathrm{d}z-2k\int_0^l Bf^2\mathrm{d}z=0\,. \tag{2.35}$$

The combination of Eqs (2.23), (2.24), (2.35) and formula (2.31) yields

$$S=2\pi\left[Gh\int_0^l A\left(\frac{\mathrm{d}f}{\mathrm{d}z}\right)^2\mathrm{d}z+2k\int_0^l Bf^2\mathrm{d}z\right]. \tag{2.36}$$

Formula (2.36) and Eqs (2.22), (2.23), (2.24) show that torsional rigidity S is always a positive quantity, i.e. $S>0$.

The exact value of the torsional rigidity S defined by Eq. (2.30) could be obtained by solving the ordinary second order differential equation of variable coefficients (2.22) taking into consideration the boundary conditions (2.23), (2.24). In several cases, however, this problem has no solution closed form. This fact shows the importance of the inequalities with which lower and upper bounds can be given for the calculation of the torsional rigidity, without knowing the solution function of the boundary value problem defined by Eqs (2.22), (2.23), (2.24).

3. Bounds for the torsional rigidity

3.1 Theorem

Inequality

$$S \leq 2\pi \frac{Gh \int_0^l A \left(\frac{dg}{dz} \right)^2 dz + 2k \int_0^l Bg^2 dz}{[g(l)]^2} \tag{3.1}$$

holds for any function of one variable $g = g(z)$ which is continuous in the closed interval $0 \leqq z \leqq l$ and is continuously differentiable in sections in the open interval $0 < z < l$ and which fulfils the condition

$$g(l) \neq 0 . \tag{3.2}$$

Demonstration

Introducing the auxiliary quantities

$$a(f, g) = Gh \int_0^l A \frac{df}{dz} \frac{dg}{dz} dz + 2k \int_0^l Bfg \, dz , \tag{3.3}$$

$$a(f, f) = Gh \int_0^l A \left(\frac{df}{dz} \right)^2 dz + 2k \int_0^l Bf^2 \, dz , \tag{3.4}$$

$$a(g, g) = Gh \int_0^l A \left(\frac{dg}{dz} \right)^2 dz + 2k \int_0^l Bg^2 \, dz \tag{3.5}$$

and making use of Schwarz's inequality, we obtain

$$|a(f, g)|^2 \leq a(f, f) a(g, g) . \tag{3.6}$$

Quantity $a(f, g)$ can also be written in another form:

$$a(f, g) = Gh \int_0^l A \frac{df}{dz} \frac{dg}{dz} dz + 2k \int_0^l Bfg \, dz = Gh \left[Ag \frac{df}{dz} \right]_{z=l} -$$

$$- Gh \left[Ag \frac{df}{dz} \right]_{z=0} - \int_0^l \left[Gh \frac{d}{dz} \left(A \frac{df}{dz} \right) dz - 2kBf \right] g \, dz =$$

$$= Gh \, g(l) \, A(l) \left[\frac{df}{dz} \right]_{z=l} . \tag{3.7}$$

In deriving formula (3.7), we carried out integration in parts and used Eqs (2.22), (2.23), (2.24) related to function $f = f(z)$. By making use of formulas (2.31) and (3.7), we find

$$a(f, g) = \frac{S}{2\pi} g(l) . \tag{3.8}$$

It goes without saying that

$$a(f,f)=\frac{S}{2\pi}. \tag{3.9}$$

The combination of formulas (3.4), (3.8), (3.9) and inequality (3.6) directly yields inequality (3.1) which had to be proved.

3.2 Theorem

The inequality

$$S\geq 2\pi Gh\frac{[A(l)q_1(l)]^2}{\int_0^l Aq_1^2\,\mathrm{d}z+\frac{2k}{Gh}\int_0^l Bq_2^2\,\mathrm{d}z} \tag{3.10}$$

holds, where the function of one variable $q_1=q_1(z)$ is continuously differentiable, at least once, in the closed interval $0\leqq z\leqq l$ and the function of one variable $q_2=q_2(z)$ is continuous in the open interval $0<z<l$. Neither function is identically equal to zero and both functions fulfil the following conditions:

$$Gh\frac{\mathrm{d}}{\mathrm{d}z}(Aq_1)-2kBq_2=0 \qquad 0<z<l, \tag{3.11}$$

$$q_1(0)=0. \tag{3.12}$$

Demonstration

Let us consider the Euclidean space characterized by the two dimensional vectors

$$\mathbf{b}=\mathbf{b}(z)=[b_1(z),b_2(z)], \qquad (0\leq z\leq l),$$

$$\mathbf{c}=\mathbf{c}(z)=[c_1(z),c_2(z)]. \qquad (0\leq z\leq l).$$

Vector sum and multiplication by a scalar are defined in the usual way, by using the corresponding coordinates, i.e. the equation

$$\lambda\mathbf{b}+\mu\mathbf{c}=[\lambda b_1+\mu c_1,\lambda b_2+\mu c_2] \tag{3.13}$$

holds for the arbitrary scalars λ and μ. The scalar product of vectors $\mathbf{b}=\mathbf{b}(z)$ *and* $\mathbf{c}=\mathbf{c}(z)$ is defined according to the following formula:

$$\{\mathbf{b},\mathbf{c}\}=Gh\int_0^l Ab_1c_1\,\mathrm{d}z+2k\int_0^l Bb_2c_2\,\mathrm{d}z. \tag{3.14}$$

On the basis of the above definitions, it can easily be seen that the relations

$$\{\mathbf{b},\mathbf{c}\}=\{\mathbf{c},\mathbf{b}\}, \tag{3.15}$$

$$\{\lambda\mathbf{b},\mathbf{c}\}=\{\mathbf{b},\lambda\mathbf{c}\}=\lambda\{\mathbf{b},\mathbf{c}\}, \tag{3.16}$$

$$\{\mathbf{b}+\mathbf{c}, \mathbf{d}\} = \{\mathbf{b}, \mathbf{d}\} + \mathbf{c}, \mathbf{d}\}, \tag{3.17}$$

$$\{\mathbf{b}, \mathbf{c}+\mathbf{d}\} = \{\mathbf{b}, \mathbf{c}\} + \{\mathbf{b}, \mathbf{d}\}, \tag{3.18}$$

$$\{\mathbf{b}, \mathbf{b}\} \geq 0 \tag{3.19}$$

hold in every case, while the formula

$$\{\mathbf{b}, \mathbf{b}\} = 0 \tag{3.20}$$

holds only if the condition

$$\int_0^l (b_1^2 + b_2^2)\, \mathrm{d}z = 0 \tag{3.21}$$

is fulfilled.

Applying Schwarz's inequality, we obtain

$$|\{\mathbf{b}, \mathbf{c}\}|^2 \leq \{\mathbf{b}, \mathbf{b}\}\, \{\mathbf{c}, \mathbf{c}\}. \tag{3.22}$$

In this relation let vectors **b** and **c** assume the form

$$\mathbf{b} = [b_1, b_2] = \left[\frac{\mathrm{d}f}{\mathrm{d}z}, f\right], \tag{3.23}$$

$$\mathbf{c} = \mathbf{q} = [q_1, q_2], \tag{3.24}$$

where vector **q** fulfils the conditions

$$Gh \frac{\mathrm{d}}{\mathrm{d}z}(Aq_1) - 2kBq_2 = 0 \qquad 0 < z < l, \tag{3.25}$$

$$q_1(0) = 0. \tag{3.26}$$

The scalar product $\{\mathbf{b}, \mathbf{c}\}$ can be transformed as follows:

$$\{\mathbf{b}, \mathbf{c}\} = Gh \int_0^l A \frac{\mathrm{d}f}{\mathrm{d}z} q_1\, \mathrm{d}z + 2k \int_0^l Bf q_2\, \mathrm{d}z =$$

$$= Gh \int_0^l \frac{\mathrm{d}}{\mathrm{d}z}(Af q_1)\, \mathrm{d}z - Gh \int_0^l f \frac{\mathrm{d}}{\mathrm{d}z}(Aq_1)\, \mathrm{d}z + 2k \int_0^l Bf q_2\, \mathrm{d}z =$$

$$= Gh\, A(l) f(l)\, q_1(l) - GhA(0) f(0)\, q_1(0) - \int_0^l f \frac{\mathrm{d}}{\mathrm{d}z}(Aq_1)\, \mathrm{d}z -$$

$$- 2k \int_0^l Bq_2 f\, \mathrm{d}z = GhA(l) q_1(l). \tag{3.27}$$

In deriving Eq. (3.27), integrations by parts were carried out involving Eqs (2.2), (3.25) and (3.26). By making use of formulas (3.36), (3.14) and (3.23), we arrive at

$$\left\{\left[\frac{\mathrm{d}f}{\mathrm{d}z}, f\right], \left[\frac{\mathrm{d}f}{\mathrm{d}z}, f\right]\right\} = \frac{S}{2\pi}. \tag{3.28}$$

Finally, the combination of formulas (3.27), (3.28) and inequality (3.22) yields inequality (3.10) which had to be proved.

3.3. Theorem

The inequality

$$S \geq 2\pi G h \frac{[A(l)\, b(l)]^2}{\int_0^l Ab^2 \, \mathrm{d}z + \frac{Gh}{2k} \int_0^l \frac{1}{B} \left[\frac{\mathrm{d}}{\mathrm{d}z}(Ab) \right]^2 \mathrm{d}z} \tag{3.29}$$

holds, where $b = b(z)$ is a function of one variable, not identically equal to zero, which fulfils the homogeneous boundary condition

$$b(0) = 0 \tag{3.30}$$

and which is continuous in the interval $0 \leqq z \leqq l$ and continuously differentiable in the interval $0 < z < l$.

Demonstration

Let the functions of one variable q_1 and q_2 take the form

$$q_1 = b(z), \tag{3.31}$$

$$q_2 = \frac{Gh}{2k} \frac{1}{B} \frac{\mathrm{d}}{\mathrm{d}z}(Ab), \tag{3.32}$$

where function $b = b(z)$, in addition to what was said in connection with the necessary conditions of derivation, fulfils the homogeneous boundary condition

$$b(0) = 0. \tag{3.33}$$

An elementary calculation shows that the vector

$$q = \left[b, \frac{Gh}{2k} \frac{1}{B} \frac{\mathrm{d}}{\mathrm{d}z}(Ab) \right] \tag{3.34}$$

fulfils the necessary conditions.

The combination of formulas (3.31), (3.32) and inequality (3.10) finally results in inequality (3.29) which had to be proved.

4. Remarks

4.1 A short discussion on inequality (3.1) shows that the sign of equality holds only if

$$g(z) = \lambda f(z), \tag{4.1}$$

where λ is a real, arbitrary constant which is different from zero.

4.2 A short discussion on inequality (3.10) shows that the sign of equality holds only if

$$q_1 = \lambda \frac{\mathrm{d}f}{\mathrm{d}z}, \tag{4.2}$$

$$q_2 = \lambda f, \tag{4.3}$$

where λ is a real, arbitrary constant not equal to zero.

4.3 Let us consider the solution functions $F = F(z)$ and $f = f(z)$ of the system of differential equations

$$F = \frac{\mathrm{d}f}{\mathrm{d}z}, \qquad 0 < z < l, \tag{4.4}$$

$$\frac{Gh}{2k} \frac{1}{B} \frac{\mathrm{d}}{\mathrm{d}z}(AF) = f. \qquad 0 < z < l. \tag{4.5}$$

By eliminating $F(z)$, a simple calculation shows that function $f(z)$ satisfies the ordinary differential equation (2.22).

On the other hand, by eliminating function $f = f(z)$, it can be proved that function $F = F(z)$ is a solution to the ordinary second order differential equation:

$$Gh \frac{\mathrm{d}}{\mathrm{d}z}\left(\frac{1}{B} \frac{\mathrm{d}}{\mathrm{d}z}(AF)\right) - 2kF = 0, \qquad 0 < z < l. \tag{4.6}$$

The boundary conditions to function $F = F(z)$ are obtained by taking into account Eqs (2.23), (2.24), (4.4) and (4.5):

$$F(0) = 0, \tag{4.7}$$

$$Gh\left[\frac{\mathrm{d}}{\mathrm{d}z}(AF)\right]_{z=l} = 2k\, B(l). \tag{4.8}$$

Substituting Eq (4.4) into Eq. (2.31), we find

$$S = 2\pi Gh\, A(l)\, F(l). \tag{4.9}$$

The same formula is obtained if we substitute Eq. (4.5) into formula (2.33). The combination of Eqs (4.3), (4.4) and formula (2.36) now yields

$$S = 2\pi\, Gh\left[\int_0^l AF^2\, \mathrm{d}z + \frac{Gh}{2k} \int_0^l \frac{1}{B}\left(\frac{\mathrm{d}}{\mathrm{d}z} AF\right)^2 \mathrm{d}z\right]. \tag{4.10}$$

With some supplement to the above formulas, a short discussion on inequality (3.29) shows that the sign of equality holds only if

$$b(z) = \lambda F(z), \tag{4.11}$$

where λ is a real, arbitrary, non-zero constant.

5. Numerical examples

Example 1.

Figure 5 shows a thin-walled bar with an annulus cross-section of variable size, limited by truncated conical surfaces.

The basic data are as follows:

$$R(0)=40\text{ mm}, \qquad R(l)=80\text{ mm},$$
$$l\sim 100\text{ mm}, \qquad h=10\text{ mm},$$
$$G=10^5\text{ N}\cdot\text{mm}^{-2}, \qquad k=10^6\text{ N}\cdot\text{mm}^{-3}$$

With

$$R(z)=40+0.4z\text{ [mm]},$$
$$R'(z)=\text{constant}=0.4,$$

the application of inequality (3.1) to the function

$$g(z)=1+2\cdot 10^4\left(\frac{z}{l}\right)^2$$

yields the upper, bound to the torsional rigidity

$$S\leq 2.82\cdot 10^{12}\text{ N}\cdot\text{mm},$$

while inequality (3.29) applied to the function

$$b(z)=\frac{z}{l}-\frac{2}{3}10^4\left(\frac{z}{l}\right)^3$$

gives

$$S\geq 2.76\cdot 10^{12}\text{ N}\cdot\text{mm}$$

as the lower bound.

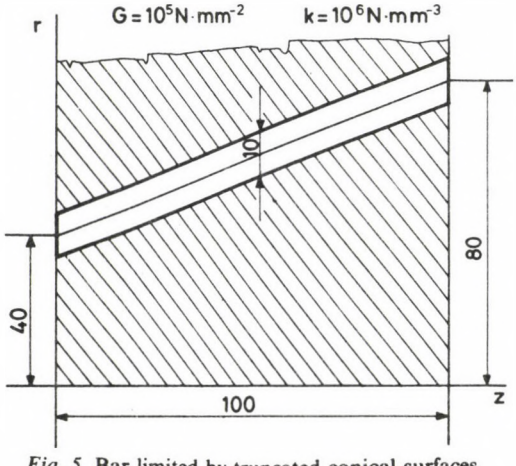

Fig. 5. Bar limited by truncated conical surfaces

Example 2.

Figure 6 shows the meridian section of a bar with an annulus cross-section, limited by circular cylindrical surfaces. In the case we have $R = R_0 = \text{constant}$ and it can easily be seen that the relation

$$A(z) = B(z) = R_0^3 = \text{constant}$$

holds. Let us introduce the notation

$$\beta^2 = \frac{2k}{Gh}.$$

With function $g(z)$ assuming the form

$$g(z) = \cosh \beta z$$

in inequality (3.4), we obtain

$$S \leq 2\pi\, GhR_0^3 \beta \tanh \beta l$$

for the upper bound to the torsional rigidity. On the other hand, with function

$$b(z) = \sinh \beta z$$

in inequality (3.29), we find

$$S \geq 2\pi\, GhR_0^3 \beta \tanh \beta l$$

as the lower bound to the torsional rigidity.

The formulas for the lower and upper bounds result in

$$S = 2\pi\, GhR_0^3 \beta \tanh \beta l$$

as the exact formula for the calculation of the torsional rigidity of bars with an annulus cross-section.

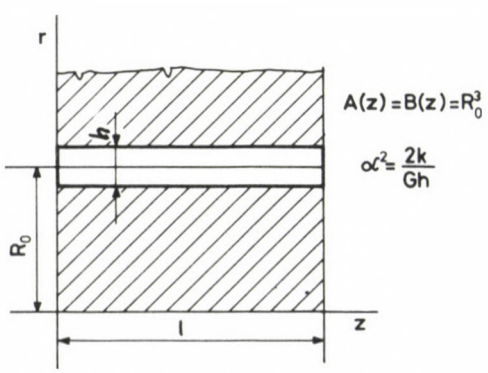

Fig. 6. Bar limited by circular cylindrical surfaces

6. Supplementary remarks

6.1 The exact solution to torsion characterized by Eqs. (1.2), (1.3), (1.4), (1.5), (1.6), (1.7), (1.8), (1.9) based on Eqs. (1.10) and (1.11), i.e. abandoning the approximations given by Eqs. (2.1), (2.5), (2.6), (2.7), (2.8), (2.9), leads to a boundary value problem related to an elliptic, partial differential equation [6].

6.2 In this paper, the solution of the torsion of thin-walled bars is traced back to the integration of an ordinary, linear, second order differential equation of variable coefficients.

6.3 The analysis of a similar problem, where the approximate assumption that the bar has a *thin-walled* cross-section is not used, is presented in [6]. That paper deals with the case when the cross-section of the bar defined by $z=0$ is a *built-in* one. In this paper, the displacement of the cross-section defined by $z=0$ is not restricted, i.e. it is a *free* cross-section.

References

1. Michell, J. H.: The uniform torsion and flexure of incomplete tores, with applications to helical springs. Proceedings of the London Math. Soc. 31 (1900), 130–146.
2. Föppl, A.: Über die Torsion von runden Stäben mit veränderlichen Durchmesser, Sitzungsber. Bayerische Akad. der Wissensch. München 35 (1905), 249–262. Berichtigung 504.
3. Willers, Fr.: Die Torsion eines Rotationskörpers um seine Achse. Zeitschr. f. Math. und Phys. 55 (1907), 225–263.
4. Timpe, A.: Die Torsion von Umdrehungskörpern. Math. Ann. Leipzig 71 (1911), 480–509.
5. Arutjunjan, N. H. Abramjan, B. L.: Kruchenie uprugih tel. Izd. Fiz-Mat. Lit. Moskva 1963, 506–516.
6. Ecsedi, I.: Some comments on the torsion of bars having an annulus cross-section of variable size supported elastically along its entire length. Acta Technica Hung. (in press).

Acta Technica Academiae Scientiarum Hungaricae, 97 (1—4), pp. 39—49 (1984)

LOWER AND UPPER BOUNDS TO THE STRAIN ENERGY OF BENT PLATES

I. ECSEDI*

[Received: 21 June 1983]

The exact value of the strain energy of elastic, bent plates with built-in edges can be given only if the solution to the governing partial differential equation of the problem is known. This paper derives inequalities which make it possible to present lower and upper bounds to the strain energy without relying on the exact solution to the problem. The demonstration of the inequalities is based on Schwarz's inequality and Green's formula.

Examples show the application possibilities of the inequalities for the lower and upper bounds to the strain energy.

Symbols

x, y, z	rectangular co-ordinates,
D	the flexural rigidity of the plate,
E	Young's modulus of the material of the plate,
ν	Poisson's ratio of the material of the plate,
h	the thickness of the plate,
$w = w(x, y)$	the perpendicular displacement of the points of the middle surface of the plate,
$p = p(x, y)$	surface load,
T	domain in plane xy defined by the middle surface of the plate,
∂T	the boundary of domain T,
$\Delta = \frac{\partial^2}{\partial x^2} + \frac{\partial^2}{\partial y^2}$	Laplace differential operator
$\partial/\partial n$	the sign of derivation carried out along the external normal to the boundary curve ∂T,
s	arc co-ordinate measured along curve ∂T,
U	the strain energy,
$r = \sqrt{x^2 + y^2}$, $\varphi = \arctan \frac{y}{x}$	polar co-ordinates

and

$$|VF|^2 = \left(\frac{\partial F}{\partial x}\right)^2 + \left(\frac{\partial F}{\partial y}\right)^2.$$

Further symbols and variables are defined in the text.

* I. Ecsedi, H-3524 Miskolc, Klapka Gy. u. 36, IX/2, Hungary

1. Introduction

Let function $w = w(x, y)$ denote the displacements of the middle surface of the plate shown in Fig. 1. The middle surface of the thin, homogeneous, isotropic, linearly elastic plate is defined by plane xy with equation $z = 0$. Knowing the displacements of the plate with its flexural rigidity assuming the form

$$D = \frac{Eh^3}{12(1-\nu^2)}, \tag{1.1}$$

the strain energy is obtained from the following equation [1]:

$$U = \frac{D}{2}\left\{\int_T (\Delta w)^2 \, \mathrm{d}T + \right.$$

$$\left. + 2(1-\nu)\int_T \left[\left(\frac{\partial^2 w}{\partial x \, \partial y}\right)^2 - \frac{\partial^2 w}{\partial x^2}\frac{\partial^2 w}{\partial y^2}\right]\mathrm{d}T\right\}. \tag{1.2}$$

The function of two variables $w = w(x, y)$ in Eq. (1.2) has to satisfy the partial differential equation

$$\Delta\Delta w = \frac{p}{D}, \qquad (x, y) \in T \tag{1.3}$$

and the boundary conditions expressing the restraints along the supports. For a plate with built-in edges along the boundary ∂T of domain T, these conditions are as follows:

$$w = 0, \qquad (x, y) \in T, \tag{1.4}$$

$$\frac{\partial w}{\partial n} = 0, \qquad (x, y) \in \partial T. \tag{1.5}$$

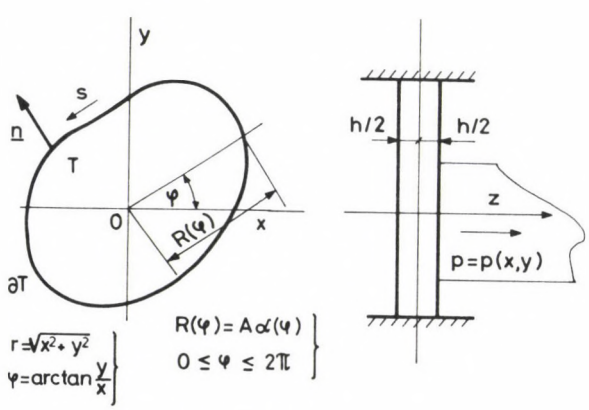

Fig. 1. Bent plate

The boundary value problem given by Eqs (1.3), (1.4), (1.5) constitutes a unique system for function $w=w(x, y)$. According to formula (6_2) on p. 169 in [2], if function $w=w(x, y)$ fulfils the homogeneous, kinematic boundary conditions (1.4), (1.5) along curve ∂T, the formula

$$\int_T \left[\left(\frac{\partial^2 w}{\partial x \, \partial y} \right)^2 - \frac{\partial^2 w}{\partial x^2} \frac{\partial^2 w}{\partial y^2} \right] \mathrm{d}T = 0 \tag{1.6}$$

holds, i.e. the strain energy of the plate with a built-in boundary can be expressed with $w=w(x, y)$ as

$$U = \frac{D}{2} \int_T (\Delta w)^2 \, \mathrm{d}T. \tag{1.7}$$

The aim of this paper is to derive inequalities making it possible to construct lower and upper bounds for the strain energy of plates with a built-in boundary.

The importance of such bounds is shown by the fact that for the exact value of the strain energy U, the solution to the boundary value problem (1.3), (1.4), (1.5) would be needed. A closed form solution or a solution relying on an infinite series, however, except for some special cases, cannot be produced.

Let us consider the functions of two variables $a=a(x, y)$ and $b=b(x, y)$ which are continuously differentiable, at least once, in the closed domain $T+\partial T$, and, at least twice, in the open domain T.

By applying Green's formula to the above functions, we obtain

$$\int_T (a \Delta b - b \Delta a) \, \mathrm{d}T = \int_{\partial T} \left(a \frac{\partial b}{\partial n} - b \frac{\partial a}{\partial n} \right) \mathrm{d}s \, . \tag{1.8}$$

With the notation

$$a = \Delta w, \qquad b = w \tag{1.9), (1.10}$$

and by combining Eqs (1.3), (1.4), (1.5), (1.9), (1.10) and formula (1.8), we arrive at

$$\frac{1}{D} \int_T pw \, \mathrm{d}T = \int_T (\Delta w)^2 \, \mathrm{d}T. \tag{1.11}$$

Introducing (1.11) into (1.7) yields

$$U = \frac{1}{2} \int_T pw \, \mathrm{d}T. \tag{1.12}$$

2. Upper bound

2.1 Theorem

Let the function of two variables $f=f(x, y)$ be continuously differentiable, at least twice, in the closed domain $T+\partial T$ and satisfing the partial differential equation

$$\Delta\Delta f=\frac{p}{D}. \tag{2.1}$$

The inequality

$$U\leq\frac{D}{2}\int_T|\Delta f|^2\,\mathrm{d}T \tag{2.2}$$

holds.

Demonstration

The demonstration is carried out on the basis of Schwarz's inequality:

$$\int_T(\Delta w)^2\,\mathrm{d}T\int_T(\Delta f)^2\,\mathrm{d}T\geq\left(\int_T\Delta w\Delta f\,\mathrm{d}T\right)^2. \tag{2.3}$$

It can easily be seen that formula

$$\int_T(\Delta w)^2\,\mathrm{d}T=\frac{2U}{D} \tag{2.4}$$

holds. With

$$a=w \qquad b=\Delta f \tag{2.5}\ (2.6)$$

in formula (1.8), we find

$$\int_T w\Delta\Delta f\,\mathrm{d}T-\int_T\Delta w\Delta f\,\mathrm{d}T=\int_{\partial T}w\frac{\partial}{\partial n}(\Delta f)\,\mathrm{d}s-\int_{\partial T}\Delta f\frac{\partial w}{\partial n}\,\mathrm{d}s. \tag{2.7}$$

Since function $f=f(x, y)$ satisfies the partial differential equation (2.1), using the conditions

$$w=0, \qquad \frac{\partial w}{\partial n}=0 \qquad (x, y)\in\partial T$$

we have

$$\int_T\Delta w\Delta f\,\mathrm{d}T=\int_T w\Delta\Delta f\,\mathrm{d}T=\frac{1}{D}\int_T wp\,\mathrm{d}T=\frac{2U}{D}. \tag{2.8}$$

Combining inequality (2.3) and formulas (2.4), (2.8) yields inequality (2.2) which had to be proved.

2.2 Comments on the practical application

It is expedient to consider the solution to the partial differential equation (2.1) as the sum of two terms:

$$f=f_0+k\,, \tag{2.9}$$

where function $f_0=f_0(x, y)$ is an arbitrary particular solution to Eq. (2.1), i.e. equation

$$\Delta\Delta f_0=\frac{p}{D}\,, \qquad (x, y)\in T \tag{2.10}$$

holds, and $k=k(x, y)$ is a biharmonic function, i.e. equation

$$\Delta\Delta k=0, \qquad (x, y)\in T \tag{2.11}$$

holds.

Using the harmonic functions $H_0=H_0(x, y)$ and $H_1=H_1(x, y)$, the biharmonic function $k=k(x, y)$ can be constructed in the following ways:

$$k=(xH_1+H_0), \qquad k=yH_1+H_0\,,$$

$$k=(x^2+y^2)H_1+H_0$$

When applying inequality (2.2), we do not find the harmonic function $H_0=H_0(x, y)$ in the expressions of the lower and upper bounds for the strain energy, since, by virtue of

$$\Delta(xH_1+H_0)=\Delta(xH_1)\,,$$

$$\Delta(yH_1+H_0)=\Delta(yH_1)\,,$$

$$\Delta[(x^2+y^2)H_1+H_0]=\Delta[(x^2+y^2)H_1]$$

they drop out of the formulas.

3. Lower bound

3.1 Theorem

Let the function of two variables $g=g(x, y)$, not identically equal to zero, be continuously differentiable, at least once, in the closed domain $T+\partial T$ and, at least twice, in the open domain T and satisfying the homogeneous, kinematic boundary conditions

$$g=0, \qquad (x, y)\in \partial T, \tag{3.1}$$

$$\frac{\partial g}{\partial n}=0, \qquad (x, y)\in \partial T. \tag{3.2}$$

The inequality

$$U \geq \frac{\left(\int_T pg \, \mathrm{d}T\right)^2}{2D \int_T (\Delta g)^2 \, \mathrm{d}T} \tag{3.3}$$

holds.

Demonstration

The demonstration is based on Schwarz's inequality:

$$\int_T (\Delta w)^2 \, \mathrm{d}T \int_T (\Delta g)^2 \, \mathrm{d}T \geq \left(\int_T \Delta w \Delta g \, \mathrm{d}T\right)^2. \tag{3.4}$$

With

$$a = \Delta w, \qquad b = g \tag{3.5) (3.6}$$

Green's formula (1.8) assumes the form

$$\int_T \Delta w \Delta g \, \mathrm{d}T - \int_T g \Delta \Delta w \, \mathrm{d}T = \int_{\partial T} \Delta w \frac{\partial g}{\partial n} \, \mathrm{d}s - \int_{\partial T} g \frac{\partial}{\partial n} \Delta w \, \mathrm{d}s \,. \tag{3.7}$$

Taking the boundary conditions (3.1), (3.2) into consideration, Eq. (3.7) yields

$$\int_T \Delta w \Delta g \, \mathrm{d}T = \frac{1}{D} \int_T pg \, \mathrm{d}T. \tag{3.8}$$

By the combination of Eqs (2.4), (3.8) and inequality (3.4), we directly obtain inequality (3.3) which had to be proved.

3.2 Remark

It is obvious that inequality (3.3) cannot be interpreted if $g = g(x, y)$ is a harmonic function, i.e.

$$\Delta g = 0, \qquad (x, y) \in T. \tag{3.9}$$

Function $g = g(x, y)$ fulfils the homogeneous, kinematic boundary conditions (3.1), (3.2) and consequently, if it is even a harmonic function, it is identically equal to zero in the closed domain $T + \partial T$.

3.3 A comment for the practical application

Let the implicit equation of the boundary curve ∂T be

$$F(x, y) = 0 \,. \tag{3.10}$$

It can be easily seen that function $g=g(x, y)$ in the form

$$g(x, y)=(F(x, y))^2, \tag{3.11}$$

and

$$g(x, y)=\cos[F(x, y)]-1 \tag{3.12}$$

fulfils all the conditions set as for $g(x, y)$ and consequently inequality (3.3) is applicable.

4. General remarks

4.1 Inequalities (2.2) and (3.3) derived for the upper and lower bounds to the strain energy are valid for both simply and multiply connected domains. In the case of a multiply connected domain T, the homogeneous, kinematic boundary conditions (1.14), (1.5) are also prescribed for the "internal" boundary curves $\partial T_1, \partial T_2 \ldots$ (Fig. 2).

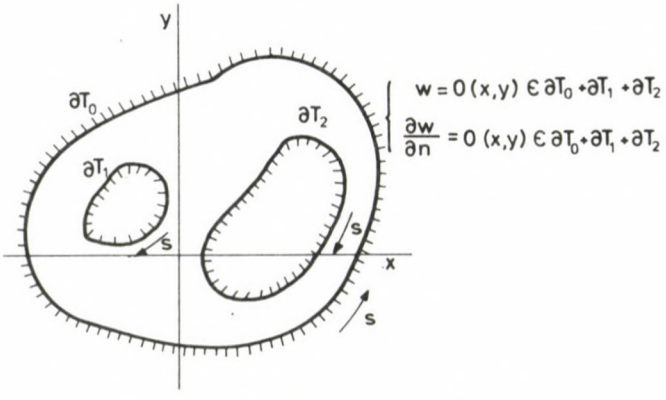

Fig. 2. Multiply-connected domain T

4.2 A short discussion shows that the sign of equality in inequality (2.2) holds only if

$$f=w+H, \tag{4.1}$$

where $H=H(x, y)$ is an arbitrary harmonic function.

4.3 A discussion on inequality (3.3) shows that the sign of equality holds only if

$$g=cw \tag{4.2}$$

where c is a real, arbitrary but non-zero constant.

5. Applications

5.1 By introducing Eq. (3.12) into inequality (3.3), we obtain the following lower bound to the strain energy:

$$U \geq \frac{\left(\int_T p(x, y)\,[F(x, y)]^2\,\mathrm{d}T\right)^2}{8D\int_T (F^2(\Delta F)^2 + |\nabla F|^4 + 2F\Delta F|\nabla F|^2)\mathrm{d}T}. \tag{5.1}$$

5.2 Let the surface load assume the value

$$p(x, y) = p_0 = \text{constant}. \tag{5.2}$$

It can easily be proved that the function

$$f(x, y) = \frac{p_0(x^2 + y^2)^2}{64D} \tag{5.3}$$

satisfies the partial differential equation (2.1). By introducing this function into inequality (2.2), we obtain the following upper bound to the strain energy:

$$U \leq \frac{p_0^2}{32D}\int_T (x^2 + y^2)\,\mathrm{d}T. \tag{5.4}$$

5.3 Let the equation of the boundary curve ∂T of the simply connected domain T in the polar coordinate system $r\varphi$ take the form

$$r = R(\varphi), \qquad 0 \leq \varphi \leq 2\pi. \tag{5.5}$$

It should be pointed out that the origin O of the polar co-ordinate system $r\varphi$ lies inside domain T and that any straight line with an origin O only intersects the boundary curve ∂T at one point, i.e. $R(\varphi)$ is a unique function of variable φ.

Let us have

$$p = p_0 = \text{constant}$$

again. Let us apply inequality (2.2) to the function

$$f = \frac{p_0 A^4}{64D}\left[1 - \left(\frac{r}{A}\right)^2\right]^2, \tag{5.6}$$

where

$$A = \max_{\varphi} R(\varphi). \tag{5.7}$$

With the notation

$$\alpha = \alpha(\varphi) = \frac{R(\varphi)}{A} \tag{5.8}$$

and making use of inequality (2.2), a long but elementary calculation yields the following upper bound to the strain energy:

$$U \leq \frac{p_0^2 A^6}{128D}\left(\frac{2}{3} I_6 - I_4 + \frac{1}{2} I_2\right). \tag{5.9}$$

In Eq. (5.9) we have

$$I_2 = \int_0^{2\pi} [\alpha(\varphi)]^2 \, \mathrm{d}\varphi \,, \tag{5.10}$$

$$I_4 = \int_0^{2\pi} [\alpha(\varphi)]^4 \, \mathrm{d}\varphi \,, \tag{5.11}$$

$$I_6 = \int_0^{2\pi} [\alpha(\varphi)]^6 \, \mathrm{d}\varphi \,. \tag{5.12}$$

5.4 In order to derive a lower bound to the strain energy of the plate discussed in the previous section, let us apply inequality (3.3) to the function

$$g(r, \varphi) = A^4 \left\{ [\alpha(\varphi)]^2 - \left(\frac{r}{A}\right)^2 \right\}^2. \tag{5.13}$$

It can easily be shown that the conditions

$$g = 0, \qquad (r, \varphi) \in \partial T, \tag{5.14}$$

$$\frac{\partial g}{\partial n} = 0, \qquad (r, \varphi) \in \partial T \tag{5.15}$$

are fulfilled and that the equation

$$\Delta g = A^2 \left[16\rho^2 - 8\alpha^2 - 4\left(\frac{\mathrm{d}\alpha}{\mathrm{d}\varphi}\right)^2 - 4\alpha \frac{\mathrm{d}^2\alpha}{\mathrm{d}\varphi^2} + \right.$$

$$\left. + 12 \frac{\alpha^2}{\rho^2}\left(\frac{\mathrm{d}\alpha}{\mathrm{d}\varphi}\right)^2 + 4 \frac{\alpha}{\rho^3} \frac{\mathrm{d}^2\alpha}{\mathrm{d}\varphi^2} \right] \tag{5.16}$$

holds, where

$$\rho = \frac{r}{A}. \tag{5.17}$$

A simple calculation results in

$$\int_T gp \, \mathrm{d}T = p_0 \frac{A^6}{6} I_6 \,. \tag{5.18}$$

By combining Eqs (5.16), (5.18) and inequality (3.3), we finally arrive at the lower bound to the strain energy

$$U \geq \frac{A^6 I_6^2}{72DB} p_0^2 \tag{5.19}$$

where

$$B=\int_0^{2\pi}\left\{10.666\alpha^6+64\alpha^4\left(\frac{\mathrm{d}\alpha}{\mathrm{d}\varphi}\right)^2+\right.$$

$$+65\alpha^5\frac{\mathrm{d}^2\alpha}{\mathrm{d}\varphi^2}+8\alpha^2\left(\frac{\mathrm{d}\alpha}{\mathrm{d}\varphi}\right)^2+16\alpha^3\left(\frac{\mathrm{d}\alpha}{\mathrm{d}\varphi}\right)^3\frac{\mathrm{d}^2\alpha}{\mathrm{d}\varphi^2}-$$

$$-48\alpha\left(\frac{\mathrm{d}\alpha}{\mathrm{d}\varphi}\right)^2-5.333\alpha^3\left(\frac{\mathrm{d}^2\alpha}{\mathrm{d}\varphi^2}\right)^2-$$

$$-32\left(\frac{\mathrm{d}\alpha}{\mathrm{d}\varphi}\right)^2\frac{\mathrm{d}^2\alpha}{\mathrm{d}\varphi^2}\alpha^2-32\left[6\alpha^4\left(\frac{\mathrm{d}\alpha}{\mathrm{d}\varphi}\right)^2+\right.$$

$$+3\alpha^2\left(\frac{\mathrm{d}\alpha}{\mathrm{d}\varphi}\right)^4+3\alpha^3\left(\frac{\mathrm{d}\alpha}{\mathrm{d}\varphi}\right)^2\frac{\mathrm{d}^2\alpha}{\mathrm{d}\varphi^2}+$$

$$+2\alpha^5\frac{\mathrm{d}^2\alpha}{\mathrm{d}\varphi^2}+\alpha^3\left(\frac{\mathrm{d}\alpha}{\mathrm{d}\varphi}\right)^2\frac{\mathrm{d}^2\alpha}{\mathrm{d}\varphi^2}+$$

$$\left.\left.+\alpha^4\left(\frac{\mathrm{d}^2\alpha}{\mathrm{d}\varphi^2}\right)^2\right]\ln\alpha\right\}\mathrm{d}\varphi\,. \tag{5.20}$$

5.5 In the case of a circular plate with radius A we have

$$\alpha(\varphi)=1, \qquad 0\leq\varphi\leq 2\pi\,. \tag{5.21}$$

Introducing Eq. (5.21) into inequality (5.9) through Eqs (5.10), (5.11), (5.12), we obtain the upper bound

$$U\leq\frac{A^6\pi}{384D}p_0^2\,, \tag{5.22}$$

Similarly, introducing Eq. (5.21) into inequality (5.19) through Eq. (5.12), we arrive at the lower bound

$$U\geq\frac{A^6\pi}{384D}p_0^2\,. \tag{5.23}$$

By comparing inequalities (5.22) and (5.23), we find that the strain energy of the circular plate with a built-in boundary, subjected to uniformly distributed load, assumes the value

$$U=\frac{A^6\pi}{384D}p_0^2\,, \tag{5.24}$$

i.e. in the inequalities (5.9) and (5.19) for circular plates the sign of equality holds.

References

1. Timoshenko, S. Woinowsky-Krieger, S.: Lemezek és héjak elmélete (Theory of Plates and Shells). Műszaki Könyvkiadó, Budapest 1966.
2. Mihlin, S. G.: Variatsionie metodi v matematicheskoi fizike. Izdatelstvo. Nauka Fiz-mat. Lit., Moskva 1970.

Acta Technica Academiae Scientiarum Hungaricae, 97 (1—4), pp. 51—63 (1984)

INEQUALITIES FOR THE STRAIN ENERGY OF POLYGON-SHAPED BENT PLATES

I. ECSEDI*

Received: 6 August, 1983

The paper presents inequalities for the strain energy of elastic, bent plates of polygon shape with simply supported edges. The derivation of the inequalities is based on some well-known theorems of mathematical-physics and the results of Kirchhoff's plate theory.

1. Symbols

x, y, z	rectangular co-ordinates,
$\mathbf{e}_x, \mathbf{e}_y, \mathbf{e}_z$	unit vectors,
$V = \frac{\partial}{\partial x}\mathbf{e}_x + \frac{\partial}{\partial y}\mathbf{e}_y$	Hamilton's differential operator,
"·"	the sign of scalar product,
$\Delta = V \cdot V = \frac{\partial^2}{\partial x^2} + \frac{\partial^2}{\partial y^2}$	Laplace differential operator,
T	simply connected domain in plane xy,
∂T	boundary of domain T,
$\partial/\partial n$	the sign of derivation carried out along the external normal to curve ∂T,
s	arc co-ordinate measured along curve ∂T,
$w = w(x, y)$	displacement of the middle surface of the plate,
p	surface load,
E	Young's modulus,
ν	Poisson's ratio,
h	the thickness of the plate (h = constant),
$D = \frac{Eh^3}{12(1-\nu^2)}$	flexural rigidity of the plate,
$v = v(x, y)$	auxiliary function,
$\Phi = \Phi(x, y)$	Prandtl's stress function,
S	torsional rigidity,
λ_1^4, λ_2^2	eigenvalues,
$\Gamma = \Gamma(x, y, \xi, \eta)$	Green's function belonging to the Laplace differential operator,
$f = f(x, y)$	auxiliary function,
$g = f(x, y)$	auxiliary function,

Further symbols and variables are defined in the text.

* Ecsedi I. Klapka Gy. u. 36, IX/2, H-3524 Miskolc, Hungary

2. Basic relations

2.1 Figure 1 shows a polygon-shaped, bent plate of constant thickness with simply supported edges. The material of the plate is homogeneous, isotropic and linearly elastic. It follows from Kirchhoff's plate theory that the strain energy U of bent plates with simply supported edges is obtained from the following formula [1]:

$$U = \frac{D}{2} \int_T (\Delta w)^2 \, \mathrm{d}T. \tag{2.1}$$

The function of two variables $w = w(x, y)$ in formula (2.1) satisfies the following boundary value problem [1], [2]:

$$\Delta\Delta w = \frac{p}{D}, \qquad (x, y) \in T, \tag{2.2}$$

$$w = 0, \qquad (x, y) \in \partial T, \tag{2.3}$$

$$\Delta w = 0, \qquad (x, y) \in \partial T. \tag{2.4}$$

2.2 Let us consider the functions of two variables $a = a(x, y)$ and $b = b(x, y)$ which are differentiable, at least once, in the closed domain $T \cup \partial T$, and at least twice, in the open domain T.

On the basis of Green's theorem on the transformation of integrals, we obtain

$$\int_T (a\Delta b - b\Delta a) \, \mathrm{d}T = \int_{\partial T} \left(a \frac{\partial b}{\partial n} - b \frac{\partial a}{\partial n} \right) \mathrm{d}s. \tag{2.5}$$

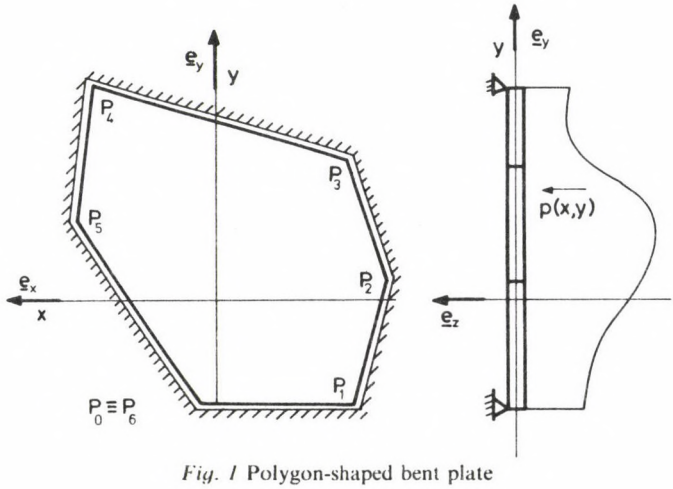

Fig. 1 Polygon-shaped bent plate

By applying formula (2.5) to the functions

$$a = w\,, \tag{2.6}$$

$$b = \Delta w \tag{2.7}$$

we arrive at

$$\int_T (\Delta w)^2 \,\mathrm{d}T = \frac{1}{D}\int_T pw \,\mathrm{d}T. \tag{2.8}$$

Introducing expression (2.8) into formula (2.1), we find

$$U = \frac{1}{2}\int_T pw \,\mathrm{d}T \tag{2.9}$$

a formula which can also be directly derived from the virtual work principles in structural mechanics.

2.3 The boundary value problem given by Eqs (2.2), (2.3), (2.4) equivalent to Dirichlet's boundary value problem related to Poisson's equation taining two unknown functions as follows:

$$\Delta v = \frac{p}{D}\,, \qquad (x, y) \in T, \tag{2.10}$$

$$v = 0\,, \qquad (x, y) \in \partial T; \tag{2.11}$$

$$\Delta w = -v\,, \qquad (x, y) \in T, \tag{2.12}$$

$$w = 0\,, \qquad (x, y) \in \partial T. \tag{2.13}$$

First, the boundary value problem defined by Eqs (2.10), (2.11) shall be solved then, by solving the boundary value problem characterized by Eqs (2.12), (2.13), the displacement $w = w(x, y)$ of the polygon-shaped plate will be obtained.

It goes without saying that the formula

$$U = \frac{D}{2}\int_T v^2 \,\mathrm{d}T \tag{2.14}$$

holds.

3. Inequalities

3.1 Theorem

Let λ_1^4 be the smallest eigenvalue of the eigenvalue problem determined by the following equations:

$$\Delta\Delta c - \lambda_1^4 c = 0\,, \qquad (x, y) \in T, \tag{3.1}$$

$$c=0\,, \qquad (x, y)\in \partial T, \tag{3.2}$$

$$\Delta c=0\,, \qquad (x, y)\in \partial T. \tag{3.3}$$

The inequality

$$U\leq \frac{1}{2D\lambda_1^4}\int_T p^2\,\mathrm{d}T \tag{3.4}$$

holds.

Demonstration

It is known that eigenvalue λ_1^4 can also be produced as the solution to the following minimization problem [4]:

$$\lambda_1^4=\min_{k(x,y)}\frac{\int_T(\Delta k)^2\,\mathrm{d}T}{\int_T k^2\,\mathrm{d}T}, \tag{3.5}$$

$$k=0 \qquad (x, y)\in \partial T. \tag{3.6}$$

By taking Eqs (3.5), (3.6) into consideration, we find

$$\lambda_1^4\int_T w^2\,\mathrm{d}T\leq \int_T(\Delta w)^2\,\mathrm{d}T. \tag{3.7}$$

The application of Schwarz's inequality to formula (2.9) yields

$$U^2=\frac{1}{4}\Big(\int_T pw\,\mathrm{d}T\Big)^2\leq \frac{1}{4}\int_T p^2\,\mathrm{d}T\int_T w^2\,\mathrm{d}T. \tag{3.8}$$

Introducing inequality (3.7) into inequality (3.8), we obtain

$$U^2\leq \frac{1}{4\lambda_1^4}\int_T p^2\,\mathrm{d}T\int_T(\Delta w)^2\,\mathrm{d}T. \tag{3.9}$$

All that is to be done now is to combine inequalities (3.9) and (2.1) and finally we arrive at inequality (3.4) which had to be proved.

3.2 Theorem

Let λ_2^2 be the smallest eigenvalue of the eigenvalue problem defined by the equations

$$\Delta k+\lambda_2^2 k=0\,, \qquad (x, y)\in T, \tag{3.10}$$

$$k=0\,, \qquad (x, y)\in \partial T. \tag{3.11}$$

The inequality

$$U \leq \frac{\int_T p^2 \, dT}{2D\lambda_2^4} \tag{3.12}$$

holds.

Demonstration

It is known that eigenvalue λ_2^2 can also be produced as the solution to the following minimization problem [4]:

$$\lambda_2^2 = \min_k \frac{\int_T |\nabla k|^2 \, dT}{\int_T k^2 \, dT}, \tag{3.13}$$

$$k = 0 \qquad (x, y) \in \partial T. \tag{3.14}$$

By taking Eq. (3.13) into consideration, we find

$$\lambda_2^2 \int_T v^2 \, dT \leq \int_T |\nabla v|^2 \, dT. \tag{3.15}$$

According to the product-functions's derivation rule and Gauss' theorem on the transformation of integrals, using Eqs (2.10) and (2.11), we obtain

$$\int_T p \frac{v}{D} \, dT = \int_T v \Delta v \, dT = \int_T \nabla \cdot (v \nabla v) \, dT - \int_T |\nabla v|^2 \, dT =$$

$$\int_{\partial T} v \frac{\partial v}{\partial n} \, ds - \int_T |\nabla v|^2 \, dT = - \int_T |\nabla v|^2 \, dT. \tag{3.16}$$

The application of Schwarz's inequality to Eq. (3.16) yields

$$\int_T \frac{p^2}{D} \, dT \int_T \frac{v^2}{D} \, dT \geq \left(\int_T |\nabla v|^2 \, dT \right)^2 \tag{3.17}$$

Introducing inequality (3.15) into inequality (3.17), we obtain

$$\int_T \frac{p^2}{D} \, dT \int_T \frac{v^2}{D} \, dT \geq \lambda_2^4 \left(\int_T v^2 \, dT \right)^2 \tag{3.18}$$

Finally, making use of inequality (3.18) and formula (2.31), we arrive at inequality (3.12) which had to be proved.

3.3 Theorem

Let function $\Phi = \Phi(x, y)$ be the solution to the boundary value problem

$$\Delta\Phi = -2, \qquad (x, y) \in T, \tag{3.19}$$

$$\Phi = 0, \qquad (x, y) \in \partial T \tag{3.20}$$

and let formulas

$$S = 2\int_T \Phi \, \mathrm{d}T \tag{3.21}$$

and

$$p(x, y) = p_0 = \text{constant} \tag{3.22}$$

hold.

The inequality to be proved is

$$U \geq \frac{p_0^2 S^2}{32Dt}, \tag{3.23}$$

where t represents the cross-sectional area of domain T:

$$t = \int_T \mathrm{d}x \, \mathrm{d}y. \tag{3.24}$$

Demonstration

If the equation

$$p(x, y) = p_0 = \text{constant}$$

holds, it goes without saying that formula

$$v(x, y) = -\frac{p_0}{2D}\Phi(x, y) \tag{3.25}$$

also holds. Eq. (3.25) relates to a prismatic bar whose cross-section is a domain T and whose torsional rigidity S is obtained from the formula

$$S = 2\int_T \Phi \, \mathrm{d}T \tag{3.26}$$

knowing Prandtl's stress function $\Phi = \Phi(x, y)$.

It follows that inequality (3.23) to be proved, establishes a relationship among different physical quantities. Introducing Eq. (3.25) into Eq. (2.14), we obtain

$$U = \frac{p_0^2}{8D}\int_T \Phi^2 \, \mathrm{d}T. \tag{3.27}$$

The application of Schwarz's inequality leads to the inequality

$$\int_T \Phi^2 \, \mathrm{d}T \int_T 1^2 \, \mathrm{d}T \geq \left(\int_T \Phi \cdot 1 \, \mathrm{d}T \right)^2 = \frac{S^2}{4} \tag{3.28}$$

from which, incorporating Eq. (3.27), we obtain inequality (3.23) we have been looking for.

3.4 Theorem

Let the function of two variables $g = g(x, y)$, not identically equal to zero in domain T, be continuously differentiable, at least once, in the closed domain $T \cup \partial T$ and at least twice, in the open domain T. The function also fulfils the homogeneous boundary condition

$$g(x, y) = 0 \qquad (x, y) \in \partial T. \tag{3.29}$$

The inequality

$$U \geq \frac{(\int_T pg \, \mathrm{d}T)^2}{2D \int_T |\Delta g|^2 \, \mathrm{d}T} \tag{3.30}$$

holds.

Demonstration

Let functions a and b in formula (2.5) assume the form

$$a = v, \tag{3.31}$$

$$b = g. \tag{3.32}$$

Introducing these functions into formula (2.5) and taking Eqs (2.10), (2.11) into consideration, we obtain

$$\int_T v \Delta g \, \mathrm{d}T = \frac{1}{D} \int_T pg \, \mathrm{d}T. \tag{3.33}$$

Schwarz's inequality now results in

$$(\int_T v \Delta g \, \mathrm{d}T)^2 \leq \int_T v^2 \, \mathrm{d}T \int_T (\Delta g)^2 \, \mathrm{d}T. \tag{3.34}$$

By combining Eqs (2.14), (3.33) and inequality (3.34), we finally arrive at inequality (3.30) which had to be proved.

A short discussion on inequality (3.30) shows that the sign of equality in (3.30) holds only if

$$g(x, y)=\beta w(x, y) \tag{3.35}$$

where β is a real, arbitrary constant which is different from zero.

Inequality (3.30) holds in every case when $g=g(x, y)$ is not a harmonic function, i.e. when it does not fulfil the condition

$$\Delta g=0 \qquad (x, y) \in T \tag{3.36}$$

in domain T. If function $g(x, y)$ fulfils conditions (3.29), (3.36), it must be identically zero in domain T.

3.5 Theorem

Let $f=f(x, y)$ be a function of two variables which is continuous in the closed domain $T \cup \partial T$ and continuously differentiable, at least twice, in the open domain T and which fulfils the conditions

$$F(x, y)=-\Delta f \geq 0\,, \qquad (x, y) \in T, \tag{3.37}$$

$$f=0\,, \qquad (x, y) \in \partial T. \tag{3.38}$$

Let function p comply with the condition

$$p(x, y)>0\,, \qquad (x, y) \in T. \tag{3.39}$$

The two inequalities

$$\frac{1}{2D} \int_T f^2(x, y)\, \mathrm{d}T \leq R_{\max}^2 U\,, \tag{3.40}$$

$$\frac{1}{2D} \int_T f^2(x, y)\, \mathrm{d}T \geq R_{\min}^2 U \tag{3.41}$$

hold, where we have

$$R_{\max}=\max_{(x, y) \in T \cup \partial T} \left\{\frac{F(x, y)}{p(x, y)}\right\}, \tag{3.42}$$

and

$$R_{\min}=\min_{(x, y) \in T \cup \partial T} \left\{\frac{F(x, y)}{p(x, y)}\right\}. \tag{3.43}$$

Demonstration

Let us consider Green's function $\Gamma=\Gamma(x, y; \xi, \eta)$ related to the Laplace operator. It follows from the characteristics of Green's function that the expressions

$$f(x, y)=\int_T F(\xi, \eta) \Gamma(x, y; \xi, \eta)\, \mathrm{d}T, \tag{3.44}$$

$$V(x, y) = -v(x, y) = \frac{1}{D} \int_T p(\xi, \eta) \Gamma(x, y; \xi, \eta) \, \mathrm{d}T \tag{3.45}$$

hold. The fact that function $\Gamma = \Gamma(x, y; \xi, \eta)$ is not negative [3] results in the following inequalities:

$$f(x, y) \geq 0, \qquad (x, y) \in T, \tag{3.46}$$

$$V(x, y) > 0, \qquad (x, y) \in T. \tag{3.47}$$

It goes without saying that the formula

$$U = \frac{D}{2} \int V^2 \, \mathrm{d}T \tag{3.48}$$

holds.

The validity of formulas (3.40), (3.41) can be demonstrated by the following inequalities:

$$F(\xi, \eta) \Gamma(x, y; \xi, \eta) = D \frac{F(\xi, \eta)}{p(\xi, \eta)} \frac{p(\xi, \eta)}{D} \Gamma(x, y; \xi, \eta) \leq$$

$$\leq D R_{\max} \frac{p(\xi, \eta)}{D} \Gamma(x, y; \xi, \eta), \tag{3.49}$$

$$F(\xi, \eta) \Gamma(x, y; \xi, \eta) = D \frac{F(\xi, \eta)}{p(\xi, \eta)} \frac{p(\xi, \eta)}{D} \Gamma(x, y; \xi, \eta) \geq$$

$$\geq D R_{\min} \frac{p(\xi, \eta)}{D} \Gamma(x, y; \xi, \eta). \tag{3.50}$$

Since the quantities in the above inequalities are not negative, carrying out the integration of (3.49), (3.50), we obtain

$$f(x, y) \leq D R_{\max} V(x, y), \tag{3.51}$$

$$f(x, y) \geq D R_{\min} V(x, y). \tag{3.52}$$

We have $f(x, y) \geqq 0$ and $V(x, y) > 0$ at every point of domain T and therefore we arrive at

$$f^2(x, y) \leq D^2 R_{\max}^2 V^2(x, y), \tag{3.53}$$

$$f^2(x, y) \geq D^2 R_{\min}^2 V^2(x, y). \tag{3.54}$$

Taking into account formula (3.48), the integration of inequalities (3.53) and (3.54) yields inequalities (3.40) and (3.41) which had to be proved.

4. Applications

4.1 Let function p assume a constant value, i.e.

$$p = p(x, y) = p_0 = \text{constant} . \tag{4.1}$$

By applying inequality (3.30) to the function

$$g = \Phi(x, y) \tag{4.2}$$

an elementary calculation yields

$$U \geq \frac{p_0^2 S}{32tD} . \tag{4.3}$$

This formula and formula (3.23) are obviously the same.

4.2 Let us consider the plate shown in Fig. 2. For the sake of simplicity, the units of the quantities in this numerical example shall not be presented. The lower and upper bounds to the strain energy of the triangle-shaped plate subjected to a distributed load of intensity

$$p = p(x, y) = 3x - \frac{3}{20} x^3 \tag{4.4}$$

are obtained from inequalities (3.40) and (3.41). It can be easily proved that inequality

$$p(x, y) > 0 \tag{4.5}$$

holds if the independent variable fulfils the condition

$$0 < x < 1 .$$

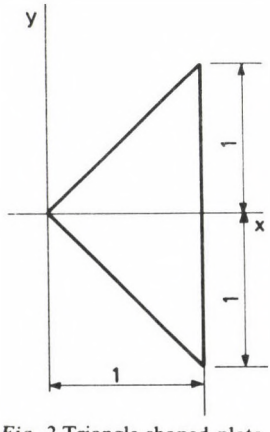

Fig. 2 Triangle-shaped plate

The function of two variables $f=f(x, y)$ fulfilling the conditions (3.37), (3.38) is now taken on as

$$f(x, y)=(x^2-y^2)(1-x)=x^2-y^2-x^3+xy^2 . \tag{4.6}$$

A simple calculation yields

$$F(x, y)=-\Delta f=3x , \tag{4.7}$$

$$R(x, y)=\frac{1}{1-\frac{1}{20}x^2} \tag{4.8}$$

$$R^2_{\min}=1 , \tag{4.9}$$

$$R^2_{\max}=1{,}108 . \tag{4.10}$$

Introducing Eqs (4.6), (4.7), (4.8), (4.9), (4.10) into inequalities (3.40), (3.41), we obtain the lower and upper bounds:

$$UD \leq 1.1125 \times 10^{-2} , \tag{4.11}$$

$$UD \geq 1.00406 \times 10^{-2} . \tag{4.12}$$

4.3 In this section a comparative theorem of simple structure will be derived, using inequalities (3.40), (3.41). Let the functions

$$p_1=p_1(x, y) \qquad \text{and} \qquad p_2=p_2(x, y)$$

denote two different surface loads acting on the plate shown in Fig. 1.

With the formulas

$$\Delta V_1=-\frac{p_1}{D} , \qquad (x, y) \in T, \tag{4.13}$$

$$V_1=0 , \qquad (x, y) \in \partial T; \tag{4.14}$$

$$\Delta V_2=-\frac{p_2}{D} , \qquad (x, y) \in T, \tag{4.15}$$

$$V_2=0 , \qquad (x, y) \in \partial T \tag{4.16}$$

we have

$$U_1=\frac{D}{2}\int_T V_1^2 \, \mathrm{d}T, \tag{4.17}$$

$$U_2=\frac{D}{2}\int_T V_2^2 \, \mathrm{d}T. \tag{4.18}$$

Let the inequalities

$$p_1(x, y) > 0 \qquad (x, y) \in T, \tag{4.19}$$

$$p_2(x, y) > 0 \qquad (x, y) \in T \tag{4.20}$$

hold. As a consequence of inequalities (4.19), (4.20), the inequalities

$$V_1(x, y) > 0, \qquad (x, y) \in T \tag{4.21}$$

$$V_2(x, y) > 0, \qquad (x, y) \in T \tag{4.22}$$

also hold.

Introducing the functions

$$f(x, y) = V_1(x, y), \tag{4.23}$$

$$V(x, y) = V_2(x, y) \tag{4.24}$$

into inequalities (3.40), (3.41), the inequalities

$$U_1 \leq \rho_{\max}^2 U_2, \tag{4.25}$$

$$U_1 \geq \rho_{\min}^2 U_2 \tag{4.26}$$

can be derived, where we have

$$\rho_{\max} = \max_{(x,y) \in T \cup \partial T} \left[\frac{p_1(x, y)}{p_2(x, y)} \right], \tag{4.27}$$

and

$$\rho_{\min} = \min_{(x,y) \in T \cup \partial T} \left[\frac{p_1(x, y)}{p_2(x, y)} \right]. \tag{4.28}$$

Inequalities (4.25) and (4.26) constitute a comparative theorem for the strain energy of plates having the same size and support system, but whose surface loads are different.

4.4 Let the functions

$$p_1 = p_1(x, y) \qquad \text{and} \qquad p_2 = p_2(x, y)$$

denote two different surface loads acting on the plate shown in Fig. 1.

Let us introduce the following relations:

$$\Delta\Delta w_1 = \frac{p_1}{D}, \qquad (x, y) \in T, \tag{4.29}$$

$$w_1 = 0, \qquad (x, y) \in \partial T, \tag{4.30}$$

$$\Delta w_1 = 0, \qquad (x, y) \in \partial T; \tag{4.31}$$

$$\Delta\Delta w_2 = \frac{p_2}{D}, \qquad (x, y) \in T, \tag{4.32}$$

$$w_2 = 0, \qquad (x, y) \in \partial T, \tag{4.33}$$

$$\Delta w_2 = 0, \qquad (x, y) \in \partial T. \tag{4.34}$$

With the above relations we have

$$U_1 = \frac{D}{2} \int_T (\Delta w_1)^2 \, \mathrm{d}T, \tag{4.35}$$

$$U_2 = \frac{D}{2} \int_T (\Delta w_2)^2 \, \mathrm{d}T. \tag{4.36}$$

Inequality (3.36) now yields

$$U_1 \geq \frac{(\int_T p_1 w_2 \, \mathrm{d}T)^2}{2D \int_T (\Delta w_2)^2 \, \mathrm{d}T} \tag{4.37}$$

from which we arrive at

$$U_1 \geq \frac{(\int_T p_1 w_2 \, \mathrm{d}T)^2}{4U_2}. \tag{4.38}$$

The importance of inequality (4.38) is shown by the fact that, knowing function $w_2 = w_2(x, y)$, a lower bound can be created for the strain energy U_1.

References

1. Berger, E. R.: Ein Minimalprinzip zur Auflösung der Plattengleichung. Ingenieur-Archiv. VII/1 1953. 39–49
2. Timoshenko, S.: Theory of Plates and Shells. New York–London–McGraw-Hill, 1940
3. Protter, M. H. and Weinberger, H. F.: Maximum Principles in Differential Equations. Prentice Hall. Inc. Englewood, New Yersey, 1967 81–88
4. Pólya, G. and Szegő, G.: Isoperimetric Inequalities in Mathematical Physics. Princeton. Princeton University Press, 1951

Acta Technica Academiae Scientiarum Hungaricae, 97 (1—4), pp. 65—68 (1984)

IDENTIFICATION OF THE SOURCE OF POLLUTION ALONG THE RIVER BED

K. V. EGOROV, G. D. KUPAYN*

[Received: 9 April 1984]

The acute problems of water resource protection requires using the methods of the contemporary theory of control and system analysis. There appears a task of getting the quantitative characteristics of pollution interrelations which are defined by the corresponding mathematical models. A method for developing such a model and the procedure of its study using a computer technique is suggested. The data obtained can be used to preserve the purity of water resources.

Studies in river pollution processes have led to the necessity of obtaining the quantitative characteristics of pollution, interrelationships of which are described by respective mathematical equations. To investigate mathematical models, the methods pertaining to the up-to-date theory of control and system analysis are applied.

This paper deals with the processes of a non-conservative pollution, i.e. that with organic substances which undergo transformation in the flow (decomposition, oxidation, sedimentation). Definition of the function of pollution may be presented as a problem for determining parameters of the mathematical models for the above process. The problem can be solved by the method of the sliding modulating functions [1].

The quality of water may be characterized by the concentration of dissolved oxygen (DO) and the biochemical consumption of oxygen (BCO). Here BCO is an index of the organic water pollution. The mathematical model of the pollution process is expressed by the modified Streeter-Phelps Eq. [2]

$$\frac{\partial L(x,t)}{\partial t} = D_L \frac{\partial^2 L(x,t)}{\partial x^2} - \frac{Q}{A}\frac{\partial L(x,t)}{\partial x} - KL(x,t) + f(x,t) \tag{1}$$

$$x \in [a,b], \quad t \in [0,T]$$

where $L(x,t)$—BCO value dependent on time t and distance x along the river-bed; Q—water-flow through A-cross-section; K-decomposition coefficient equal to summed up co-efficients of self-purification and sedimentation; $f(x,t)$—the source of pollution reduced to the BCO.

* K. V. Egorov, G. D. Kupayn, MEI, E 250 Moscow, USSR

The problem of identification of equation (1) is formulated as follows: one knows the structure of the mathematical model as expressed by equation (1) and the numerical values of empiric co-efficients Q, D_L, A, *and* K; it is required to identify the function of the pollution source $f(x, t)$ by measuring the function of state $L(x, t)$.

In general, it is impossible to determine the arbitrary function $f(x, t)$, therefore, the problem is simplified assuming that

$$f(x, t) = w(x)v(t) \tag{2}$$

This assumption means that the temporal distribution of BCO—$v(t)$ is known and uniform along the river-bed. The unknown function $w(x)$ contains information on the location and intensity of the pollution source.

Furthermore, assuming that $L(x, t)$ is a generalized function of order 2 and determined according to the space of the principal functions

$$K^2(G) = \left\{ \varphi(x, t) : \varphi \in E_2(G) \begin{matrix} \forall (x, t) \in \partial G[\varphi(x, t) = 0] \\ \forall (x, t) \in \partial G[\varphi(x, t) \neq 0] \end{matrix} \right\} \tag{3}$$

where $G = (a, b) \times (0, T)$ is an open area of Euclid's two-dimensional space E_2 with the border-line ∂G; $\varphi(x, t)$ principal function derived from $K^2(G)$ or the modulating one.

According to the rule of differentiating the generalized functions

$$\langle D^k y, \varphi \rangle = (-1)^k \langle y, D^k \varphi \rangle \quad \varphi \in K(G) \tag{4}$$

and taking into account the linearity of the scalar product, Eq. (1) takes the following form:

$$-\left\langle L(x, t), \frac{\partial \varphi(x, t)}{\partial t} \right\rangle = D_L \left\langle L(x, t), \frac{\partial^2 \varphi(x, t)}{\partial x^2} \right\rangle + \frac{Q}{A} \left\langle L(x, t), \frac{\partial \varphi(x, t)}{\partial x} \right\rangle -$$

$$- K \langle L(x, t), \varphi(x, t) \rangle + \langle f(x, t), \varphi(x, t) \rangle . \tag{5}$$

Taking down the last term of expression (5) and considering the assumption (2)

$$\langle f(x, t), \varphi(x, t) \rangle = \langle w(x), v(t), \varphi(x, t) \rangle \tag{6}$$

To reduce the problem of determining function $w(x)$ for the identification of parameters, one reduces $w(x)$ to a piece-constant function. To do this we divide the interval $[a, b]$ into n sections Δx long and assume that in each section $w(x) = \text{const}$. Then expression (6) for every i-th section may be represented by

$$\langle f(x, t), \varphi(x, t) \rangle = w_i(x^i) \langle v(t), \varphi_i(x^i, t) \rangle$$

$$i = 1; \ldots n \qquad x^i \in [x_i - \Delta x, x_i] . \tag{7}$$

In this case Eq. (5) is considered in n areas of the kind of

$$G_i = (x^i - \Delta x, x^i) \times (0, T) \tag{8}$$

and in n spaces of generalized functions $K^2(G_i)$ with the carriers

$$\sup \varphi_i(x^i, t) = \overline{(x^i - \Delta x, x^i) \times (0, T)} \tag{9}$$

Let us regroup the terms of Eq. (5) so as to elucidate the function of spatial distribution of the pollution source.

$$w_i(x^i)\langle v(t), \varphi_i(x^i, t)\rangle = -D_L \left\langle L(x^i, t), \frac{\partial^2 \varphi_i(x^i, t)}{\partial x^2} \right\rangle -$$

$$- \frac{Q}{A} \left\langle L(x^i, t), \frac{\partial \varphi_i(x^i, t)}{\partial x} \right\rangle + K\langle L(x^i, t), \varphi_i(x^i, t)\rangle -$$

$$- \left\langle L(x^i, t), \frac{\partial \varphi_i(x^i, t)}{\partial t} \right\rangle. \tag{10}$$

The mean value of the function $w_i(x^i)$ is presented by the n-dimensional vector

$$\mathbf{w} = \text{col}\,[(w_1(x^1), w_2(x^2), \ldots w_n(x^n)] \tag{11}$$

A diagonal matrix is introduced

$$\mathbf{Z} = \text{diag}\,[\langle v(t), \varphi_1(x^1, t)\rangle \ldots \langle v(t), \varphi_n(x^n, t)\rangle], \tag{12}$$

and n-vector $\mathbf{h}$ with the components

$$h_i = -D_L \left\langle L(x_i, t), \frac{\partial^2 \varphi_i(x_i, t)}{\partial x^2} \right\rangle \cdot \frac{Q}{A} \left\langle L(x^i, t), \frac{\partial \varphi_i(x^i, t)}{\partial x} \right\rangle +$$

$$+ K\langle L(x^i, t), \varphi_i(x^i, t)\rangle - \left\langle L(x^i, t), \frac{\partial \varphi_i(x^i, t)}{\partial t} \right\rangle \tag{13}$$

Bearing in mind indices (11), (12) and (13) we can put down equation (10) in the form of a matrix

$$\mathbf{w} = \mathbf{Z}^{-1}\mathbf{h}. \tag{14}$$

The components of the obtained parameter vector are the successive segments of the spatial distribution function of the pollution source and its intensity, considered in the sections and averaged in each of them.

The above used linear mathematical model of the pollution process (1) is rather a simplified description of the real processes. On the one hand, the photosynthesis and pollution by inorganic sources are not taken into consideration. On the other hand, the real processes are not linear due to the scale-eduction of oxygen in bubbles, that, in its turn depends on the temperature and other ecologic factors. However, more complicated pollution models would require the knowledge of additional empiric coefficients, and the consideration of non-linearity impedes the use of such models in connection with computing difficulties.

References

1. Купайн, Г. Д., Чекалин, В. Г.: Обобщение процедуры идентификации на основе метода скользящих модулирующих функций. Докл. АН Тадж. ССР, 1981, т. XXIV, № 5, с. 288—291
2. Ikeda, S., Miaymoto, S., Sawaragi, Y.: Int. Y Systems Sci., vol. 5, (1974) № 8
3. Егоров, К. В., Купайн, Г. Д.: О моделировании засорения потоков. Доклады IV Всесоюзной конференции охраны окружающей среды. Киев, 1981.

Acta Technica Academiae Scientiarum Hungaricae, 97 (1—4) pp. 69—83 (1984)

RELATIONSHIPS AND APPLICATION POSSIBILITIES OF THE THEORIES OF MICROELASTIC CONTINUA

J. FÜZY,* J. VAS**

[Received: 1 September 1982]

In the recent decades, several theories of higher degrees of freedom have been developed, under the collective name "microelastic continuum theories". An analysis is given in this paper for the derivation of the best known such theories from the theory of a continuum of 12 degrees of freedom—that of the deformable directors. In knowledge of the rule of derivation, several microelastic continua, not examined up to now, will be shown to be interpretable. One of them will be discussed in detail, together with physical application possibilities.

Symbols

i, j, k, l, p, q — subscripts, with possible values of 1, 2, 3;
$'i$ — symbol of partial differentiation;
$a_{i,i}$ —divergence of vector a_i (under validity of Einstein's summarizing convention);
$a_{,i}$ — gradient of scalar a;
$'ii$ — Laplacian operator;
U_i — displacement vector;
d_{ij} — micro deformation tensor;
D_{ij} — macro deformation tensor;
γ_{ij} — relative deformation tensor;
κ_{ijk} — tensor of hyperdeformations;
S_{ij} — macro stress tensor;
σ_{ij} — tensor of relative stresses;
μ_{ijk} — hyper stress tensor;
f_k — rotation vector;
e — function of intrinsic volume change;
p_i — density vector of body force;
$\emptyset_{ij}$ — density tensor of double (or hyper) stresses distributed across the volume (analogous to body forces);
δ_{ij} — Kronecker-delta, of value 1 for $i=j$, else 0;
e_{ijk} — Levi–Cività tensor, of values $+1$, -1, 0,
depending on whether its subscripts are different and even permutations $(+1)$, odd permutations (-1), or they include identical ones (0);
d_{ij}^D — deviator part of tensor d_{ij}.

* Füzy, J., H-1012, Budapest, Márvány u. 1/b, Hungary
** Vas, J., H-2000, Szentendre, Vasvári P. u. 43. Hungary

2. Introduction

Since the establishment of the equations of classic continuum mechanics a great number of solutions have been developed for a wide range of problems.

Initially almost exclusively linear elastic material laws were applied. The modification of the material equations permitted the researchers to model the behaviours of materials with visco-elastic, plastic, visco-plastic, etc. properties.

These modifications, refinements do not exceed, however, the model's fundamental hypotheses on the material particle motion.

A modification of Duhem's theory ([6], 1893) was developed by Cosserat Brothers ([7], 1909). They added further three degrees of freedom to the original three ones of the motion of a material point—assumed in the classic theory of continua,—introducing, in addition to the displacement, the kinematically independent rotation of the material point. Under these fundamental conditions the stress tensor is symmetric no more (invalidating the Boltzmann axiom) and equilibrium of the elementary parallelepiped required to introduce moment stresses.

Originally, Duhem suggested a body to be regarded as a collection not only of points, but also of directions associated with the points. These vectors to be called directors are able to independently vary their direction and magnitude.

This approach to theories of higher degrees of freedom—such as that by Cosserat—makes it possible to describe effects which cannot be taken into consideration in the classic model.

The Cosserat theory gained application not sooner than 50 years after its discovery ([14], 1958 Günther); ([13], 1960 Grioli); ([24, 25, 26], 1958–1967 Schaefer).

Nearly simultaneously to the rediscovery, but without the knowledge of this theory—as complement to the classic theory—the so-called pseudo-Cosserat model arose, where the rotation of the material point was defined as a kinematic constrained connection due to the asymmetry of the deformation tensors [1, 2, 29, 30, 31].

Similarly to the classic theory, this theory also involves three degrees of freedom but here the deformed condition is described by the tensor derived from the displacement vector, that is, the antimetric part describes the rotation of the material point. Now, the rotation vector is not an independent kinematic variable any more but the rotation of the displacement vector.

In the recent 25 years several new, interesting theories of elasticity have arisen, featured by certain distinction between "micro" and "macro" material structures. One of them is the theory of deformable directors [18], by another denomination the theory of multipolar continua [12] where—in conformity with Duhem's theory—directors are assigned to the material points, and the director tip displacements are further degrees of freedom. Directors may be of an arbitrarily high number.

The theory by Mindlin [18] limits the number of directors to three corresponding to the threedimensional Euclidean space, lending 12 degrees of freedom to the material point. Each material particle is assumed to have an inherent micro-

volume. This unit cell may also be interpreted as a molecule, a crystallite or a grain of the given material. Accordingly, the continuum can be conceived as a collection of these material points where in each of them—in addition to the material point displacement—an intrinsic micro deformational state independent of the displacement is interpreted, expressing the displacement of the apexes of the triad of directors. Accordingly, the continuum is composed of unit or micro cells with deformations yielding nine degrees of freedom of the theory, further three arising from the displacement of a preferential point (e.g. centroid) of the unit cell [9, 18]. There is a wide variety of symbols, denominations in fundamentally similar theories by different authors. Current denominations are: microelastic, multipolar, dipolar, generalized Cosserat ... etc. theories. Theories are referred to as those by Mindlin, Toupin, Eringen, Suhubi, Ericksen–Truesdell, Green–Rivlin, etc.

It should be pointed out that most of these denominations refer to the generalized continuum model or a special case of it, relying essentially on the same assumptions.

In the following, we will refer to the general theory as the Mindlin theory, using his symbols [18] and concept denominations. Starting out from Mindlin's general theory, special cases will be derived by reducing the kinematic degrees of freedom of the material point. No kinematic effects will be considered. The effect of deformational geometry changes will be ignored.

Exclusively linear elastic solids will be examined, assuming slow deformations, and irrelevance of displacement to the final condition.

3. The Mindlin theory

According to the Mindlin theory of microelastic continua [18], "inside" the elementary point—essentially an elementary volume of finite size—a micro deformation tensor is interpreted, as an independent kinematic variable. This tensor d_{ij} is homogeneous inside the elementary point (microcell), but is not in the macro space, this, it has a gradient according to a macro variable.

Its symmetric part is the micro strain tensor $d_{(ij)}$, and its antimetric part $d_{[ij]}$ is a micro rotation tensor. In the theory of the so-called deformable directors, a director triad is assigned the elementary point, kinematically independently varying size and direction in course of the deformation of the medium. In this case the director apexes will have displacement components exactly corresponding to the elements of tensor d_{ij}.

We mention here that, obviously, the components of micro rotation tensor $d_{[ij]}$ are the components of rigid rotation of the so-called Cosserat "trièdre" [3].

Let us define the usual—this time macro—strain tensor:

$$D_{(ij)} = \frac{1}{2}(U_{j,i} + U_{i,j}) \tag{1}$$

and the so-called relative deformation tensor which is the difference of the gradient of the macro displacement vector and the micro deformation tensor:

$$\gamma_{ij} = U_{j,i} - d_{ij} \tag{2}$$

as well as the macro gradient of the micro deformation tensor which is a third-order tensor of the hyper deformations:

$$\kappa_{ijk} = d_{jk,i}. \tag{3}$$

Let the fundamental kinematic variables be macro displacement vector U_i and micro deformation tensor d_{ij}, unique functions of the macro space coordinates. Equations (1), (2) and (3) are the set of geometric equations of the microelastic continuum theory. Of the compatibility equations equivalent to them, the macro deformation tensor satisfies the equation

$$e_{mik} e_{nlj} D_{kl,ij} = 0. \tag{4}$$

Further equations are obtained by taking the integral of (2) and (3) with respect to an arbitrary closed curve C in the continuum:

$$\oint_{(C)} \gamma_{ij} \mathrm{d}x_i = \oint_{(C)} U_{j,i} \mathrm{d}x_i - \oint_{(C)} d_{ij} \mathrm{d}x_i, \tag{5}$$

$$\oint_{(C)} \kappa_{ijk} \mathrm{d}x_i = \oint_{(C)} d_{jk,i} \mathrm{d}x_i. \tag{6}$$

Assuming, however, the compatibility of the displacement and deformation fields, we have

$$\oint_{(C)} U_{j,i} \mathrm{d}x_i = 0, \qquad \oint_{(C)} d_{jk,i} \mathrm{d}x_i = 0 \tag{7}$$

and the compatibility equations for tensors of relative and hyper deformations will be obtained from (5) and (6), applying Stokes' theorem, in the form:

$$e_{mij} \kappa_{jkl,i} = 0,$$

$$\gamma_{ij,k} e_{kil} + \kappa_{kij} e_{kil} = 0. \tag{8}$$

The body in question is assumed to be of constant temperature and to be exempt from stresses and strains at this temperature, insisting on the examination of small deformations alone.

Accordingly, the strain energy density function can be defined in the function of the deformation tensors introduced above as

$$W = W(D_{ij}, \gamma_{ij}, \kappa_{ijk}). \tag{9}$$

W can be applied to define the symmetric macro stress tensor

$$S_{(ij)} = \frac{\partial W}{\partial D_{ij}}, \tag{10}$$

the tensor of relative stresses:

$$\sigma_{ij} = \frac{\partial W}{\partial \gamma_{ij}}, \tag{11}$$

and the tensor of hyper or double stresses:

$$\mu_{ijk} = \frac{\partial W}{\partial \kappa_{ijk}}. \tag{12}$$

The deformation energy density function is homogeneous quadratic function of the deformation tensors, a positive definite one. In the case of centrosymmetric, isotropic material model applied also by Mindlin, the density function W of deformation energy becomes:

$$\begin{aligned} W = & \frac{1}{2}\lambda D_{ii}D_{jj} + \mu D_{ij}D_{ij} + \frac{1}{2}b_1\gamma_{ii}\gamma_{jj} + \frac{1}{2}b_2\gamma_{ij}\gamma_{ij} + \\ & + \frac{1}{2}b_3\gamma_{ij}\gamma_{ji} + g_1\gamma_{ii}D_{jj} + g_2(\gamma_{ij}+\gamma_{ji})D_{ij} + \\ & + a_1\kappa_{iik}\kappa_{kjj} + a_2\kappa_{ikk}\kappa_{jkj} + \frac{1}{2}a_3\kappa_{iik}\kappa_{jjk} + \\ & + \frac{1}{2}a_4\kappa_{ijj}\kappa_{jkk} + a_5\kappa_{ijj}\kappa_{kik} + \frac{1}{2}a_8\kappa_{iji}\kappa_{kjk} + \\ & + \frac{1}{2}a_{10}\kappa_{ijk}\kappa_{ijk} + a_{11}\kappa_{ijk}\kappa_{jki} + \frac{1}{2}a_{13}\kappa_{ijk}\kappa_{ikj} + \\ & + \frac{1}{2}a_{14}\kappa_{ijk}\kappa_{jik} + \frac{1}{2}a_{15}\kappa_{ijk}\kappa_{kji}. \end{aligned} \tag{13}$$

The variation equations of motion directly yield the twelve equilibrium equations [18]:

$$(S_{(ij)} + \sigma_{ij})_{,i} + p_j = 0, \qquad \text{a)}$$

$$\mu_{ijk,i} + \sigma_{jk} + \Phi_{jk} = 0. \qquad \text{b)} \tag{14}$$

4. Deduction of various known micro-elastic continuum theories

There are several publications interpreting the known continuum theories as special cases of the general theory. Also Eringen [9] and Mindlin [18] interpret the Cosserat and the pseudo-Cosserat models in this way. Most of the authors concerned with the Cosserat and the pseudo-Cosserat models present the classic continuum theory as a special case of them [20]. The subsequent method will be applied to interpret possible special cases of the micro-elastic theory with 12 degrees of freedom.

A unified approach can be applied to the special theories if we distinguish them according to the degrees of freedom of the material point. Special cases will be presented deductively from the general theory applying restrictions on the twelve degrees of freedom, examining the properties and the role of the components of the microdeformation tensor via the deduced cases.

This procedure involves also the classification of the theories taking local deformations into consideration.

The unified discussion is advantageous by making it possible to involve the known theories (classic, Cosserat, pseudo-Cosserat) in a general theory, helping to detect their deeper correlations.

Beyond that, models can be generated that can perhaps include a means to describe certain physical phenomena. This deductive discussion provides for the completeness of the interpreted theories.

Restriction of the degrees of freedom will be seen to be insufficient itself to the unique selection of a special theory, further stipulations on the material constant are needed.

Thereby special cases of the general theory are assigned to multi-model groups with identical degrees of freedom of the material point.

4.1 Derivation of the Cosserat continuum theory

Starting from the definition (2) of the relative deformation tensor, let us decompose it to symmetric and skew symmetric parts:

$$\gamma_{ij} = D_{ij} + \frac{1}{2}(U_{j,i} - U_{i,j}) - d_{(ij)} - d_{[ij]}. \tag{15}$$

In the following, ( ) and [ ] in tensor subscripts will refer to symmetry, and to skew symmetry, respectively; except for the macro strain and stress tensors stated above to be symmetric.

Degrees of freedom of the material point are reduced to 6 under the following conditions:

$$d_{(ij)} = 0. \tag{16}$$

The remaining kinematic variables are the three components of the macro and the three components of the micro deformation tensor. Established with the rotation vector (as invariant vector), this latter becomes:

$$d_{[ij]} = e_{ijk} f_k. \tag{17}$$

The rigid-body rotation of the micro-cell is, from (17):

$$f_k = \frac{1}{2} d_{[ij]} e_{ijk}. \tag{18}$$

Taking (17) and (16) into consideration, the relative deformation tensor becomes

$$\gamma_{(ij)} = D_{ij} \qquad \text{a)}$$

$$\gamma_{[ij]} = \frac{1}{2}(U_{j,i} - U_{i,j}) - e_{ijk} f_k. \qquad \text{b)} \quad (19)$$

Forming the invariant vector of γ_{ij}, i.e. multiplying (19) by $1/2e_{ijq}$, taking into consideration

$$e_{ijk} e_{ijq} = 2\delta_{kq} \qquad (20)$$

yields

$$\gamma_q = \frac{1}{2} \gamma_{ij} e_{ijq} = \frac{1}{2} U_{j,i} e_{ijq} - f_q. \qquad (21)$$

With the aid of the fundamental equations of the general theory, the hyper deformation tensor is obtained as:

$$\kappa_{ijk} = d_{[jk],i} = f_{l,i} e_{jkl}. \qquad (22)$$

The hyper deformation tensor is seen from its subscripts j, k in (22) to be skew symmetric, so that according to (17), it can be produced by means of a tensor by one order lower:

$$\kappa_{ijk} = e_{jkl} \kappa_{il}. \qquad (23)$$

Now, κ_{ijk} has 9 independent components—in contrast the 27 in the general case.

The equilibrium equation (14b) decomposed to symmetric and skew symmetric parts is written as

$$\mu_{i[jk],i} + \sigma_{[jk]} + \Phi_{[jk]} = 0 \qquad \text{a)}$$

$$\mu_{i(jk),i} + \sigma_{(jk)} + \Phi_{(jk)} = 0. \qquad \text{b)} \quad (24)$$

Introducing—arbitrarily for the time being—the simplifications and conditions:

$$\mu_{i(jk)} = 0 \qquad \text{a)}$$

$$\Phi_{(jk)} = 0 \qquad \text{b)}$$

$$\mu_{i[jk]} = e_{jkl} \mu_{il} \qquad \text{c)} \quad (25)$$

yields, in conformity with (14):

$$\mu_{il,i} + \frac{1}{2} \sigma_{[pq]} e_{pql} + \Phi_{jk} e_{jkl} = 0, \qquad (26)$$

$$\sigma_{(jk)} = 0, \qquad (27)$$

this latter being a stipulation on the material constants. Making use of (10), (11) and (12), (13) yields the material constants:

$$g_1 + b_1 = 0 \qquad \text{a)}$$

$$g_2 + b_2 + b_3 = 0. \qquad \text{b)} \quad (28)$$

Eq. (13) also yields:

$$S_{ij}=(\lambda+g_1)D_{kk}\delta_{ij}+2(\mu+g_2)D_{ij} \quad \text{a)}$$

$$\sigma_{[ij]}=(b_2-b_3)\gamma_{[ij]}. \quad \text{b)} \quad (29)$$

S_{ij} is a symmetric and $\sigma_{[ij]}$ is a skew symmetric tensor so it is expedient to comprise them in a general stress tensor:

$$\bar{S}_{ij}=S_{ij}+\sigma_{[ij]}. \quad (30)$$

Since the symmetric part of the relative deformation tensor and the macro strain tensor are the same, tensor

$$\gamma_{ij}=U_{j,i}-d_{[ij]} \quad (31)$$

can be considered as the deformation tensor.

Now, making use of (30), the stress tensor becomes:

$$\bar{S}_{ij}=(\lambda+g_1)\gamma_{kk}\delta_{ij}+2(\mu+g_2)\gamma_{(ij)}+(b_2-b_3)\gamma_{[ij]}, \quad (32)$$

or, introducing new constants:

$$\bar{S}_{ij}=2C_2\gamma_{(ij)}+C_1\gamma_{kk}\delta_{ij}+\nu_4\gamma_{[ij]} \quad (33)$$

where

$$C_2=\mu+g_2, \quad \text{a)}$$

$$C_1=\lambda+g_1, \quad \text{b)}$$

$$\nu_4=b_2-b_3. \quad \text{c)} \quad (34)$$

The stress tensor equilibrium equation becomes

$$\bar{S}_{ij,i}+p_j=0. \quad (35)$$

Also relationships between hyper-stresses and -deformations are obtained from the general theory [18]. Taking restrictions (25) and (23) into consideration we obtain

$$\mu_{ij}=\nu_1\kappa_{(ij)}+\nu_2\kappa_{[ij]}+\nu_3\delta_{ij}\kappa_{kk} \quad (36)$$

where:

$$\nu_1=a_{10}-a_{13}-a_{11}+a_{15} \quad \text{a)}$$

$$\nu_2=a_{10}-a_{13}-2(a_2-a_3)-(a_{11}-a_{15}) \quad \text{b)}$$

$$\nu_3=a_{11}-a_{15} \quad \text{c)} \quad (37)$$

and

$$\kappa_{ij}=f_{j,i} \quad (38)$$

For restriction (25a) the conditions

$$a_1=s_5 \quad \text{a)}$$

$$a_3 = a_8 \qquad \text{b)}$$

$$a_{14} = a_{15} \qquad \text{c)} \quad (39)$$

have to be satisfied between material constants.

In publications, constants in (36) are usually produced as:

$$\nu_1 = \frac{2C_2L^2}{12} \qquad \text{a)}$$

$$\nu_2 = \frac{2C_2L^2\mu_1}{12} \qquad \text{b)}$$

$$\nu_3 = \frac{2C_2L^2\mu_2}{12} \qquad \text{c)} \quad (40)$$

where L is length, and μ_1 and μ_2 are nondimensional quantities. This way of formulation is of importance since the physical meaning of material characteristic L is easy to define, and it can be seen that it is a magnitude close to that of the mean cell size. For certain materials, it can be determined in bending tests [25]. C_2 in (29) was formed of the modulus of elasticity E and Poisson's ratio ν as:

$$C_2 = \frac{E}{2(1+\nu)}. \qquad (41)$$

Equilibrium Eqs (26) and (35), material equations (32) and (36) as well as geometry Eqs (31) and (38) make up the fundamental equation system of the Cosserat continuum.

4.2 Theory of the micropolar (pseudo-Cosserat) continuum

Let us restrict the general theory as:

$$d_{(ij)} = 0 \qquad \text{a)}$$

$$d_{[ij]} = \frac{1}{2}(U_{j,i} - U_{i,j}). \qquad \text{b)} \quad (42)$$

Restriction (42b) means that the rotation vector of the material point is defined by the kinematic constraint connection

$$f_k = \frac{1}{2} U_{j,i} e_{ijk} \qquad (43)$$

and the degrees of freedom of the material point decrease to 3.

Taking (42) into consideration, the relative deformation tensor becomes:

$$\gamma_{(ij)} = D_{ij} \qquad \text{a)}$$

$$\gamma_{[ij]} = 0 \qquad \text{b)} \quad (44)$$

and the hyper deformation tensor assumes the form

$$\kappa_{i[jk]} = d_{[jk],i} = e_{jkl} f_{l,i} \qquad \text{a)}$$

$$\kappa_{i(jk)} = 0 \qquad \text{b)} \quad (45)$$

Substituting (43) into (45a), we arrive at

$$\kappa_{i[jk]} = \frac{1}{2} e_{jkl} e_{lqp} U_{p,qi}, \tag{46}$$

hence

$$\kappa_{kl} = \frac{1}{2} e_{lqp} U_{p,qk}. \tag{47}$$

Applying the same simplifications (25) as in the Cosserat theory, the material equation (36) becomes

$$\mu_{ij} = \nu_1 \kappa_{(ij)} + \nu_2 \kappa_{[ij]}, \tag{48}$$

since

$$\kappa_{kk} = 0 \tag{49}$$

holds.

In conformity with condition (44b), the skew symmetric part of the relative deformation tensor is zero, hence stress tensor (29b) is non-zero only if:

$$(b_2 - b_3) \to \infty. \tag{50}$$

Equilibrium equation (26) now becomes the defining equation of $\sigma_{[ij]}$:

$$\frac{1}{2} \sigma_{[ij]} e_{ijk} + \mu_{ik,i} + \frac{1}{2} \Phi_{ij} e_{ijk} = 0 \tag{51}$$

and the other equilibrium equation is identical to (35), where

$$\bar{S}_{ij} = C_1 D_{kk} \delta_{ij} + 2C_2 D_{ij} + \sigma_{[ij]}. \tag{52}$$

Material equations (52) and (44), geometry equations

$$D_{ij} = \frac{1}{2} (U_{i,j} + U_{j,i}) \tag{53}$$

and (47), as well as equilibrium equations (35) and (51) are fundamental equations of the pseudo-Cosserat theory [20, 25].

If (50) is not prescribed then, in conformity with (44), the skew symmetric part of the stress tensor will be zero, hence (51) will be identically satisfied if conditions

$$\mu_{ik} = 0 \qquad \text{a)}$$

$$\Phi_{ij} e_{ijk} = 0 \qquad \text{b)} \quad (54)$$

hold.

These conditions also yield the fundamental equations of the classic continuum theory, again with 3 degrees of freedom.

4.3 Derivation of the classic continuum theory

A certain derivation of the classic theory starting from the pseudo-Cosserat model has been referred to in Section 4.2.

Using restrictions

$$\gamma_{ij}=0 \tag{55}$$

and

$$\begin{aligned} \mu_{ijk}&=0 && \text{a)}\\ \Phi_{ij}&=0 && \text{b)}\\ g_1&=g_2=0 && \text{c)} \end{aligned} \tag{56}$$

the general theory yields the fundamental equations of the classic continuum theory:

$$S_{ij,i}+p_j=0 \qquad \text{a)}$$

$$D_{ij}=\frac{1}{2}(U_{i,j}+U_{j,i}) \qquad \text{b)}$$

$$S_{ij}=\lambda\delta_{ij}D_{kk}+2\mu D_{ij} \qquad \text{c)} \tag{57}$$

4.4 Micro-elastic continua without micro rotation

With

$$d_{ij}=d_{(ij)} \tag{58}$$

the relative deformation tensor assumes the form

$$\gamma_{(ij)}=D_{ij}-d_{(ij)} \qquad \text{a)}$$

$$\gamma_{[ij]}=\frac{1}{2}(U_{j,i}-U_{i,j}) \qquad \text{b)} \tag{59}$$

or, decomposing $d_{(ij)}$ to deviator and isotropic parts,

$$\gamma_{ij}=U_{j,i}-\frac{d_{kk}}{3}\delta_{ij}-d^{D}_{(ij)}. \tag{60}$$

The first scalar invariant of the relative deformation tensor is

$$\gamma_{kk}=U_{k,k}-d_{kk} \tag{61}$$

showing the affinity between the isotropic part of the micro deformation tensor and an independent volumetric deformation (dilatation). In this model, dilatation (spherical strain), a phenomenon in granular media, may also occur for shear strain (the first scalar invariant of the macro strain tensor is zero).

Further developing the theory, symmetry of the micro deformation tensor yields

$$\kappa_{i(jk)} = d_{(jk),i} \qquad \text{a)}$$

$$\kappa_{i[jk]} = 0 \qquad \text{b)} \quad (62)$$

that is, the hyper deformation tensor has now 18 independent elements.

Introducing simplifications (58) and (62) into (13), the function of the deformation energy density becomes:

$$W = S_{ij} D_{ij} + \sigma_{(ij)} \gamma_{(ij)} + \sigma_{[ij]} \gamma_{[ij]} + \mu_{i(jk)} \kappa_{i(jk)} \qquad (63)$$

where

$$S_{ij} = \lambda \delta_{ij} D_{kk} + 2\mu D_{ij} + g_1 \delta_{ij} \gamma_{kk} + g_2 (\gamma_{ij} + \gamma_{ji}) \qquad \text{a)}$$

$$\sigma_{[ij]} = (b_2 - b_3) \gamma_{[ij]} \qquad \text{b)}$$

$$\sigma_{(ij)} = g_i \delta_{ij} D_{kk} + 2 g_2 D_{ij} + b_1 \delta_{ij} \gamma_{kk} + (b_2 + b_3)(\gamma_{ij} + \gamma_{ji}) \qquad \text{c)} \quad (64)$$

where λ and μ are Lamé constants known from the classic theory of elasticity and the other constants are defined by (13).

The construction of the density function (63) of the deformation energy shows that the term

$$\mu_{i[jk]} \kappa_{i[jk]} \qquad (65)$$

is omitted since $\kappa_{i[jk]}$ is zero. Thus, from energetical aspects, two hyper stress tensor fields $\underset{1}{\mu}_{ijk} - \underset{2}{\mu}_{ijk}$ are equivalent if

$$\underset{2}{\mu}_{ijk} = \underset{1}{\mu}_{ijk} + \omega_{i[jk]} \qquad (66)$$

where $\omega_{i[jk]}$ is an arbitrary function which is skew symmetric concerning subscripts j, k.

Let e.g.

$$\omega_{i[jk]} = 0 \qquad \text{a)}$$

$$\underset{1}{\mu}_{i[jk]} = \underset{2}{\mu}_{i[jk]} = 0. \qquad \text{b)} \quad (67)$$

The equilibrium equations of the theory are obtained from (14) after simplifications:

$$(S_{ij} + \sigma_{ij})_{,i} + p_j = 0 \qquad \text{a)}$$

$$\mu_{i(jk),i} + \sigma_{(jk)} + \Phi_{(jk)} = 0 \qquad \text{b)} \quad (68)$$

or, excluding the skew symmetric parts of the double stresses distributed across the volume: $\Phi_{[ij]} = 0$, the skew symmetric part of the equilibrium equation (14b), taking (67) into consideration, yields

$$\sigma_{[ij]} = 0 \qquad (69)$$

that is, in conformity with (64b), relation

$$b_2 = b_3. \tag{70}$$

must hold.

Thereby the deformation energy density function is transformed from (63) to:

$$W = S_{ij} D_{ij} + \sigma_{(ij)} \gamma_{(ij)} + \mu_{i(jk)} \kappa_{i(jk)}. \tag{71}$$

Restrictions (67) on the material constants are equivalent to:

$$a_1 = a_5 \qquad \text{a)}$$

$$a_8 = a_3 \qquad \text{b)}$$

$$a_{14} = a_{15} \qquad \text{c)} \tag{72}$$

hence the missing material equation becomes:

$$\begin{aligned} \mu_{p(qr)} = {} & [2a_1 \kappa_{iip} + a_4 \kappa_{pii}] \delta_{qr} + [(a_2 + a_3) \kappa_{iir} + \\ & + a_1 \kappa_{rii}] \delta_{pq} + [(a_2 + a_3) \kappa_{iiq} + a_1 \kappa_{qii}] \delta_{pr} + \\ & + (a_{10} + a_{13}) \kappa_{pqr} + (a_{11} + a_{14}) (\kappa_{rpq} + \kappa_{qpr}) \end{aligned} \tag{73}$$

In this interpretation of the model, the micro-cell deformation is pure dilatation and distorsion.

Further simplifying the model by excluding the micro-cell distorsion, hence

$$d_{(ij)} = e \delta_{ij} \tag{74}$$

transforms the relative deformation tensor, using (59), to:

$$\gamma_{(ij)} = D_{ij} - e \delta_{ij} \qquad \text{a)}$$

$$\gamma_{[ij]} = \frac{1}{2} (U_{j,i} - U_{i,j}). \qquad \text{b)} \tag{75}$$

The physical purport of the scalar function "e" introduced above is to be some "intrinsic volume change"; the fundamental relationships of continua with this feature have been previously presented by the Authors [32, 33].

5. Conclusions

Mindlin's theory on micro-deformational continua has been shown to make it possible to derive several known microelastic continuum theories, restricting the degrees of freedom rather than the material constants. In this conception it is obvious that several continuum theories—not discussed so far—can be generated in a similar way. Obviously, not all the resulting theories will have a real physical reason but there

must be some which are applicable to simulate some physical phenomenon. Thus the continuum with "intrinsic volume change" presented in the last Section is likely to suit simulation of the behaviour of granular materials. Shear deformation of these materials is known to be accompanied by volume change, they are compressed or expanded depending on their material constants. Efforts have been made to simulate behaviour of such media by a continuum, introducing a new—independent—scalar function: the voids ratio [5]. In this approximation, the analogy with the theory deduced from the Mindlin theory is obvious.

References

1. Aero, E. L., Kuvshinskii: Fundamental equations of the theory of elastic media with rotationally interacting particles. Fizika Tverdago Tela 2, 1399–1409 (1960) Translation: Soviet Physics Solid State 2 (1961) 1272–1281.
2. Afanasiev-Nikolaevski: On some examples of media with microstructure of continuous particles. Int. J. Solids Structures 5 (1969), 671–678.
3. Cosserat, E. and F.: Théorie des Corps Déformables, Herman and Fils, Paris, 1909.
4. Cowin, S. C.: Stress functions for Cosserat elasticity. Int. J. Solids Structures 6 (1970), 389–398.
5. Cowin, S. C., Goodman, M. A.: A variational principle for granular materials. ZAMM 56 (1976), 281–286.
6. Duhem, P.: Le potentiel thermodynamique et la pression hydrostatique. Ann. ecole norm. 10 (1983), 187.
7. Ericksen, J. L., Truesdell, C.: Exact theory of stress and strain in rods and shells. Arch. Rational Mech. Anal. 1 (1958), 295–323.
8. Eringen, A. C.: Nonlinear theory of continuous media. McGraw Hill, New York 1962.
9. Eringen, A. C.: Linear theory of micropolar elasticity, J. Math. Mech. 15 (1966), 909.
10. Eringen, A. C., Suhubi, E. S.: Nonlinear theory of simple microelastic solids. I. Int. J. Engn. Sci. 2 (1964), 189–203.
11. Fizikai kézikönyv műszakiaknak (Manual of Physics for Engineers). Vols I, II. Műszaki Könyvkiad, Budapest 1980. (in Hungarian)
12. Green, A. E., Rivlin, R. S.: Multipolar continuum mechanics. Arch. Rational Mech. Anal. 17 (1964), 113–147.
13. Grioli, G.: Elasticità Asimmetrica, Ann. di Mat. pura ed appl., Ser. IV 50 (1960).
14. Günther, W.: Zur Statik und Kinematik des Cosseratschen Kontinuums. Abh. Braunschweigische Wiss. Ges. 10 (1958).
15. Kessel, S.: Die Spannungsfunktionen des Cosserat-Kontinuum. ZAMM 47 (1967), 329–336.
16. Kröner, E.: Mechanics of Generalized Continua. Springer-Verlag, Berlin–Heidelberg–New York, 1968.
17. Kunin: Model uprugoi sredy s prostranstvennoi dispersiei. Prickl. Math. i. Mekh. 30 (1966).
18. Mindlin, R. D.: Micro-structure in linear elasticity. Arch. Ration. Mech. Anal. (1964), 51–78.
19. Mindlin, R. D., Tiersten, H. F.: Effects of couple stresses in linear elasticity. Arch. Rat. Mech. Anal. 11 (1962).
20. Muki, R., Strenberg, E.: The influence of couple-stresses on singular stress concentrations in elastic solids. ZAMM 16, 99 (1965), 611–648.
21. Nowacki, W.: Theory of micropolar elasticity. Springer Verlag, Wien–New York, Udine 1970.
22. Pei Chi Chai, Pagano, N. J.: Elasticity. Van Nostrand, Princeton–New Jersey–Toronto–London 1967.
23. Rogula, D.: Moment stresses and the symmetry of the stress tensor in bodies with no local structure. Bulletin de L'Académie Polonaise des Sciences. Série des sciences-techniques, Volume XVIII. No 4 (1970).
24. Schaefer, H.: Die Spannungfunktionen des dreidimensionalen Kontinuums; statische Deutung und Randwerte, Ingenieur Archiv, Nov. 1958.
25. Schaefer, H.: Das Cosserat-Kontinuum. ZAMM 47 (1967), 485–498.
26. Schaefer, H.: Versuch einer Elastizitätstheorie des zweidimensionalen ebenen Cosserat-Kontinuums. Misz. Angew. Math. Festschrift Tollmien, Akademie-Verlag, Berlin 1962.

27. Schivje: Note on couple stresses. I. Mech. Phys. Solids Jan. (1966).
28. Severino, L. Koh.: A special theory of microelasticity. Int. J. Engng Sci. (1970), 8, 583–593.
29. Toupin, R. A.: Elastic materials with couple stresses. Arch. Rational Mech. Anal. 11 (1962), 415–448.
30. Toupin, R. A.: Theories of elasticity with couple-stress, Arch. Rational Mech. and Anal. 17 (1964), 85–112.
31. Truesdell, C., Toupin, R. A.: The classical field theories. Encyclopedia of Physics. Vol. III/1. Springer, Berlin–Göttingen–Heidelberg.
32. Füzy, J., Vas, J.: Civil engineering application of micro-elastic continuums. ÉTI Special Edition of the "Scientific Proceedings" Series. Budapest, 1985.
33. Füzy, J., Vas, J.: Proposed continuum model for stimulating the behaviour of granular materials. Acta Techn. Hung. 95 (1982), 49–53.

Acta Technica Academiae Scientiarum Hungaricae, 97 (1—4), pp. 85—91 (1984)

RELATIONSHIP BETWEEN FILLING BREAKAGE, TURNS OF TWIST AND MOISTURE CONTENT

B. GREGA*,

[Received: 30 August 1983]

The effect of turns of twist and the moisture content of cotton weft yarns on the number of filling breakages is examined in order to determine the optimum turns of twist and moisture content leading to the lowest possible number of filling breakages.

Frequency of filling breakages in weaving mills during manufacture is influenced by several weaving parameters such as:

(a) turns of twist;
(b) moisture content;
(c) elementary fibre length;
(d) tearing strength of weft;
(e) friction along elementary fibres, etc.

Among the listed weaving parameters, the influence of turns of twist and of moisture percentage in the yarn, on the frequency of filling breakages, will be examined.

Fitting numbers will be shown to be sufficient to determine the optimum number of filling breakages from two-variable functions of filling breakage vs. turns of twist or filling breakage vs. moisture percentage rather than from a three-variable function. Test have been made on five pure cotton yarns of different counts, every time leading to similar results.

Our tests referred to a pure cotton yarn of count Nm 40. The tested yarn was made of 58.5% of Sovietic, 21% of USA, and 20.5% of Nicaraguan cotton. Elementary fibres averaged 29 mm, production mean temperature was 25.5 °C. Measured points are the most illustrative if plotted in a spatial Cartesian coordinate system. Value triad points in a spatial Cartesian coordinate system appear to be located along an elliptic paraboloid correlation surface of the form:

$$v = f(s, r) = a + b_1 s + b_2 r + b_3 s^2 + b_4 r^2$$

where v is the number of filling breakages per 10.000 shoots, s the twist, and r the moisture percentage of the tested yarn.

* Dr. Grega, B., H-1126 Budapest, Németvölgyi út 22, Hungary

For easier understanding, let

$$s = X_1,$$

$$r = X_2,$$

$$s^2 = X_3,$$

$$r^2 = X_4,$$

then

$$V = a + b_1 X_1 + b_2 X_2 + b_3 X_3 + b_4 X_4 . \tag{1}$$

Normal equation system of the correlation function above is

$$na + b_1 \Sigma(X_1) + b_2 \Sigma(X_2) + b_3 \Sigma(X_3) + b_4 \Sigma(X_4) = \Sigma(V),$$

$$a\Sigma(X_1) + b_1 \Sigma(X_1^2) + b_2 \Sigma(X_2 X_1) + b_3 \Sigma(X_3 X_1) + b_4 \Sigma(X_4 X_1) = \Sigma(V X_1),$$

$$a\Sigma(X_2) + b_1 \Sigma(X_1 X_2) + b_2 \Sigma(X_2^2) + b_3 \Sigma(X_3 X_2) + b_4 \Sigma(X_4 X_2) = \Sigma(V X_2),$$

$$a\Sigma(X_3) + b_1 \Sigma(X_1 X_3) + b_2 \Sigma(X_2 X_3) + b_3 \Sigma(X_3^2) + b_4 \Sigma(X_4 X_3) = \Sigma(V X_3),$$

$$a\Sigma(X_4) + b_1 \Sigma(X_1 X_4) + b_2 \Sigma(X_2 X_4) + b_3 \Sigma(X_3 X_4) + b_4 \Sigma(X_4^2) = \Sigma(V X_4).$$

Variables and their means differ by

$$X_1 - \bar{X}_1 = x_1,$$

$$X_2 - \bar{X}_2 = x_2,$$

$$X_3 - \bar{X}_3 = x_3,$$

$$X_4 - \bar{X}_4 = x_4,$$

$$v - \bar{V} = v_1$$

transforming the normal equation system of the correlation function to:

$$b_1 \Sigma(x_1^2) + b_2 \Sigma(x_2 x_1) + b_3 \Sigma(x_3 x_1) + b_4 \Sigma(x_4 x_1) = \Sigma(v_1 x_1),$$

$$b_1 \Sigma(x_1 x_2) + b_2 \Sigma(x_2^2) + b_3 \Sigma(x_3 x_2) + b_4 \Sigma(x_4 x_2) = \Sigma(v_1 x_2),$$

$$b_1 \Sigma(x_1 x_3) + b_2 \Sigma(x_2 x_3) + b_3 \Sigma(x_3^2) + b_4 \Sigma(x_4 x_3) = \Sigma(v_1 x_3),$$

$$b_1 \Sigma(x_1 x_4) + b_2 \Sigma(x_2 x_4) + b_3 \Sigma(x_3 x_4) + b_4 \Sigma(x_4^2) = \Sigma(v_1 x_4)$$

and its constant value from (1):

$$a = \frac{\Sigma(V)}{n} - b_1 \frac{\Sigma(X_1)}{n} - b_2 \frac{\Sigma(X_2)}{n} - b_3 \frac{\Sigma(X_3)}{n} - b_4 \frac{\Sigma(X_4)}{n} =$$

$$= \bar{V} - b_1 \bar{X}_1 - b_2 \bar{X}_2 - b_3 \bar{X}_3 - b_4 \bar{X}_4 .$$

Unknown coefficients of the correlation function will be obtained from the tabulated values below (Tables I and II)

Table I

Measurement No. n_i	Filling break 10 000 shoots v_i	Turns of twist/m $X_{1i}=s_i$	Moisture % $X_{2i}=r_i$	$X_{3i}=s_i^2$	$X_{4i}=r_i^2$	$x_1=X_1-\bar{X}_1$	$x_2=X_2-\bar{X}_2$	$x_3=X_3-\bar{X}_3$	$x_4=X_4-\bar{X}_4$	$v_1=V-\bar{V}$
1	3.79	1076	3.9	1 157 776	15.21	−65.5	−0.66	−146 733.5	−5.78	1.86
2	2.94	1097	4.1	1 203 409	16.81	−44.5	−0.46	−101 100.5	−4.18	1.01
3	2.61	1107	4.2	1 225 449	17.64	−34.5	−0.36	−79 060.5	−3.35	0.68
4	1.63	1121	4.2	1 256 641	17.64	−20.5	−0.36	−47 868.5	−3.35	−0.30
5	1.12	1140	4.4	1 299 600	19.36	−1.5	−0.16	−4 909.5	−1.63	−0.81
6	0.93	1156	4.7	1 336 336	22.09	14.5	0.14	31 826.5	1.10	−1.00
7	1.02	1162	4.9	1 350 244	24.01	20.5	0.34	45 734.5	3.02	−0.91
8	0.91	1170	4.8	1 368 900	23.04	28.5	0.24	64 390.5	2.05	−1.02
9	1.29	1182	5.1	1 397 124	26.01	40.5	0.54	92 614.5	5.02	−0.64
10	3.06	1204	5.3	1 449 616	28.09	62.5	0.74	145 106.5	7.10	1.13
	19.30	11 415	45.6	13 045 095	209.9					

Table II

x_1^2	x_1x_2	x_1x_3	x_1x_4	x_2^2	x_2x_3	x_2x_4	x_3^2
4290.25	43.23	9 611 044.20	378.590	0.4356	96 844.11	3.8148	21 530 720 022.25
1980.25	20.47	4 498 972.20	186.010	0.2116	46 506.23	1.9228	10 221 311 100.25
1190.25	12.42	2 727 587.20	115.575	0.1296	28 461.78	1.2060	6 250 562 660.25
420.25	7.38	981 304.25	68.675	0.1296	17 232.66	1.2060	2 291 393 292.25
2.25	0.24	7 364.25	2.446	0.0256	785.52	0.2608	24 103 190.25
210.25	2.03	461 484.25	15.950	0.0196	4 455.71	0.1540	1 012 926 102.25
420.25	6.97	937 557.25	61.910	0.1156	15 549.73	1.0268	2 091 644 490.25
812.25	6.84	1 835 129.20	58.425	0.0576	15 463.72	0.4920	4 146 136 490.25
1640.25	21.87	3 750 887.20	203.310	0.2916	50 011.83	2.7108	8 577 445 610.25
3906.25	46.25	9 069 156.20	443.750	0.5476	107 378.81	5.2540	21 055 896 342.25
14 872.5	167.7	33 880 486.2	1534.64	1.964	382 680.1	18.048	77 202 139 300.25

Based on the tabulated values, unknown coefficients are obtained from the equation system:

$$14\,872.5b_1 + 167.7b_2 + 33\,880\,486.2b_3 + 1534.64b_4 = \\ = -200.39\,,$$

$$167.7b_1 + 1.964b_2 + 382\,680.1b_3 + 18.048b_4 = \\ = -1.903\,,$$

$$33\,880\,486.2b_1 + 382\,680.1b_2 + 77\,202\,139\,300.5b_3 + \\ + 3\,504\,242.6b_4 = -444\,885.85\,,$$

$$1534.64b_1 + 18.048b_2 + 3\,504\,242.6b_3 + 166.126b_4 = \\ = -16.0543$$

having roots:

$$b_1 = -0.688\,051\,5\,,$$

$$b_2 = -23.578\,939\,,$$

$$b_3 = 0.000\,298\,,$$

$$b_4 = 2.535\,087\,7\,,$$

the function constant being:

$$a = \bar{V} - b_1\bar{X}_1 - b_2\bar{X}_2 - b_3\bar{X}_3 - b_4\bar{X}_4 \approx 1.93 + 0.688\,0515 \cdot 1141.5 + \\ + 23.578\,939 \cdot 4.56 - 0.000\,298 \cdot 1\,304\,509.5 - 2.535\,087\,7 \cdot 20.99 = \\ = 452.9054\,.$$

x_3x_4	x_4^2	v_1x_1	v_1x_2	v_1x_3	v_1x_4	v_1^2
848 119.63	33.4084	−121.830	−1.2276	−272 924.31	−10.7508	3.4596
422 600.09	17.4724	−44.945	−0.4646	−102 111.50	−4.2218	1.0201
264 852.67	11.2225	−23.460	−0.2448	−53 761.14	−2.278	0.4624
160 359.47	11.2225	6.150	0.1080	14 360.55	1.0050	0.0900
8 002.485	2.6569	1.215	0.1296	3 976.695	1.3203	0.6561
35 009.15	1.2100	−14.500	−0.1400	−31 826.50	−1.1000	1.0000
138 118.19	9.1204	−18.655	−0.3094	−41 618.395	−2.7482	0.8281
132 000.52	4.2025	−29.070	−0.2448	−65 678.31	−2.0910	1.0404
464 924.79	25.2004	−25.920	−0.3456	−59 273.28	−3.2128	0.4096
1 030 256.10	50.4100	70.625	0.8362	163 970.34	8.0230	1.2769
3 504 242.6	166.126	−200.39	−1.903	−444 885.85	−16.0543	10.2132

Thus, the wanted elliptic paraboloid correlation function has the equation:

$$v = f(s, r) = 452.9054 - 0.688\,051\,5s - 23.578\,939r +$$

$$+ 0.000\,298s^2 + 2.535\,087\,7r^2 .$$

Now let us determine the extremal value of the function. The function may have an extremal value where its first partial derivatives with respect to the independent variables are zero, that is, where:

$$\frac{\partial r}{\partial s} = -0.688\,051\,5 + 0.000\,596\,s = 0 ,$$

$$\frac{\partial v}{\partial r} = -23.578\,939 + 5.070\,175\,4r = 0 .$$

Hence:

$$s = 1154.4488 \approx 1155 \text{ twists/m} ,$$

$$r = 4.650\,517\,4 \approx 4.7\% .$$

The pertaining function value, hence the filling breakage is:

$$\{v\}_{\substack{s=1154.4488 \\ r=4.650\,5174}} = 0.918\,14 \approx 0.92 .$$

The second partial derivatives being

$$\frac{\partial^2 v}{\partial s^2} = 0.000\,596 > 0,$$

$$\frac{\partial^2 v}{\partial r^2} = 5.070\,175\,4 > 0 ,$$

$$\frac{\partial^2 v}{\partial s \partial r} = 0 ,$$

the resulting Hesse's function determinant is:

$$H = \begin{vmatrix} \frac{\partial^2 v}{\partial s^2} & \frac{\partial^2 v}{\partial s \partial r} \\ \frac{\partial^2 v}{\partial r \partial s} & \frac{\partial^2 v}{\partial r^2} \end{vmatrix} = \begin{vmatrix} 0.000\,596 & 0 \\ 0 & 5.070\,175\,4 \end{vmatrix} = 0.003\,021\,8 > 0 .$$

Therefore there exists an extremal value; and since all the second-order pure partial derivatives are positive, the function has a minimum at:

$$P_{opt}(1154.4488; 4.650\,517\,4; 0.918\,14) .$$

Accordingly, in the tested yarn of count Nm = 40, of 1155/m turns of twist and 4.7% of moisture, the expected optimum filling breakage per 10 000 shoots is 0.92.

Let us now consider the fitting of the correlation surface in the measured value range. Among the three variables, the total correlation coefficient determinant for the fitting is:

$$r = \sqrt{\frac{b_1 \Sigma(v_1 x_1) + b_2 \Sigma(v_1 x_2) + b_3 \Sigma(v_1 x_3) + b_4 \Sigma(v_1 x_4)}{\Sigma(v_1^2)}} = \sqrt{\frac{A}{B}}$$

where

$$A = -0.688\,051\,5 \cdot (-200.39) - 23.578\,939 \cdot (-1.903) + 0.000\,298 \cdot (-444\,885) +$$

$$+ 2.535\,087\,7 \cdot (-16.054\,3)$$

$$B = 10.2132 .$$

The result is

$$r = \sqrt{\frac{A}{B}} = \sqrt{0.927\,655\,3} = 0.963\,148\,6 ,$$

Simultaneously the partial correlation coefficient between filling breakage and turns of twist can be reckoned by

$$r_1 = 0.955\,946\,6 ,$$

and between the filling breakage and the moisture percentage by

$$r_2 = 0.952\,746 .$$

Thus, the established function $v = f(s, r)$ serves to predict, for a yarn of the tested count the number of filling breakages per 10 000 shoots for specified turns of twist and moisture percentage, and/or how to adjust the turns of twist and the moisture percentage for an optimum filling breakage number. Every test performed with any possible yarn count showed a correlation to exist between turns of twist, yarn moisture and expected number of filling breakages. Thus, in any case, a function can be determined with a minimum where filling breakage is optimum.

As a conclusion it can be stated that the effect of turns of twist of the yarn and the moisture content on the filling breakage must not be neglected. To now, yarn turns of twist, and moisture percentages have been empirically specified from factory observations.

The presented method lends itself to increase the accuracy of specifying both weaving parameters. Experiments showed with increasing turns of twist the number of filling breakages to decrease to a while, to have a minimum (optimum from production aspects), then, further increasing the turns of twist, the number of filling breakages rises again. The statements above lead to the conclusion that from the aspect of factory production, in weft yarns the optimum turns of twist have to be maintained.

The effect of turns of twist on the filling breakage may be interpreted as the possibility, for lower turns of twist of elementary fibres, to slide along each other in the yarn, increasing the risk of filling breakage. Beyond the optimum turns of twist, a higher number would produce an increased pressure normal to the yarn midline, causing elementary fibres to slip out of the cross section that, in turn, decreases, the yarn becomes thinner, and the filling breakage more frequent. This effect is still worsened by possible yarn looping. With the increase of moisture content, the other weaving parameter, adhesive force between yarn and vapour, initially increase the friction between the elementary fibres. At the optimum of the moisture content, filling breakage is the minimum. Further increasing the yarn moisture, friction between elementary fibres decreases, raising the expected number of filling breakages.

References

1. Minakov, M. Z.: Prediction of Weaving Breakages from Estimated Yarn Quality. (In Russian). Textilnaya Prom. Moscow, January 1969.
2. Reijonen, A.: Moisture Content of Cloths. (In Finnish). Nykitekstiili, November 1963.
3. Diethelm, A.: La réduction des tensions de filage au continu. L'Industrie Textile, Paris, septembre 1960.
4. Manato, T.: Wrinkling and elastic recovery of elementary fibres. (In Japanese). J. Text. Mach. Osaka, March 1964.
5. Lenox, P.: Yarn Production. Cognetex tell how to improve quality and raise productivity. The Textile Institute and Industry, Manchester, January 1981.
6. Grega, B.: Correlation calculus and applications in textile industry. (In Hungarian). Publication of the Institute of Postgraduate Engineering Education, Budapest, September 1964.

Acta Technica Academiae Scientiarum Hungaricae, 97 (1—4), pp. 93—102 (1984)

FILLING BREAKAGE AS STOCHASTIC FUNCTION OF ELEMENTARY FIBRE LENGTH AND TURNS OF TWIST AS VARIABLES

B. GREGA*

[Received: 30 August 1983]

The effect of elementary fibre length and the applied turns of twist on the number of filling yarn breakage is examined. For any count, the optimum elementary fibre length and turns of twist with the possible least inherent filling breakage number may be predetermined.

Beside strength, length is the topmost quality factor of cotton fibres. Fibres being relatively short, any millimeter of length difference is of a great importance. According to practical experience, under otherwise identical conditions, the turns of twist to be applied in spinning depend essentially on the elementary fibre length.

Only practical observations are available on the effect of yarn moisture, tensile strength, turns of twist and of elementary fibre length on the filling breakage, as formulae for their exact correlation are missing.

It is possible to determine the optimum elementary fibre length and the pertaining turns of twist where the expected number of filling breakages of the processed yarn is the lowest. Four pure cotton yarns of different counts were tested, in each case leading to similar results. In the following, results stochastically determined from pure cotton yarn of count BD 20 will be presented. The tested medium fibre length cotton types were the following:

(a) Sovietic 1A,
(b) Sovietic 2A,
(c) USA SM — 1/4,
(d) Turkish M,
(e) Nicaraguan SM.

While taking the measurements, workshop temperature was 26 °C, at 40.3% r.h.

Points corresponding to triads of measured elementary staple length, applied turns of twist, and number of filling breakages lie at some correlation surface. Be the equation of the surface wanted

$$v = f(s, l) = a + b_1 s + b_2 l + b_3 sl + b_4 s^2 + b_5 l^2$$

* Dr. Grega, B., H-1126 Budapest, Németvölgyi út 22, Hungary

where v is the number of filling breakages per 10.000 shoots, s the applied turns of twist, and l the mixed staple length. For the sake of simplicity, let:

$$s = X_1,$$

$$l = X_2,$$

$$sl = X_3,$$

$$s^2 = X_4,$$

$$l^2 = X_5,$$

Then

$$v = a + b_1 X_1 + b_2 X_2 + b_3 X_3 + b_4 X_4 + b_5 X_5 .$$

Transformation

$$X_1 - \bar{X}_1 = x_1,$$

$$X_2 - \bar{X}_2 = x_2,$$

$$X_3 - \bar{X}_3 = x_3,$$

$$X_4 - \bar{X}_4 = x_4,$$

$$X_5 - \bar{X}_5 = x_5,$$

$$v - \bar{v} = v_1$$

yields the normal equation system:

$$b_1 \Sigma(x_1^2) + b_2 \Sigma(x_1 x_2) + b_3 \Sigma(x_1 x_3) + b_4 \Sigma(x_1 x_4) + b_5 \Sigma(x_1 x_5) = \Sigma(v_1 x_1),$$

$$b_1 \Sigma(x_2 x_1) + b_2 \Sigma(x_2^2) + b_3 \Sigma(x_2 x_3) + b_4 \Sigma(x_2 x_4) + b_5 \Sigma(x_2 x_5) = \Sigma(v_1 x_2),$$

$$b_1 \Sigma(x_3 x_1) + b_2 \Sigma(x_3 x_2) + b_3 \Sigma(x_3^2) + b_4 \Sigma(x_3 x_4) + b_5 \Sigma(x_3 x_5) = \Sigma(v_1 x_3),$$

$$b_1 \Sigma(x_4 x_1) + b_2 \Sigma(x_4 x_2) + b_3 \Sigma(x_4 x_3) + b_4 \Sigma(x_4^2) + b_5 \Sigma(x_4 x_5) = \Sigma(v_1 x_4),$$

$$b_1 \Sigma(x_5 x_1) + b_2 \Sigma(x_5 x_2) + b_3 \Sigma(x_5 x_3) + b_4 \Sigma(x_5 x_4) + b_5 \Sigma(x_5^2) = \Sigma(v_1 x_5)$$

for determining the unknown coefficients b_1, b_2, b_3, b_4 and b_5.

Values of the unknown coefficients will be calculated from measurement values tabulated below (Tables I–IV).

Percentage standard deviations of independent variable values (turns of twist and elementary fibre length) are $s_1 = 4.21\%$, $s_2 = 1.41\%$.

Equation system for determining the unknown coefficients is

$$9446 b_1 + 82.99 b_2 + 13\,833\,134 b_3 + 359\,406.206 b_4 + 5248.9503 b_5 =$$

$$= -60.58 ,$$

Table I

Measurement No n_i	Filling breakages 10 000 shoots v_i	Turns of twist/m $X_{1i}=s_i$	Elementary staple length (mm) $X_{2i}=l_i$	$s_i^2=X_{3i}$	$s_i l_i=X_{4i}$	$l_i^2=X_{5i}$	$x_1=X_1-\bar{X}_1$	$x_2=X_2-\bar{X}_2$
1	0.94	738	31.92	544 644	23 556.96	1018.8864	10	0.186
2	1.03	724	32.16	524 176	23 283.84	1034.2656	−4	0.426
3	1.14	756	31.70	571 536	23 965.20	1004.8900	28	−0.034
4	1.21	716	32.33	512 656	23 148.28	1045.2289	−12	0.596
5	1.28	772	31.64	595 984	24 426.08	1001.0896	44	−0.094
6	1.32	713	31.56	508 369	22 502.28	996.0336	−15	−0.174
7	1.43	708	31.43	501 264	22 252.44	987.8449	−20	−0.304
8	1.46	778	32.41	605.284	25 214.98	1050.4081	50	0.676
9	1.76	693	31.17	480 249	21 600.81	971.5689	−35	−0.564
10	2.23	682	31.02	465 124	21 155.64	962.2404	−46	−0.714
	13.8	7280	317.34	5 309 286	231 106.51	10072.456		

Table II

$x_3 = X_3 - \bar{X}_3$	$x_4 = X_4 - \bar{X}_4$	$x_5 = X_5 - \bar{X}_5$	$v_1 = v - \bar{v}$	x_1^2	$x_1 x_2$	$x_1 x_3$	$x_1 x_4$	v_1^2	$x_1 x_5$
13715.4	446.309	11.6408	−0.44	100	1.860	137154.0	4463.090	0.1936	116.4080
−6752.6	173.189	27.0200	−0.35	16	−1.704	27010.4	−692.756	0.1225	108.0800
40607.4	854.549	−2.3556	−0.24	784	−0.952	1137007.2	23927.372	0.0576	−65.9568
−18272.6	37.629	37.9833	−0.17	144	−7.152	219271.2	−451.548	0.0289	−455.7996
65055.4	1315.429	−6.1560	−0.10	1936	−4.136	2862437.6	57878.876	0.0100	−270.8640
−22559.6	−608.371	−11.2120	−0.06	225	2.610	338394.0	9125.565	0.0036	168.1800
−29664.6	−858.211	−19.4007	0.05	400	6.080	593292.0	17164.220	0.0025	388.0140
74355.4	2104.329	43.1625	0.08	2500	33.800	3717770.0	105216.450	0.0064	2158.1250
−50679.6	−1509.841	−35.6767	0.38	1225	19.740	1773786.0	52844.435	0.1444	1248.6845
−65804.6	−1955.011	−45.0052	0.85	2116	32.844	3027011.6	89930.506	0.7225	2070.2392
				9446	82.99	13833134	359406.206	1.292	5248.9503

Table III

x_2^2	x_2x_3	x_2x_4	x_2x_5	x_3^2	x_3x_4	x_3x_5
0.034 596	2 551.0644	83.013 474	2.165 188 8	188 112 197.16	6 121 306.4	159 658.22
0.181 476	−2 876.6076	73.778 514	11.510 520	45 597 606.76	−1 169 476.0	−182 455.25
0.001 156	−1 380.6516	−29.054 666	0.080 090 4	1 648 960 934.76	34 701 013	−95 654.791
0.355 216	−10 890.4690	22.426 884	22.638 046	333 887 910.76	−687 579.66	−694 053.64
0.008 836	−6 115.2076	−123.650 32	0.578 664 0	4 232 205 069.16	85 575 759	−400 481.04
0.030 276	3 925.3704	105.856 55	1.950 888 0	508 935 552.16	13 724 606	252 998.23
0.092 416	9018.0384	260.896 140	5.897 812 8	879 988 493.16	25 458 486	575 514.00
0.456 976	50 264.2500	1422.526 400	29.177 850	5 528 725 509.16	156 468 224.5266	3 209 364.90
0.318 096	28 583.2940	851.550 320	20.121 658	2 568 421 856.16	76 518 137	1 808 080.80
0.509 796	46 984.4840	1395.877 800	32.133 712	4 330 245 381.16	128 648 716.8506	2 961 549.10
1.988 84	120 063.565	4063.221	126.254 43	20 265 080 510.4	525 355 192.1766	7 594 460.00

Table IV

x_4^2	$x_4 x_5$	x_5^2	$v_1 x_1$	$v_1 x_2$	$v_1 x_3$	$v_1 x_4$	$v_1 x_5$
199 191.720	5 195.3938	135.508 22	−4.4	−0.081 84	−6 034.776	−196.375 96	−5.121 952
29 994.429	4 679.5667	730.080 4	1.4	−0.149 1	2 363.41	−60.616 15	−9.457
730 253.990	−2 012.9756	5.548 851 3	−6.72	0.008 16	−9 745.776	−205.091 76	0.565 344
1 415.9416	1 429.2735	1442.731 0	2.04	−0.101 32	3 106.342	−6.396 93	−6.457 161
1 730 353.4	−8 097.7809	37.896 336	−4.4	0.009 4	−6 505.54	−131.542 9	0.615 6
370 115.27	6 821.0556	125.708 94	0.9	0.010 44	1 353.576	36.501 26	0.672 72
736 526.12	16 649.894	376.387 16	−1.0	−0.015 2	−1 483.23	−42.910 55	−0.970 035
4 428 200.5	90 828.100	1863.001 4	4.0	0.054 08	5 948.432	168.346 32	3.453
2 279 619.8	53 866.144	1272.826 9	−13.3	−0.214 32	−19 258.248	−573.73958	−13.557 146
3 822 068.0	87 985.661	2025.468	−39.1	−0.606 9	−55 933.91	−1661.7593	−38.254 42
14 327 739	257 344.324	8015.1572	−60.58	−1.086 6	−86 189.72	−2673.584 52	−68.511 05

$$8299b_1 + 1.988\,84b_2 + 120\,063.565b_3 + 4063.221b_4 + 126.254\,43b_5 =$$
$$= -1.0866\,.$$

$$13\,833\,134b_1 + 120\,063.565b_2 + 20\,265\,080\,510.4b_3 + 525\,359\,192.7766b_4 +$$
$$+ 7\,594\,460.6b_5 = -86\,189.72\,.$$

$$359\,406.206b_1 + 4063.221b_2 + 525\,359\,192.7766b_3 + 14\,327\,739b_4 +$$
$$+ 257\,344.324b_5 = -2673.584\,52\,.$$

$$5248.9503b_1 + 126.254\,43b_2 + 7\,594\,460.6b_3 + 257\,344.324b_4 +$$
$$+ 8015.1572b_5 = -68.511\,05\,.$$

Roots of this equation system

$$b_1 = -0.505\,424\,3\,,$$
$$b_2 = -4.058\,029\,,$$
$$b_3 = 0.000\,343\,9\,,$$
$$b_4 = -0.000\,128\,,$$
$$b_5 = 0.064\,624\,9$$

and the function constants:

$$a = \bar{v} - b_1\bar{X}_1 - b_2\bar{X}_2 - b_3\bar{X}_3 - b_4\bar{X}_4 - b_5\bar{X}_5 = 253.3844\,.$$

Thus, the wanted correlation functions:

$$v = f(sl) = 253.3844 - 0.505\,424\,3s - 4.058\,029l + 0.000\,343\,9s^2 -$$
$$- 0.000\,128sl + 0.064\,624\,9l^2$$

The function may have an extremal value where

$$\frac{\partial v}{\partial l} = -0.505\,423\,4 + 0.000\,687\,8s - 0.000\,128l = 0.$$

$$\frac{\partial v}{\partial l} = -4.058\,029 - 0.000\,128s + 0.129\,249\,8l = 0.$$

Roots of the equation system:

$$s_{\text{opt}} = \frac{3980.017}{5.372\,447\,2} = 740.820\,14 \text{ s/m} \approx 741 \text{ s/m}.$$

$$l_{\text{opt}} = 32.130\,425 \text{ mm} \approx 32.13 \text{ mm}.$$

Pure partial derivatives of second order being

$$\frac{\partial^2 v}{\partial s^2} = 0.000\,687\,8 > 0\,,$$

$$\frac{\partial^2 v}{\partial l^2} = 0.129\,249 > 0\,,$$

the Hesse's function determinant is

$$H = \begin{vmatrix} \frac{\partial^2 v}{\partial s^2} & \frac{\partial^2 v}{\partial s\,\partial l} \\ \frac{\partial^2 v}{\partial l\,\partial s} & \frac{\partial^2 v}{\partial l^2} \end{vmatrix} = \begin{vmatrix} 0.000\,687\,8 & -0.000\,128 \\ -0.000\,128 & 0.129\,249\,8 \end{vmatrix} =$$

$$= 8888.1616 \cdot 10^{-8} > 0$$

Thus, an extremal value exists, and since all the pure second-order partial derivatives are positive, stochastic function $v = f(s, l)$ has a minimum. Extremal value (minimum) point of the function is

$$P_{\text{opt}}(741;\ 32.13;\ 0.97)$$

Accordingly, for the tested yarn of count 20 of 741 turns of twist per m, and 32.13 mm staple length, the expected minimum filling breakage per 10 000 shoots is 0.97.

Let us now consider the fitting of the correlation surface in the range of measurement points. Total correlation coefficient between filling breakage, turns of twist and staple length, characteristic of fitting, is with

$$A = b_1 \Sigma(v_1 x_1) + b_2 \Sigma(v_1 x_2) + b_3 \Sigma(v_1 x_3) + b_4 \Sigma(v_1 x_4) + b_5 \Sigma(v_1 x_5)$$

$$B = \Sigma(v_1^2)$$

$$r = \sqrt{\frac{A}{B}} = \sqrt{\frac{1.284}{1.292}} = 0.996\,899\,.$$

Thus, the determined correlation function is nearly analytic.

In addition, it is essential to know partial correlation coefficient of the relationship between the number of filling breakages and the staple length:

$$r_{v_{1s}} = \sqrt{\frac{b_2 \Sigma(v_1 x_2) + b_5 \Sigma(v_1 x_s)}{\Sigma(v_1^2)}}\,.$$

Utilizing measurement values

$$r_{v_{ls}} = \sqrt{\frac{1.229\,965\,3}{1.292}} = 0.975\,697\,4\,,$$

is a rather fair value.

Utilizing the determined stochastic function $v = f(s, l)$ for the tested yarn count, the expected number of filling breakages per 10 000 shoots for the specified turns of twist and staple length can be predicted, and the turns of twist and staple length can be determined, so as to produce the lowest number of filling breakages. Tests for the complete range of yarn counts show a strict stochastic correlation between turns of twist, staple length and expected number of filling breakages. Thus, in every case the stochastic function is a minimum where the number of filling breakages is the lowest, and so can be determined.

As a conclusion, proper selection of the turns of twist of the yarn and of the staple length is decisive for the productivity of weaving mills by optimizing the expected filling breakage number.

Until recently, turns of twist pertaining to staple lengths of elementary fibres in weft yarns to be processed have been empirically determined, based on factory observations.

The actual method permits, however, to require a much higher accuracy in selecting these two important weaving parameters. Investigations showed for a constant staple length with increasing turns of twist the filling breakage number to decrease for a while, then, after a minimum, with a further increase of the turns of twist, to increase again. Manufacturing aspects are imposed to provide for optimum turns of twist and staple lengths for weft yarns to be utilized. For turns of twist lower than optimum, elementary fibres in the complete yarn may slip along each other, total friction between elementary fibres is lower than the yarn's tensile strength, increasing the risk of breakage. For higher than optimum turns of twist, the increased pressure acting on the yarn midline may cause some elementary fibres to slip out of the yarn cross section, reducing it, increasing thereby the number of expected filling breakages. For higher turns of twist, the number of filling breakages is further increased by the risk of yarn looping.

For the same turns of twist, and short fibre lengths, if the total friction due to compacting forces is below the yarn tensile strength, the fibre is likely to slip out of the yarn. With increasing elementary fibre lengths, there is a lesser risk of yarn breakage, that has a minimum at a given fibre length, but with a further increase of elementary fibre lengths, the filling breakage tends somewhat to rise, since tensile stresses in outer fibres of the yarn reduce its tensile strength.

References

1. Bukaev, P. T.: Causes of filling breakage in automatic looms. (In Russian). *Textilnaya Promishlennost*, Ivanovo, April 1964, p. 27–28.
2. Bidadorov, R. V.: Testing the stress of weft yarns in looms. (In Russian). *Textilnaya Promishlennost*, Ivanovo, September 1968, p. 32–35.
3. Mourot, A.: La régulation servo-électrique de la tension au métier à filer. *L'Industrie Textile*, Paris, Avril 1952, 192–194.
4. Walter, H.: Der Einfluß der Spannung auf den Ausfall des Gewebes. *Textil Praxis*, Stuttgart. Januar 1969.
5. Zilahi, M.: Raw Material for the Textile Industry (In Hungarian). Tankönyvkiadó, Budapest 1933.
6. Grega, B.: Correlation Calculus and its Uses in the Textile Industry. (in Hungarian). Institute of Postgraduate Engineering Education, G.38. Budapest 1964.

Acta Technica Academiae Scientiarum Hungaricae, 97 (1—4), pp. 103—110 (1984)

STRESS FUNCTION OF SINGLE-LAYER RETICULATED SHELLS AND ITS RELATION TO THAT OF CONTINUOUS MEMBRANE SHELLS

I. HEGEDŰS*

[Received: 14 February, 1984]

The paper shows that the stress state of a single-layer reticulated shell of general triangular network can be described by a stress function which is perfectly analogous to Pucher's stress function of membrane shells. The stress function can be interpreted as the equation of a polyhedron having a ground plan network identical with that of the reticulated shell.—It is also shown that the bar force system of the reticulated shell can be considered as a strongly degenerated membrane force system of a specially shaped and loaded membrane shell.

Pucher's differential equation is generally used in determining stress states of membrane shells. If the external load of the shell consists of distributed forces normal to the ground plan, the problem of determining its membrane forces can be stated as a boundary value problem of a second order linear partial differential equation of variable coefficients. Using Cartesian co-ordinates x, y and denoting the shape function by $z(x, y)$ and the function of the external load by $p(x, y)_z$, the differential equation

$$\frac{\partial^2 z}{\partial x^2}\frac{\partial^2 F}{\partial y^2} - 2\frac{\partial^2 z}{\partial x \partial y}\frac{\partial^2 F}{\partial x \partial y} + \frac{\partial^2 z}{\partial y^2}\frac{\partial^2 F}{\partial x^2} = p_z \tag{1}$$

of the stress function F expresses the equilibrium condition of the vertical component of internal and external forces acting on an infinitesimal element cut out of the shell. Equilibrium conditions of horizontal components are automatically fulfilled, the membrane forces being derived from the stress function as follows:

$$N_x = \frac{\partial^2 F}{\partial y^2}\sqrt{\frac{1+\left(\frac{\partial z}{\partial x}\right)^2}{1+\left(\frac{\partial z}{\partial y}\right)^2}}, \qquad N_y = \frac{\partial^2 F}{\partial x^2}\sqrt{\frac{1+\left(\frac{\partial z}{\partial y}\right)^2}{1+\left(\frac{\partial z}{\partial x}\right)^2}}, \qquad N_{xy} = \frac{-\partial^2 F}{\partial x \partial y} \tag{2}$$

The sufficient condition of using the stress function is that the derivatives of z in Eqs (1) and (2) have to be finite over the ground plan of the shell, i.e. its surface must not contain points of discontinuity in the 0th and 1st derivatives or points with tangent planes normal to the x, y co-ordinate plane, and all the second derivatives in Eq. (1) must not vanish at the same point, i.e. the surface must not contain points of zero curvatures (plane points).

* Hegedüs I. H-2083 Solymár, Váci Mihály u. 10, Hungary

There is an alternative way to express the equilibrium conditions of the external and internal forces acting on the shell. If a shell element has a circular boundary in the ground plan, the following equation holds:

$$\operatorname{abs} \int_0^{2\pi} [N_r \mathbf{n} + N_{r\varphi} \mathbf{t}] \frac{\dfrac{\partial z}{r\partial\varphi}}{\sqrt{1+\left(\dfrac{\partial z}{r\partial\varphi}\right)^2}} r \, d\varphi + \int_0^{2\pi} \int_0^r p_z \rho \, d\rho \, d\varphi = 0 \tag{3a}$$

where N_r and $N_{r\varphi}$ are the normal and tangential membrane forces along the boundary and $\mathbf{n}$ and $\mathbf{t}$ denote the unit vectors of their directions. Using the relations between the membrane forces and the stress function F, the above condition can be written as

$$\int_0^{2\pi} \left[\left(\frac{\partial^2 F}{r^2 \partial\varphi^2} + \frac{1}{r} \frac{\partial F}{\partial r} \right) \frac{\partial z}{\partial r} - \left(\frac{\partial}{\partial} \frac{\partial F}{r\partial\varphi} \right) \frac{\partial z}{r\partial\varphi} \right] r \, d\varphi + \int_0^{2\pi} \int_0^r p_z \rho \, d\rho \, d\varphi = 0 \tag{3b}$$

The first integrals in both equations represent the resultant of the membrane forces acting along the boundary, and the second ones give the resultant of the loads. Integrating by parts, Eq. (3b) can be transformed in such a way that functions F and z formally exchange their roles:

$$\int_0^{2\pi} \left[\left(\frac{\partial^2 z}{r^2 \partial\varphi^2} + \frac{1}{r} \frac{\partial z}{\partial r} \right) \frac{\partial F}{\partial r} - \left(\frac{\partial}{\partial r} \frac{\partial z}{r\partial\varphi} \right) \frac{\partial F}{r\partial\varphi} \right] r \, d\varphi + \int_0^{2\pi} \int_0^r p_z \rho \, d\rho \, d\varphi = 0 . \tag{3c}$$

The similarity between the static behaviour of membrane shells and that of single layer reticulated shells suggests the idea of searching a stress function of bar forces of reticulated shells which describes the stress state of reticulated shells analogously to that of membrane shells described by F in Eqs (1)–(3).

The research carried out by Dean and al. [1] and, independently of them, by the author [2] shows that it is possible to obtain such functions. If the projections of the joints of a network form a translationally symmetric point system in ground plan, properly chosen combinations (differences) of the actual values of a function at these points can be interpreted at each point as horizontal components of the bar forces acting in the bars attached by hinges to the point in question. If these horizontal components form a system of equilibrium at each joint, the arbitrarily chosen function determines a set of vertical nodal forces which can be considered as the external load. Its elements can be calculated by formulating the missing third equilibrium condition for each joint. These equations expressing the equilibrium of vertical components are analogous to Eq. (1). The translational symmetry of the projected network permits us to write down the system of equations as a single difference equation. This equation may show some similarities to Eq. (1), but in general, i.e. if the projected network is a

general triangular network having no symmetries, the differences in the equation cannot be interpreted.

In the following analyses we will show that a stress function of single layer space grids, analogous to that of continuous membrane shells, can be defined in the case of general triangular projected network, and, moreover, that this function is a solution of a singular differential equation of the stress function of a polyhedron shaped "membrane shell", loaded by concentrated forces at its summits.

Let z and F be two polyhedrons with identical projected network in the horizontal x, y plane. (Letters z and F refer to the analogy with the shape and stress functions used in Eqs (1)–(3).) To avoid degenerated cases, let us assume that each face of z and F has a normal with a positive component in vertical direction (Figs 1a. and b.). Let radii be drown from the origin to a fixed horizontal plane H in such a way that the i-th radius is perpendicular to the i-th face of the polyhedron F, and let the point of intersection of the i-th radius on the plane be denoted by P_i. If the i-th and j-th faces are adjacent ones, let P_i and P_j be connected by a straight line (Fig. 2). Having connected all pairs of points belonging to the adjacent faces, we obtain a polygonal plane network. This network can be considered as a dual of the common projected network of z and F, with the following correspondences:

— Each node in the dual network corresponds to a triangle in the primal network; the corresponding triangle is the projection of a face-triangle of F.

— Each dual line corresponds to a primal line so that the dual line connecting P_i and P_j corresponds to the projection of the edge lying on the intersection of the adjacent i-th and j-th faces of F; the corresponding primal and dual lines are normal to each other.

— Each node in the primal network corresponds to a polygon in the dual network; the polygon which corresponds to the projection of the k-th summit of F is bordered by lines corresponding to the projections of edges intersecting each other at the k-th summit.

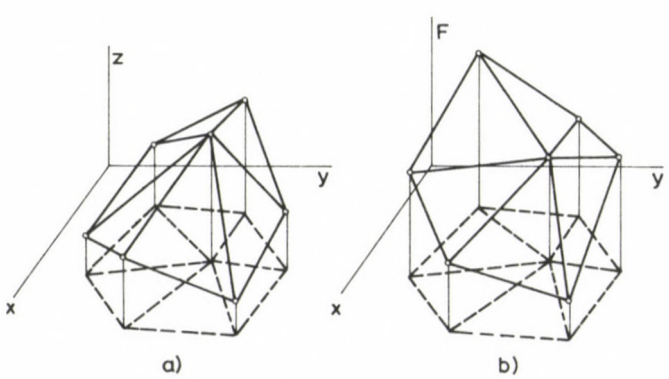

Fig. 1

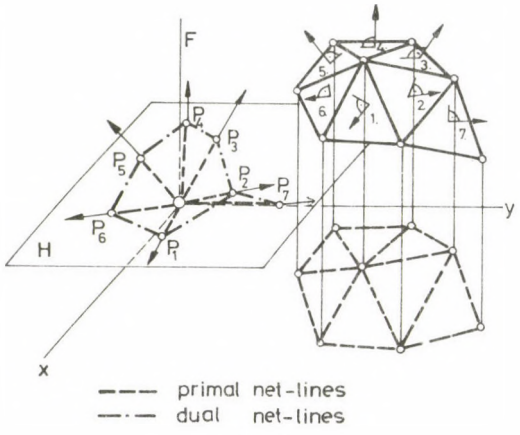

Fig. 2

The k-th polygon of the dual network can be interpreted as the closed projection vector polygon of forces acting along the edges of z which intersect each other at the k-th summit, if we rotate the polygon by an angle equal to $\pi/2$. Since this interpretation holds for each summit of z, the dual network can be considered as a rotated combined vector diagram of forces which satisfy the horizontal equilibrium conditions at each primal node, or as that of projected bar forces of a single-layer reticulated shell with hinged joints which has a network identical with that of the polyhedron z. The external forces acting at the summits or joints can be calculated by using the equilibrium conditions of the vertical components of the forces. Since the horizontal projection vector diagrams are closed polygons, the external forces must not have horizontal components.

To sum up, we can state that the polyhedrons z and F of common projection network determine a system of vertical nodal forces acting on z in a way as presented.

To derive algebraic relations between the functions z and F and the external forces, let us assume the distance of the plane of the dual network and the co-ordinate plane x, y as unity.

The position vector of the dual node which belongs to the projection of the face triangle ABC of F is (Fig. 3)

$$\mathbf{t}_{ABC}=(\mathbf{r}_A+\mathbf{k}\cdot F_A-\mathbf{r}_B-\mathbf{k}\cdot F_B)\times(\mathbf{r}_B+\mathbf{k}\cdot F_B-\mathbf{r}_C-\mathbf{k}\cdot F_C)/T_{ABC}=$$

$$=\left[\frac{\mathbf{r}_A\times\mathbf{k}}{T_{ABC}}(F_B-F_C)+\frac{\mathbf{r}_B\times\mathbf{k}}{T_{ABC}}(F_C-F_A)+\frac{\mathbf{r}_C\times\mathbf{k}}{T_{ABC}}(F_A-F_B)\right]+\mathbf{k}$$

where $\mathbf{i}, \mathbf{j}, \mathbf{k}$ are the unit vectors in the x, y and z directions resp. and $\mathbf{r}_A+\mathbf{k}F_A$, $\mathbf{r}_B+\mathbf{k}F_B$, $\mathbf{r}_C+\mathbf{k}F_C$ are the vectors of the summits A, B, C of F,

$$T_{ABC}=\mathbf{k}(\mathbf{r}_A\times\mathbf{r}_B+\mathbf{r}_B\times\mathbf{r}_C+\mathbf{r}_C\times\mathbf{r}_A)$$

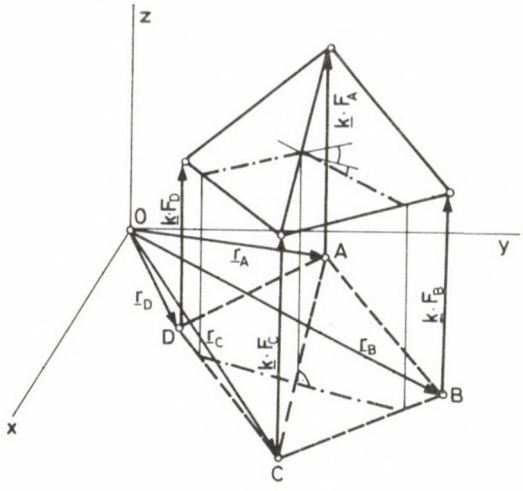

Fig. 3

is the double area of the projection of the triangle ABC. Determining the vector of the dual node belonging to the adjacent face triangle CDA and subtracting the two vectors, we obtain the vector of the dual of the edge AC:

$$\mathbf{t}_{AC}=\mathbf{t}_{ABC}-\mathbf{t}_{CDA}$$

The length of $\mathbf{t}_{AC}$ is equal to the projection $\bar{N}_{AC}$ of the force N_{AC} acting along the edge AC:

$$\begin{aligned}\bar{N}_{AC}=\frac{1}{|\mathbf{r}_C-\mathbf{r}_A|}\Bigg\{&F_A\left[\frac{(\mathbf{r}_B-\mathbf{r}_C)(\mathbf{r}_C-\mathbf{r}_A)}{T_{ABC}}+\frac{(\mathbf{r}_D-\mathbf{r}_C)(\mathbf{r}_C-\mathbf{r}_A)}{T_{CDA}}\right]+\\&+F_C\left[\frac{(\mathbf{r}_A-\mathbf{r}_B)(\mathbf{r}_C-\mathbf{r}_A)}{T_{ABC}}+\frac{(\mathbf{r}_A-\mathbf{r}_D)(\mathbf{r}_C-\mathbf{r}_A)}{T_{CDA}}\right]+\\&+F_B\frac{(\mathbf{r}_C-\mathbf{r}_A)^2}{T_{ABC}}+F_D\frac{(\mathbf{r}_C-\mathbf{r}_A)^2}{T_{CDA}}\Bigg\}.\end{aligned}\tag{4}$$

Taking into account that

$$T_{ABC}=\overline{AC}\cdot\overline{AB}\cdot\sin(BAC)=\overline{CA}\cdot\overline{CB}\cdot\sin(ACB),$$

$$T_{CDA}=\overline{AC}\cdot\overline{AD}\cdot\sin(CAD)=\overline{CA}\cdot\overline{CD}\cdot\sin(DCB),$$

$$(\mathbf{r}_B-\mathbf{r}_C)(\mathbf{r}_C-\mathbf{r}_A)/|\mathbf{r}_C-\mathbf{r}_A|=-\overline{CB}\cdot\cos(ACB),$$

$$(\mathbf{r}_D-\mathbf{r}_C)(\mathbf{r}_C-\mathbf{r}_A)/|\mathbf{r}_C-\mathbf{r}_A|=-\overline{CD}\cdot\cos(DCA),$$

$$(\mathbf{r}_A-\mathbf{r}_B)(\mathbf{r}_C-\mathbf{r}_A)/|\mathbf{r}_C-\mathbf{r}_A|=-\overline{AB}\cdot\cos(BAC),$$

$$(\mathbf{r}_A-\mathbf{r}_D)(\mathbf{r}_C-\mathbf{r}_A)/|\mathbf{r}_C-\mathbf{r}_A|=-\overline{AD}\cdot\cos(CAD),$$

we obtain:

$$\bar{N}_{AC} = -F_A\left(\frac{\operatorname{ctg}(ACB)}{\overline{CA}} + \frac{\operatorname{ctg}(DCA)}{\overline{CA}}\right) + F_B \frac{1}{\overline{CB}\cdot\sin(ACB)} -$$

$$-F_C\left(\frac{\operatorname{ctg}(BAC)}{\overline{CA}} + \frac{\operatorname{ctg}(CAD)}{\overline{CA}}\right) + F_D \frac{1}{\overline{AD}\cdot\sin(CAD)} \tag{5}$$

Eq. (5) permits us to present another geometric interpretation of $\bar{N}_{AC}$, idependently of the dual network. That is, $\bar{N}_{AC}$ is equal to the change of slope of a broken line which is the line of intersection of F and a vertical plane normal to the projection of the intersected edge AC (Fig. 3). The elements of the load are determined by computing the original (not projected) values of the edge forces and producing the sum of their vertical components at each summit. The resulting vertical forces can be directly determined by producing at each primal node the sum of the products of the projected forces and the slopes of the corresponding edges of z.

An interesting feature of Pucher's differential equation is that the formal exchange of the role of F and z does not affect the function of the external load (see also Eqs (1)–(3)). The above derivation can be extended to show that this interchangeability in our case also holds. Namely, we obtain the same results as obtained before, if we produce the sum of the products of the change of slope of broken lines lying on z and the slopes of the edges of F. Another feature of Pucher's differential equation is that by adding the equation of an arbitrary chosen plane to F or z we do not affect the external load. We can easily prove the same invariancy in our case too.

Let us investigate what assumptions have to be used for directly deriving our results from Pucher's differential equation. Let us consider a membrane shell which fits a triangular network of a reticulated shell. This "membrane shell" is far from being a usual one, because it may have edges and it has to have summits. Despite of these unusual properties we assume that a stress function exists which describes the state of stress of the structure subjected to vertical loads acting at the summits. Let the equation of the surface be

$$z = z_0 + \delta z$$

where z_0 is the equation of the polyhedron. The other part of z is not determined by the assumption that the network of z_0 fits the surface z, but δz must vanish along the lines of fitting. Since Pucher's differential equation contains only linear differential operators, we can decompose this equation, written in a concise form as $\mathscr{L}(z, F) = p$, as follows:

$$\mathscr{L}(z, F) = \mathscr{L}(z_0 + \delta z, F) = \mathscr{L}(z_0, F) + \mathscr{L}(\delta z, F).$$

Let us assume that z_0 and F perfectly determine the state of stress of the reticulated shell with hinged joints having the same network as the polyhedron z_0. If this assumption is correct, then $\mathscr{L}(\delta z, F)$ has to vanish at every point of the surface. Since δz is not determined by the network, $\mathscr{L}(\delta z, F)$ can only vanish everywhere if the second derivatives of F vanish inside each triangular domain bordered by the projections of

the netlines. This condition does not concern the points lying on the projection lines, because here—denoting by t the co-ordinate parallel to the projection line and by n the co-ordinate normal to it—$\partial^2(\delta z)/\partial t^2 = 0$ is ensured by $\delta z = 0$, hence $(\partial^2 z/\partial t^2)(\partial^2 F/\partial n^2) = 0$ can also hold when $\partial^2 F/\partial n^2 \neq 0$. A surface having nonzero curvatures only above the netlines of a triangular network has to be a polyhedron having a projected network coinciding with that in question, hence the stress function which satisfies our previous assumption has to be the equation of such a polyhedron. Since Eqs (2) cannot be interpreted along the edge lines of the polyhedron, we have to render the relation between the internal forces and the stress function more exact. Let Δ be a small line section of direction n in the xy plane, perpendicularly bisected by the projection of an edge line. The resultant of the projected membrane normal forces acting on this section can be formally obtained as follows:

$$\bar{N}(\Delta) = \int_{-\Delta/2}^{+\Delta/2} \frac{\partial^2 F}{\partial n^2} \, \mathrm{d}n = \left[\frac{\partial F}{\partial n}\right]_{-\Delta/2}^{+\Delta/2}.$$

Though the integrand inside the domain of integration becomes infinite, the integral itself is finite. If we fix the lower or upper limit of integration and let Δ to tend to zero, the integral vanishes, because the same value of $\partial F/\partial n$ belongs to both end points of Δ. However, if we let Δ tend to zero in such a way that the end points of Δ remain at different sides of the bisecting line, the integral tends to a nonzero value:

$$\lim_{\Delta \to 0} \bar{N}(\Delta) = \bar{N}.$$

This integral represents the projection of a force. In our case the corresponding edge lines of the polyhedrons z and F have common ground plan projections, hence the forces belonging to the edges of F represent forces acting along the edges of z. The fact that the integral vanishes at the regular points shows that the internal part of the triangles bordered by the edges is in a state free of stresses, thus the external loads at the summits are balanced only by the edge forces, analogously to the single-layer space grids with hinged joints.

Using Gauss's theorem, we can prove that this generalized interpretation of membrane forces does not hurt our fundamental assumptions, since horizontal equilibrium conditions are satisfied everywhere.

The external forces defined by the polyhedron functions can be determined using Eqs (3b) or (3c). If the domain of integration does not contain any nodes, the value of the first integral is zero, hence the second integral also vanishes. If the integration is performed for a small circular domain around a node, Eqs (3b) and (3c) express the equilibrium of two forces: one is the resultant of the edge forces intersecting each other at the summit, and the other is the external nodal force.

Summing up the results of our analysis we can state that the states of stress of a membrane polyhedron and a single-layer space grid with hinged joints which have

identical triangular networks and are loaded by the same system of vertical forces acting at the summits or joints respectively, can be considered as identical and both can be described by the same stress function. Hence this function can be considered as the stress function of the single-layer space grid, too.

The value of our results is shown by the fact that they make it possible to extend the use of various methods based on the analogies between membrane shells and space grids which have been used so far only in the cases of regular networks.

References

1. Dean, L. D.: On the statics of latticed shells. *I.A.B.S.E. Publications* 25, 1965.
2. Hegedüs, I.: The analysis of membrane shells and latticed shells with the aid of component uniaxial states of strain. Bulletin of the First Scientific Conference of the Mechanical and Engineering Research Group of the Hungarian Academy of Sciences. Budapest, (1974) (in Hungarian).

Acta Technica Academiae Scientiarum Hungaricae, 97 (1—4), pp. 111—122 (1984)

BUCKLING OF SANDWICH COLUMNS WITH THIN FACES UNDER DISTRIBUTED NORMAL LOADS

I. HEGEDŰS*, L. P. KOLLÁR**

[Received: 17 January 1984]

The paper derives the differential equation of buckling of thin-faced sandwich beams (i.e. beams developing flexural and shear deformations as well) and presents two methods for the calculation of the critical load and the buckled shape of such columns, provided the distribution of the normal forces is given as a power series.

Some examples are presented to illustrate the applications of the methods. The results are shown on diagrams, and are compared with approximate results obtained by the application of Föppl's theorem.

1. Introduction

The stability analysis and design of bent and compressed structures usually neglects the influence of shear strains on deflections, on stresses and on the value of the critical load. However, the error caused by this approximation may exceed the allowable inaccuracy in several cases, e.g., sandwich structures, coupled shear walls and built-up columns.

This paper deals with such cases and presents an analysis on the calculation of the critical load of columns with shear deformations, subjected to arbitrarily distributed axial loads.

The solution of the problem for the case of a uniformly distributed compressive load can be found in [2].

In our paper we solve the problem for forces given by a power function or power series, and moreover, we generalize and refine some statements made in [2].

2. The differential equation of buckling

Let us consider a column built-in at the bottom and free at the top, subjected to a distributed axial load of intensity $q(z)$. The height of the column is H (Fig. 1).

The bending stiffness is denoted by

$$B = EI,$$

* Hegedűs, I. H-2083 Solymár, Váci Mihály u. 10. Hungary
** Kollár, L. P. H-1122 Budapest, Karap u. 9. Hungary

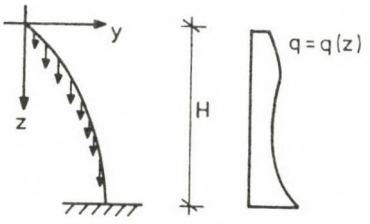

Fig. 1. The cantilever with the co-ordinate system

and the shear stiffness is

$$S = AG/n.$$

Let us write the formulas for the internal forces and moments, $N(z)$, $Q(z)$ and $M(z)$ of the cantilever with the aid of the horizontal displacement $y(z)$. The positive signs are shown in Fig. 2.

The vertical force (equal to the normal force in the case of small displacements) is:

$$N(z) = \int_0^z q(\zeta)\mathrm{d}\zeta. \tag{2.1}$$

The shearing force becomes:

$$Q(z) = N(z)\frac{\mathrm{d}y}{\mathrm{d}z}. \tag{2.2}$$

The bending moment is:

$$M(z) = \int_0^z [y(z) - y(\zeta)]q(\zeta)\mathrm{d}\zeta. \tag{2.3}$$

The relationships between the bending and shear deflections [3, 4] and the internal forces are the following.

The "bending curvature" from the "bending displacement" (y_M) is:

$$\frac{\mathrm{d}^2 y_M}{\mathrm{d}z^2} = -\frac{M}{B} \tag{2.4}$$

and the "shear distortion" from the "shear displacement" (y_S) becomes:

$$\frac{\mathrm{d}y_S}{\mathrm{d}z} = \frac{Q}{S}. \tag{2.5}$$

The total displacement of the cantilever consists of the sum of bending and shear displacements:

$$y = y_M + y_S. \tag{2.6}$$

Let us differentiate Eq. (2.3) with respect to z. We thus obtain

$$\frac{\mathrm{d}M}{\mathrm{d}z} = \frac{\mathrm{d}}{\mathrm{d}z}\int_0^z [y(z) - y(\zeta)]q(\zeta)\mathrm{d}\zeta = \frac{\mathrm{d}y(z)}{\mathrm{d}z}\int_0^z q(\zeta)\mathrm{d}\zeta = \frac{\mathrm{d}y(z)}{\mathrm{d}z}N(z). \tag{2.7}$$

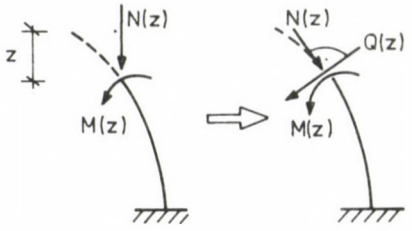

Fig. 2. The forces acting on the cross section "z"

Let us differentiate Eq. (2.6) three times and let us substitute the appropriate derivatives of (2.4) and (2.5) into it.

Making use of (2.7) and (2.2) we obtain

$$\frac{d^3y}{dz^3} = -\frac{1}{B}N(z)\frac{dy}{dz} +$$

$$+\frac{1}{S}\left[\frac{d^2N(z)}{dz^2}\frac{dy(z)}{dz} + 2\frac{dN(z)}{dz}\frac{d^2y(z)}{dz^2} + N(z)\frac{d^3y(z)}{dz^3}\right]. \tag{2.8}$$

In the case of $N = pz$, Eq. (2.8) becomes identical with the differential equation of buckling presented in [2], thus Eq. (2.8) can be considered a generalization of that equation.

To simplify the discussion, let us introduce a new variable

$$\zeta = \frac{z}{H},$$

and let us denote the differentiations with respect to ζ by commas. Hence Eq. (2.8) becomes:

$$y''' = -\frac{H^2}{B}Ny' + \frac{1}{S}[N''y' + 2N'y'' + Ny'''']. \tag{2.9}$$

We can reduce (2.9) to a second order differential equation by introducing the tangent of the deformed axis as a new variable instead of y.

If we write the equilibrium equation of buckling with the bending displacement y_M instead of the complete displacement y, we again obtain a homogeneous differential equation of the third order. This equation can also be reduced to a second order one by introducing the rotation of the normal of the cross section as a new variable (which is different from the previous tangent due to the influence of shear strain γ).

y'_M can be expressed with the aid of y' in the following way. Let us differentiate Eq. (2.6) once with respect to z, and introduce expressions (2.5) and (2.2) into it. We thus obtain

$$y' = y'_M + \frac{N}{S}y',$$

hence we arrive at

$$y'_M = \frac{S-N}{S}y'. \tag{2.10}$$

Let us denote the "bending rotation" by φ:

$$\varphi = y'_M .$$

Using (2.9) and (2.10) or using expressions having been used in the derivation of Eq. (2.9), we obtain a comparatively simple differential equation of buckling

$$\varphi'' = N\left(\frac{1}{S}\varphi'' - \frac{H^2}{B}\varphi\right) \tag{2.11}$$

which, in our case, simplifies the boundary conditions too.

3. The boundary conditions

Firstly, we will give the boundary conditions for (2.9).

a) At the top of the bar the horizontal displacement is equal to zero, because we have fixed the origin of the coordinate system at the end of the cantilever:

$$y(0) = 0. \tag{3.1}$$

b) The bending moment is also equal to zero at the top, hence using (2.4) we have

$$y''_M(0) = 0. \tag{3.2}$$

Using (2.5) and (2.6), the same condition written in the terms of y is as follows:

$$y''(0)\left[1 - \frac{N(0)}{S}\right] - \frac{1}{S}N'(0)y'(0) = 0. \tag{3.3}$$

c) At the built-in lower end the "bending rotation" is equal to zero:

$$y'_M(1) = 0. \tag{3.4}$$

Using (2.5) and (2.6), the same condition expressed by y assumes the form

$$y'(1)\left[1 - \frac{N(1)}{S}\right] = 0. \tag{3.5}$$

This boundary condition is satisfied if $y'(1) = 0$, that is if $y'_M(1) + y'_T(1) = 0$. According to (2.2), the shearing force also vanishes, hence both $y'_T(1)$ and $y'_M(1)$ have to vanish, and moreover, the following expression must hold (see (2,7) and (2,4)):

$$y'''_M(1) = 0. \tag{3.6}$$

On the other hand, the boundary condition can also be fulfilled if $1 - [N(1)/S] = 0$, that is if $N(1) = S$. In this case the value of $y'(1)$ can be arbitrary. Solutions belonging to $y'(1) = 0$ or $N(1) = S$ exclude each other except if we have $y'(1) = 0$ and the normal force, caused by the critical load at the lower end, is equal to S.

Equation (2.11) needs only two boundary conditions. At the free upper end the bending moment has to be equal to zero, hence:

$$\varphi'(0)=0 \tag{3.7}$$

and at the built-in lower end the "bending rotation" must be zero:

$$\varphi(1)=0. \tag{3.8}$$

It seems that in this case we have avoided the problem caused by the ambiguity of the boundary condition (3.5).

Actually, in the case of $N=S$, the relation between y' and φ expressed by Eq. (2.10) becomes indetermined.

4. Solution of the differential equation by means of a power series

In the case of uniformly distributed load the differential equation (2.9) has been solved using a power series in [2].

In this section we will generalize the results of [2] applying the same method and we will solve the equation (2.9) for a more general case.

Let the function of the normal force be:

$$N(z)=N_n\left(\frac{z}{H}\right)^n=N_n\zeta^n \tag{4.1}$$

wherein n is an arbitrary positive integer, N_n is a parameter depending on the load, whose value is positive if $N(z)$ means compression.

Substituting (4.1) into (2.9), we obtain

$$y'''-\lambda[n(n-1)\zeta^{n-2}y'+2n\zeta^{n-1}y''+\zeta^n y''']+\lambda\beta\zeta^n y'=0 \tag{4.2}$$

where

$$\lambda=\frac{N_n}{S}, \tag{4.3}$$

$$\beta=\frac{H^2S}{B}. \tag{4.4}$$

([2] denotes by β the value of (4.4) multiplied by 7.84.)

Let us attempt to find the solution of the incomplete third order differential equation in the form of the power series:

$$y=\sum_{k=0}^{\infty}a_k\zeta^k \tag{4.5}$$

wherein $a_0, \ldots, a_k, \ldots$ are unknown coefficients. The first three derivatives of (4.5) are as follows:

$$y' = \sum_{k=1}^{\infty} k a_k \zeta^{k-1}, \tag{4.6}$$

$$y'' = \sum_{k=2}^{\infty} k(k-1) a_k \zeta^{k-2}, \tag{4.7}$$

$$y''' = \sum_{k=3}^{\infty} k(k-1)(k-2) a_k \zeta^{k-3}. \tag{4.8}$$

Let us substitute these derivatives into the differential equation (4.2). The solution function (4.5) has to satisfy the differential equation for any value of ζ, so that the coefficient of each power of ζ must equal zero.

Hence a formula can be generated for the successive determination of the unknown coefficients:

$$a_k = 0 \qquad \text{if} \quad 2 < k \leq n, \tag{4.9}$$

$$a_k = \lambda a_{k-n} \frac{k[(k-1)(k-2) + 2n(k-1) + n(n-1)}{k(k-1)(k-2)}, \qquad \text{if} \quad n < k \leq n+2, \tag{4.10}$$

$$a_k = \frac{\lambda}{k(k-1)(k-2)} \{a_{k-n}(k-n-2)[(k-n-1)(k+n-2) + n(n-1)] - a_{k-n-2}\beta(k-n-2)\}, \qquad \text{if} \quad n+2 < k. \tag{4.11}$$

Expression (4.5) has to satisfy not only the differential equation but also the boundary conditions.

From condition (3.1) we obtain

$$a_0 = 0. \tag{4.12}$$

From equation (3.3) and (4.1) we find that this boundary condition can be satisfied, if

$$y''(0) - \lambda y'(0) = 0, \qquad \text{if} \quad n = 1 \tag{4.13}$$

and

$$y''(0) = 0, \qquad \text{if} \quad n > 1. \tag{4.14}$$

Hence we have

$$a_2 = \frac{\lambda}{2} a_1, \qquad \text{if} \quad n = 1, \tag{4.15}$$

$$a_2 = 0, \qquad \text{if} \quad n > 1. \tag{4.16}$$

Finally, the solution function has to satisfy the boundary condition (3.5). This can be achieved in two ways. Either

$$\sum_{k=1}^{\infty} k a_k = 0, \tag{4.17}$$

or

$$\lambda = 1. \tag{4.18}$$

must hold.

Let the second case be temporarily excluded from the discussion.

The buckling shape (4.5) belonging to the indifferent state of equilibrium is indefinite because of an indetermined constant factor, so that we can give any (nonzero) value to a_1 (which appears in the expressions of all other coefficients).

For the sake of simplicity let this value be:

$$a_1 = 1. \tag{4.19}$$

Eq. (4.9) to (4.12) and (4.15) or (4.16) are recursion formulas for the coefficients of the power series (4.5), in which all coefficients depend on a_1.

We have to determine the series of the coefficients in such a way that it satisfies Eq. (4.17) too. Choosing suitable values for β, we can construct an arbitrary number of such series. The solution to the problem requires to determine the series which belongs to the smallest value of λ.

The smallest value of λ can easily be determined using a step-by-step approximation, but this procedure needs a computer.

The recursion formulas of the coefficients obviously show that in the case of $\lambda = 1$ the power series is divergent, while in the case of $\lambda < 1$ it is convergent, independently of the value of β. However, it is not sure that we can satisfy Eq. (4.17) in the case of any value of β.

Actually, the results of the computer analysis have shown that there is a monotonously increasing sequence of numbers

$$\beta_0 = 0 < \beta_1 < \beta_2 < \ldots < \beta_n < \ldots$$

that represent lower limits of β for any value of n.

The value of λ is equal to 1, and Eq. (4.17) cannot be satisfied, if β is below the limiting β_n value. If $\beta > \beta_n$, then the coefficients can satisfy Eq. (4.17) and the calculation yields a value $\lambda < 1$.

We found that β_1 does not differ from π in the first three decimals but this coincidence may be accidental. So far we could not find a direct way for deriving exact values of the numbers β_n.

Some other values of β_n can be found in the diagram presented in Fig. 3.

The surprising result that λ does not depend on B and on H if $\beta < \beta_n$ can be explained by clarifying the role of S in buckling.

In the case of "slender" beams (i.e. if $\beta > \beta_n$) the possibility of shear deformation reduces the critical load in such a way that rising deformation due to a given loss of

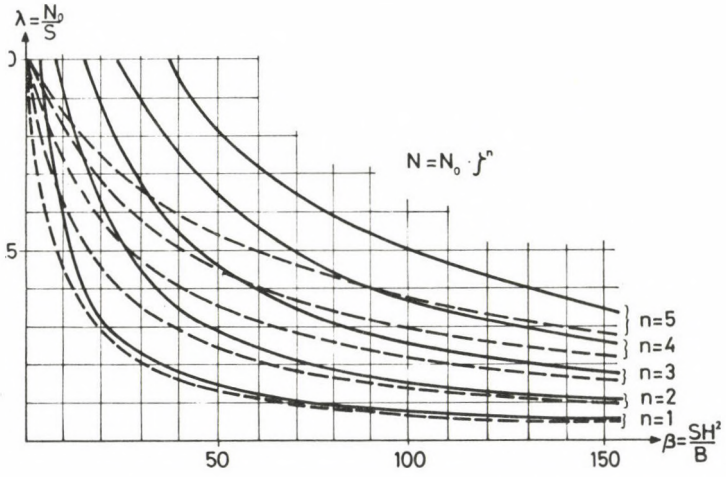

Fig. 3. Parameter λ as a function of the ratio of rigidities in the case of different normal loads whose distributions are described by power functions of the n-th degree

potential energy of the loads is hindered by less internal resistance than that in the case of no shear deformation. On the other hand, in the case of $\beta < \beta_n$, when the beam is "not slender", the normal force can reach, in a certain cross section, the value of the shear stiffness before "global" buckling, and the beam gets into an indifferent state of equilibrium because the shear strain becomes indefinite here, independently of the "global" state of deformation of the beam.

4.1 Results of numerical analyses

Values of λ are plotted against β with full lines due to load distributions characterized by different values of n in Fig. 3.

The curves determined with (4.17) intersect the line $\lambda = 1$ (4.18) at the values of β_n. If β is not far from β_n, then the coefficients a_k of the power series decrease very slowly, so that the sequence of partial sums badly converges to the solution. However, the speed of calculation can be improved also in this case using asymptotic expressions for coefficients a_k belonging to higher powers of ζ. We used this trick for obtaining approximate values of β_n too.

It is not easy to see in Fig. 3 that if $\beta \to \infty$ (i.e. if the shear deformation tends to zero), we get results in agreement with the elementary buckling theory of beams [1] (Table I).

Table I

n	1	2	3	4	5	6
$m=\lim_{\beta\to\alpha_n}\lambda\beta$	7.84	16.10	27.26	41.30	58.24	78.07

$$N_{cr}=m\frac{B}{H^2}. \tag{4.20}$$

The "exact" results can be compared with the approximate ones in Fig. 3. Values plotted with dotted lines were calculated by using a formula based on Föppl's theorem [2].

To use the theorem we need the "pure" critical loads. The critical load for "pure shear" is equal to S.

The critical load for "pure bending", N_{cr_B} can be calculated by using Eq. (4.20) and Table I (for $n\leq 6$).

According to the theorem we have

$$N_{cr}\geq\left(\frac{1}{N_{cr_B}}+\frac{1}{S}\right)^{-1} \tag{4.21}$$

wherein N_{cr} is the "exact" critical load, taking both bending and shear deformation into account.

If the sandwich beam has a low shear stiffness, the approximate value (4.21) of the critical load can be $30-40\%$ less then the exact value.

The comparison also shows that shifting the dotted lines to the left by β_n results in an approximate fitting of the corresponding full and dotted lines.

Hence

$$N_{cr}\approx S\left(1+\frac{SH^2}{mB}-\frac{\beta_n}{\beta}\right)^{-1} \tag{4.22}$$

can be used as a very good approximation of the critical load.

5. Solution of the differential equation by using a successive approximation

Let the function of the normal force be a polynomial of the n-th order

$$N(\zeta)=N_0\cdot\alpha(\zeta) \tag{5.1}$$

where

$$\alpha(\zeta)=\alpha_0+\alpha_1\zeta+\ldots+\alpha_n\zeta^n. \tag{5.2}$$

For the sake of uniqueness of $\alpha(\zeta)$, let the expression $\alpha(\zeta) \leq 1$ hold in the interval $0 \leq \zeta \leq 1$, with the equality valid at least at one point of the interval.

Introducing (5.1) into (2.11), we obtain

$$\varphi'' = \lambda(\varphi'' - \beta\varphi)\alpha(\zeta) \tag{5.3}$$

where

$$\lambda = \frac{N_0}{S}$$

and

$$\beta = \frac{SH^2}{B}.$$

We carry out the approximation as follows.

Let us take a simple function φ_0 that satisfies the boundary conditions (3.7) and (3.8) e.g.

$$\varphi_0 = 1 - \frac{3}{2}\zeta^2 + \frac{1}{2}\zeta^3. \tag{5.4}$$

The following recursion formula will be used:

$$\varphi''_{i+1} = (\varphi''_i - \beta\varphi_i)\alpha(\zeta). \tag{5.5}$$

Performing two integrations we obtain for φ_{i+1}:

$$\varphi_{i+1} = C_1 + C_2\zeta + a_2^{i+1}\zeta^2 + a_3^{i+1}\zeta^3 + \ldots + a_m^{i+1}\zeta^m, \tag{5.6}$$

where C_1 and C_2 are integration constants. (The upper indices of the coefficients a_k^{i+1} are not powers of exponentiation.) φ_{i+1} has to fulfil the boundary conditions (3.7) and (3.8), hence we have

$$C_2 = 0$$

and

$$C_1 = -\sum_{j=2}^{m} a_j^{i+1}.$$

In this way the boundary conditions stated for φ are fulfilled in each step of the recursion, while it generates approximate polynomials for φ of higher and higher degrees m.

If the method is convergent, namely if

$$\lim_{i \to \infty} (r \cdot \varphi_{i+1} - \varphi_i) = 0, \qquad 0 \leq \zeta \leq 1$$

holds, then, in the case of $\lambda = r$, φ_i satisfies the boundary conditions and, in addition, also the differential equation.

To avoid loss of accuracy caused by using too great or too small numbers in the calculation, it is useful to normalize φ_i in each step e.g. in such a way that we divide each coefficient by C_1. In this case C_1 has to tend to λ.

We found that the method is convergent for arbitrary functions $\alpha(\zeta)$. It produces the critical λ value even if it is independent of B.

5.1 Numerical example showing the application of successive approximation

The importance of successive approximation is shown by the fact that we can use it for arbitrary distribution of normal forces.

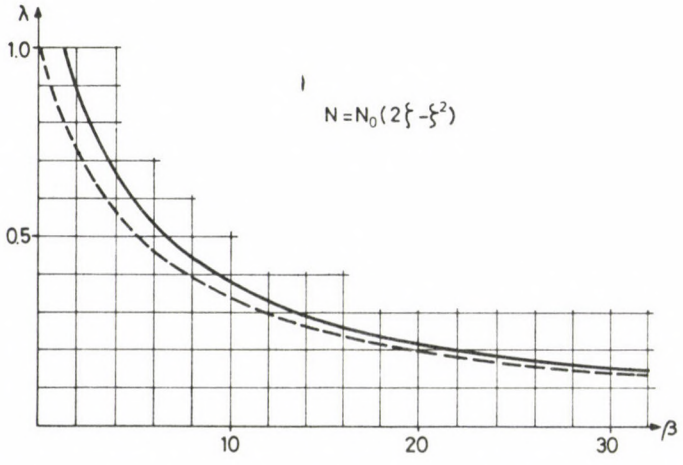

Fig. 4. Numerical example for the case of a normal load distributed according to a parabola of the second order

Let the distribution of the normal force be e.g. a second order parabola:

$$\alpha(\zeta) = 2\zeta - \zeta^2.$$

Using successive approximation for different values of β, we can plot the critical parameters belonging to them as shown with full line in Fig. 4.

Let us compare these results with those obtained by Föppl's theorem.

In the case of infinite shear stiffness the critical load of the cantilever is [5]:

$$N_{cr_B} = 5.1 \frac{B}{H^2},$$

and in the case of infinite bending rigidity it is equal to S.

Figure 4 also shows the approximate values of λ, depicted the above "pure" critical loads, with dotted line. As can be seen, the maximum relative error of the approximate formula exceeds 20%.

References

1. Timoshenko, S., Gere, I.: Theory of Elastic Stability. McGraw-Hill, New York,1961.
2. Zalka, K.: Buckling of a cantilever subjected to distributed normal loads, taking shearing deformation into account. Acta Techn. Hung. 89 (1979), 497–508.
3. Allen, H. G.: Analysis and Design of Structural Sandwich Panels. Pergamon Press, Oxford 1969.
4. Plantema, F. J.: Sandwich Construction. The Bending and Buckling of Sandwich Beams, Plates and Shells. John Wiley et Sons, New York, 1961.
5. Kovács, O., Fáber, G.: The Handbook of Elastic Stability. Műszaki Könyvkiadó, Budapest (1963). (In Hungarian.)

Acta Technica Academiae Scientiarum Hungaricae, 97 (1—4), pp. 123—131 (1984)

BUCKLING OF SANDWICH COLUMNS WITH THICK FACES SUBJECTED TO AXIAL LOADS OF ARBITRARY DISTRIBUTION

I. HEGEDŰS*—L. P. KOLLÁR**

[Received: 17 January 1984]

The paper presents the differential equations of buckling of sandwich columns with thick faces and a method based upon successive approximation to determine the critical load and buckling shape of columns subjected to an axial load distributed according to a polynomial function. The paper also presents a table for the calculation of the critical load of sandwich columns with various ratios of rigidities and subjected to uniformly distributed axial loads.

1. Introduction

The elementary theory of sandwich beams neglects the bending rigidity of the sandwich faces, or simply considers it as a small component of the total bending rigidity. This assumption usually does not cause any essential inaccuracy in the calculations. However, there are some engineering problems in which the elementary theory of sandwich beams proves deficient because of the above mentioned simplification.

Buckling of not slender sandwich beams can be considered as a typical example of such problems. The elementary theory of sandwich beams yields S (the shearing rigidity) for the upper limit of the critical load of not slender sandwich beams. However, many observations have shown that in several cases, due to "local rigidities", the critical load can significantly exceed this limit.

The aim of this paper is to deal with this problem and to develop a method which can be used in the case of almost arbitrarily loaded sandwich cantilever beams for calculating a more accurate value of the critical load than those presented so far.

* I. Hegedűs, H-2083 Solymár, Váci Mihály u. 10. Hungary
** L. P. Kollár, H-1122 Budapest Karap u. 9. Hungary

2. The differential equation of buckling of sandwich columns with thick faces

The principal difference between the thin- and thick-faced sandwich beams is that in the case of the latter the bending rigidity of the entire column is to be considered as if it consisted of two parts:

$$B = B_0 + B_l \tag{1}$$

Here B_l is the "local" bending rigidity, namely the sum of the bending rigidities of the two faces, referred to their own centroidal axes, and B_0 is the "global" bending rigidity of the sandwich beam with thick faces, obviously this is the part of B that belongs to the *Steiner* terms of moment of inertia of the composed cross-section.

The curvature of the axis of the deformed sandwich column consists of two parts (as it was also assumed in the elementary theory [4]):

$$\frac{d^2y}{dz^2} = \frac{d}{dz}(\varphi + \gamma) \tag{2}$$

where φ is the rotation of the normal of the cross section, and γ is the shear strain (angular distortion) of the cross section (Fig. 1). According to the two parts of the bending rigidity, the bending moment belonging to the change of curvature consists of two parts too:

$$M = -B_0 \frac{d\varphi}{dz} - B_l \frac{d}{dz}(\varphi + \gamma) = -B \frac{d\varphi}{dz} - B_l \frac{d\gamma}{dz}. \tag{3}$$

The main difference between the thin- and thick-faced sandwich beams is that with the former ones the change in curvature caused by the shear strain can develop without any resistance, while with the latter ones it causes bending moments in the faces. This is the reason of having a second term $(-B_l\, d\gamma/dz)$ in Eq. (3).

The total shearing force of the cross section consists of two parts too:

$$Q = -B_0 \frac{d^2\varphi}{dz^2} - B_l \frac{d^2}{dz^2}(\varphi + \gamma) = -B \frac{d^2\varphi}{dz^2} - B_l \frac{d^2\gamma}{dz^2}. \tag{4}$$

It is only a part of the shearing force $(B_0\, d^2\varphi/dz^2)$ which gives rise to shear stresses in the core of the cross section, so that it is only this part that causes shear strain:

$$\gamma = -\frac{B_0}{S} \frac{d^2\varphi}{dz^2} \tag{5}$$

Introducing (5) into the expression of the shearing force (4), we obtain a differential equation which contains only one of the unknown deformation parts. Disregarding irrelevant rigid-body displacements, the buckling shape of a sandwich cantilever beam under distributed normal forces can be described by using the function of rotation $\varphi(z)$.

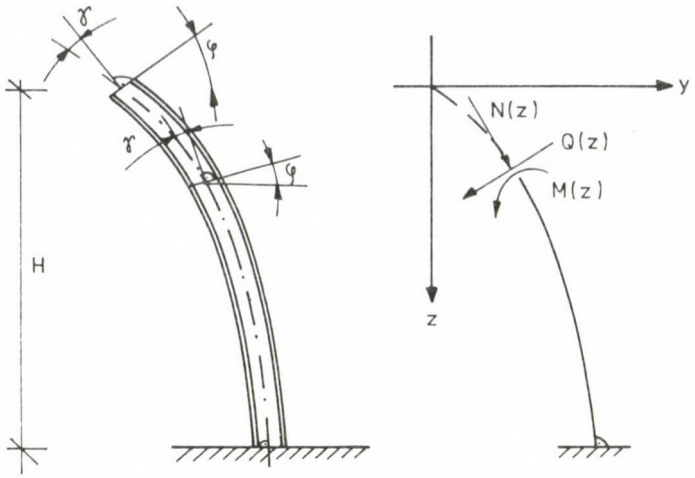

Fig. 1. Positive deformations and forces of the sandwich column

Hence, if we can express the differential equation of equilibrium and its boundary conditions in terms of $\varphi(z)$, there is no need of determining $y(z)$.

Let us set the cross sectional shearing force equal to the component of the load that is normal to the axis of the deformed beam. Assuming small displacements we obtain

$$-B\frac{\mathrm{d}^2\varphi}{\mathrm{d}z^2}-B_l\frac{\mathrm{d}^2\gamma}{\mathrm{d}z^2}=N(z)_{\mathrm{cr}}(\varphi+\gamma). \tag{6}$$

Let us write the normal force as follows:

$$N(z)=N\alpha(z),$$

and denote the critical value of N by N_{cr}. Introducing the appropriate derivatives of (5) into Eq. (6), we arrive at

$$\frac{B_0B_l}{S}\frac{\mathrm{d}^4\varphi}{\mathrm{d}z^4}-(B_0+B_l)\frac{\mathrm{d}^2\varphi}{\mathrm{d}z^2}+N_{\mathrm{cr}}\alpha(z)\left(\frac{B_0}{S}\frac{\mathrm{d}^2\varphi}{\mathrm{d}z^2}-\varphi\right)=0. \tag{7}$$

Fixing the origin at the upper end of the cantilever (Fig. 1), the boundary conditions of the differential equation are as follows:

$$\begin{aligned}
&\text{at}\quad z=H \qquad \varphi=0 \qquad (\text{built-in end}),\\
&\text{at}\quad z=0 \qquad \mathrm{d}\varphi/\mathrm{d}z=0 \qquad (M_0=0),\\
&\text{at}\quad z=H \qquad \mathrm{d}^2\varphi/\mathrm{d}z^2=0 \qquad (\text{clamped faces}),\\
&\text{at}\quad z=0 \qquad \mathrm{d}^3\varphi/\mathrm{d}z^3=0 \qquad (M_l=0).
\end{aligned} \tag{8a to d}$$

Since the mathematical formulation of buckling is an eigenvalue problem of a linear differential equation and its boundary conditions, we have to determine the smallest eigenvalue belonging to an eigenfunction, which satisfies the (7) differential equation and fulfils its boundary conditions (8a to d).

3. Sandwich cantilever subjected to constant compression

In the case of $\alpha(z) \equiv 1$, namely if the load is a concentrated force at the top of the cantilever, we can easily solve the problem. Due to the regularity in the signs of the even derivatives of the differential equation, the solution can be constructed of trigonometric functions. The functions

$$\varphi(z)_k = \varphi^{(k)} \cos \frac{(2k-1)\pi z}{2H}, \qquad k = 1, 2 \ldots$$

also fulfil the boundary conditions. Introducing these functions into Eq. (7), we obtain the formula for the critical load:

$$N_{\mathrm{cr}}^{(k)} = \left[\left(\frac{(2k-1)^2 \pi^2 B_0}{(2H)^2} \right)^{-1} + S^{-1} \right]^{-1} + \frac{(2k-1)^2 \pi^2 B_l}{(2H)^2}. \tag{9a}$$

We obtain the smallest critical force by substituting $k = 1$ into (9a). We can also give a physical interpretation of the terms in Eq. (9a). The inverse of the first term in the square bracket and the last term of the expression are critical loads (N_{E0}^k and N_{El}^k) of *Euler* beams with flexural rigidities B_0 and B_l respectively. S is the critical load of a sandwich

Table I. The value of $N_{\mathrm{cr}} H^2/B$ in the case of uniformly distributed axial load

B_l/B SH^2/B	0	0.05	0.1	0.2	0.3	0.4	0.5	0.6	0.7	0.8	0.9	1.0
0.	0.	0.392	0.784	1.567	2.351	3.135	3.918	4.702	5.486	6.269	7.053	7.837
0.2	0.200	0.904	1.314	2.102	2.882	3.658	4.432	5.021	5.957	6.698	7.385	7.837
0.5	0.500	1.465	1.917	2.717	3.486	4.238	5.025	5.691	6.378	7.015	7.552	7.837
1.0	1.000	2.142	2.642	3.449	4.185	4.887	5.551	6.179	6.757	7.265	7.658	7.837
2.0	2.000	3.094	3.589	4.366	5.026	5.618	6.178	6.679	7.111	7.473	7.729	7.837
π	3.141	3.869	4.313	5.000	5.583	6.098	6.556	6.960	7.303	7.575	7.629	7.837
5.0	4.211	4.709	5.057	5.637	6.117	6.532	6.892	7.202	7.458	7.655	7.787	7.837
10.0	5.597	5.861	6.080	6.457	6.773	7.052	7.279	7.466	7.620	7.736	7.810	7.837
20.0	6.570	6.706	6.828	7.045	7.230	7.388	7.522	7.632	7.719	7.783	7.823	7.837
50.0	7.287	7.344	7.395	7.571	7.574	7.641	7.700	7.749	7.787	7.815	7.832	7.837
100.0	7.554	7.583	7.609	7.657	7.700	7.736	7.767	7.792	7.812	7.826	7.834	7.837
∞	7.837	7.837	7.837	7.837	7.837	7.837	7.837	7.837	7.837	7.837	7.837	7.837

beam with thin faces and with infinite bending rigidity. This latter critical load is independent of the buckling shape. Introducing the above critical forces into (9a), we obtain

$$N_{cr}^{(k)} = [(N_{E0}^{(k)})^{-1} + S^{-1}]^{-1} + N_{El}^{(k)}. \tag{9b}$$

This equation is identical with the formula derived on the basis of *Föppl*'s theorem for the estimation of N_{cr} of a sandwich beam with thick faces, subjected to an arbitrarily distributed normal load. Thus in the case of the boundary conditions used above and of a single concentrated force at the top of the column this approximate formula proves to be exact.

4. Solution to the problem in the case of arbitrary distributed axial forces

If the function $\alpha(z)$ in Eq. (7) is not constant, then the solution of the problem becomes more difficult. We can use *Föppl*'s theorem (9b) and by so doing we obtain a lower limit for the value of the critical load. To use this method we should know the critical forces N_{E0} and N_{El} belonging to the given distribution of the normal load. These values, however, can be found only for some special cases in reference books and manuals [1], [5]. In many cases *Rayleigh*'s quotient or some analogous expressions [1], [7] may yield a close upper limit in the following way.

Firstly, we have to take an arbitrary simple function that fulfils the boundary conditions. Let us denote it by ψ. Let us substitute it into Eq. (7) and multiply the equation by $(\psi - B_0/S \cdot d^2\psi/dz^2)$. Integrating from 0 to H, we can express the coefficient to be found in place of N_{cr}. Let us denote this coefficient by $R(\psi)$. With integration by parts and by taking the boundary conditions into account we obtain the following quotient, analogous to *Rayleigh*'s one:

$$R(\psi) = \frac{\int_0^H \left\{(B_0 + B_l)\left(\frac{d\psi}{dz}\right)^2 + \frac{B_0(B_0+2B_l)}{S}\left(\frac{d^2\psi}{dz^2}\right)^2 + \frac{B_0^2 B_l}{S^2}\left(\frac{d^3\psi}{dz^3}\right)^2\right\} dz}{\int_0^H \alpha(z)\left[\psi - \frac{B_0}{S}\frac{d^2\psi}{dz^2}\right]^2 dz}. \tag{10}$$

As *Rayleigh*'s quotient, $R(\psi)$ also shows the ratio of internal to external works. If ψ is an exact buckling shape, $R(\psi)$ becomes equal to the exact critical load.

In the case of usual types of loads and usual ratios of rigidities, the interval between the limits yielded by *Föppl*'s theorem and by a *Rayleigh*-type quotient is rather large. Hence, in order to obtain a more exact result we need a more accurate calculation.

Results of such an improved calculation are presented in Table 1. for the case of a uniformly distributed normal load. The method we developed for taking into account

practically any distribution of load takes advantage of the good efficiency of the *Rayleigh*-type quotients in approximating the critical load. It is a step-by-step procedure which uses approximate polynomials of higher and higher degree, and makes it possible to carry out a monotonous partial minimization of the *Rayleigh*-type quotient shown in Eq. (10).

Let us take first the two simplest polynomials of different degrees which fulfil the boundary conditions

$$\psi_{\mathrm{I}} = 1 - \frac{6}{5}\left(\frac{z}{H}\right)^2 + \frac{1}{5}\left(\frac{z}{H}\right)^4,$$
$$\psi_{\mathrm{II}} = 1 - \frac{10}{9}\left(\frac{z}{H}\right)^2 + \frac{1}{9}\left(\frac{z}{H}\right)^5, \tag{11a, b}$$

and take their linear combination

$$\varphi_0 = \mu_0 \psi_{\mathrm{I}} + (1 - \mu_0)\psi_{\mathrm{II}} \tag{12}$$

which minimizes the value of $R(\varphi_0)$. The numerical analyses showed that this approximate value is in most cases already sufficiently accurate for practical purposes. If we need a better approximation, we may determine a new approximate polynomial, using the expression:

$$\frac{\mathrm{d}^4\psi_i}{\mathrm{d}z^4} = \left[R(\varphi_i)\alpha\left(\varphi_i - \frac{B_0}{S}\frac{\mathrm{d}^2\varphi_i}{\mathrm{d}z^2}\right) + (B_0 + B_l)\frac{\mathrm{d}^2\varphi_i}{\mathrm{d}z^2}\right]\frac{S}{B_0 B_l} \tag{13}$$

where $R(\varphi_i)$ is the minimum value of the *Rayleigh*-type quotient determined in the previous step with the aid of (12). Integrating four times, we can determine the ψ_i polynomial which satisfies all boundary conditions. This polynomial can be used for getting a refined approximate polynomial φ_{i+1} by determining the coefficients of the linear combination in (14)

$$\varphi_{i+1} = \mu_i \varphi_i + (1 - \mu_i)\psi_i \tag{14}$$

which minimize the value of $R(\varphi_{i+1})$. Further refinement can be achieved by repeating the two steps of the iteration resulting in polynomials of higher and higher degree.

The amount of calculation using the above method is rather great, but the convergence is excellent. At most the fourth iteration step yields a value for the critical force which can be regarded as exact, even in the case of any distribution of the load.

5. Numerical example

Let us determine the critical load of the coupled shear-wall shown in Fig. 2. The total height is 30 m. Let the wall be subjected to a uniformly distributed axial load:

$$N(z) = N_{\mathrm{cr}}\frac{z}{H}.$$

First, we have to determine the rigidities B_0, B_l and S of the replacement sandwich beam with thick faces, as follows.

$$B_0 = 2 \times E \times 0.1 \times 1.2 \times 2.4^2 = 1.3824 \times E \,[\mathrm{kN} \times \mathrm{m}^2]$$

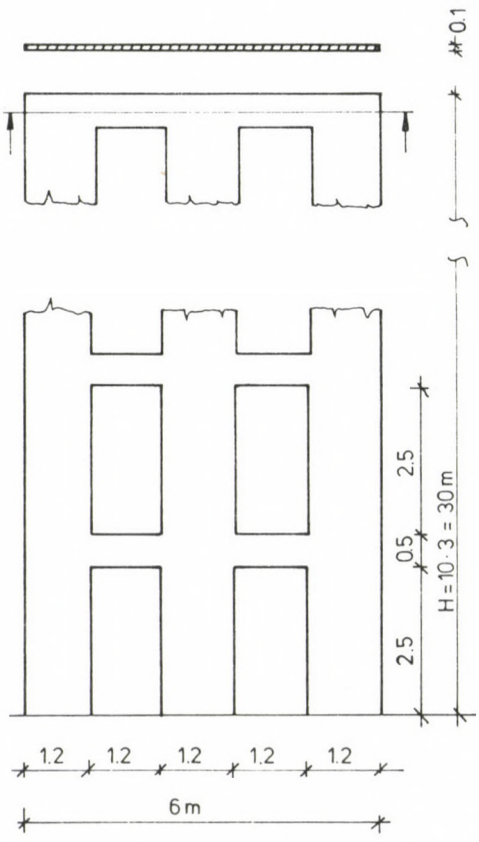

Fig. 2. The shear-wall analysed in the numerical example

where E denotes the modulus of elasticity in $\mathrm{kN/m^2}$ units.

$$B_l = 3\,\frac{E \times 0.1\,1 \times 2^3}{12} = 0.0432 \times E \,[\mathrm{kN} \times \mathrm{m}^2]$$

As the formula shows, in this case B_l consists of the bending rigidities of the three vertical wall-strips, with respect to their own centroidal axis.

In determining the shearing rigidity S, we only take into account the deformation possibilities of the parts of the wall not shaded in Fig. 3. Using the notations in Fig. 3, we obtain

$$S = \frac{b(2\alpha+1)}{\alpha\left(\dfrac{\hat{b}^3}{3B_2} + \dfrac{\hat{b}}{S_2}\right) + (2\alpha+1)\dfrac{b^2\hat{a}}{a^2 S_1} + \dfrac{b^2\hat{a}^2}{4B_1 a}\left[2\alpha - 1 + \dfrac{\hat{a}}{3a}(2\alpha+1)\right] + \dfrac{b^2\hat{a}(a-\hat{a})(2\alpha-1)}{4aB_1}},$$

where

$$\alpha = \frac{\frac{\hat{b}^3}{3B_3} + \frac{\hat{b}}{S_3} + \frac{b^2\hat{a}}{2B_1}}{\frac{\hat{b}^3}{3B_2} + \frac{\hat{b}}{S_2} + \frac{b^2\hat{a}}{B_1}}$$

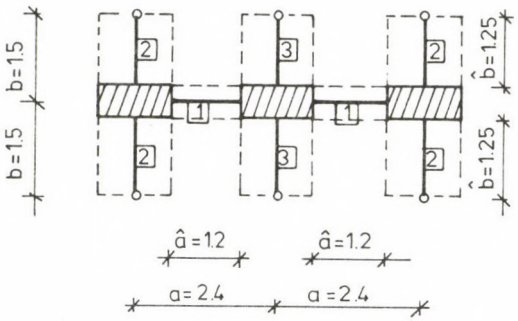

Fig. 3. The substituting model of a shear-wall section

and

$B_1 = I_1 E$ is the bending rigidity of the horizontal wall-strips; in our case it is equal to $B_1 = 0.001\,042 \times E\,[\mathrm{kNm}^2]$;

$B_2 = I_2 E$ is the bending rigidity of the outside vertical wall-strips;

$B_3 = I_3 E$ is the bending rigidity of the middle vertical wall-strip; in our case $B_2 = B_3 = 0.0144 \times E\,[\mathrm{kNm}^2]$;

$S_1 = A_1 G/n$ is the shear rigidity of the horizontal wall-strips, A_1 is the area of its cross-section, G is the modulus of shear and n is a numerical factor depending on the shape of the cross section; in our case $A_1 = 0.05\ \mathrm{m}^2$, $G = E/2.5$ and $n = 1.2$, hence $S_1 = 0.016\,67 \times E\,[\mathrm{kN}]$;

$S_2 = A_2 G/n$ is the shearing rigidity of the outside vertical wall-strips;

$S_3 = A_3 G/n$ is the shearing rigidity of the middle vertical wall-strip; in our case $A_2 = A_3 = 0.12\ \mathrm{m}^2$, so that $S_2 = S_3 = 0.04 \times E\,[\mathrm{kN}]$.

Substituting the numerical values in the expressions of S and α, we obtain

$$\alpha = 0.5143$$

and

$$S = 0.01356 \times E\,[\mathrm{kN}]\,.$$

Knowing B_0, B_l and SH^2, we can determine the value of the critical load with the aid of a computer program (or with the aid of Table 1). We obtain

$$\frac{N_{cr} H^2}{B_0 + B_l} = 5.461\,,$$

hence

$$N_{cr} = 0.00865 \times E\,[\mathrm{kN}]\,.$$

Let us consider the shear-wall as a sandwich cantilever with thin faces. The shearing rigidity is the same as in the previous case, and the bending rigidity is

$$B = B_0 + B_l = 1.4256 \times E\,[\mathrm{kNm}^2]\,.$$

The ratio of the rigidities is:

$$\frac{SH^2}{B} = 8.559\,,$$

hence, using the diagram of [2] or [6], we obtain

$$N_{cr} = 0.0083 \times E\,[\mathrm{kN}]\,.$$

This value is not too far from the "exact" one.
If we change the total length of the shear-wall from $H = 30$ m to $H = 18$ m, we obtain the value of the critical load of the sandwich beam with thick faces as

$$N_{cr} = 0.0157 \times E\,[\mathrm{kN}]\,.$$

Let us now consider the shear-wall as a sandwich cantilever with thin faces. The ratio of the rigidities is:

$$\frac{SH^2}{B} = 3.081 < 3.14\,,$$

therefore the value of the critical load depends only on the shearing rigidity. Hence we obtain

$$N_{cr} = S = 0.01356 \times E\,[\mathrm{kN}]\,.$$

This is only 86% of the "exact" critical load, so that this approximation is not accurate enough.

References

1. Timoshenko, S., Gere, I.: Theory of Elastic Stability. McGraw-Hill, New York 1961.
2. Zalka, K.: Buckling of a cantilever subjected to distributed normal loads, taking shearing deformation into account. *Acta Techn. Hung.* 89 (1979), 497–508.
3. Allen, H. G.: Analysis and Design of Structural Sandwich Panels. Pergamon Press, Oxford, 1969.
4. Plantema, F. J.: Sandwich Contruction. The Bending and Buckling of Sandwich Beams, Plates and Shells. John Wiley et Sons, New York 1961.
5. Kovács, O., Fáber, G.: The Handbook of Elastic Stability. Műszaki Könyvkiadó, Budapest 1963 (in Hungarian).
6. Hegedűs, I., Kollár, L. P.: Buckling of sandwich columns with thin faces under distributed normal loads *Acta Techn. Hung.* (In print.).
7. Halász, O.: Steelconstructions III/1. Theory of Stability (Manuscript) Tankönyvkiadó, Budapest 1980. (In Hungarian).

Acta Technica Academiae Scientiarum Hungaricae, 97 (1—4), pp. 133—175 (1984)

INITIAL POSTBUCKLING BEHAVIOUR OF SHALLOW SADDLE-SHAPED HYPAR SHELLS SUPPORTED BY SHEAR DIAPHRAGMS, UNDER UNIFORM LOAD

L. JANKÓ*

[Received: 3 January 1983]

This paper is one of a series on the stability of hypar shells. — Relying on the analysis of bifurcation phenomena in hypar shells starting from a state assumed as undeformed, and of symmetric nonlinear structural behaviour, the initial post-buckling behaviour will now be considered. Based on earlier research of the Author, the slope of *the tangent at the beginning* of the post-buckling (decreasing or increasing) load capacity diagram may fairly be approximated but this paper will suggest a method for constructing a diagram valid *in the range* of deflections much (though by less than an order) exceeding the shell thickness. With the aid of this method, the effect of prebuckling (pre-bifurcational deformations) on the buckling load can also be taken into consideration. The accuracy of the method in this case is fairly good. The *initial post-buckling* behaviour and the *type of the bifurcation points* can also be characterized.

Symbols

$A_0, B_0, \ldots$
$A_{00}, B_{00}, \ldots$
$A, B, \ldots$ — coefficients in function $p-w$ of the asymmetric equilibrium path;

$B = \dfrac{Eh^3}{12(1-\mu^2)}$ — specific bending stiffness;

$C_{ij} = \cos\dfrac{i\pi}{2a}x \cdot \cos\dfrac{j\pi}{2b}y,$

$D = \dfrac{Eh}{1-\mu^2}$ — specific extensional stiffness;

E — modulus of elasticity (Young's modulus);

F — stress function of middle surface forces ($F'' = N_x$, $F'' = -N_{xy}$, $F'' = N_y$; in a bifurcation phenomenon: $F = F_0 + \bar{F}$; generally: $F = \Sigma\Sigma F_{ij0}$, actually $F = F_1 + F_2$);

F_0 — stress function of the prebuckling state (actually $F_0 = F_1$);

$\bar{F}$ — first variation of function F_0 (actually $\bar{F} = F_2$);

F_1, F_2 — symmetric and antimetric components ($F_{i_1 j_1 0} \equiv F_1$ and $F_{i_2 j_2 0} \equiv F_2$) resp., of stress function F;

$F_{i_1 j_1}, F_{i_2 j_2}$ — amplitudes of symmetric and antimetric (F_1 and F_2, resp.) stress function components ($F_1 = F_{i_1 j_1} \cdot S_{i_1 j_1}$, $F_2 = F_{i_2 j_2} \cdot S_{i_2 j_2}$),

* Dr. L. Jankó, H-1113 Budapest Dávid F. u. 5, Hungary

I_0, J_0 — numbers of terms in buckling eigenfunction ($\bar{w} = \Sigma\Sigma w_{ij} S_{ij}$) for the undeflected prebuckling state, $i = 1, \ldots, I_0$; $j = 1, \ldots, J_0$;

I_1, J_1 — as for I_0, J_0 but referring to the deflection function of the nonlinearly deformed middle surface;

M_x, M_y, $M_{xy} = M_{yx}$ — specific bending moments and twisting moments in the shell;

N_x, $N_{xy} = N_{yx}$, N_y — specific values of middle surface forces;

Q_x, Q_y — specific values of transverse shear forces;

$R_x = \dfrac{a^2}{2f_a}$ — curvature radius of shallow arches in direction x (convex from above);

$R_y = \dfrac{-b^2}{2f_b}$ — curvature radius of shallow arches in direction y (concave from below);

$\dfrac{R_x|R_y|}{h^2} = \dfrac{a^2 b^2}{4 f_a f_b} = \dfrac{\beta^4}{4\zeta^2\gamma^2\alpha}$ — dimensionless magnitude in the formula of load parameter c;

$S_{ij} = \sin\dfrac{i\pi}{2a} x \cdot \sin\dfrac{j\pi}{2b} y$,

a_1, a_2, a_3 — coefficients in function $p - w$ describing the symmetric equilibrium path by a single-term deflection function w;

a_{11}, a_{12}, . . . a_{45} — coefficients in the general nonlinear differential equation system of the equilibrium path;

$a_{i_1 j_1}$, $b_{i_1 j_1}$, $a_{i_2 j_2}$, $b_{i_2 j_2}$, $c_{i_1 j_1}$ — short notations, see in Table II;

$2a$, $2b$ — lengths of boundary projections along x and y, resp.;

$c = \dfrac{p}{E} \cdot \dfrac{R_x|R_y|}{h^2} = \dfrac{p}{E} \dfrac{\beta^4}{4\zeta^2\gamma^2\alpha}$ — load parameter;

c_{cr}^{lin}, $c_{cr,d}^{lin}$ — as for c but referring to buckling loads p_{cr}^{lin}, $p_{cr,d}^{lin}$ (bifurcation);

$\bar{c}_{cr}$ — as for c but referring to the snap-buckling load $\bar{p}_{cr}$;

f_a, f_b — vault rise along x and y, resp.;

h — shell thickness;

i, j — buckling half-wave numbers in directions x and y, resp. ($i = 1, \ldots, I_0$; $j = 1, \ldots, J_0$ for bifurcation from undeflected prebuckling state; $i = 1, \ldots, I_1$, $j = 1, \ldots, J_1$ for the deflection function w of a non-linear equilibrium path);

i_1, j_1 — half-wave numbers of the symmetric component of deflection function w (for both axes $\bar{x}$ and $\bar{y}$);

i_2, j_2 — half-wave numbers of the antimetric component of deflection function w (for the $\bar{x}$- and/or $\bar{y}$-axis);

p — intensity of the uniformly distributed, symmetric surface load acting in direction of the z-axis per unit ground plan projection;

p_{cr}^{lin} — buckling load of bifurcation from prebuckling state considered *undeflected* ($w_0 = 0$; linear buckling theory);

$\bar{p}_{cr}$ — snap-buckling load (critical load of buckling by equilibrium limitation; non-linear buckling theory);

$p_{cr,d}^{lin}$ — buckling load of bifurcation from the linear critical load of bifurcation from symmetrically *deflected* prebuckling state ($w_0 \neq 0$; linear buckling theory);

u, v — displacements along surface tangents in x- or y-direction;

$z(x, y)$; $\bar{z}(\bar{x}, \bar{y})$ — ordinates of the middle surface of the shell;

w — normal displacement (deflection) of points of the middle-surface (in a bifurcational phenomenon $w = w_0 + \bar{w}$; in general: $w = \Sigma\Sigma w_{ij0}$, actually: $w = w_1 + w_2$),

w_{i0} — function of normal displacement (deflection) of points of the middle-surface in the prebuckling state (actually: $w_0 = w_1$); at the shell centre ($x = a$, $y = b$) $w_0 = w_{i_1 j_1}$;

$\bar{w} = \delta w^0$ — normal displacement (deflection) variation in bifurcation phenomena;

w_1, w_2 — symmetric and antimetric components ($w_{i_1 j_1 0} \equiv w_1$ and $w_{i_2 j_0} \equiv w_2$) resp., of deflection function w;

$w_{i_1 j_1}$, $w_{i_2 j_2}$ — amplitudes of symmetric (w_1) and antimetric (w_2) components, resp., of w ($w_1 = w_{i_1 j_1} \cdot S_{i_1 j_1}$, $w_2 = w_{i_2 j_2} \cdot S_{i_2 j_2}$),

$\alpha = \frac{f_a}{f_b}$ — vault rise ratio;

$\beta = \frac{a}{h}$ — shell parameter;

$\gamma = \frac{a}{b}$ — side ratio;

δ — symbol of variation formation (short notation for $\delta w_0 \equiv \bar{w}$);

$\zeta = \frac{f_b}{h} = \frac{\beta \rho}{\gamma}$ — shell parameter;

η — coordinate in a plane fitting the z-axis, pointing to the second system of straight surface generators;

$\lambda = \frac{p_{cr}^{\text{lin}}}{E}$ — eigenvalue;

μ — transverse contraction coefficient (0.2);

ξ — coordinate in a plane fitting the z-axis, pointing to the first system of straight surface generators;

$\rho = \frac{f_b}{b}$ — shell parameter;

ω — half of the angle subtended between the director planes;

$\Delta\Delta(\ \ ) = (\ \ )^{\text{IV}} + 2(\ \ )^{\cdot\cdot\text{II}} + (\ \ )^{::}$ — biharmonic differential operator;

$L_p(f_1, f_2) = f_1^{\text{II}} f_2^{\cdot} - 2 f_1^{\cdot\text{I}} f_2^{\cdot\text{I}} + f_1^{\cdot} f_2^{\text{II}}$ Pucher's differential operator.

1. Introduction

First, we discussed the phenomenon of *bifurcation* in the case of saddle-shaped hypar shells supported by shear diaphragms from an assumed undeflected prebuckling state ($w_0 = 0$) in [9], then we analysed some peculiarities of the symmetric equilibrium path for *large deformations* in [10].

Relying on methods in [1], [3], [18] for examining the equilibrium path, we have developed an approximate method for taking the effect of prebuckling deflections (w_0) modifying the buckling load into consideration ($p_{cr}^{\text{lin}} \to p_{cr,d}^{\text{lin}}$).

According to our numerical results, the prebuckling deflections may either increase or reduce the buckling load p_{cr}^{lin}. Although no special method was developed in

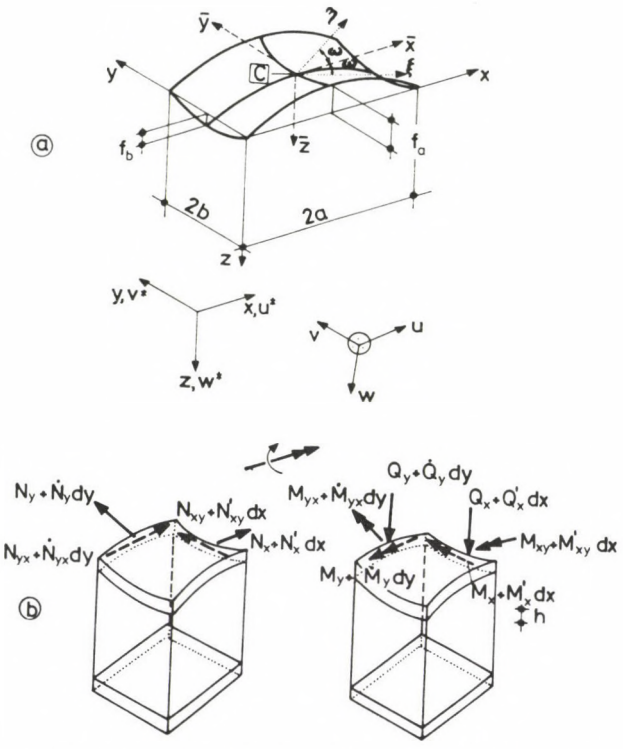

Fig. 1. Geometry data. Internal forces and displacements

[10] for the numerical analysis of the postcritical state after bifurcation, it was pointed out that the mentioned method for determining buckling loads $p_{cr,d}^{\text{lin}}$ could show whether the branch of diagram $p-w$ directly after bifurcation is of an *increasing* or *decreasing* nature.

Of course, definition of the full stability behaviour still requires further research on e.g. the effect of geometrical imperfections, the possibility of local buckling, etc.

Before solving these perspective problems, it seems imperative to develop a method which takes into consideration the prebuckling deflections w_0 modifying the buckling loads and which describes the initial postbuckling behaviour more accurately than the one presented in [10]. This method will be given in the following.

2. Basic assumptions, approximations, fundamentals, definitions

Boundary arches are assumed to be supported by shear diaphragms: they are rigid in the vertical plane, soft laterally and torsionally.

The effect of a uniform shell load along the z-axis, symmetric to both planes $\bar{x}\bar{z}$ and $\bar{y}\bar{z}$, referred to unit ground plan projection, is considered.

The shell is assumed to be geometrically perfect, shallow and of a linear elastic material.

Buckling modes extending to all the surface are considered.

Geometrical nonlinearity is reckoned with by means of Donnell's equations. Their two main peculiarities [12] are as follows. They assume that the shell is shallow (at least within a buckling half-wave) and they include at most quadratic terms (w'^2 etc.) of the power series of the derivatives of displacement w, justifying the denomination "theory of limited large deformations".

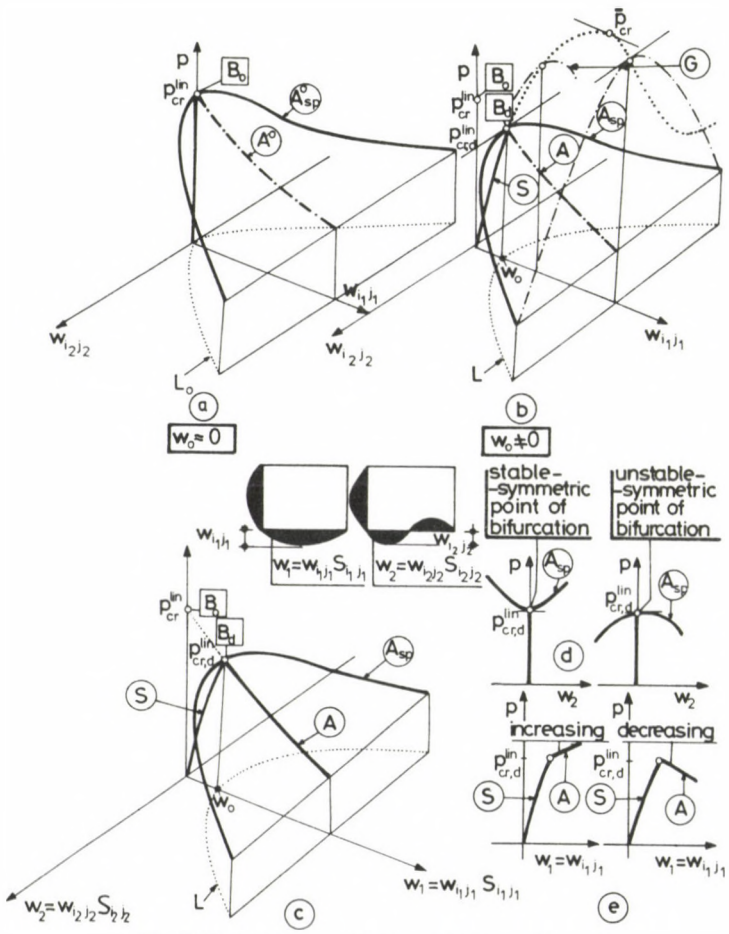

Fig. 2. The spatial equilibrium path ($a-c$: $S-A_{sp}$)
Bifurcation point types ($d-e$)

It is to be noted that the deformed prebuckling state of the hypar shell will be called *deflected prebuckling state* (deflection: $w_0 \neq 0$).

For the sake of representation in three dimensional space, the postbuckling deflection mode in Fig. 2 consists of a constant symmetric (w_1) and a variable antimetric (w_2) component. As antimetric component, the *dominant* term ($i_2 = 2, j_2 = 1$ or $i_2 = 3, j_2 = 1$ or $i_2 = 4, j_2 = 2$) of the buckling mode corresponding to the buckling load according to the linear buckling theory has been taken. The load-bearing process starts according to the heavy-line branch of diagram S in Fig. 2. Until bifurcation point B_d, the deflection mode has only symmetric components [10].

Postbuckling behaviour after bifurcation is described by *space curve* A_{sp}. This space curve is obtained as a section along plane curve L of a surface described by the twovariable function $p = p(w_{i_1 j_1}, w_{i_2 j_2})$. Equation of plane curve L determines the ratio of amplitude $w_{i_1 j_1}$ to $w_{i_2 j_2}$. It is obvious (but it is also proved in Section 5) that for the saddle-shaped hypar shell both this load-bearing surface and the space curve A_{sp} are symmetrical about plane $w_{i_2 j_2} = 0$, namely the structure shows an *identical* behaviour upon formation of either a positive or a negative antimetric component.

Projecting space curve A_{sp} onto plane $w_{i_2 j_2} = 0$ yields *plane curve* A. The meaning of this curve becomes clearer from representing the load to be equilibrated as a function of symmetric and antimetric components (w_1 and w_2) of the deflection of typical shell points (Fig. 2c).

Post-bifurcational equilibrium paths of any middle surface point *but* the shell centre C (Fig. 1) and of the shell *centre C in a special position* are described by space curve A_{sp} and by plane curve A, respectively. Namely, the shell centre has no antimetric deflection, hence plane curve A after bifurcation is a *degenerating* special case of space curve A_{sp}. The space curve equation system is presented in Section 5, analysis results are, however, *represented in plane* in Figs 2c and 3, as complete equilibrium path $A - S$.

Doing so is permitted, since the presentation of bifurcation points according to Fig. 2d (pp. 65, 91, 122 in [2]; p. 384 in [6]; pp. 50–55 in [17]) is equivalent to that according to Fig. 2e (Section 1.2 in [12]). Namely, projections of space curve A_{sp} on plane $w_1 = 0$, and on $w_2 = 0$ have been plotted in Figs 2d, and 2e, respectively. *Stable symmetry* or *unstable symmetry* of the bifurcation points in Fig. 2d can be described from another aspect by terms *increasing* or *decreasing* according to Fig. 2e.

The following definitions will also be used in this paper:

a) If the load is equilibrated along the whole loading process by internal forces corresponding to deflection mode w symmetrical about both planes $\bar{x}\bar{z}$ and $\bar{y}\bar{z}$, this process (or, for the sake of simplicity, the relevant $p - w$ diagram) is called *symmetrical equilibrium path.*

The construction of these diagrams was presented in [10], featured by deflection $w = 0$ belonging to load $p = 0$, then, with increasing load, by either a "*shell-type*" load capacity diagram (S in Figs 2 and 3), or a monotonous increasing one typical of ordinary flat plates. The term "shell-type" refers to middle surface forces bearing most of the loads.

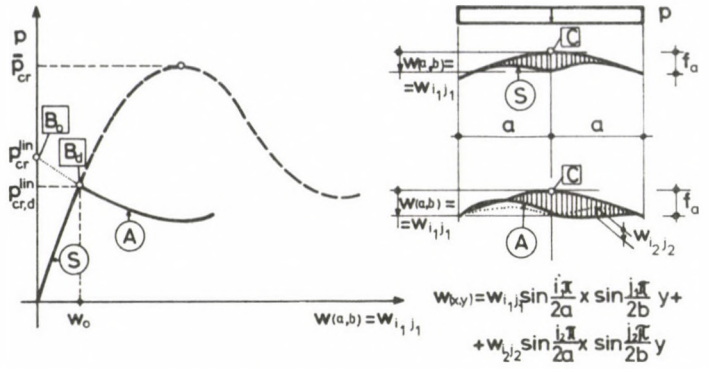

Fig. 3. In-plane representation of symmetric and asymmetric equilibrium paths S and A, resp.

The monotonous increasing character is irrelevant to the bifurcation phenomenon [10], mentioned purely for the sake of completeness.

b) Load can be equilibrated ($p-w$) also by the following means (Fig. 2c, and $S-A$ diagram in Fig. 3):

The symmetrically deformed shell surface buckles at a certain deflection value w_0 of the shell centre, to act thereafter in a deflection mode composed of symmetric and antimetric components.

The load-bearing process represented, for the sake of simplicity, by its $p-w$ diagram mainly featured by an asymmetric deflection function w involving both symmetric and antimetric deflection components corresponding to the load symmetric about planes $\bar{x}\bar{z}$ and $\bar{y}\bar{z}$, is called *asymmetric equilibrium path A.*

Deflection function w belonging to the asymmetric equilibrium path differs from that for a symmetric equilibrium path by involving also the antimetric buckling mode of the bifurcation corresponding to the so-called undeflected prebuckling state (or more precisely, as much of it as is allowed by the actual computational facilities).

Disregarding deformations w_0 in the undeflected prebuckling state, the start of equilibrium path A would be at buckling load p^{lin}_{cr} [9] (B_0 in Fig. 2a).

By virtue of assumption $w_0=0$ it involves no symmetric deflection component.

The asymmetric equilibrium path can only be interpreted *after bifurcation point* B_d, namely because of deformation w_0 in the undeflected prebuckling state, range $w_1=0\div w_0$ involves no antimetric deflection component (expounded in Section 5). By definition, the deflection mode belonging to curve S at B_d has no antimetric component. Similarly, the buckling mode corresponding to A has no *finite* antimetric component here either, namely B_d is a bifurcation point, where the amplitude of the antimetric component is of an infinitesimal undefined magnitude.

Algorithm given in Section 5 defining curve A yields bifurcation point B_d, as well as w_0 and $p^{lin}_{cr,d}$. The bifurcation point and the subsequent initial postbuckling diagram are determined by a mixed analytical-graphical method. Plane curve A obtained from

the algorithm is shifted parallel to itself to B_d, or more precisely, is started from there, then intersected by curve S. Buckling load $p_{cr,d}^{\text{lin}}$ is at the "intersection" of the two curves.

Gioncu's approach (p. 468 in [6]) to the analysis of the buckling of a spherical shell is in accordance with the foregoing. It should be stressed that diagram A is not interpreted in range $0 \div w_0$, and in fact, curve A does not intersect, but starts from S. The graphic operation of "intersecting" is a mere technical trick to simplify the practical implementation and to increase the accuracy of determining points B_d involving known exact p_{cr}^{lin} (B_0) values ([9], and Appendix). For more information see Section 5.

Essentially, instead of directly solving the basic equations [4], [19] of bifurcation in buckling form $\bar{w}$,

$$B\Delta\Delta\bar{w} - L_p(\bar{F}, w_0 + z) - L_p(F_0, \bar{w}) = 0, \tag{2.1}$$

$$\Delta\Delta\bar{F} + D(1-\mu^2)\,[L_p(\bar{w}, z) + L_p(\bar{w}, w_0)] = 0, \tag{2.2}$$

from undeflected prebuckling state deformed to w_0, we look for the eigenvalue as the coincidence of the symmetric (first) and asymmetric (second) states of equilibrium.

Besides of being much less cumbersome and more accurate in a sense, this method is also advantageous by directly producing the initial postbuckling diagram. Higher accuracy means that such an exact solution of Eqs (2.1)–(2.2) (containing nonlinear relationship $p - w_0$) as that for p_{cr}^{lin} ($w_0 = 0$) in [9] cannot generally be expected from the usual mixed analytic-numerical methods.

The curve section after bifurcation point B_d is a part of the asymmetric path of equilibrium; it is called the *postcritical* load-bearing diagram. Accordingly, the antimetric component of the postbuckling diagram has been assumed to be identical with the *dominant* term of the bifurcation buckling mode. This assumption is reasonable if only the *initial* postbuckling diagram is wanted. In structural engineering no deflections by an order of magnitude greater than the shell thickess are allowed thus analysis of this range will be abandoned.

This range would perhaps necessitate to modify the buckling mode and to increase the exactness of the nonlinear buckling theory itself.

As many terms of the antimetric components of the asymmetric equilibrium path (thus, of the buckling eigenfunction in [9]) and of its symmetric components are taken into consideration as permitted by computational facilities; in the actual case one of each (w_1 and w_2): the *dominant* term of buckling eigenfunctions in [9] (2.1)–(2.2): $\bar{w} \to w_2$ (see also Section 3) and the first term of the buckling mode in [10] ($w_0 \to w_1$).

These approximations have little effect. On the one hand, [9] showed that the buckling eigenfunction has a term which, even in the worst case, over 70 to 85% of the buckling load p_{cr}^{lin} belongs to, thus that is the dominant term. Computing with this dominant term alone leads to generally much less error than with one term for p_{cr}^{lin}. Namely now the error is referred to the *exact* p_{cr}^{lin} value, the dominant load component in some ordinate p (e.g. $p_{cr,d}^{\text{lin}}$) in Fig. 3.

On the other hand, calculating with single-term or double-term symmetric deflection modes, values of the critical snap-buckling load $\bar{p}_{cr}$ generally differ by less than 10%. Bifurcation B_d generally takes place in the initial section of diagram $p-w$, and therefore, results of calculating with a single-term and a many-term symmetric function w are still nearer to each other.

3. Bifurcation from a prebuckling state considered undeflected ($w_0 = 0$)

Statements made in the detailed discussion of this scope [9] and which will be referred to later are summarized here first.

Buckling loads are obtained by solving the eigenvalue equation

$$\mathbf{A}\bar{w} = \lambda \bar{w} \tag{3.1}$$

where

$$\lambda = \frac{E}{p_{cr}^{\text{lin}}} \tag{3.2}$$

is the eigenvalue wanted, and

$$\bar{w} = \sum_{i}^{I_0} \sum_{j}^{J_0} w_{ij} S_{ij} = \sum_{i}^{I_0} \sum_{j}^{J_0} \bar{w}_{ij} \tag{3.3}$$

is the eigenfunction for the solution by the Galerkin method. Since this is a finite series, $\bar{w}$ is theoretically the approximation of the exact eigenfunction.

Matrix **A** may be written with the aid of the real, positive definite diagonal matrix **D** and the real symmetric matrix **B**:

$$\underset{(N_0 \times N_0)}{\mathbf{A}} = \underset{(N_0 \times N_0)}{\mathbf{D}^{-1}} \cdot \underset{(N_0 \times N_0)}{\mathbf{B}},$$

$$\mathbf{D} = \langle d_{11}, d_{22}, \ldots, d_{kk}, \ldots, d_{N_0 N_0} \rangle, \tag{3.4}$$

$$N_0 = I_0 \cdot J_0.$$

Because of the general orthogonality about the weight function, matrix **B** is a *hypermatrix* with a "chessboard-like" arrangement of nonzero blocks and of their elements.

By adequately permuting rows and columns (exchange of subscripts), matrix **B** can be transformed to a *hyperdiagonal* form of four blocks: $\tilde{\mathbf{B}}$. Now the original eigenvalue problem reduces to four smaller eigenvalue problems.

This hyperdiagonal form is seen in Fig. 4. (Waveline overdash refers to the fact that $\tilde{\mathbf{B}}$ is obtained from **B** by permutation.) Each block represents a typical buckling mode. The numbers in the block elements indicate the buckling half-wave numbers (i, j) of each term of eigenfunction $\bar{w}$. Blocks underlying the calculations are simpler in form

i',j'
1,1
1,3
1,J0
3,1
3,3
3,J0
J0,J0
2,2
2,J0-1
4,2
JO-1,JO-1
2,1
2,3
2,J0
4,1
JO-1,J0
k
l
I
II
III

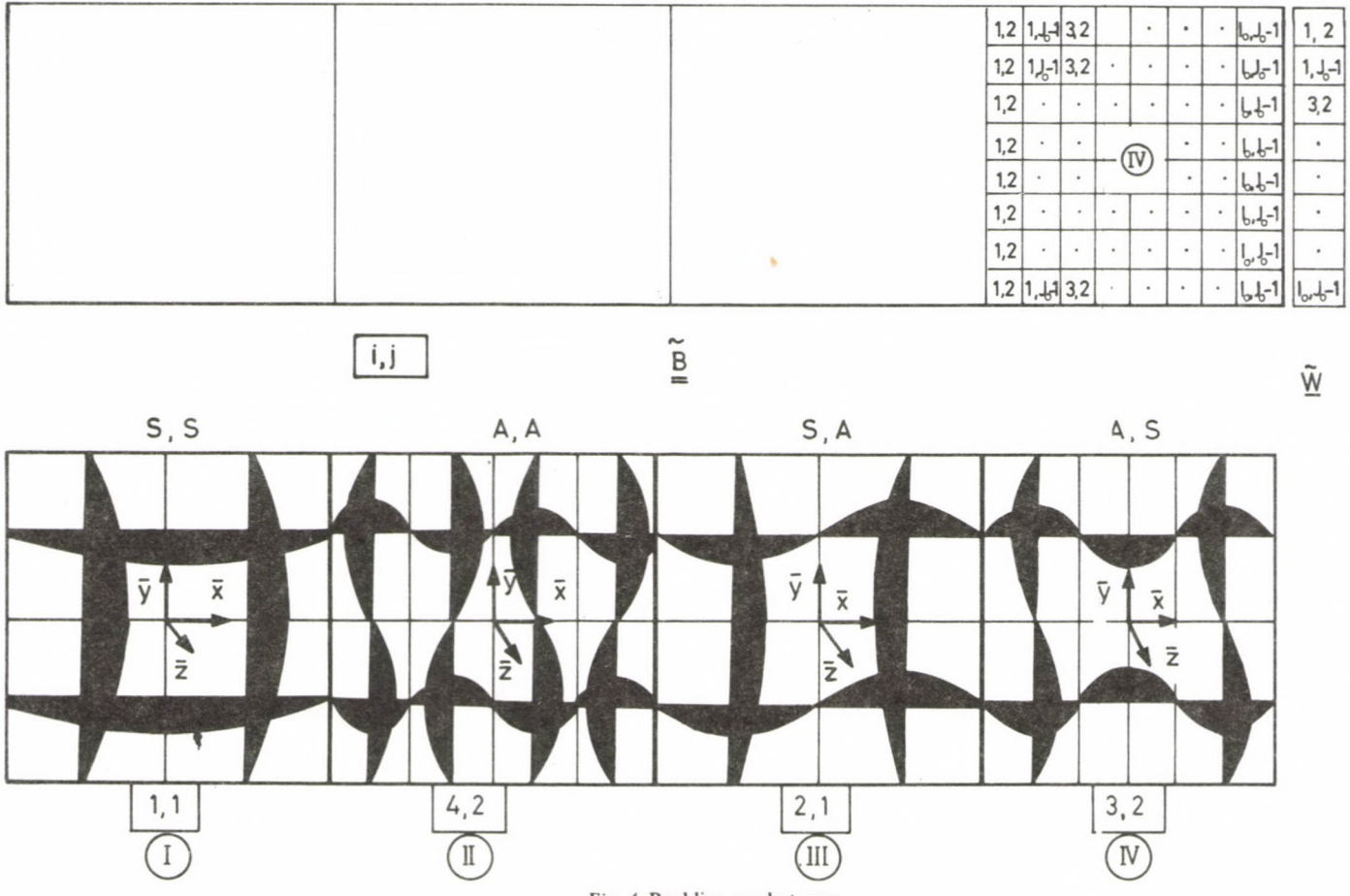

Fig. 4. Buckling mode types

than those in Fig. 4 since, as stated in [9], as a special case of the Cholesky decomposition, each of the four blocks can be symmetrized.

Let now $\tilde{\mathbf{B}}_k$ denote blocks $k = I, II, III, IV$.

$$\tilde{\mathbf{C}}_k = \tilde{\mathbf{D}}_k^{-\frac{1}{2}} \tilde{\mathbf{B}}_k \tilde{\mathbf{D}}_k^{-\frac{1}{2}} \tag{3.5}$$

$$(\tilde{\mathbf{C}}_k - \lambda \mathbf{E}_k)\mathbf{x} = 0. \tag{3.6}$$

The eigenvalues needed are obtained as the minimum of the eigenvalues of the four symmetric blocks $\tilde{\mathbf{C}}_k$.

Each of the four possible types of the buckling mode in Fig. 4 are described by the respective *dominant* buckling mode. The types consist of four combinations of symmetry (S) and antimetry (A).

It should be noted that mode I (doubly-symmetric) is of mainly theoretical significance, namely such a bifurcation occurs only in the surrounding of a seminormal shell ($\alpha = 1$) bearing loads mainly by bending forces, plate-like, thus, the corresponding buckling load is a fictitious one, not to be concerned with further.

We mention here that load parameter values

$$c_{cr}^{\text{lin}} = \frac{p_{cr}^{\text{lin}}}{E} \frac{R_x \mid R_y \mid}{h^2} \tag{3.7}$$

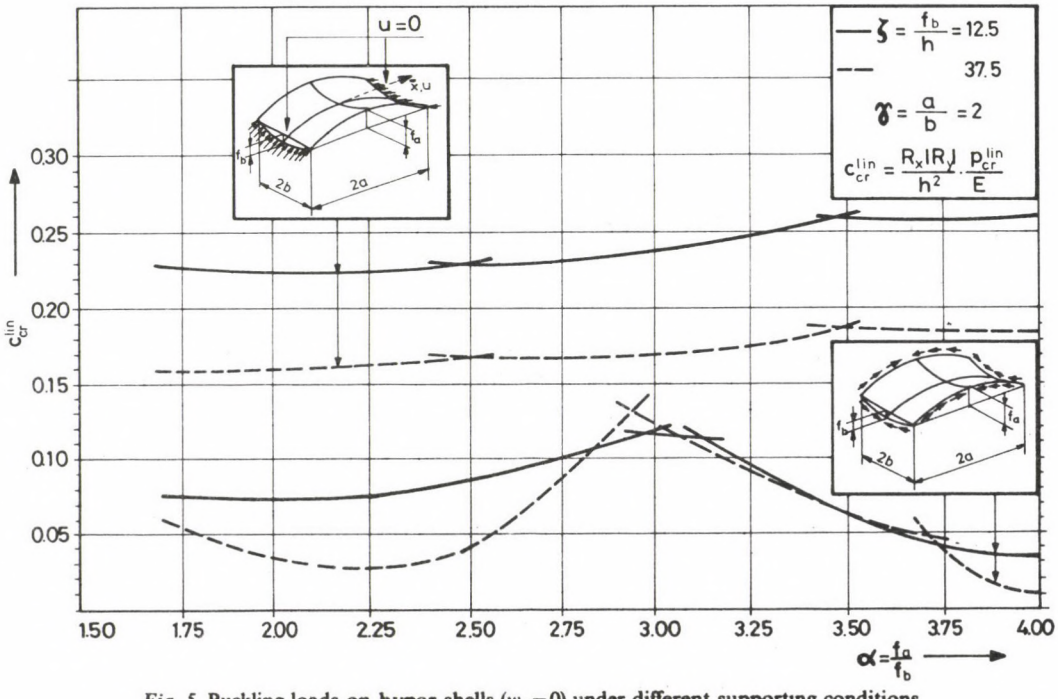

Fig. 5. Buckling loads on hypar shells ($w_0 = 0$) under different supporting conditions

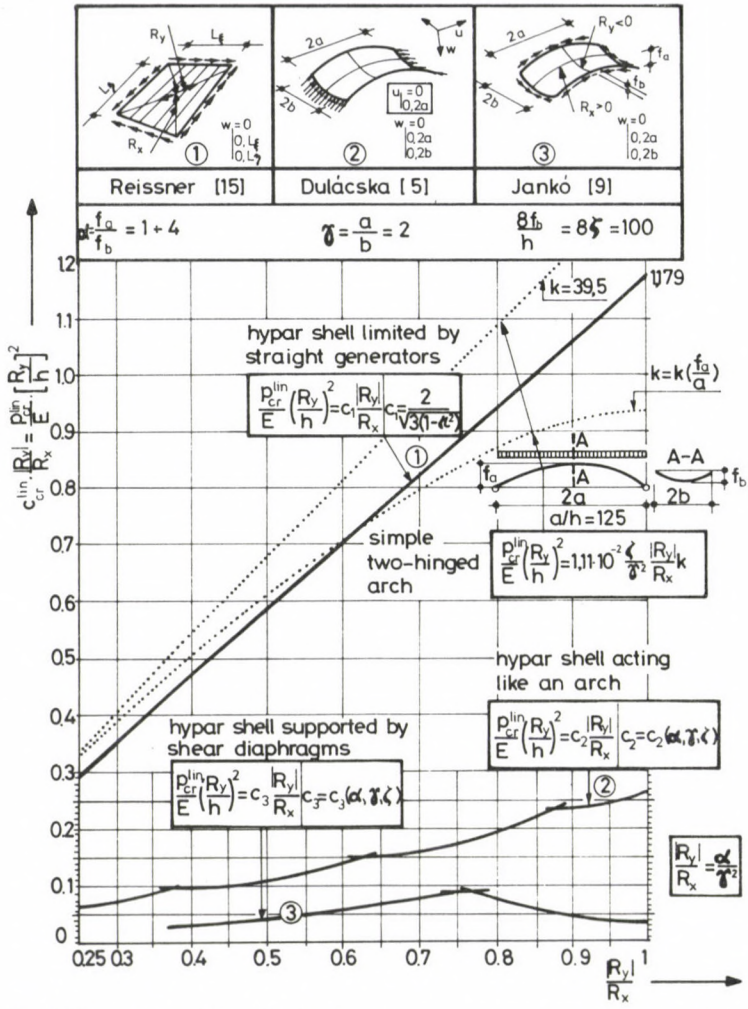

Fig. 6. Comparison of buckling loads concerning various hypar shells ($w_0 = 0$)

for loads p_{cr}^{lin} are graphically compiled in Appendix by means of the method in [9] outlined above. Computations refer to the domain of geometry parameters typical of reinforced concrete shells, in some respect (ζ) deviating from the domain of reference in [9].

Let us make some comments confirming conclusions deduced from diagrams in [9]. Namely in the meantime Dulácska has published the stability analysis of a saddle-shaped hypar shell *acting like an arch*, seen in Figs 5 and 6 [5], under the following

boundary conditions: edges $x=0, 2a$ are hinged ($u=0$), edges $y=0, 2b$ are supported by shear diaphragms. The diaphragms are rigid in the vertical plane, but soft laterally and torsionally. Displacement w is zero along the whole boundary, known to prevent inextensional deformation [13].

The table presented in [5] has been applied to produce the garland curve in top of Fig. 5. The garland curve in the bottom has been obtained by the method in [9]. The comparison of the diagrams seems to confirm the correctness of the methods in [5] and [9].

Obviously, the buckling load of the saddle-shaped hypar shell supported by shear diaphragms has to be much lower than that of one acting like an arch (with two fixed edges). Still more conclusions could be drawn by answering the question why deviations are the greatest for ratios $\alpha=4$ and 2.25?

Let us start from the statement in [9] that the *upper limit* of the buckling load of a saddle-shaped hypar shell supported by shear diaphragms is the buckling load of a shell buckling in the same mode, in so-called *homogeneous stress state* described by the middle surface forces $N_x=\text{const.}$, $N_y=N_{xy}=0$. By definition also this latter shell acts like an arch in direction x but membrane deformations are only restricted under boundary condition $w=0$. (Opposite to [5], horizontal displacement is everywhere possible.) This way of supporting is known to permit inextensional deformation [13]. According to [9], for normal shells ($\alpha=4$) and three-quarter normal-type shells ($\alpha=2.25$) *this upper limit is rather close to* the buckling load of shells supported by shear diaphragms (last paragraph in Section 4.2 in [9]), that is, from the aspect of buckling, saddle shaped shells in homogeneous stress state or supported by shear diaphragms can be considered as about equivalent. Now, since ways of supporting of shells acting like an arch in [5] and in [9] (and supported by shear diaphragms in [9]) differ by inextensional deformation *allowed* in [9] and *inhibited* in [5]. The two kinds of buckling loads exhibit maximum difference between $\alpha=4$, and $\alpha=2.25$ since shells supported by shear diaphragms are able to inextensional buckling *at a relatively low wave number* exactly for these geometrical ratios, where the minima of the garland curves in [9] are expected to be.

Calculations perfectly followed this train of thought [9]: the buckling eigenfunction corresponded to block *III* for $\alpha=4$, and to block *IV* for $\alpha=9/4$ in Fig. 4. The *dominant* terms of eigenfunctions (*III* : $i=2, j=1$; *IV* $i=3, j=2$) are exactly the deflection modes permitting inextensional deformation defined in [8].

Solutions in [5] and [9] are compared in Fig. 6 with Reissner's result for hypar shells limited by straight generators [15] free from lateral thrust.

Also the hypar shell limited by straight generators is free from lateral thrust but along the characteristic lines and not along the principal curvature arches, and the boundary condition $w=0$ *along characteristic* lines excludes inextensional deformation [13]. The hypar shell limited by straight generators buckling *with a high wave number* along the compressed principal curvature arch is seen to be much less sensitive to

instability than are saddle shells *supported along the principal curvature* arches, buckling with relatively low wave numbers.

Buckling of both saddle-shaped shells features a relatively *low buckling wave number* but ways of supporting according to [5] and to [9] produce rather different buckling loads, namely in certain cases ($\alpha = 2.25, 4$), buckling of the saddle-shape shell in [9] does not involve extension of the middle surface, but if it does, its load capacity is lower than that of a shell of hinged support in one direction.

Purely for the sake of interest, buckling loads of a two-hinged arch with geometry data of the shell disregarding shell-arch effect, etc.) where plotted in dotted line.

The upper and lower curves in dotted line show results without reckoning, and reckoning, with horizontal displacement effects, respectively (after [11] and [14]).

4. On the symmetric equilibrium path

Symmetric load bearing diagrams calculated according to the non-linear theory of second order ($p-w$) can be produced by the method in [10]. Solution relying on the two-term deflection mode w and the two-term stress function F was discussed in [10].

Well, since bifurcation from a deformed prebuckling state usually affects the lower section of diagram $p-w$ based on symmetric w (see later in Section 6) it is often sufficient to reckon with the deflection mode

$$w = w_{i_1 j_1} * S_{i_1 j_1} . \tag{4.1}$$

In this case the relationships to produce the symmetric load bearing diagram $p-w$ (or $c-w/h$) are as follows:

$$a_1 \frac{w_{i_1 j_1}}{h} + a_2 \left(\frac{w_{i_1 j_1}}{h}\right)^2 + a_3 \left(\frac{w_{i_1 j_1}}{h}\right)^3 = \frac{\mathbf{p}}{E} \frac{R_x | R_y |}{h^2} = c , \tag{4.2}$$

$$4\alpha(\zeta\gamma)^2 a_1 = \frac{\pi^6}{3072(1-\mu^2)} i_1 j_1 (i_1^2 + \gamma^2 j_1^2)^2 + \frac{\pi^2}{4} i_1 j_1 \gamma^4 \zeta^2 \frac{(\alpha j_1^2 - i_1^2)^2}{(i_1^2 + \gamma^2 j_1^2)^2} , \tag{4.3}$$

$$4\alpha(\zeta\gamma)^2 a_2 = -\frac{\pi^2}{2} \gamma^4 \zeta i_1^2 j_1^2 \frac{\alpha j_1^2 - i_1^2}{(i_1^2 + \gamma^2 j_1^2)^2} , \tag{4.4}$$

$$4\alpha(\zeta\gamma)^2 a_3 = \frac{2\pi^2}{9} \gamma^4 i_1^3 j_1^3 \frac{1}{(i_1^2 + \gamma^2 j_1^2)^2} . \tag{4.5}$$

5. The equation of the asymmetric equilibrium path

5.1 Basic equations

The nonlinear equilibrium and compatibility differential equation system for shallow shells undergoing "limited" large deformations (Section 2) can be written as ([4]. [15], [22]):

$$B\Delta\Delta w - L_p(F, z) - L_p(F, w) - p = 0\,, \tag{5.1}$$

$$\Delta\Delta F + D(1-\mu^2)\left[L_p(w, z) + \frac{1}{2}L_p(w, w)\right] = 0\,. \tag{5.2}$$

5.2 Deflection and stress function

The Galerkin's method is known to be applicable also by assuming both deflection mode w and stress function F as sums of linear independent terms [22] (cf. e.g. [10]).

Each term of function w has to satisfy the following geometrical and statical boundary conditions of the problem:

$$w_{ij0}\,|_{\substack{x=0\\x=2a}} = 0\,, \qquad w_{ij0}\,|_{\substack{y=0\\y=2b}} = 0\,,$$
$$w''_{ij0}\,|_{\substack{x=0\\x=2a}} = 0\,, \qquad \ddot{w}_{ij0}\,|_{\substack{y=0\\y=2b}} = 0\,. \tag{5.3a–d}$$

Each term of stress function F has to satisfy the statical boundary conditions of being supported by shear diaphragms (that is the edge members are free from lateral thrust):

$$F''_{ij0}\,|_{\substack{y=0\\y=2b}} = 0, \qquad \ddot{F}_{ij0}\,|_{\substack{x=0\\x=2a}} = 0. \tag{5.4a–b}$$

Accordingly, the two functions are assumed in general as function series

$$w = \sum_{i}^{I_1}\sum_{j}^{J_1} w_{ij}\cdot S_{ij} = \sum_{i}^{I_1}\sum_{j}^{J_1} w_{ij0}\,, \tag{5.5}$$
$$i = 1, 2, 3, \ldots, I_1$$
$$j = 1, 2, 3, \ldots, J_1$$

$$F = \sum_{i}^{I_2}\sum_{j}^{J_2} F_{ij}\cdot S_{ij} = \sum_{i}^{I_2}\sum_{j}^{J_2} F_{ij0} \tag{5.6}$$
$$i = 1, 2, 3, \ldots, I_2$$
$$j = 1, 2, 3, \ldots, J_2$$

In conformity with Section 2, actual computational facilities admit series w and F to consist of two terms each. The expected error has been discussed in Section 2, while it will be seen below that reckoning with more terms would result in a very cumbersome procedure.

Thus, approximate functions w and F are:

$$w = w_1 + w_2 , \tag{5.7}$$

$$w_1 = w_{i_1 j_1 0} = w_{i_1 j_1} * S_{i_1 j_1}, \qquad w_2 = w_{i_2 j_2 0} = w_{i_2 j_2} * S_{i_2 j_2} \tag{5.8a–b}$$

$$F = F_1 + F_2 , \tag{5.9}$$

$$F_1 = F_{i_1 j_1 0} = F_{i_1 j_1} * S_{i_1 j_1}, \qquad F_2 = F_{i_2 j_2 0} = F_{i_2 j_2} * S_{i_2 j_2} \tag{5.10a–b}$$

Among the approximate functions ("Ansatz" functions) above, w_1 and F_1 are symmetric about both axes $\bar{x}\bar{z}$ and $\bar{y}\bar{z}$.

Terms w_2 and F_2 are, however, antimetric about planes $\bar{x}\bar{z}$ and/or $\bar{y}\bar{z}$. (For details see conclusion of Section 2, and discussion of four buckling types in Section 3.)

5.3 Solution by the Galerkin's method

Equations defining in general this variation of the Galerkin's method are [22]:

$$\int_0^{2a} \int_0^{2b} X S_{i'j'} \, dx \, dy = 0 , \tag{5.11}$$

$$i' = 1, 2, 3, \ldots, I_1$$

$$j' = 1, 2, 3, \ldots, J_1$$

$$\int_0^{2a} \int_0^{2b} Y S_{i'j'} \, dx \, dy = 0 . \tag{5.12}$$

$$i' = 1, 2, 3, \ldots, I_2$$

$$j' = 1, 2, 3, \ldots, J_2$$

In our case, the error function X in Eq. (5.11) is the left-hand side of the equilibrium equation (5.1) obtained by substituting Eqs (5.7) in to (5.10):

$$X = B\Delta\Delta w - L_p(F, z) - L_p(F, w) - p . \tag{5.13}$$

By analogy, error function Y in (5.12) is the left-hand side of the compatibility equation (5.2) obtained by substituting Eqs (5.7) in to (5.10):

$$Y = \Delta\Delta F + D(1-\mu^2)\left[L_p(w, z) + \frac{1}{2} L_p(w, w)\right] . \tag{5.14}$$

Performing operations in Eqs (5.11) and (5.12) yields the non-linear algebraic equation system:

$$a_{11}\frac{w_{i_1j_1}}{h}+a_{12}\frac{w_{i_1j_1}}{h}\frac{F_{i_1j_1}}{E}+a_{13}\frac{w_{i_2j_2}}{h}\frac{F_{i_2j_2}}{E}+a_{14}\frac{w_{i_1j_1}}{h}\frac{F_{i_2j_2}}{E}+$$

$$+a_{15}\frac{w_{i_2j_2}}{h}\frac{F_{i_1j_1}}{E}+a_{16}\frac{F_{i_1j_1}}{E}+a_{17}\frac{P}{E} \qquad =0,$$

$$a_{21}\frac{w_{i_2j_2}}{h}+a_{22}\frac{w_{i_1j_1}}{h}\frac{F_{i_1j_1}}{E}+a_{23}\frac{w_{i_2j_2}}{h}\frac{F_{i_2j_2}}{E}+a_{24}\frac{w_{i_1j_1}}{h}\frac{F_{i_2j_2}}{E}+ \qquad (5.15a\text{–}d)$$

$$+a_{25}\frac{w_{i_2j_2}}{h}\frac{F_{i_1j_1}}{E}+a_{26}\frac{F_{i_2j_2}}{E}+a_{27}\frac{P}{E} \qquad =0,$$

$$a_{31}\frac{F_{i_1j_1}}{E}+a_{32}\frac{w_{i_1j_1}}{h}+a_{33}\left(\frac{w_{i_1j_1}}{h}\right)^2+a_{34}\frac{w_{i_1j_1}}{h}\frac{w_{i_2j_2}}{h}+a_{35}\left(\frac{w_{i_2j_2}}{h}\right)^2=0,$$

$$a_{41}\frac{F_{i_2j_2}}{E}+a_{42}\frac{w_{i_2j_2}}{h}+a_{43}\left(\frac{w_{i_1j_1}}{h}\right)^2+a_{44}\frac{w_{i_1j_1}}{h}\frac{w_{i_2j_2}}{h}+a_{45}\left(\frac{w_{i_2j_2}}{h}\right)^2=0.$$

which, of course, is formally identical to equation system (3.21a–d) derived in [10], so in the following, many of relevant relationships in [10] can be adopted.

Namely, because of antimetry, some of the coefficients $a_{11}, a_{12}, \ldots, a_{44}, a_{45}$ are zero (general orthogonality) and the others equal Eqs (3.22a–z) in [10].

To ease recognition of zeroed terms, we present Tables Ia and Ib compiled from the details of the Galerkin's orthogonalization procedure for (5.11) and (5.12). These tables are momentarily irrespective of whether the basic equations of the symmetric equilibrium path in [10] or those of the actual asymmetric one are to be derived. Operations prescribed in Table I lead to the integral expressions:

$$\left.\begin{aligned}
&\int_0^{2a}\int_0^{2b} S^n_{i_2j_2}\,dx\,dy=0, \quad n=1,3,\ldots\\
&\int_0^{2a}\int_0^{2b} S^2_{i_1j_1}S_{i_2j_2}\,dx\,dy=0,\\
&\int_0^{2a}\int_0^{2b} C_{i_1j_1}C_{i_2j_2}S_{i_1j_1}\,dx\,dy=0,\\
&\int_0^{2a}\int_0^{2b} C^2_{i_1j_1}S_{i_2j_2}\,dx\,dy=0,\\
&\int_0^{2a}\int_0^{2b} C^2_{i_2j_2}S_{i_2j_2}\,dx\,dy=0.
\end{aligned}\right\}\quad \text{if either } i_2 \text{ or } j_2 \text{ is even}$$

With the above integral expressions we obtain the following coefficients assuming zero in (5.15a–d):

$$a_{14}=a_{15}=a_{22}=a_{23}=a_{27}=a_{34}=a_{43}=a_{45}=0\,. \tag{5.16a–g}$$

Finally, the complete system of coefficients is compiled in Table II. Nonzero terms are identical to coefficients in (3.22a–z) [10].

Now, let us express $F_{i_1j_1}/E$ from row c and $F_{i_2j_2}/E$ from row d of (5.15a–d) (making use of (5.16a–g). Substituting them into rows a) and b) leads to two equations where $w_{i_1j_1}$ and $w_{i_2j_2}$ are unknown if p is known:

$$A_0\frac{w_{i_1j_1}}{h}+B_0\left(\frac{w_{i_1j_1}}{h}\right)^2+C_0\left(\frac{w_{i_1j_1}}{h}\right)^3+D_0\frac{w_{i_1j_1}}{h}\left(\frac{w_{i_2j_2}}{h}\right)^2+E_0\left(\frac{w_{i_2j_2}}{h}\right)^2+\frac{P}{E}=0\,,$$

$$\left[A_{00}+B_{00}\frac{w_{i_1j_1}}{h}+C_{00}\left(\frac{w_{i_1j_1}}{h}\right)^2+D_{00}\left(\frac{w_{i_2j_2}}{h}\right)^2\right]\left(\frac{w_{i_2j_2}}{h}\right)=0\,. \tag{5.17a–b}$$

The coefficients in the above equations assume the form:

$$A_0=\frac{1}{a_{17}a_{31}}[a_{11}a_{31}-a_{16}a_{32}]\,,$$

$$B_0=\frac{-1}{a_{17}a_{31}}[a_{12}a_{32}+a_{16}a_{33}]\,,$$

$$C_0=\frac{-1}{a_{17}a_{31}}a_{12}a_{33}\,, \tag{5.18a–e}$$

$$D_0=\frac{-1}{a_{17}a_{31}}\left[a_{12}a_{35}+\frac{a_{13}a_{31}a_{44}}{a_{41}}\right],$$

$$E_0=\frac{-1}{a_{17}a_{31}}\left[a_{16}a_{35}+\frac{a_{13}a_{31}a_{42}}{a_{41}}\right],$$

$$A_{00}=a_{21}-\frac{a_{26}a_{42}}{a_{41}}\,,$$

$$B_{00}=-\frac{a_{24}a_{42}}{a_{41}}-\frac{a_{25}a_{32}}{a_{31}}-\frac{a_{26}a_{44}}{a_{41}}\,, \tag{5.19a–d}$$

$$C_{00}=-\frac{a_{24}a_{44}}{a_{41}}-\frac{a_{25}a_{33}}{a_{31}}\,,$$

$$D_{00}=-\frac{a_{25}a_{35}}{a_{31}}\,.$$

The analysis of Eqs (5.17a–b) leads to the following conclusions:

(a) Two-variable function (5.17a) of amplitudes $w_{i_1j_1}$ and $w_{i_2j_2}$ can be represented as a surface where plane sections $w_{i_1j_1}=$const. are second-degree parabolae with a

Table Ia

$$\int_0^{2a}\int_0^{2b} g_k S_{i_1 j_1}\,dx\,dy = I_k$$

k	g_k	I_k
1	$B\Delta\Delta w$	$a_{11}\dfrac{w_{i_1 j_1}}{h}$
2	$-L_p(F_1, w_1)$	$a_{12}\dfrac{w_{i_1 j_1}}{h}\dfrac{F_{i_1 j_1}}{E}$
3	$-L_p(F_2, w_2)$	$a_{13}\dfrac{w_{i_2 j_2}}{h}\dfrac{F_{i_2 j_2}}{E}$
4	$-L_p(F_2, w_1)$	$a_{14}\dfrac{w_{i_1 j_1}}{h}\dfrac{F_{i_2 j_2}}{E}$
5	$-L_p(F_1, w_2)$	$a_{15}\dfrac{w_{i_2 j_2}}{h}\dfrac{F_{i_1 j_1}}{E}$
6	$-L_p(F, z)$	$a_{16}\dfrac{F_{i_1 j_1}}{E}$
7	$-p$	$a_{17}\dfrac{p}{E}$
8	$\Delta\Delta F$	$a_{31}\dfrac{F_{i_1 j_1}}{E}$
9	$D(1-\mu^2)L_p(w, z)$	$a_{32}\dfrac{w_{i_1 j_1}}{h}$
10	$D(1-\mu^2)\dfrac{1}{2}L_p(w_1, w_1)$	$a_{33}\left(\dfrac{w_{i_1 j_1}}{h}\right)^2$
11	$D(1-\mu^2)L_p(w_1, w_2)$	$a_{34}\dfrac{w_{i_1 j_1}}{h}\dfrac{w_{i_2 j_2}}{h}$
12	$D(1-\mu^2)\dfrac{1}{2}L_p(w_2, w_2)$	$a_{35}\left(\dfrac{w_{i_2 j_2}}{h}\right)^2$

horizontal tangent at $w_{i_1 j_1}=0$, symmetric about plane $w_{i_2 j_2}=0$ (curves G in Fig. 2b). These parabolae fit plane curve S defined by Eq. (5.17a) for the case $w_{i_2 j_2}=0$. Irrespective of a proportionality factor, the equation obtained in this way is identical to Eq. (4.2) for the symmetric equilibrium path involving a single-term deflection component. We need not use the surface itself, since the ratio of amplitudes $w_{i_1 j_1}$ to $w_{i_2 j_2}$ is defined by Eq. (5.17b), thus, Eqs (5.17a–b) define *space curve* A_{sp} in Fig. 2, describing the *postbuckling equilibrium path*. Equation (5.17b) is illustrated by plane curve L in Fig. 2b, arising from starting point w_0 of bifurcation, and having another zero point along axis $w_{i_1 j_1}$ (this bifurcation possibility for very large deflections $w_{i_1 j_1}$ is omitted from the diagram).

(b) $w_{i_2 j_2}=0$ is also a solution of Eq. (5.17b) leading to curve S mentioned under *a* (which can be obtained also according to Section 4). We point out that curve S presented in Section 6 was determined not by algorithm (Eq. (4.2)) based on the above-mentioned single-term symmetric deflection component but by the more exact one with two terms introduced in [10].

Table Ib

$$\int_0^{2a}\int_0^{2b} g_k S_{i_2 j_2} dx dy = I_k$$

k	g_k	I_k
1	$B\Delta\Delta w$	$a_{21}\dfrac{w_{i_2 j_2}}{h}$
2	$-L_p(F_1, w_1)$	$a_{22}\dfrac{w_{i_1 j_1}}{h}\dfrac{F_{i_1 j_1}}{E}$
3	$-L_p(F_2, w_2)$	$a_{23}\dfrac{w_{i_2 j_2}}{h}\dfrac{F_{i_2 j_2}}{E}$
4	$-L_p(F_2, w_1)$	$a_{24}\dfrac{w_{i_1 j_1}}{h}\dfrac{F_{i_2 j_2}}{E}$
5	$-L_p(F_1, w_2)$	$a_{25}\dfrac{w_{i_2 j_2}}{h}\dfrac{F_{i_1 j_1}}{E}$
6	$-L_p(F, z)$	$a_{26}\dfrac{F_{i_2 j_2}}{E}$
7	$-p$	$a_{27}\dfrac{p}{E}$
8	$\Delta\Delta F$	$a_{41}\dfrac{F_{i_2 j_2}}{E}$
9	$D(1-\mu^2)L_p(w, z)$	$a_{42}\dfrac{w_{i_2 j_2}}{h}$
10	$D(1-\mu^2)\dfrac{1}{2}L_p(w_1, w_1)$	$a_{43}\left(\dfrac{w_{i_1 j_1}}{h}\right)^2$
11	$D(1-\mu^2)L_p(w_1, w_2)$	$a_{44}\dfrac{w_{i_1 j_1}}{h}\dfrac{w_{i_2 j_2}}{h}$
12	$D(1-\mu^2)\dfrac{1}{2}L_p(w_2, w_2)$	$a_{45}\left(\dfrac{w_{i_2 j_2}}{h}\right)^2$

(c) It follows from the statements on curve L that $w_{i_2 j_2}$ is a *complex number* in range $w_{i_1 j_1} = 0 \div w_0$, that is, $w_{i_2 j_2}$ is not interpreted here. The heavy-line part of curve S in Fig. 2 is valid here. Solving the expression in square brackets of Eq. (5.17b) for $w_{i_2 j_2}$ and substituting the obtained relationship into (5.17a) yields equation for plane curve A in Fig. 2b:

$$A + B\frac{w_{i_1 j_1}}{h} + C\left(\frac{w_{i_1 j_1}}{h}\right)^2 + D\left(\frac{w_{i_1 j_1}}{h}\right)^3 = -\frac{p}{E}, \tag{5.20}$$

where

$$A = \frac{-p_{cr}^{\text{lin}}}{E},$$

$$B = A_0 - \frac{A_{00}D_0 + B_{00}E_0}{D_{00}}, \tag{5.21a–d}$$

Table II. Coefficients of the non-linear equation system (5.15a–d)

$$a_{i_1 j_1} = \frac{1}{(i_1^2+\gamma^2 j_1^2)^2}, \quad b_{i_1 j_1} = \alpha j_1^2 - i_1^2, \quad c_{i_1 j_1 i_2 j_2} = \frac{i_2^2 j_2^2 [i_1^2 j_1^2 - 2(i_1^2 j_2^2 + i_2^2 j_1^2)]}{i_1 j_1 (4i_2^2 - i_1^2)(4j_2^2 - j_1^2)}, \quad a_{i_2 j_2} = \frac{1}{(i_2^2+\gamma^2 j_2^2)^2}, \quad b_{i_2 j_2} = \alpha j_2^2 - i_2^2$$

$a_{11} = \frac{\pi^4}{192(1-\mu^2)} \frac{Ebh}{\beta^3} \frac{1}{a_{i_1 j_1}}$	$a_{12} = -\frac{2}{3}\pi^2 \frac{Eh}{ab} i_1 j_1$	$a_{13} = 2\pi^2 \frac{Eh}{ab} c_{i_1 j_1 i_2 j_2}$	$a_{14} = 0$	$a_{15} = 0$
			$a_{16} = \frac{\pi^2}{2} \frac{Ef_b}{ab} b_{i_1 j_1}$	$a_{17} = -\frac{16}{\pi^2} Eab \frac{1}{i_1 j_1}$
$a_{21} = \frac{\pi^4}{192(1-\mu^2)} \frac{Ebh}{\beta^3} \frac{1}{a_{i_2 j_2}}$	$a_{22} = 0$	$a_{23} = 0$	$a_{24} = a_{13}$	$a_{25} = a_{24}$
			$a_{26} = \frac{\pi^2}{2} \frac{Ef_b}{ab} b_{i_2 j_2}$	$a_{27} = 0$
$a_{31} = \frac{\pi^4}{16} \frac{Eb}{a^3} \frac{1}{a_{i_1 j_1}}$	$a_{32} = -\frac{\pi^2}{2} \frac{Eh^2 f_b}{ab} b_{i_1 j_1}$	$a_{33} = \frac{\pi^2}{3} \frac{Eh^3}{ab} i_1 j_1$	$a_{34} = 0$	$a_{35} = \frac{a_{44}}{2}$
$a_{41} = \frac{\pi^4}{16} \frac{Eb}{a^3} \frac{1}{a_{i_2 j_2}}$	$a_{42} = -\frac{\pi^2}{2} \frac{Eh^2 f_b}{ab} b_{i_2 j_2}$	$a_{43} = 0$	$a_{44} = -2\pi^2 \frac{Eh^3}{ab} c_{i_1 j_1 i_2 j_2}$	$a_{45} = 0$

$$C = B_0 - \frac{B_{00}D_0 + C_{00}E_0}{D_{00}},$$

$$D = C_0 - \frac{C_{00}D_0}{D_{00}}.$$

Equation (5.20) is the equation of the projection of space curve A_{sp} on plane $w_{i_2j_2} = 0$, describing the projection of the initial postbuckling diagram called *asymmetric* equilibrium path.

Constant A in (5.20) is obtained from

$$A = -\frac{E_0 A_{00}}{D_{00}}.$$

This constant belongs to $w_{i_1j_1} = 0$, thus, it is the buckling load p_{cr}^{lin} (with a negative sign) of the bifurcation assumed undeformed ($w_0 \approx 0$, [9]). Since it was exactly determined in [9] and in the Appendix to this paper, relationship $A = -p_{cr}^{\text{lin}}/E$ (5.21a) will be applied in the following. Thereby the projection of space curve A_{sp} defined by Eqs (5.17a–b) does not start from the approximate point B_d obtained from the equation system but is shifted "parallel" to itself to start from point B_0 for the buckling load p_{cr}^{lin}.

Shifting is done by interpreting Eq. (5.20) *temporarily* also in range $0 \div w_0$, and calculating constant A as stated above.

Postbuckling diagrams in Section 6 are produced by graphically plotting Eq. (5.20), but plane curve A *is only interpreted in range* $w_{i_1j_1} \geq w_0$ *following its intersection with curve* S (curve A in heavy-line in Fig. 2c).

The projection of the intersection is point w_0 mentioned under *(a)* involving buckling load $p_{cr,d}^{\text{lin}}$ of bifurcation from the deflected prebuckling state (B_d in Fig. 2). Thus w_0 is obtained graphically, rather than from (5.17b). By definition, deflection mode at B_d belonging to curve S has no antimetric component ($w_{i_2j_2} = 0$). As stated under *(a)*, curve A has no antimetric component of a *finite* magnitude either, since B_d is the starting point of the bifurcation where the amplitude of the antimetric component is an infinitesimal, undefined magnitude. In final account, the graphic method *is needed from practical* rather than theoretical aspects. Namely, Eq. (5.20) yields the projection of the postbuckling diagram in range $w_{i_1j_1} \geq w_0$, also point w_0 and its equivalent point $B_d(p_{cr,d}^{\text{lin}})$ can be analytically determined by this method although not at the required accuracy. Its causes are the following:

— diagram S is only described by a single-term deflection mode (inducing to apply the more accurate curves S of [10]);
— it yields constant $A(p_{cr}^{\text{lin}}, w_0 = 0)$ at a poorer accuracy than in [9] or in the Appendix to this paper.

According to the graphic method (Section 6), the slight first error is significantly reduced by using the more accurate curves S in [10] (or the corresponding algorithm). See the final statements in Section 2 (one term, two terms) in this connection.

The second error is eliminated by applying the buckling load parameters given in the Appendix.

For the error of the method describing the asymmetric equilibrium path (A) by a single term see Section 2.

6. Numerical results

Bifurcation from deformed prebuckling state, initial postbuckling (load-bearing) behaviour

Let us consider Fig. $A2$ in the Appendix presenting buckling load parameters c_{cr}^{lin} for geometric ratio $\zeta = f_b/h = 20$ relying on the method in [9] ($w_0 = 0$).

Substituting magnitudes c_{cr}^{lin} into Eq. (5.21a), the load capacity diagrams (5.20) (or their counterparts biased by ratio $R_x|R_y|/h^2$) were determined: these are the asymmetric equilibrium paths A in Figs 7 to 15. The *symmetric* component of the *asymmetric* buckling mode is characterized by the half-wave numbers $i_1 = 1, j_1 = 1$:

$$w_1 = w_{i_1 j_1} * S_{i_1 j_1}. \tag{6.1}$$

The *antimetric* component—as stated in Section 2—is the *dominant* term of the buckling eigenfunction of bifurcation assumed to be undeflected:

$$w_2 = w_{i_2 j_2} * S_{i_2 j_2}. \tag{6.2}$$

Half-wave numbers i_2 and j_2 (indicated in parentheses at each asymmetric mode curve in Figs 7 to 15) can be determined by confronting Figs A2 and 4.

Each curve section in Fig. A2 is marked by the Roman number in Fig. 4 identifying the relevant block (see also instructions in the Appendix).

The *symmetric* equilibrium path was determined by the method in [10] (see also in Section 4).

In Figs 7 to 15, the intersections of the symmetric and asymmetric equilibrium paths are indicated by small circles: these are the buckling loads $p_{cr,d}^{\text{lin}}(w_0 \neq 0)$ of bifurcation from a deflected prebuckling state. The direct neighbourhood of the bifurcation points, including part of the initial postbuckling range, are drawn in heavy line, to help recognizing the type of *bifurcation points* defined in Fig. 3.

Bifurcation points in domain $\alpha \sim 2.3 \div 3.3$ appear to be of the *unstable symmetric* type: the postbuckling load capacity *decreases*.

Bifurcation points in ranges $\alpha \sim 3.3 \div (<4)$ and $\alpha \sim 1.75 \div 2.2$ are of the *stable symmetric* type: the postbuckling load capacity *increases*.

Let us make some comments on the foregoing:

— no analyses have been made on ratios near the seminormal shells ($\alpha = 1$) since those cases are characterized either by snap-through or by plate-like increase [9], [10];
— hypar shells defined in Section 5 have *no unstable asymmetric* bifurcation point;
— for ratios $\alpha \sim 3 \div 3.5$, reckoning with deformations w_0 in prebuckling state, a critical buckling mode different from that for the assumption $w_0 = 0$ may emerge. For

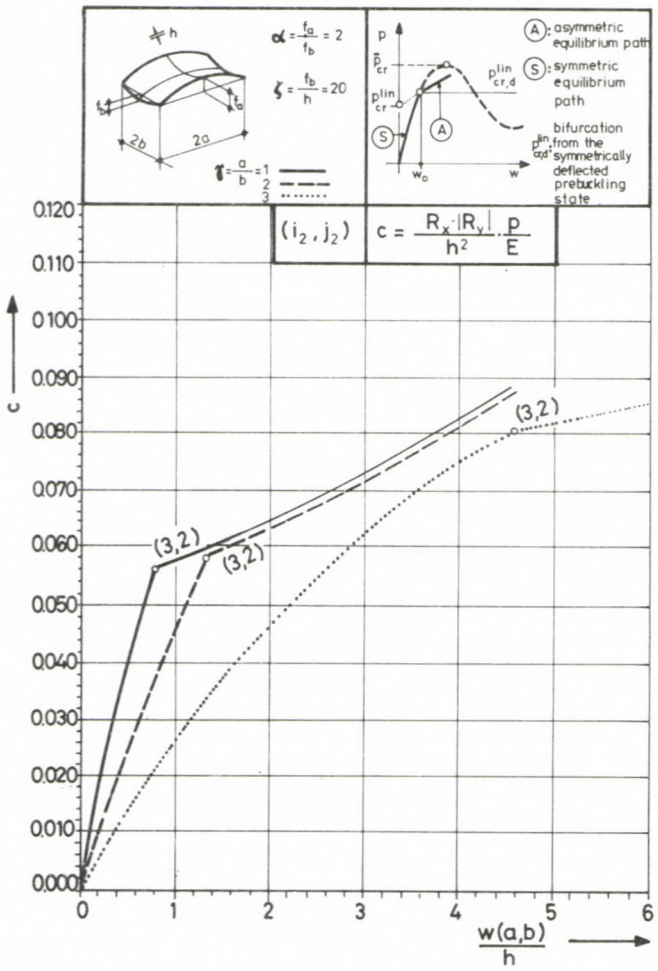

Fig. 7. Symmetric and asymmetric equilibrium paths

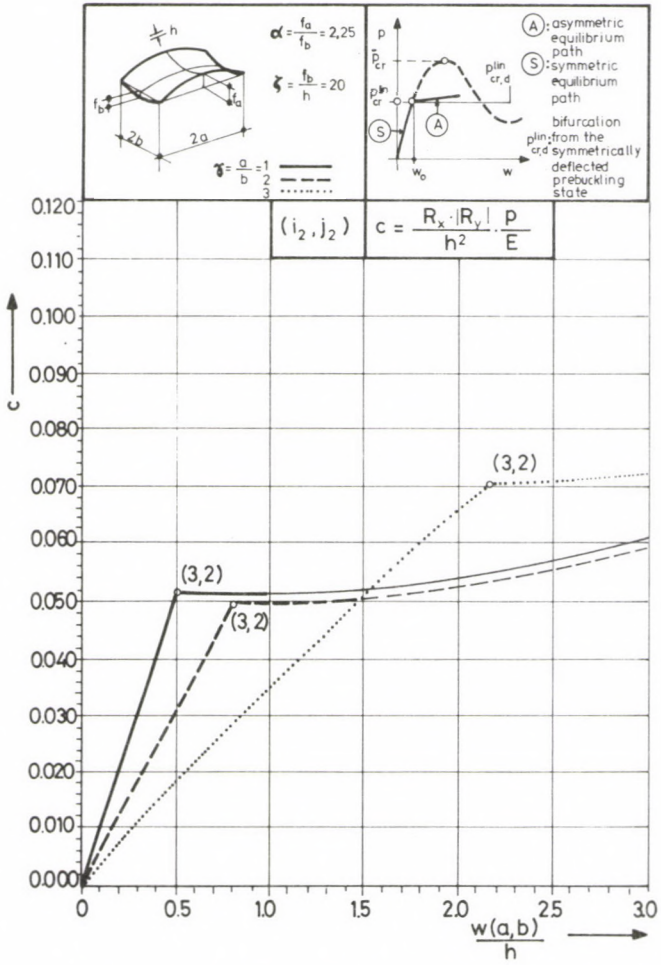

Fig. 8. Symmetric and asymmetric equilibrium paths

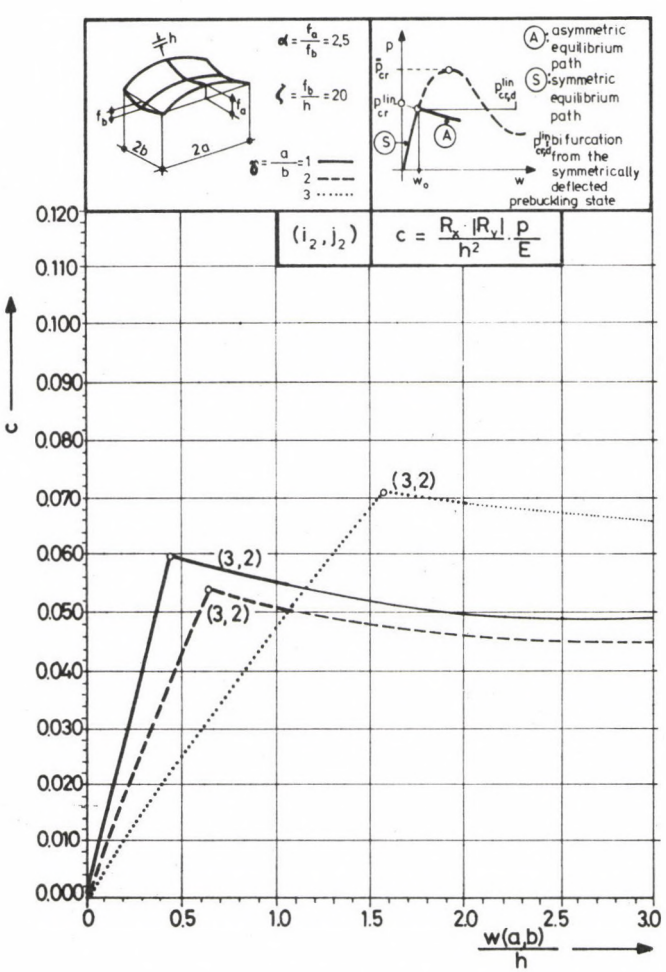

Fig. 9. Symmetric and asymmetric equilibrium paths

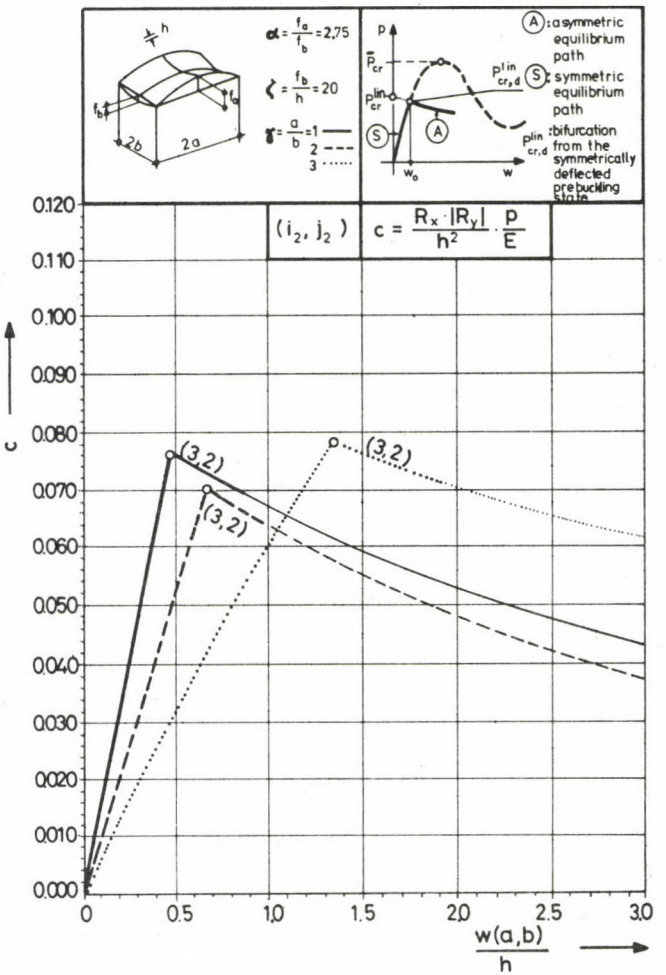

Fig. 10. Symmetric and asymmetric equilibrium paths

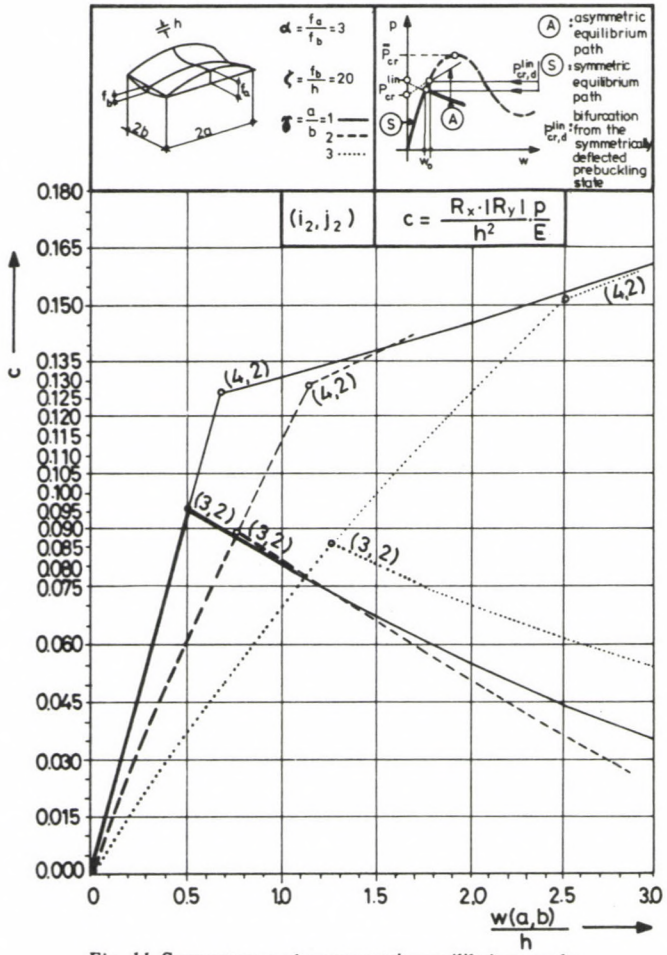

Fig. 11. Symmetric and asymmetric equilibrium paths

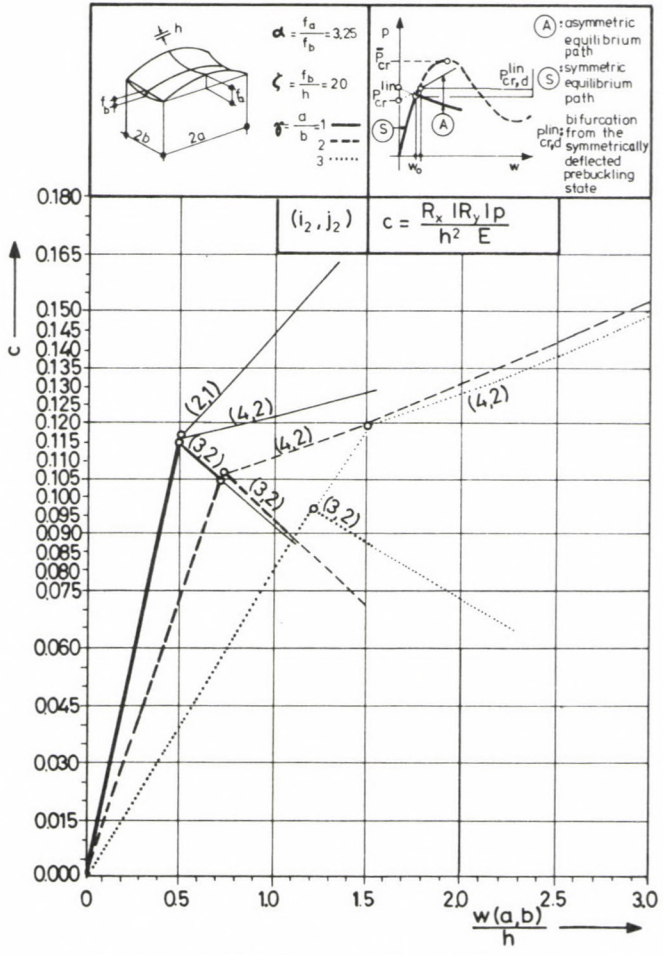

Fig. 12. Symmetric and asymmetric equilibrium paths

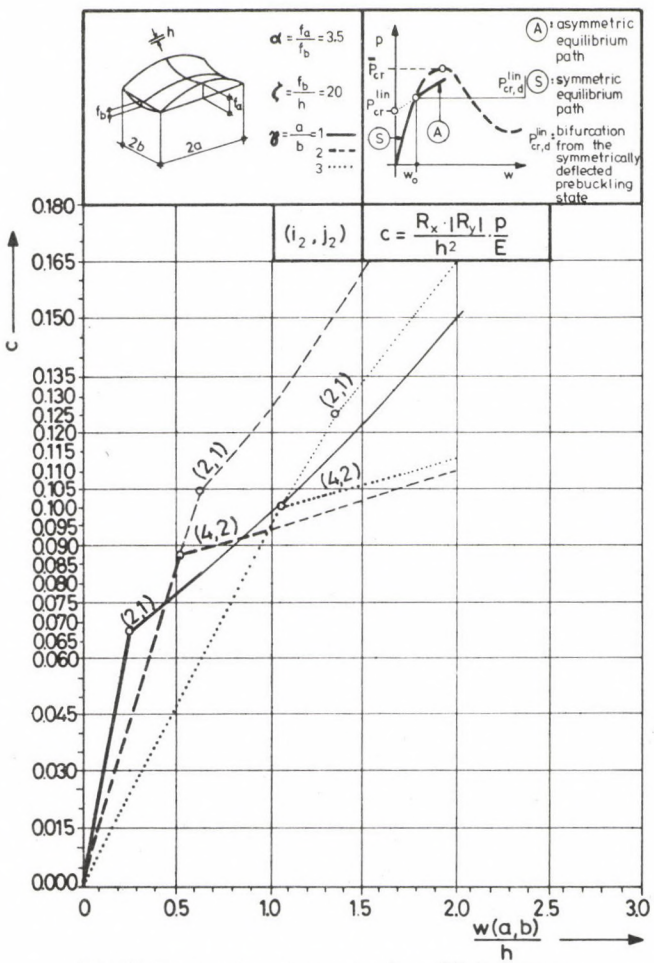

Fig. 13. Symmetric and asymmetric equilibrium paths

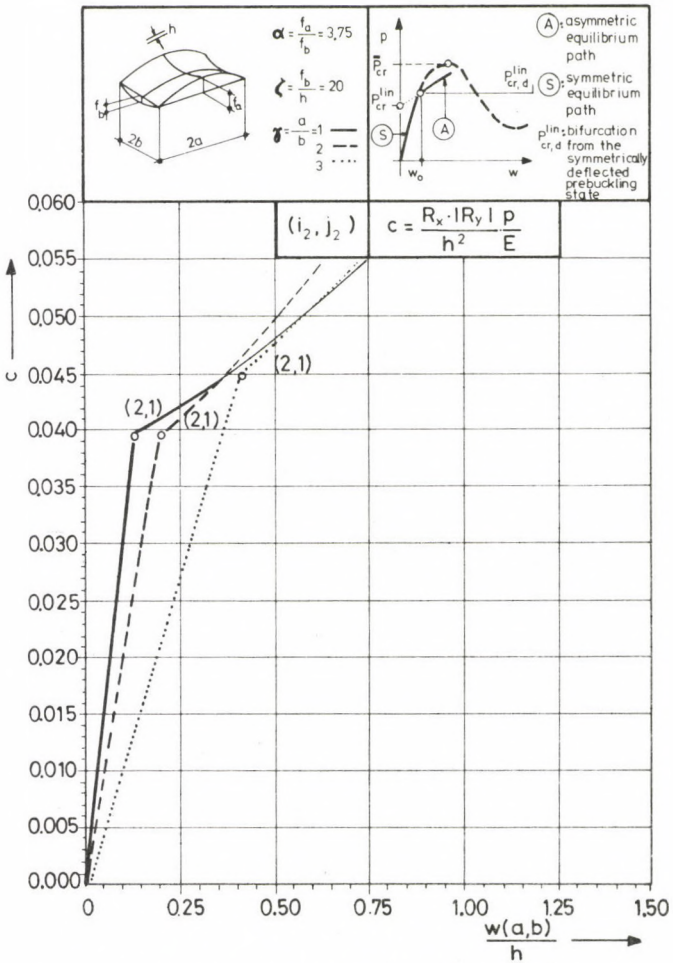

Fig. 14. Symmetric and asymmetric equilibrium paths

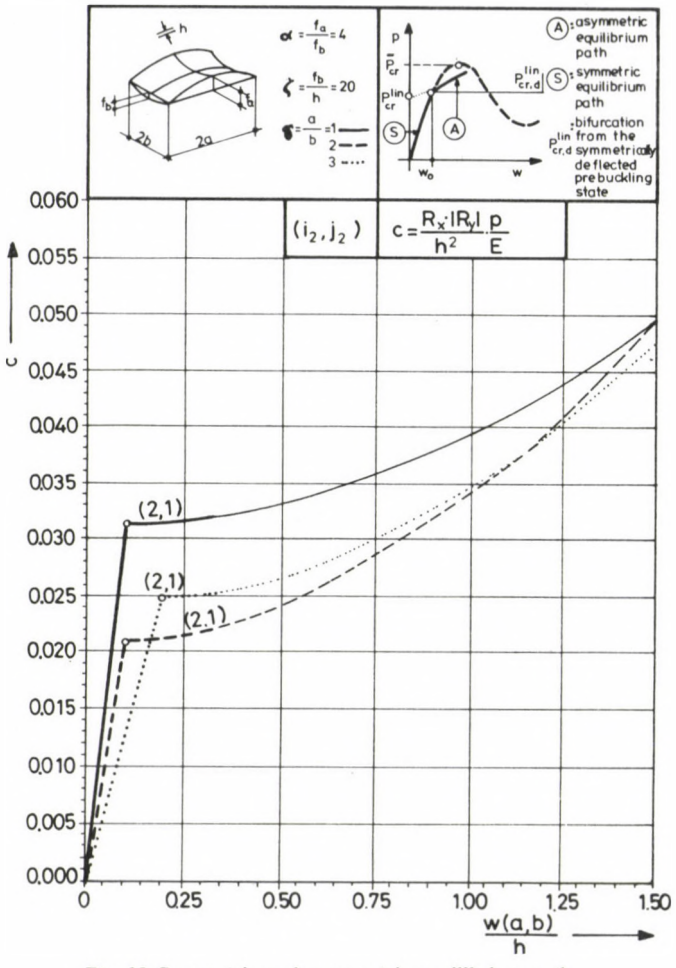

Fig. 15. Symmetric and asymmetric equilibrium paths

instance, in Fig. 11, buckling mode ($i_2=4, j_2=2$) corresponding to block *II* in Fig. 4 for $a/b=2$, $w_0=0$ is the critical one (yielding the least p_{cr}^{lin}) but taking w_0 into consideration, buckling mode for block *IV* becomes risky because of the decreasing postbuckling behaviour with increasing $w(i_2=3, j_2=2)$.

Special consideration is due to shells buckling mostly inextensionally $\alpha=2.25$ and $\alpha=4$ (Section 3). Their bifurcation points are of the *stable symmetric* type due to *plate-like* buckling. This method is obviously *the most exact* for these shells ($\alpha=4$) prevailing in practice where w_0 has little effect.

The above will be physically explained in Section 8.

7. Numerical analysis

Effect of deformations (deflections) in the prebuckling state on the buckling load ($w_0 \neq 0$, $p^{lin}_{cr,d}$)

Plotting intersections (bifurcation points $c^{lin}_{cr,d}$, $w_0 \neq 0$) marked with small circles in Figs 7 to 15 offers a possibility of comparison with garland curves in Fig. A2: Figs 16, 17, 18.

In view of deformations in the prebuckling state, buckling loads may either

decrease ($\alpha \sim 2.2 \div 3.2$),

or

increase ($\alpha \sim 3.2 \div 4$).

As before, buckling half-wave numbers of the *dominant* term of the corresponding buckling mode of the bifurcation assumed to be undeformed are written in parentheses at the curves. According to Section 2, each is an antimetric component of the asymmetric buckling mode.

With increasing side ratio a/b, the effect of deflections w_0 increases.

It should be pointed out that near the ratio $\alpha \sim 3.25$ the three curves of buckling modes *II*, *III*, *IV* have almost a common intersection. Particular attention should be

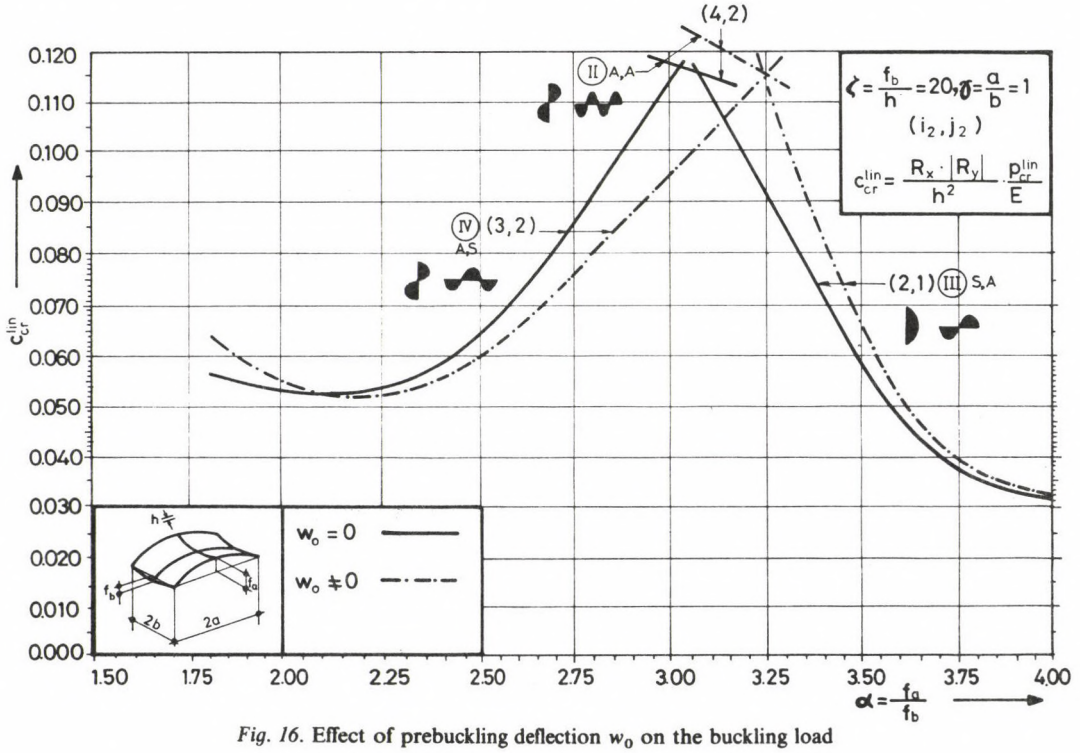

Fig. 16. Effect of prebuckling deflection w_0 on the buckling load

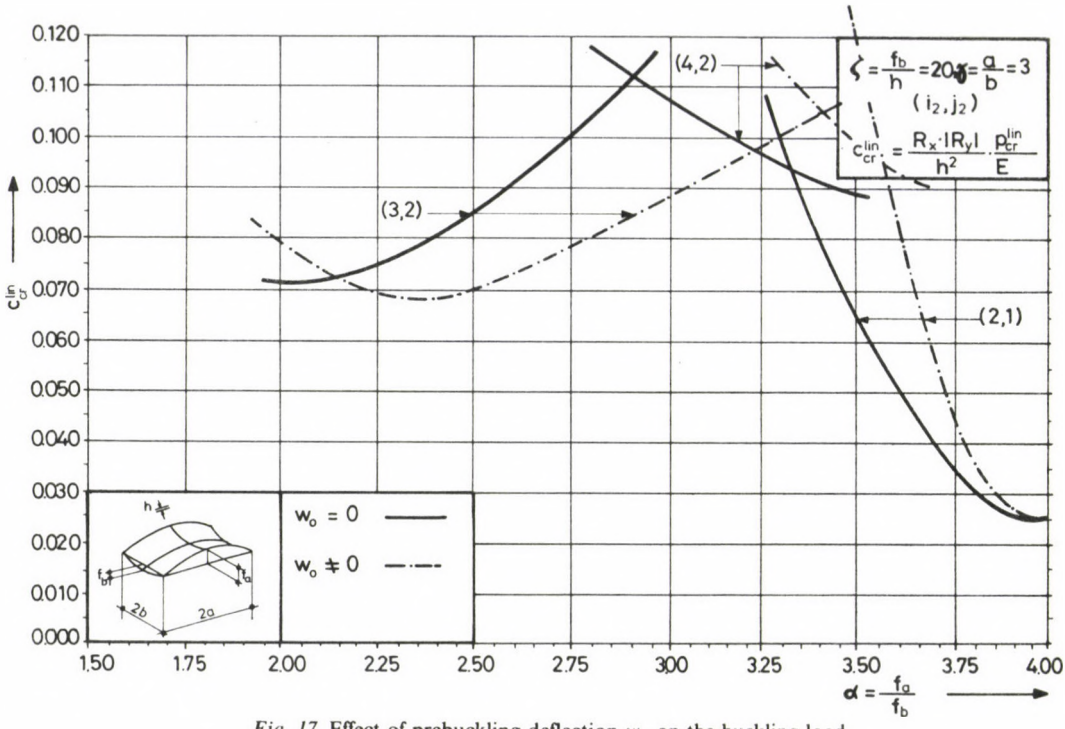

Fig. 17. Effect of prebuckling deflection w_0 on the buckling load

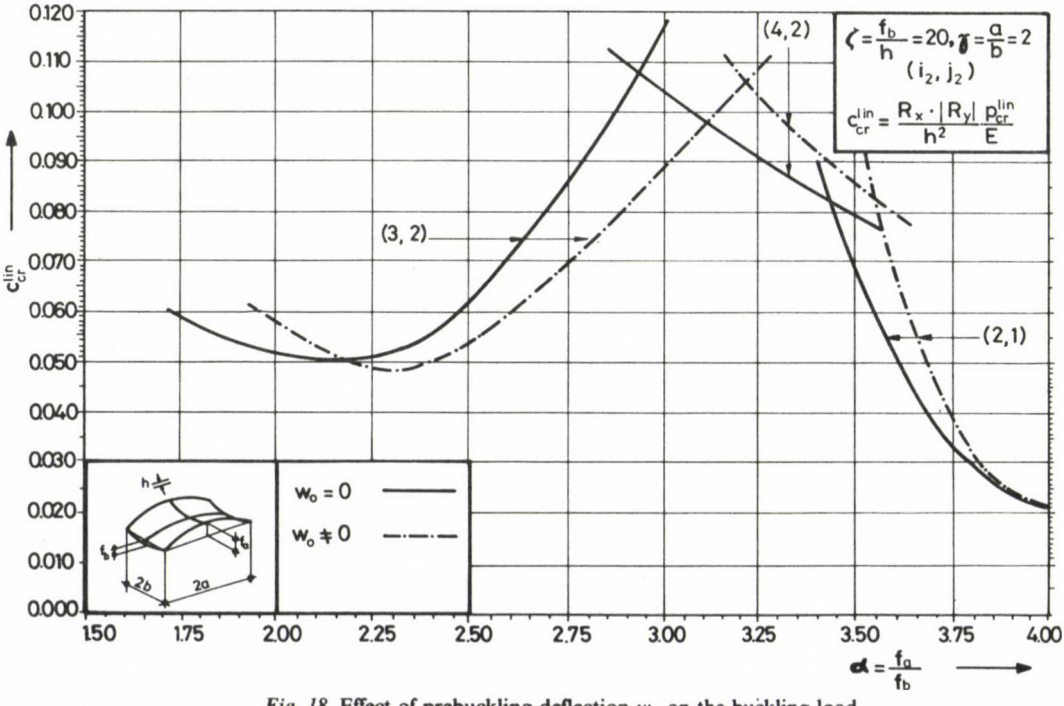

Fig. 18. Effect of prebuckling deflection w_0 on the buckling load

paid to this fact when the *geometrical imperfections* (initial eccentricities) are taken into account since under certain circumstances the closeness of the buckling loads of two, otherwise stable symmetric bifurcation points can result in a structure very sensitive to geometrical imperfections (Chapter 10 in [17]).

In the actual case the bifurcation point corresponding to the buckling mode of blocks *II* ($i=4$, $j=2$) and *III* ($i=2$, $j=1$) in Fig. 12 is stable symmetric with a postbuckling load capacity *increasing* with increasing w. Bifurcation point assigned to block *IV* ($i=3, j=2$) is unstable symmetric with a postcritical load capacity *decreasing* with increasing w.

All these facts lead to the conclusion that, properly reckoning with *geometrical imperfections*, the peak of the garland curve of buckling loads ($\alpha \sim 3$) flattens considerably. We intend to carry out research in this field in the future.

8. Comparative analysis

Let us compare first Hutchinson's [7] results on *toroidal* shells with our research on saddle-shaped hypar shells. Then we will present the approximate solution determining the character of the initial postbuckling behaviour given in [10].

Hutchinson's shell and solution method are entirely different from our ones but the results on the basis of way of looking can be compared. An element can be cut out of the toroidal shell (Fig. 19), corresponding by shape and by supporting conditions to the hypar shell in *homogeneous stress state* discussed in Section 3 and in [9], the same places where also the relationship between this latter and the effectively supported hypar shell was analyzed.

Accordingly, similarity of behaviours between the hypar shell in homogeneous stress state and the toroidal shell leads to the conclusion that certain similarities exist between the buckling or postbuckling behaviour of the hypar shells supported by shear diaphragms and of the toroidal shell. Figure 19 was adopted from Hutchinson [7] with some alteration of symbols. It is obvious from Fig. 19c that the initial postbuckling behaviour can be plate-like (horizontal tangent), decreasing or increasing. Thus, also the postbuckling behaviour of the toroidal shell features a variety like that of the saddle-shape hypar shell as seen in Fig. 3. By modifying geometric parameters e.g. increase can change to decrease etc.

Essentials of our approximate solution presented in [10] are seen in Fig. 20. Bushnell [1], Dulácska [3] and Wedellsborg [18] determined the *upper critical load* p_{cr}^{u} of *imperfect* spherical shells and cylindrical shells—because of the excessive computing labour demand—by fair approximation based on a physical approach. The approximation consisted essentially *in modifying the shell geometry* by imperfection w_k (Fig. 20a, Dulácska's approximate solution [3]) and obtaining the approximate *upper* critical loads p_{cr}^{u} by solving the eigenvalue problem of the deformed (deflected) shells (the original curvature radius R becomes R_k as a function of w_k). Dulácska [3]

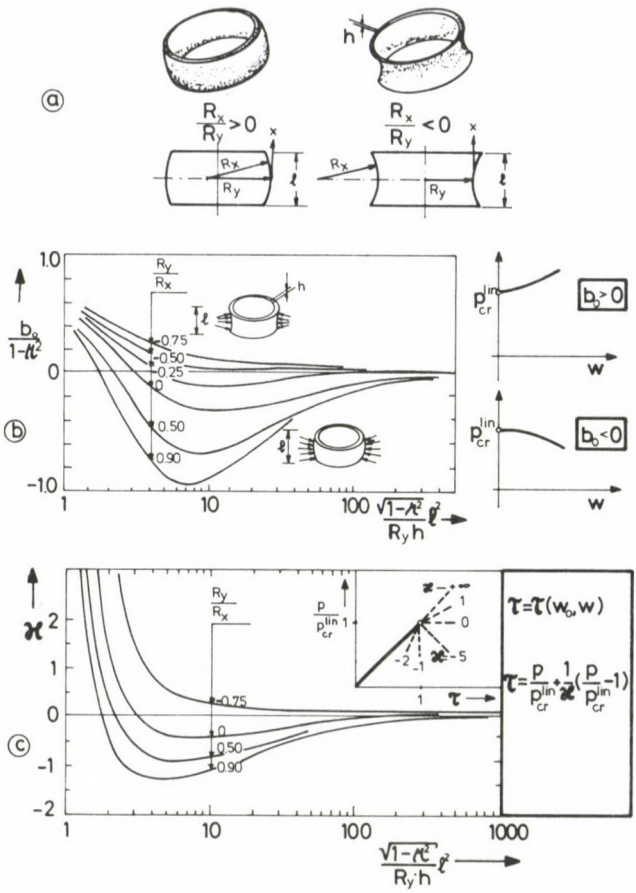

Fig. 19. Initial postbuckling behaviour of toroidal shells after Hutchinson

demonstrated that the decrease of the critical load (i.e. $p_{cr}^{lin} \rightarrow p_{cr}^{u}$) is mainly caused by imperfection and *geometrical non-linearity is only of slight effect.*

These are the fundamentals of the determination of the buckling load ($p_{cr,d}^{lin}$ in Fig. 20d) for the bifurcation phenomenon of saddle-shaped hypar shells from a deformed prebuckling state according to [10]. In our case there is no imperfection but there is deformation (deflection) w_0 in the prebuckling state. The slight effect of geometrical non-linearity is seen from diagram *S*.

Geometry parameters changed by prebuckling deformations w_0 are indicated by asterisks. Subscript *a* in symbol $\tilde{w}_{0a}$ refers to *average* deflection of the *entire* structure as distinct from deflection of the shell centre at ordinate p_{cr}^{lin}.

Let e.g. a buckling load marked *1* belong to parameter α, then *2* will belong to the smaller α^*.

Parameter ζ always increases, associated with increased load capacity. The arch in direction x becomes softer, the one in direction y becomes stiffer, with a decrease of

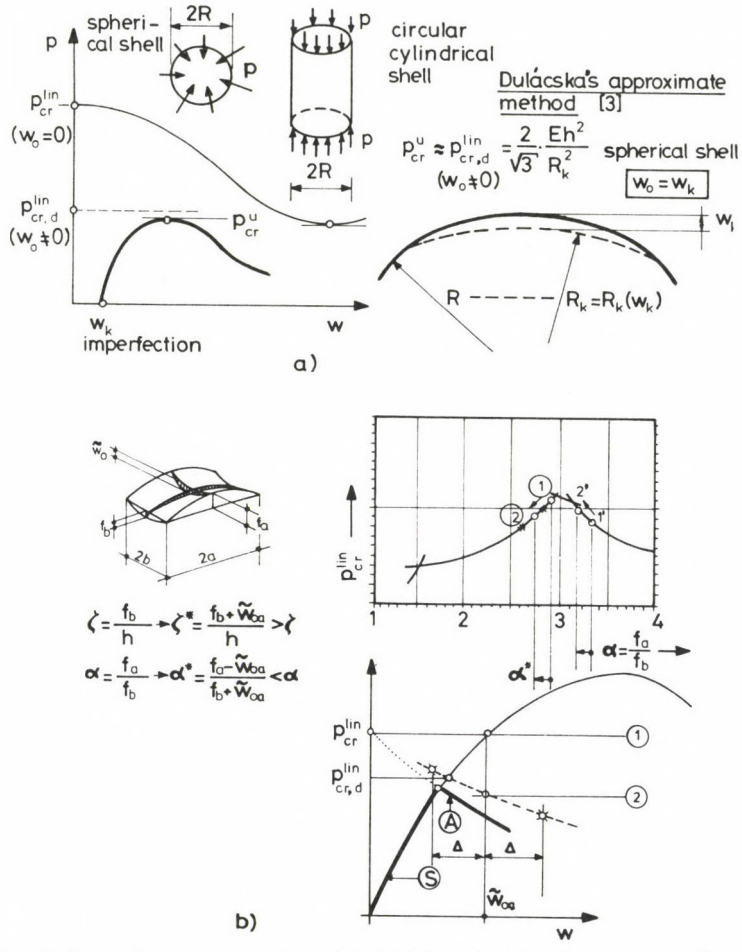

Fig. 20. Approximate construction of the initial postbuckling load capacity diagram

load capacity (*2*) as resultant of these two opposite effects. The same procedure at points $\tilde{w}_{0a} \pm \Delta$ rather close to $\tilde{w}_{0a}$ would yield the dash-line curve section in the bottom part of the figure. Its intersection with non-linear load bearing diagram S is an approximation of the buckling load $p_{cr,d}^{lin}$. The assumed exact solution is plotted in heavy line.

According to [10], this method *indicates at the same time* the type of load bearing diagrams for small postbuckling deformations. They were found in [10] to be *increasing* for about $\alpha = 3 \div 4$, and *decreasing* for about $\alpha = 2 \div 3$, in conformity with Section 6.

It should be pointed out that the approximation presented in [10] was applied to produce the postbuckling diagrams in Section 6 where buckling loads $p^{\text{lin}}_{cr,d}$ *most differed* from those obtained under condition $w_0 = 0$ (see Section 7). Ordinates of diagrams and loads $p^{\text{lin}}_{cr,d}$ obtained by the method in [10] were found to differ by less than 10% from those in Section 6 in the examined range of parameters.

The actual treatment of this problem, more detailed than justified by [10], is motivated by the fact that, although these more exact analyses *confirm the correctness* of the approximate method in [10], but the physical purport is better illustrated by the approximate solution. In fact, the form of the garland curves of the initial postbuckling loads permits to conclude on the increase or decrease of the initial postbuckling diagram. Garland curve forms were physically explained in [9] and in Section 3 in this paper.

Prebuckling deformations change the curvature conditions of the original shell form. (The arch in direction x softens, that in direction y stiffens.) Accordingly, not only the membrane load capacity ratio in direction x to y is altered but the ratio of load bearing shares of membrane to plate effect, and even the measure of the load capacity mobilized by the resultant of both effects. To follow this complex process by computation is half not so difficult in possession of the garland curves, *in the narrow surrounding* of deflection $\tilde{w}_{0a}$ assigned to p^{lim}_{cr} of symmetric $p-w$ diagram S (Fig. 20b).

Last but not least, there is no contradiction in solving a non-linear problem (postbuckling diagram) in the range of deflections sufficiently close to the bifurcation point approximately by linear buckling theory (eigenvalue retrieval). Namely, in conformity with the mentioned statement by Dulácska [3], the effect of geometrical non-linearity is *much less* than that of the shell middle surface deformation (deflection) w_0. Within a narrow domain about the bifurcation point, the geometrical non-linearity only slightly affects the value of the ordinates of the postbuckling diagram. Thus, the *non-linear terms* of this slight effect *can be omitted* from the algorithm of this non-linear problem. Since in the meantime the shell form must also be modified it becomes the eigenvalue problem of a *shell with modified geometry* compared to the original one. These considerations are confirmed by favourable findings made in numerically comparing the method in [10] and the one presented above (the difference is less then 10%).

9. Conclusions

As a continuation of our earlier research, a method has been presented for determining the *buckling load* of saddle-shaped hypar shells supported by shear diaphragms, *deformed* under symmetric, uniform loads.

The buckling load is obtained as the intersection of the symmetric and asymmetric load bearing diagrams. The *asymmetric* diagram corresponds to a deflection function which has an antimetric component too.

The analysis of the pòstbuckling section of the asymmetric load bearing diagram (equilibrium path) valid for postbuckling, *initial* so-called "limited" large deformations showed the bifurcation points to be, depending on geometry proportions, either:

a) of *stable symmetric* type

$$\alpha \sim 1.75 \div 2.2 \qquad \text{and} \qquad \alpha \sim 3.3 \div 4$$

shells with *increasing* postbuckling load capacities or

b) of *unstable symmetric* type

$$\alpha \sim 2.3 \div 3.3$$

a geometry domain with *decreasing* postbuckling load capacities.

No *unstable asymmetric* bifurcation point was found; this possibility can be excluded in hypar shells.

This method confirms the approximate method given in [10] but now, of course, the present method is suggested for application.

The garland curves for the buckling loads for the bifurcation from an undeflected assumed prebuckling state ($w_0 = 0$) are given in the Appendix.

APPENDIX

In [9] an algorithm was suggested for determining the buckling loads for the bifurcation assumed to be undeformed ($w_0 = 0$) (see also in Section 3), then it was applied to construct garland curves and finally some conclusions were drawn on the nature of the phenomenon.

These garland curves yield $1/E$ times the buckling loads (p_{cr}^{lin}/E) as a function of four parameters (α, β, γ, ρ).

From certain aspects, the representation in the form

$$c_{cr}^{\text{lin}} = \frac{p_{cr}^{\text{lin}}}{E} \frac{R_x |R_y|}{h^2} = \frac{p_{cr}^{\text{lin}}}{E} \frac{\beta^4}{4\zeta^2 \gamma^2 \alpha}$$

is *more convenient*, partly by facilitating comparison of the results with those for dome shells [12] and partly by involving a distorting transformation bringing counterparts c_{cr}^{lin} of load parameters p_{cr}^{lin}/E — differing by an order of magnitude for certain geometry proportions—significantly nearer to each other. As for the first argument, magnitude h^2 was shown to result from $\sqrt{BD}$, facilitating the application of the method by Dulácska [12] for taking reinforced concrete properties into consideration.

The tables and diagrams in the Appendix were compiled with the aid of the method presented in [9].

Now, three parameters are directly involved:

$$\alpha = \frac{f_a}{f_b}, \qquad \gamma = \frac{a}{b}, \qquad \zeta = \frac{f_b}{h}.$$

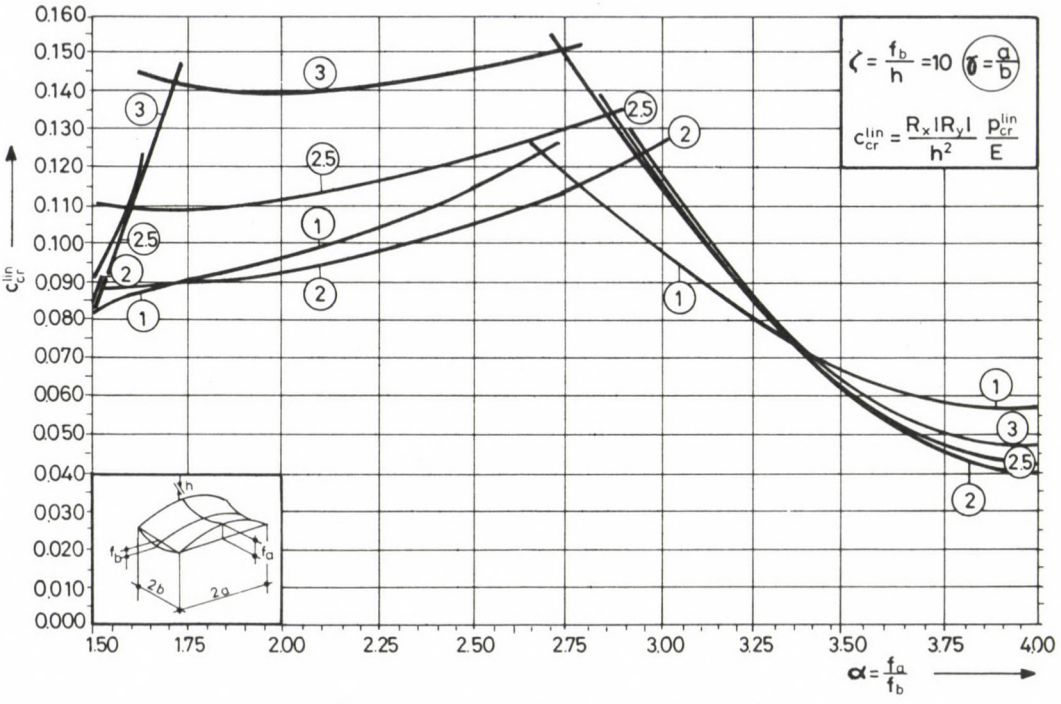

Fig. A1. Buckling load on hypar shells ($w_0 = 0$)

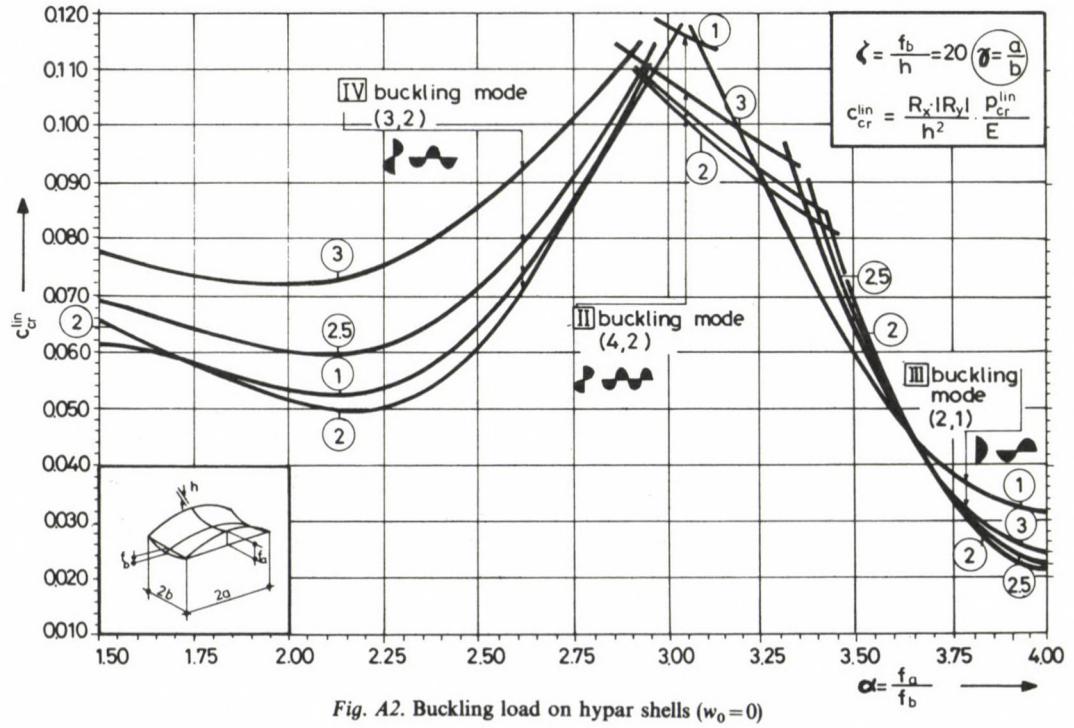

Fig. A2. Buckling load on hypar shells ($w_0 = 0$)

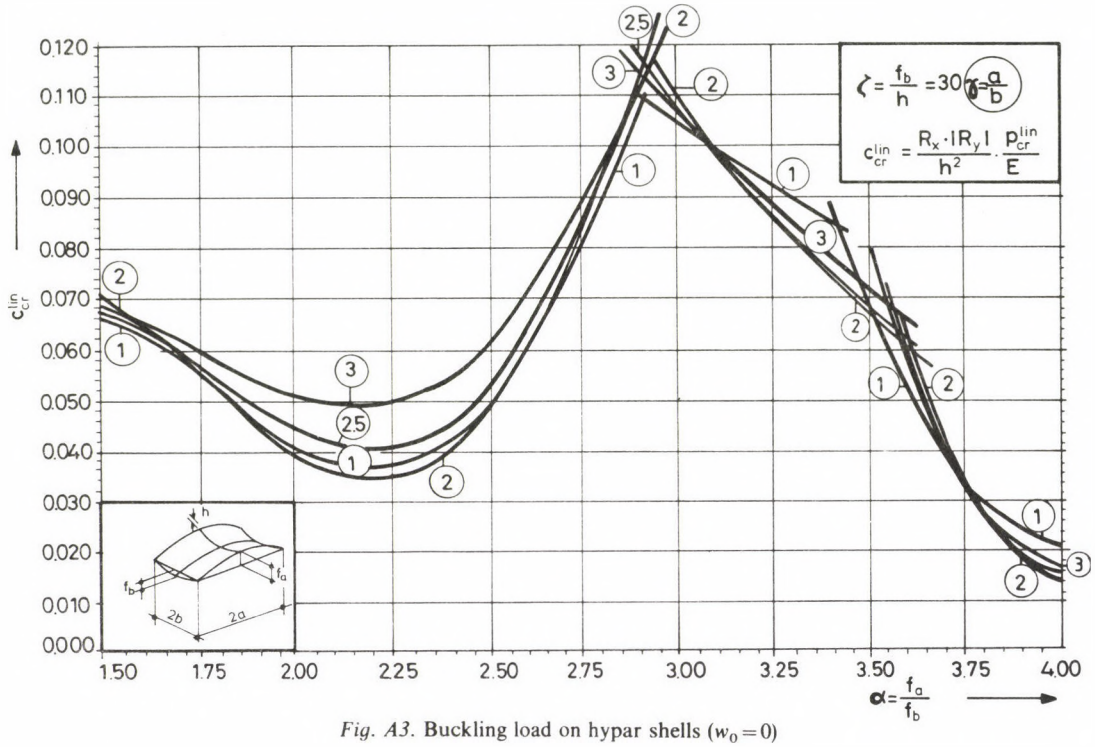

Fig. A3. Buckling load on hypar shells ($w_0 = 0$)

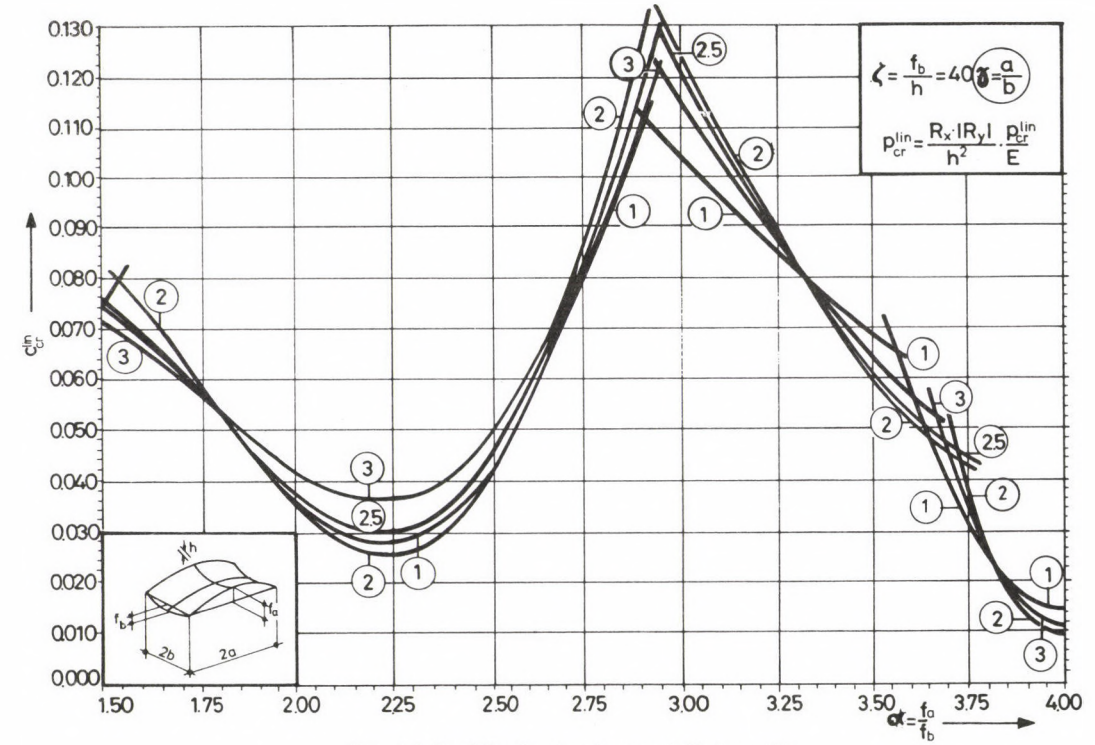

Fig. A4. Buckling load on hypar shells ($w_0 = 0$)

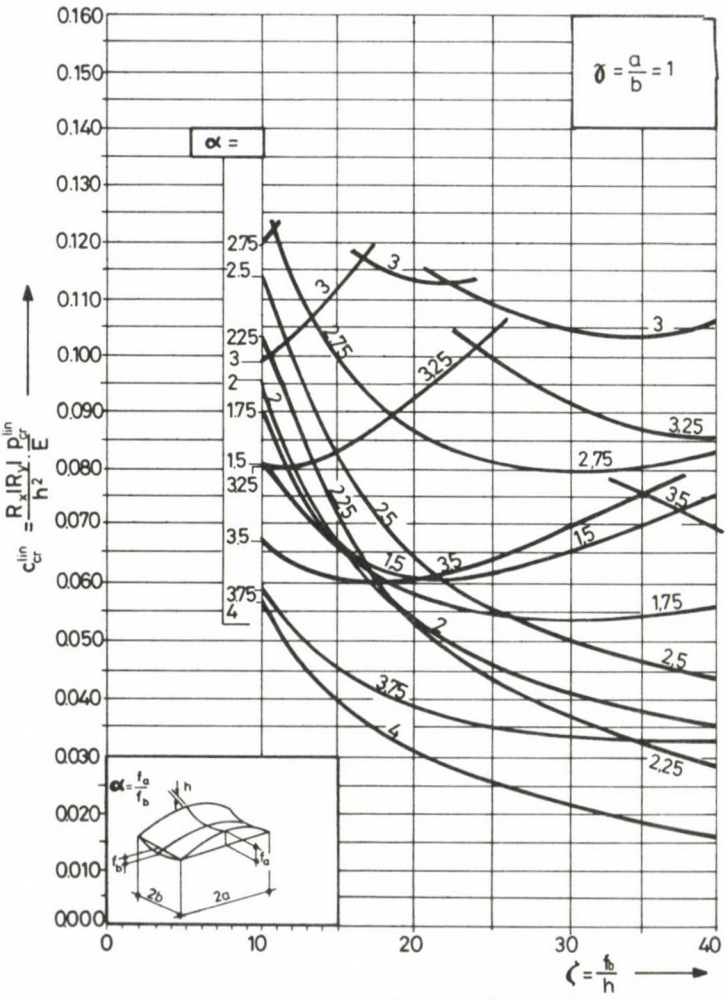

Fig. A5. Buckling load on hypar shells ($w_0 = 0$)

In conformity with the formula above, parameter β is needed only for determining the real value of the buckling load.

It should be pointed out that this practical representation involves a distorting transformation to the dependence of the real buckling load values on parameters γ and ζ, namely:

— in reality, buckling loads for $\gamma = 3$ much exceed those for $\gamma = 1$;

— with increasing parameter ζ, the buckling load increases in any case (at a difference from c_{cr}^{lin} in Figs A5 to A8). The position of the curves in Figs A1 to A4 for the four buckling modes in Fig. 4 is as follows:

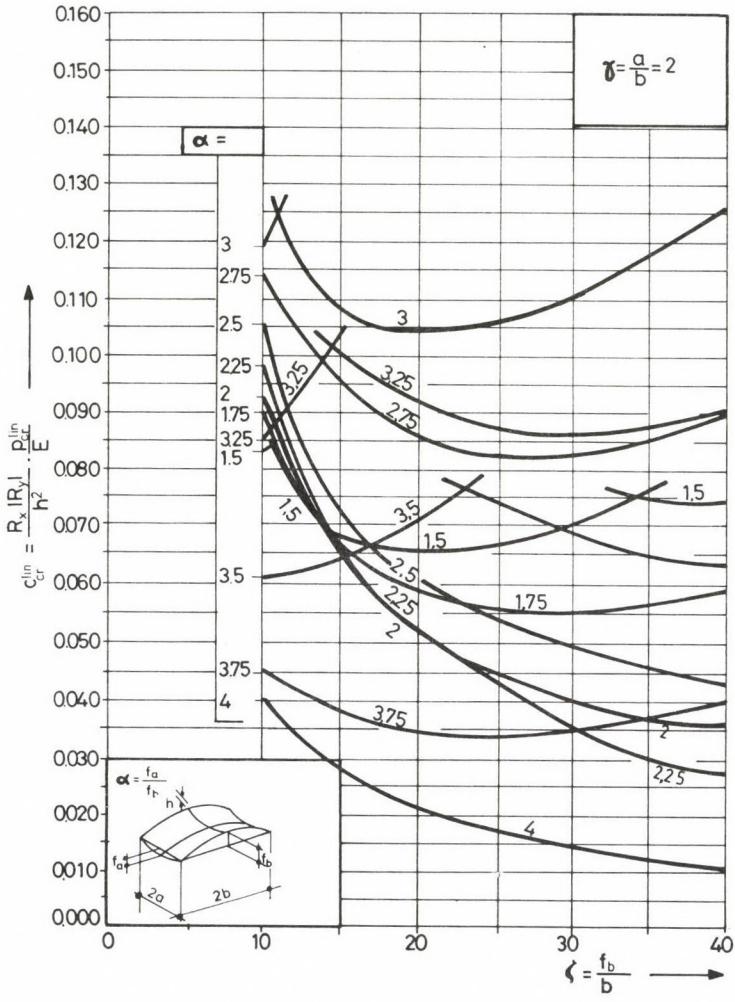

Fig. A6. Buckling load on hypar shells ($w_0 = 0$)

— Block *I*: the corresponding buckling mode is symmetrical about two axes ($\bar{x}$, $\bar{y}$), it may be critical for a ratio $\alpha \sim 1 \div 1.75$.

— Block *II*: sited between buckling modes corresponding to blocks *III* and *IV*: near ratio $\alpha \sim 3$, it obliquely cuts the intersection of the mentioned two blocks. Its dominant term is $i = 4$, $j = 2$.

— Block *III*: it is always critical near the normal shell ($\alpha = 4$), it generally covers the range $\alpha \sim 4 \div 3$. Its dominant term is $i = 3$, $j = 1$.

— Block *IV*: it is always critical near the shell of three-quarter normal type ($\alpha = 2.25$), it generally covers the range $\alpha \sim 1.5 \div 3$. Its dominant term is $i = 3$, $j = 2$.

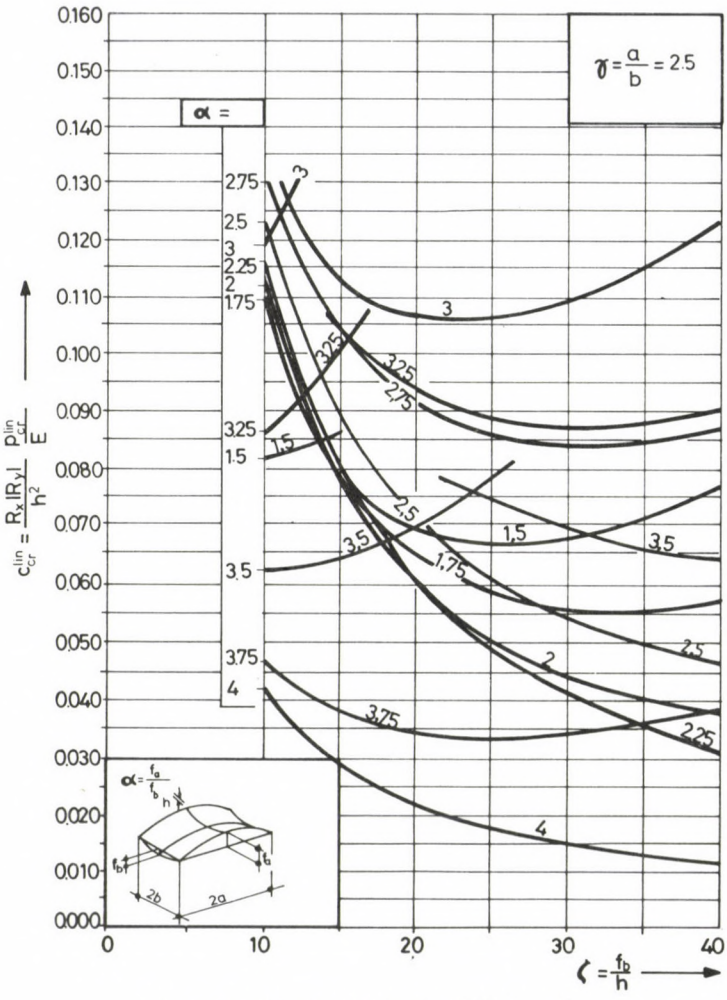

Fig. A7. Buckling load on hypar shells ($w_0 = 0$)

It is interesting that the critical buckling mode may vary not only with parameter α (Figs A1 to A4) but also with ζ near ratio $\alpha \sim 3$ (see e.g. the garland curve for $\alpha = 3$ in Fig. A5: it starts at block *III*, to change to block *IV* at $\zeta \sim 15 \div 20$, and ends by the mode corresponding to block *II*). Inclusion of block *I* is of theoretical significance: a buckling eigenfunction symmetrical about two axes cannot be critical but near the seminormal shell involving bending forces ($\alpha \sim 1 \div 1.75$, Fig. A1).

The diagrams presented in this paper can be considered as those in [9], *improved* partly to cover a much wider range of geometry parameters, and partly *to involve* numerical analyses for *block II*.

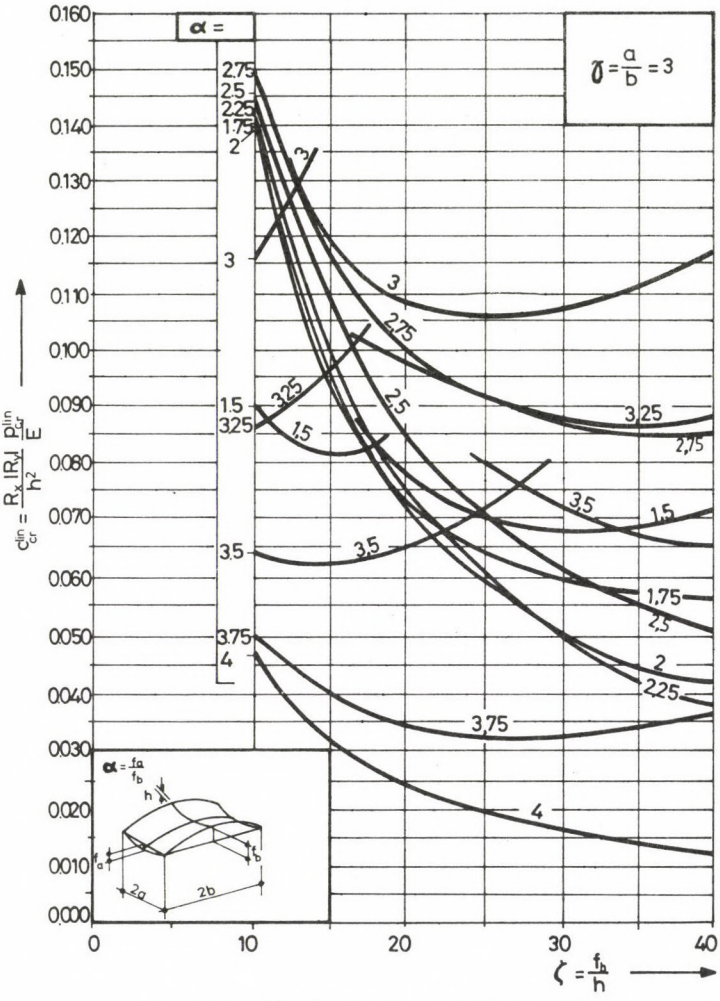

Fig. A8. Buckling load on hypar shells ($w_0 = 0$)

Most of the diagrams in [9] refer to geometry parameters where the buckling mode corresponding to block *II* is not critical ($\zeta = 3.33$, 5, 6.66, 7.5, 10,...) a corresponding curve being mainly missed near ratio $\alpha \sim 3$ in Figs 10, 12, and 13 of [9].

These are, however, *irrelevant* to the correctness of the theoretical statements and conclusions in [9] (places of minima and maxima; inextensional cases; the shell which is the most sensitive to geometrical imperfections is near ratio the $\alpha \sim 3$, etc.).

We point out that the complete assumed buckling mode had now generally 16 $\div$ 20 terms, and in conformity with Section 3, this extended eigenvalue problem

decomposed to four eigenvalue problems, of 4 or 5 terms each Fig. 4, blocks (*I*, *II*, *III*, *IV*; see also [9]).

Accordingly, *it is recommended to use this Appendix*, the more so, since the involved data cover much wider geometric ranges than did the previous ones.

References

1. Bushnell, D.: Symmetric and nonsymmetric buckling of finitely deformed eccentrically stiffened shells of revolution. AIAA Journ. 5 (1967), 1455–1462.
2. Croll, J. G. A., Walker, A. C.: Elements of structural stability. Macmillan, London 1972.
3. Dulácska, E.: A héjak hullámossága kritikus terhet csökkentő hatásának vizsgálata lineáris elmélettel. Építés- és Építészettudomány, 8 (1976) 3–4, 278–283 (in Hungarian). (An approximate imperfection analysis of shells by using linear buckling theory.)
4. Dulácska, E.: Vibration and stability of anisotropic shallow shells. Acta Techn. Hung. 65 (1969), 225–260.
5. Dulácska, E.: Az ívszerűen működő hiperbolikus paraboloid nyereghéj stabilitása. (Buckling of saddle-shaped hypar shells acting like an arch). Műszaki Tudomány 57 (1979), 381–387 (in Hungarian).
6. Gioncu, V.: Thin Reinforced Concrete Shells. Special Analysis Problems. Editura Academiei Bucureşti — J. Wiley and Sons, Chichester–New York–Brisbane–Toronto 1979.
7. Hutchinson, J. W.: Initial post-buckling behavior of toroidal shell segments. Int. J. Solid Structures, 3 (1967), 97–115.
8. Jankó, L.: Analyse des Verhältnisses zwischen Membran- und Biegeschnittkräften in sattelförmigen, flachen, normalkraftfrei gelagerten HP-Schalen unter gleichmäßig verteilter Belastung. Acta Techn. Hung. 91 (1980), 19–55.
9. Jankó, L.: Untersuchung der Stabilität sattelförmiger, flacher, normalkraftfrei gelagerter HP-Schalen unter gleichmäßig verteilter Belastung. Acta Techn. Hung. 91 (1980), 265–301.
10. Jankó, L.: Untersuchung der Gleichgewichtszustände sattelförmiger, flacher, normalkraftfrei gelagerter HP-Schalen unter gleichmäßig verteilter Belastung, mit besonderer Berücksichtigung des Durchschlagens und der Abzweigung. Acta Techn. Hung. 91 (1980), 419–467.
11. Kollbrunner, C. F., Meister, M.: Knicken, Biegedrillknicken, Kippen. Springer, Berlin–Göttingen–Heidelberg 1961.
12. Kollár, L., Dulácska, E.: Buckling of shells for engineers. Akadémiai Kiadó, Budapest 1984 and John Wiley & Sons, Chichester–New York–Brisbane–Toronto–Singapure 1984.
13. Kollár, L.: Héjak nyúlásmentes alakváltozásai. (Inextensional deformations of shells). Építés- és Építészettudomány 3 (1971), 19–38 (in Hungarian).
14. Pflüger, A.: Stabilitätsprobleme der Elastostatik. 2. Aufl. Springer, Berlin–Göttingen–Heidelberg–New York 1964.
15. Reissner, E.: On some aspects of the theory of thin elastic shells. Boston Society of Civil Engineers (1955), 100–133.
16. Timoshenko, S. P., Gere, J.: Theory of Elastic Stability. McGraw-Hill Book Company. New York–Toronto–London 1961.
17. Thompson, J. M. T., Hunt, G. W.: A general theory of elastic stability. J. Wiley and Sons, London–New York–Sydney–Toronto 1973.
18. Wedellsborg, B. W.: Critical buckling load on large spherical shells. Journ. Struct. Divis. Proc. ASCE, 88 (1962), 111–121.
19. Weinitschke, H. J.: On asymmetric buckling of shallow spherical shells. J. Math. Phys. 44 (1965), 141–163.
20. Weinitschke, H. J.: On the stability problem for shallow spherical shells. J. Math. Phys. 38 (1960), 209–301.
21. Weinitschke, H. J.: On the nonlinear theory of shallow spherical shells. J. Soc. Indust. Appl. Math. 6 (1958), 209–232.
22. Wolmir, A. S.: Biegsame Platten und Schalen. VEB Verlag für Bauwesen, Berlin 1962.

Acta Technica Academiae Scientiarum Hungaricae, 97 (1—4), pp. 177—196 (1984)

ON MATHEMATICAL STOCHASTIC MODELLING AND OPTIMIZATION OF CONSTRUCTION PROCESSES

Č. JARSKÝ

[Received: January 1984]

Research and Development Establishment of Structural Engineering Trust, Prague, Czechoslovakia.

A mathematical model for different construction processes is proposed in the article. The model uses the stochastic simulation method for the calculation because it enables the valuation of the construction process including random influences (e.g. weather conditions, failures of machinery, people, etc.). First, the basic principles of mass operation processes (queuing processes) are briefly described and reasons for the choice of the stochastic simulation method for the model are given. In the further part technological, technical and economic points of view for the optimization and judgement of different variants of the simulated construction process are stated. The principles of the proposed multipurpose model which is capable of the simulation of different construction processes (e.g. earthmoving and concrete laying works, panel house erections, transport processes etc.) are then described. An example of the simulation of concrete laying works is given and some facts about the practical use for optimization of loading and transport of gravel at the Gabčíkovo—Nagymaros waterworks are stated.

1. Introduction

On building sites situations it very often occurs that one equipment (e.g. excavator) attends another equipment (e.g. dumptrucks) and creates a mass operation process. It is intuitively clear that the design of both equipments has to be in harmony, that overdimensioning and then a little utilization of the serving equipment would be connected with high costs and output losses in the operation of such a system. Similar processes can be described as queuing processes that can be characterized as flowing processes, influenced by random interference. Because of this interference, sometimes queues may occur in front of the channels of service (e.g. excavators), sometimes channels of service may not work, because no units (e.g. dumptrucks) are available. Usually there are more stages (phases) of service in such a process sometimes in one phase several parallel channels of service are used. A circular (closed) system representing earthmoving works with 4 phases of service in line (first phase—two parallel excavators, second phase—road, third phase—two parallel places of dumping, fourth phase—road back) is illustrated in Fig. 1, the same system but on open one is in Fig. 2. According to the survey [5] worked out at the Faculty of Civil Engineering of the Czech Technical University of Prague the best method for evaluation and judgement of similar systems composed of more phases of service in line with the possibility of parallel channels of service in different phases, is the stochastic simulation using the Monte Carlo method.

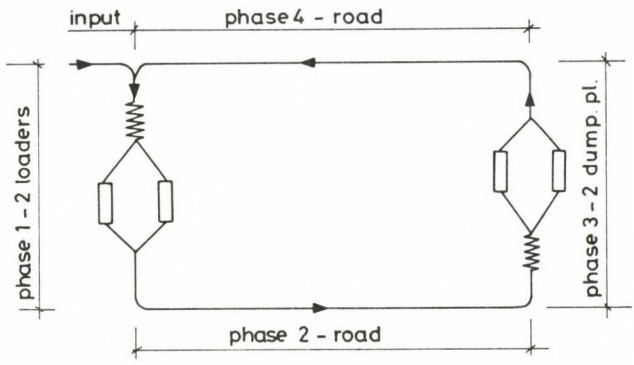

Fig. 1

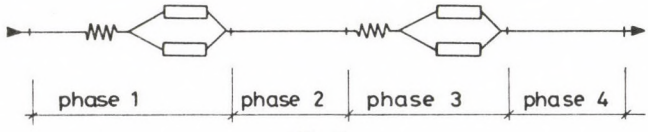

Fig. 2

However, some very simple systems can be calculated by the queuing theory, see [3], [13], especially those consisting of only one phase of service with some parallel channels, but for more difficult systems with more phases of service in line the direct calculation using the queuing theory is not possible in practice, since the differential equations obtained in this case is impossible to solve. Utility of the use of stochastic methods for the construction process, simulation has been discussed for a long time and the advantage of these against the deterministic calculation is known now. One of many reasons is that the construction process is influenced by so many factors (weather, terrain and water conditions, failures of machinery, people, etc.) that it is very difficult or even impossible to state precisely as to the conditions for a deterministic calculation and judgement of a construction process (see also [5], [7] and [12]).

The aim of the author's work was to create a multipurpose mathematical model connected with a computer program which would enable the simulation and then the analysis of different mechanized construction processes consisting of several phases of service in line, together with the possibility of several parallel channels of service in some (or every) phases, using the stochastic method of the simulation. The task was solved in [7]. Some parts of the solution have been published in [6], [8] and [9].

2. Description of the method of simulation of the process and the following analysis

2.1 Fundamental conditions of calculation

The mathematical model of a construction process simulates a circular (Fig. 1) or an open (Fig. 2) system with which the process can be described. The multiple use of the model enables the simulation of several difficult systems (e.g. concrete laying or panel house erections see Fig. 3), having a combination of a circular and an open subsystem. The main part of the model is the time synthesis and the following analysis of the process. The random quantity is the actual service time in the channel (e.g. filling of a dumptruck by an excavator, time of driving through a road, etc.), which is generated by a random number generator. The distribution function used for generating the values of time depends on the input data that are available for different processes. The exact distribution of service time in the channel should be obtained by site monitoring. For some kinds of processes it is already known [12], [14]. The used generator enables the producing of random numbers for rectangular, exponential, Poisson's, Erlang's and a normal distribution and for the distribution experimentally obtained by time monitoring on site. It was created originally with the help of [1].

The simulated circular system works from the time of arrival of the first unit into the first phase of service in the first round (usually in time 0.0) to the time of departure of the last unit from the last phase of service in the last round (including possible failures of units and times of repairs). After generating the times of arrivals of a certain number of units into the system and synthetizing the work in the first phase in the first round, the time of departure from the calculated phase equals the time of arrival into the following phase of service. That means that the time of departure from the last phase of service in

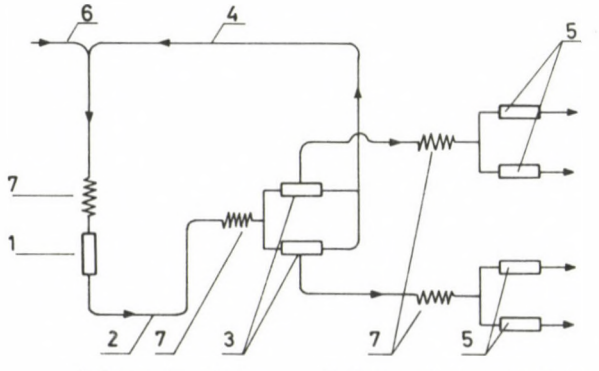

Fig. 3

the previous round equals the time of arrival into the first phase in the next round of service.

The simulated open system assumes the acceptance of a certain number of units in the first round, while times of arrivals of them are generated. After passing the last phase of service the units leave the system. In the following round new times of arrivals of the same number of units into the first phase are generated as in the first round, the generated random time interval between the arrivals of two units into the system being added to the time of arrival of the last unit into the system in the previous round, and this value means the arrival of the first unit into the system in the following round. The total time of operation of an open system is measured in the same way as for the circular system.

Priority in service is applied for all units in one round, which means that units in the queue in the previous round block the channels of service for units doing the next round, except those being repaired. If the channel of service is being repaired it cannot be used for accompanying the units, it is therefore blocked, units have to wait or use the other parallel channel if it exists. Repair of the unit does not block any channel of service. The time of repair is another random quantity used in the model with its own distribution function and is therefore generated by the random number generator.

Two sorts of phases are considered. The first kind are actual machines (e.g. excavators, concrete plants etc.) which are capable of serving only one unit during a certain time period. The other kinds are roads where several units can be "served" during a certain time period.

2.2 Brief description of the principles of the model

The mathematical model is generally illustrated in the flow chart in Fig. 4.

First of all, the essential input data which consist of the general characteristics of the site, data concerning the system (e.g. number of phases of service, number of rounds, number of units, number of parallel channels of service in every phase, etc.), data about arrivals into the system, data about the channels of service (the kind of distribution function for generating of times of service and its characteristics, average time of service, theoretical output, chance of a failure, average time of repair, costs for operation and non operation per time unit, energy consumption per time unit, etc.) and similar data about units (including the capacity of a unit) are read. The main data are controlled. Then the model generates the times of arrivals of the units into the system and proceeds to the main simulation of the process in case of the circular system, in the case of an open system it goes directly to the main work simulation, because the times of arrivals of the units into the system are generated directly during the simulation of the work.

The actual work of the process is simulated in the main part of the model. During this simulation all instants of the times of arrivals of the units in all phases of service, of

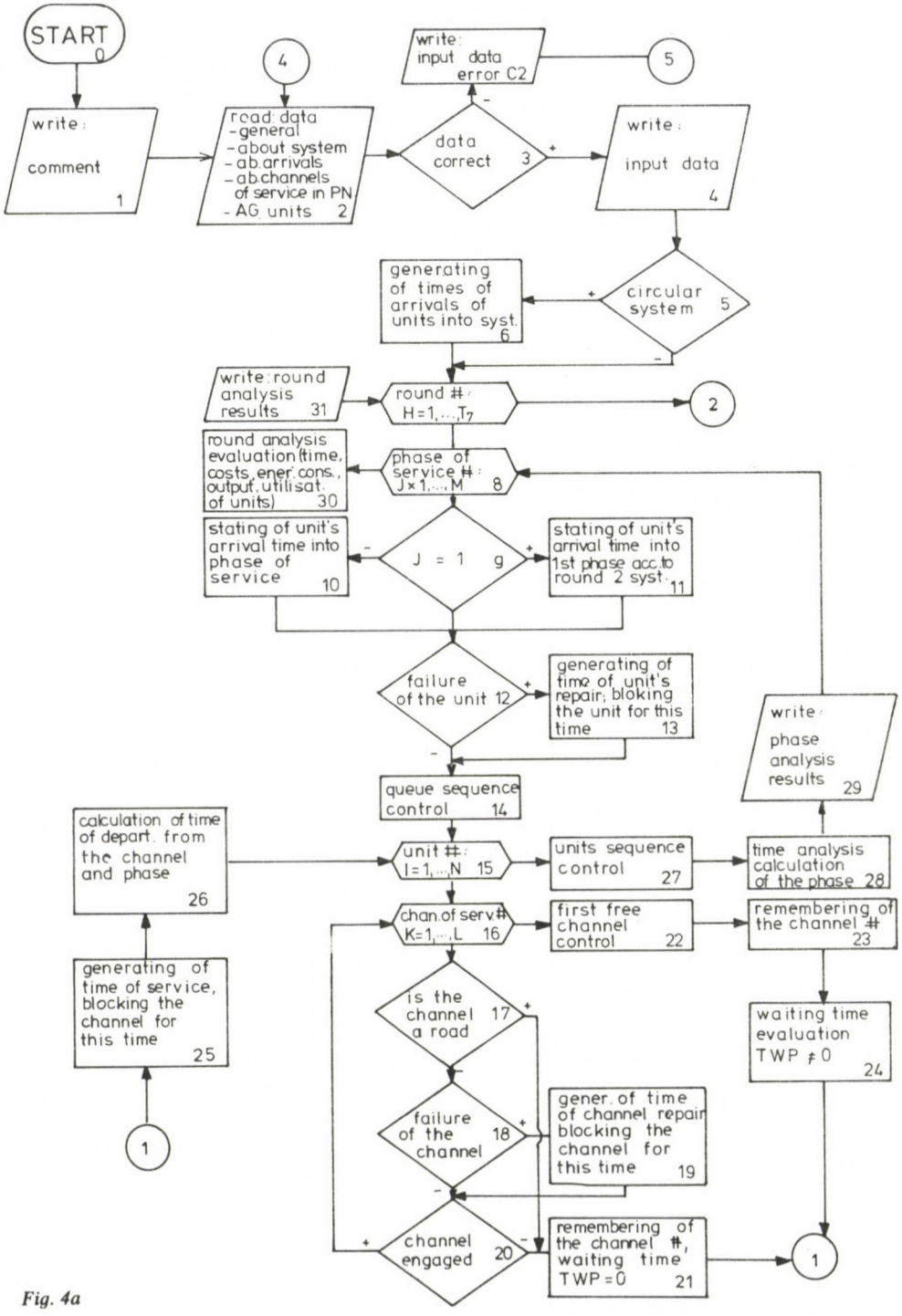
START 0
write: comment 1
4
read: data - general - about system - ab. arrivals - ab. channels of service in PN - AG. units 2
data correct 3
write: input data error C2
5
write: input data 4
circular system 5
generating of times of arrivals of units into syst. 6
write: round analysis results 31
round # H=1,...,T7
2
round analysis evaluation (time, costs, ener. cons., output, utilisat. of units) 30
phase of service # J=1,...,M 8
stating of unit's arrival time into phase of service 10
J = 1 g
stating of unit's arrival time into 1st phase acc. to round 2 syst. 11
failure of the unit 12
generating of time of unit's repair; bloking the unit for this time 13
queue sequence control 14
write: phase analysis results 29
calculation of time of depart. from the channel and phase 26
unit #: I=1,...,N 15
units sequence control 27
time analysis calculation of the phase 28
chan. of serv. # K=1,...,L 16
first free channel control 22
remembering of the channel # 23
generating of time of service, blocking the channel for this time 25
is the channel a road 17
waiting time evaluation TWP ≠ 0 24
1
failure of the channel 18
gener. of time of channel repair blocking the channel for this time 19
channel engaged 20
remembering of the channel #, waiting time TWP = 0 21
1

Fig. 4a

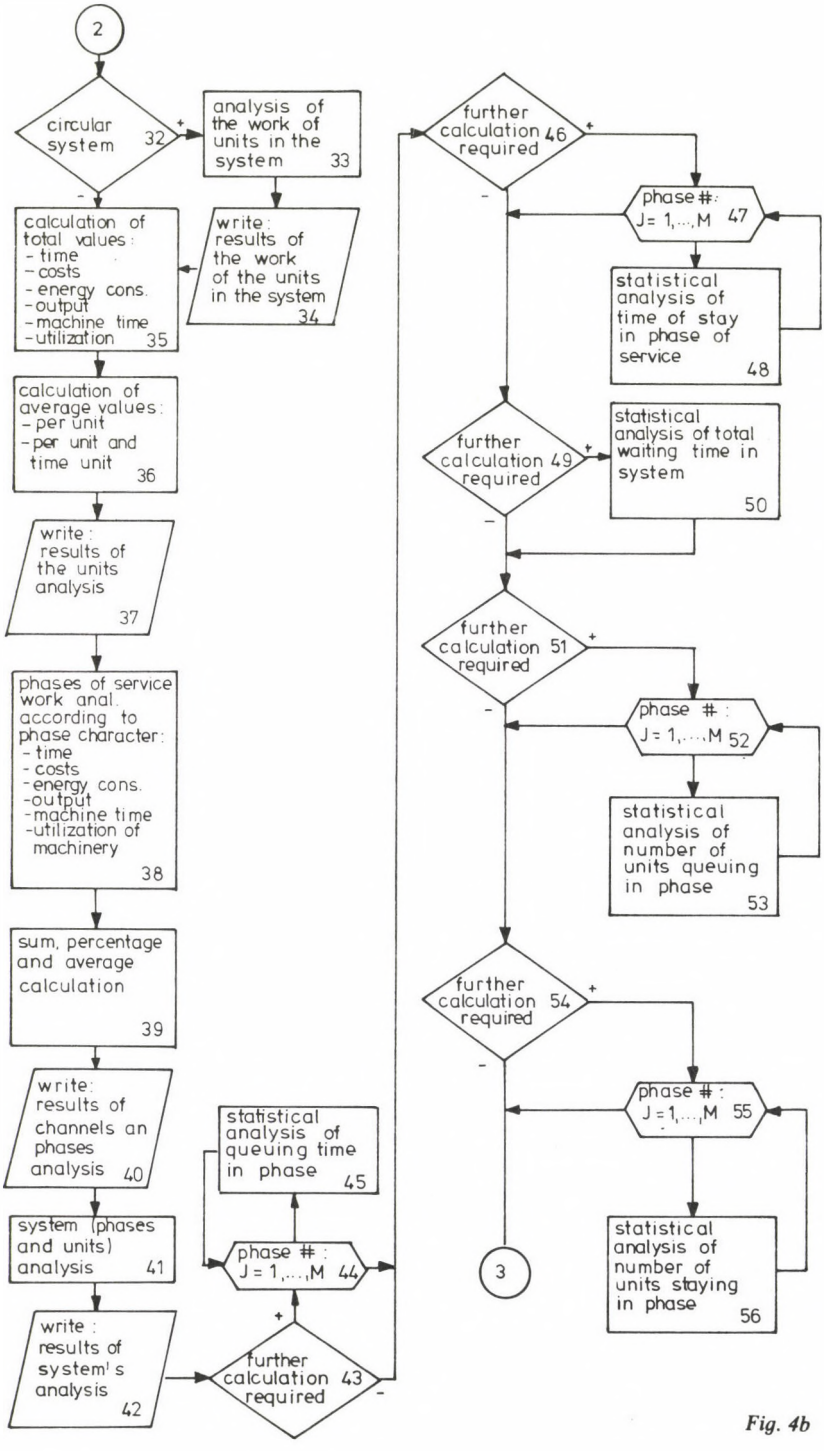
2
circular system 32
+
analysis of the work of units in the system 33
-
calculation of total values: - time - costs - energy cons. - output - machine time - utilization 35
write: results of the work of the units in the system 34
calculation of average values: - per unit - per unit and time unit 36
write: results of the units analysis 37
phases of service work anal. according to phase character: - time - costs - energy cons. - output - machine time - utilization of machinery 38
sum, percentage and average calculation 39
write: results of channels an phases analysis 40
system (phases and units) analysis 41
write: results of system's analysis 42
further calculation 43 required
+
-
phase #: J = 1,...,M 44
statistical analysis of queuing time in phase 45
further calculation 46 required
+
-
phase #: J = 1,...,M 47
statistical analysis of time of stay in phase of service 48
further calculation 49 required
+
-
statistical analysis of total waiting time in system 50
further calculation 51 required
+
-
phase #: J = 1,...,M 52
statistical analysis of number of units queuing in phase 53
further calculation 54 required
+
-
phase #: J = 1,...,M 55
statistical analysis of number of units staying in phase 56
3

Fig. 4b

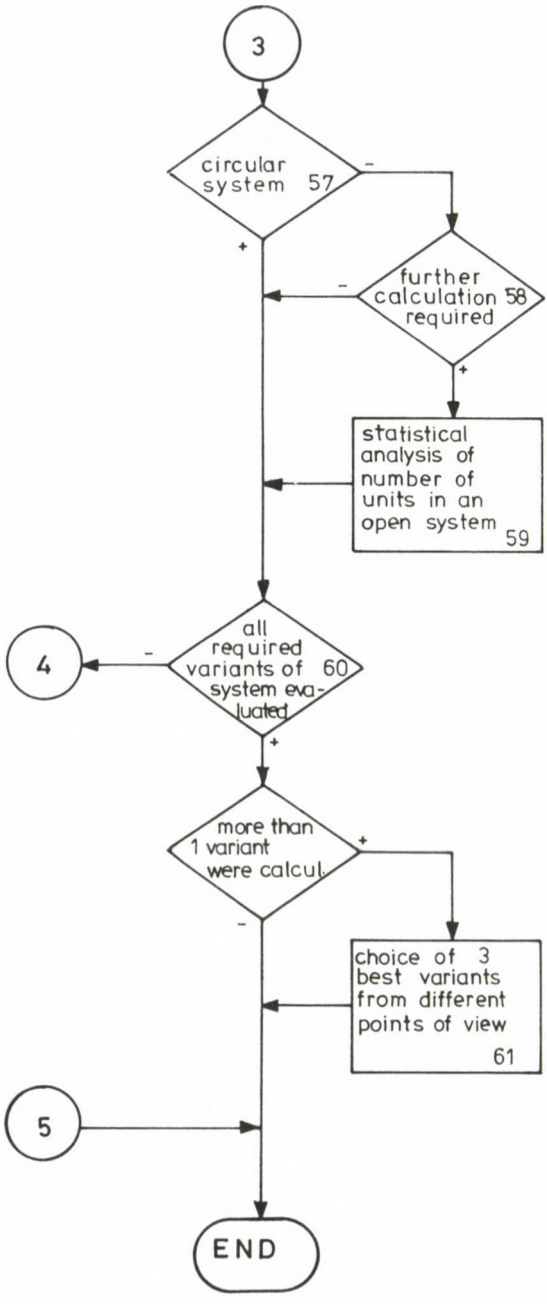
3
circular system 57
-
+
further calculation required 58
-
+
statistical analysis of number of units in an open system 59
all required variants of system evaluated 60
-
4
+
more than 1 variant were calcul.
+
-
choice of 3 best variants from different points of view 61
5
END

Fig. 4c

the beginning of work in the channels and departures of the units from the phases and the times of repair of the machinery, if any, in all rounds of moving the units have to be calculated, according to the number of the phases. Therefore, according to first the number of the rounds and the character of the system (circular or open) the times of arrivals into phases j of unit i, in the h-th round $TINP(h, i, j)$ are calculated. Then all units are controlled against failure, see par. *3.1.* If a failure occurs the time of the repair of the unit $TRU(h, i, j)$ is generated. Further the queue sequence of the units according to their times of arrivals $TINP(h, i, j)$ and the times of repairs $TRU(h, i, j)$ is stated. Then the model tries to put unit i into a channel of service k for operation (attendance).

If the channel is a road no queue is created and the unit is immediately "attended" and proceeds to the next phase of service. If the channel is an actual machine the channel failure control proceeds in a similar manner as for the units, the channel being blocked during the time of repair. The model then decides whether the channels of service is engaged or not. This decision consists of several conditions which are described in a more particular manner in par. *3.2.* If the channel k is free, unit i is attended without waiting, the waiting time of the unit i in phase j in the round h $TWP(h, i, j) = 0$. If the channel k is engaged the model tries the next available parallel channel in the phase. If all parallel channels in the phase are engaged, the model finds the channel which will be free first and puts the unit into it. The model remembers the number of the channel k that will accompany unit i and the waiting time of unit i $TWP(h, i, j)$ is calculated. Then the actual time of operation TOP, which means the time of attending the unit i by the channel k (see par. *2*), is generated by the random number generator according to the characteristics of the channel read in the input data file. The channel with actual machines (excluding roads) is blocked for the period of attending a unit. Next the time of departure from phase j of unit i in the round h $TOUTP(h, i, j)$ is evaluated according to formula (1). Thus, the simulation

$$TOUTP(h, i, j) = TINP(h, i, j) + TWP(h, i, j) + TOP \tag{1}$$

of work (attendance) in phase j continues for all units. The results of this time synthesis of the process in this phase are printed. The simulation of the process continues for all phases of service in one round in a similar way and the model then calculates the results of the time synthesis, costs and energy consumption and utilization of machinery in the simulated round. Afterwards, the work of the process for all rounds required is modelled in the same way.

After this synthesis (simulation) the part having different characteristics of the work of all parts of the system and of the whole system are calculated. The model analyses the total value, average value and percentage for time of work, time of non work, time of waiting, time of repairs, machine time; total costs, costs for repairs and work, energy consumption, amount of work done, output of the system, productivity of labour and utilization of the machinery—for units, channels of service (excluding roads) and for all machinery in the system.

The next part of the model does a statistical analysis of the different quantities if this is required. The statistical analysis enables obtaining the results of the simulation in the same form of probability distribution as e.g. queuing theory methods. The average values, the dispersion variance and the distribution function of the queuing time of one unit in different phases of service, of the time of standing of one unit in different phases of service, of the total waiting time of one unit in a round and for a circular system in the system and of the time of standing of one unit in a round, in the system, can be calculated. This part of the model also evaluates the absolute number of cases occurring at certain time intervals, the relative number of those and the cumulative probability of a certain time period, which means the probability of waiting or standing of one unit for less or equal the time period being evaluated; and the reverse cumulative probability of a certain time period, which means the probability of waiting or standing of one unit for longer than the time period being evaluated. Similar statistical analysis of the number of units queuing or standing in different phases during certain time periods, or for an open system the number of units standing in the system during these time periods, including the calculation of the probability characteristics can be done, as well. Thus, the simulation and analysis of 1 variant of the process is finished.

The model then calculates further variants of the system required. After all variants are evaluated (the highest number is 20), the last part of the model chooses the three best variants from different points of view (e.g. time, costs, energy consumption, utilization of machinery, etc.). The points of view that formulate the quality requirements in the course of the process are described in a particular manner in par. *2.3*.

The program based on the described model was created in two different versions. One version enables to evaluate different variants of the system, including the use of different machinery in the same phase of service, in different variants, but requires new input data for every variant. The other version evaluates different variants of the system by using the same data, viz. the same system of phases and channels of service, it only decreases the number of the units in the system (dumptrucks, etc.) for a certain number.

A smaller version of both programs evaluates a maximum of 5 rounds, 4 phases of service in the round, 5 parallel channels of service in every phase with 20 units working in a circular system, that means 100 units for an open system and requires about 125 kB of the computer memory. The calculation of 1 variant including the statistical analysis lasts about 10 sec. This version simulates approximately one or two days work of the system (depending on distances and average times of service in different phases).

The large version of both programs calculates a maximum of 20 rounds, 8 phases of service in the round, 5 parallel channels of service in every phase, with 25 units working in a circular system, that means 500 units for an open system. This version requires about 500 kB of the computer memory and about 1–2 weeks operation of the system can be simulated. Naturally, even bigger versions of the program could be created by only changing the dimensions of the used arrays.

2.3 Choice of the best variant of the simulated process

If more than one variant of the process were evaluated the last part of the model enables the choice of the three best variants of the process from different points of view. The used points of view that express the quality requirements in the course of construction process are not only economical, but most of all technological. They were stated according to the survey [5] and to the experience obtained at the Dept. of Mechanization and Processing of Structures of the Faculty of Civil Engineering of Czech Technical University of Prague in [7]. The points of view are as follows:

— total time of work of the system,
— output per time unit,
— utilization of machinery,
— total machinetime,
— total cost,
— cost per measure unit of the product,
— total energy consumption
— energy consumption per measure unit of the product.

According to these requirements first the whole system, second the units and third the separate phases of service are graded and the optimum is chosen. In this model no complex utility function was stated as it is often used in construction economics because in the construction process design and research there is usually only one overriding point of view (e.g. depending on the contractor's possibilities and resources).

3. Particular description of some important parts of the model

3.1. Failure control and simulation of the time of repair

The previously described model simulates random failures of machinery (units and channels of service). The likelihood of failure of the probability of a failure EPS is read by the program in the data file for every machine (e.g. 0.02). In the failure control section of the model (Fig. 4, block 12) a random number XI with the rectangular distribution in the (0; 1) interval is generated. If the condition (2) is fulfilled a failure of machinery occurs and the time

$$EPS \geqq \mathrm{XI} \tag{2}$$

of repair is then generated, using the exponential probability distribution. The average time of repair is obtained from the data file. The machine is blocked for use during its repair time. For units, the time of repair $TRU(h, i, j)$ is added to the time of arrival of the unit i into the phase j $TINP(h, i, j)$ and the unit that was being repaired is marked (by $ANS(i) = 1$). Other units have the value of $ANS(i) = 0$. In case of the channel of service repairs, the time of repair TR is added to the value $TOUT1(j, k)$ which means the time when the channel k in the phase j will be free and prepared to attend the next unit. By this addition the channel is blocked for the time TR, as well.

3.2. Channel engagement control

Channel engagement control described in Fig. 4, bl. 20 consists of several conditions. In a round, the channel can be occupied during a certain time by units which have not been repaired and have the value of $ANS(i)=0$; the highest time limit of those marked $TOUT1(j, k)$ for the phase j and channel k, as described in Fig. 5, and from the time $TIN2(j, k)$ to $TOUT2(j, k)$ by units which have been repaired ($ANS(i)=1$).

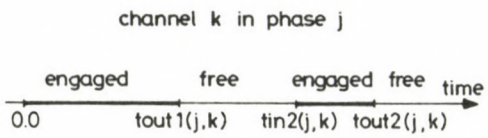

Fig. 5

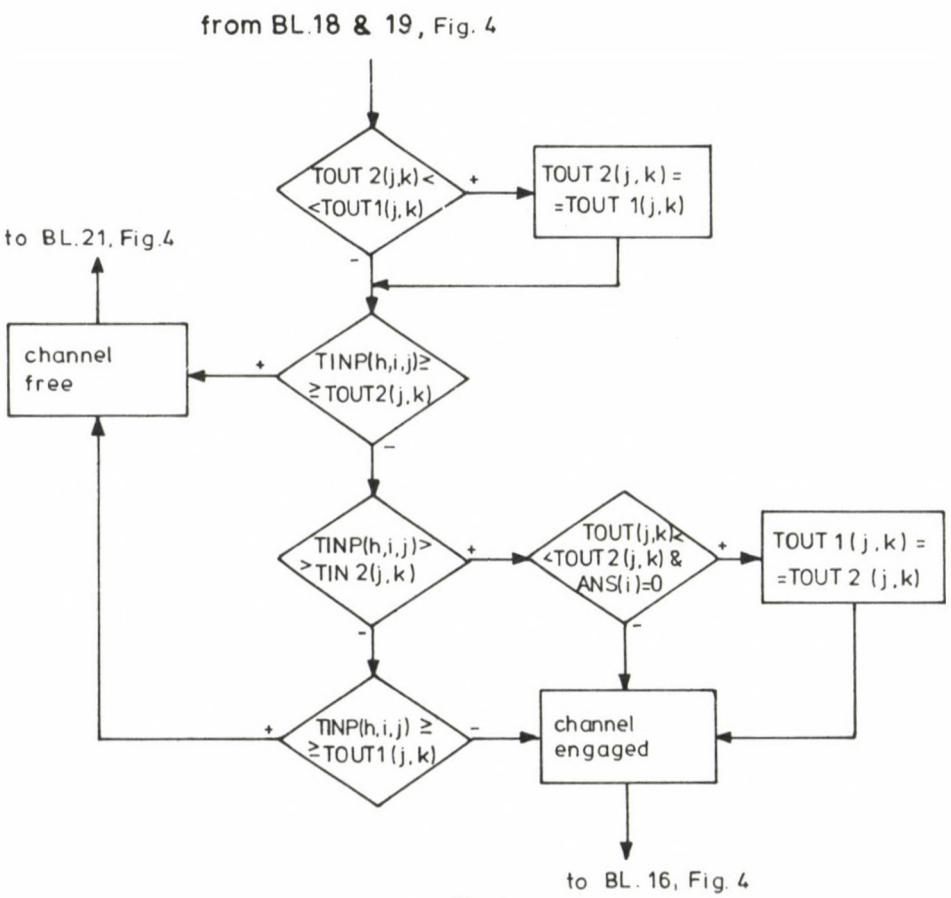

Fig. 6

This means that in the next round the channel is free during the time period of $TOUT1(j, k)$ to $TIN2(j, k)$ and from $TOUT2(j, k)$ later on. All these conditions must be controlled in the bl. 20 in Fig. 4 as is illustrated in particular in Fig. 6. In case of the channel repair the value $TOUT1(j, k)$ may be greater than $TOUT2(j, k)$, then the $TOUT2(j, k)$ value is made equal to $TOUT1(j, k)$ because of the channel being blocked.

According to the chosen channel for attending the unit, the condition of unit having been repaired or not, and the time of service, new values for $TOUT1(j, k)$, $TIN2(j, k)$ and $TOUT2(j, k)$ are stated in block 25 in Fig. 4 in order to be prepared for evaluation of the next unit of that round or for the next round.

4. Possibilities for the use of the model

The proposed mathematical model of mechanized building processes can be used for simulating different variants of similar processes as illustrated in Figs 1, 2 and 3. It is possible to design bigger and smaller variants of these systems. By using the proposed model such processes as e.g. earthmoving works (excavation, loading, scraper use, etc.), concrete laying works, assembling processes of panel houses, various transport processes etc. can be simulated. The proposed model is multipurpose in contrast to stochastic simulation models described e.g. in [1], [4] and [12], where an extra model with an extra program for simulating of every single process was used. A further advantage of the proposed model is that it calculates and simulates the process at the time intervals which are not equal, as in the models in [1], [2], [12], but they depend on arrivals or departures of units into or from the phases of service. According to the possibility of evaluation of more variants of the system and the following choice of the three best variants, the most suitable variant of a building process can be designed according to the demands or possibilities of the contractor.

The program simulates the performance of the system not only in the stochastic but in the deterministic way, too, if this is required. This enables a particular theoretical research and critical evaluation of the methods so far being used for the design and output calculation of similar processes. The proposed model helps to obtain the same probabilistic characteristics for more difficult systems, as a direct calculation by using the queuing theory in case of some simple systems [13], [14]. It is capable of accepting all necessary information e.g. weather influence, terrain influence, influence of the material handled, etc. in stating the input data, e.g. the average time of service in a phase. It also considers the influences which are very difficult or impossible to state in advance, e.g. traffic density, because of using the random number generator in generating the actual time of operation of a service channel in a phase.

The disadvantage in using the model is that not too much time for monitoring the evaluation of the essential input data has been made so far. Once these data are available, the significance and accuracy of the results obtained by the proposed and similar further developed models will certainly increase.

5. Theoretical example-simulation of concrete laying works

The process of concrete laying works which was simulated by the small version of the program is described in Fig. 3. The process consists of one circular (closed) subsystem which has 4 phases of service, in which the first phase (concrete plant) and the third one belong to the first kind (with the possibility of queue) and the 3rd phase has 2 parallel channels of service (2 concrete pumps), 2nd and 4th phase representing roads belong to the second kind. The following parts of the process are simulated by two open subsystems, modeling the exits from the concrete pumps, pipes for the transport of concrete and 4 gangs of concrete layers (two in each subsystem).

In the modeling of the concrete laying works, first the circular subsystem was simulated—the part of the process representing the transport of the concrete from the concrete plant to the building site. In this part of the calculation the terms of the departures of the units (concrete mixers) from the 3rd phase were stated, that means the terms of the finishing of the pouring of the concrete into the concrete pumps (first or second channel of service in this phase). Those time instants were read as the inputs of the units (in this part of the calculation one unit means 2.5 m^3 of concrete) into the open subsystems representing the laying of concrete. The average of the digital characteristics of all aspects for the choice of the best variant of the whole system was calculated after all runs of the program. 8 variants of the process were simulated with equal parameters of the channels of service, while the number of units requiring for the service in the circular subsystem was 20, in the first variant and in next ones this number was decreased by 2. The units in the circular subsystem are the concrete mixers AM 8 with the capacity of 2.5 m^3 of concrete, measured cost for work 1.20 Kčs/min, average time of repair 90 mins and measured costs for repair 2 Kčs/min. In the open subsystems the units are created by 2.5 m^3 of concrete. The input data about the phases of service for the stochastic versions of calculation are in Table I. For the deterministic versions of the simulation only the probability distribution of the time of service is modified, as constant. Four versions of the process were simulated—2 stochastic (the first with the likelihood of failure of machines 0.0, the 2nd 0.01) and 2 deterministic with the same values of the likelihood of failure.

A part of the results of the simulation of this process is described in Tabs II–V where one can compare the values of the utilization of the machinery in the system, the actual labour consumption per measure unit of the product, costs per measure unit of the product and the output of the system. The results are drawn up in Figs 7 and 8. It is to be seen that the most advantageous variant has 8 concrete mixers and 1 concrete pump which is enough for concrete laying, because of the small capacity of the concrete plant. The differences of the results obtained by the deterministic and stochastic simulation are described in these figures as well.

Table I

Phase		Name	Theoretical output (m/min)	Measure costs for (Kčs/min)		Average time of servicing the unit (min)	Probability distribution of time of service and its parameter	Average time of repair (Min)	Measured costs for repair (Kčs/min)
Number	Sort			Work	Non-working				
–	–	Input of units	–	–	–	1.5	exponent.	–	–
				Circular subsystem					
1	1	Concrete plant CIFA	0.5	2.50	2.00	5.0	Elang's KR = 5	120	2.00
2	2	Road	–	–	–	20.0	normal $\sigma = 10$	–	–
3	1	2 concrete pumps	0.4	1.50	1.00	4.0	Erlang's KR = 5	60	1.50
4	2	Road	–	–	–	15.0	normal $\sigma = 5$	–	–
				Open subsystems					
1	1	Concrete pump	0.4	1.50	1.00	5.0	Erlang's KR = 10	60	1.50
2	2	Pipeline	–	–	–	1.5	konst.	–	–
3	1	2 gangs of concr. layers	0.17	1.50	1.50	15.0	Erlang's KR = 10	–	–

Table II. *Concrete laying works* — see Fig. 3
Stochastic model—without failures

No. of variant	No. of units	Utilization of machines (−)	Actual labour consumption (*MTU/MU*)	Cost of *MU* (Kčs/*MU*)	Output (*MU/TU*)
1	20	0.58	41.70	52.60	0.50
2	18	0.58	40.30	50.90	0.48
3	16	0.61	36.90	46.90	0.47
4	14	0.63	35.52	45.40	0.44
5	12	0.71	27.50	35.40	0.48
6	10	0.71	30.00	39.00	0.41
7	8	0.69	27.37	35.60	0.37
8	6	0.65	30.00	39.20	0.29

Table III. *Concrete laying works*—see Fig. 3
Stochastic model—likelihood of failure of machines 0.01

No. of variant	No. of units	Utilization of machines (−)	Actual labour consumption (*MTU/MU*)	Cost of *MU* (Kčs/*MU*)	Output (*MU/TU*)
1	20	0.59	41.60	52.61	0.50
2	18	0.63	38.14	49.09	0.50
3	16	0.59	38.54	49.52	0.45
4	14	0.59	38.12	49.63	0.41
5	12	0.64	32.60	42.78	0.41
6	10	0.71	28.03	36.36	0.42
7	8	0.49	40.30	55.00	0.18
8	6	0.67	28.37	37.04	0.30

Table IV. *Concrete laying works*—see Fig. 3
Deterministic model—without failures

No. of variant	No. of units	Utilization of machines (−)	Actual labour consumption (*MTU/MU*)	Cost of *MU* (Kčs/*MU*)	Output (*MU/TU*)
1	20	0.56	44.65	56.24	0.46
2	18	0.58	41.11	52.00	0.46
3	16	0.60	37.58	47.77	0.46
4	14	0.64	34.07	43.58	0.45
5	12	0.68	30.60	39.42	0.44
6	10	0.74	27.18	35.34	0.43
7	8	0.76	25.60	33.54	0.39
8	6	0.71	27.40	35.99	0.31

Table V. *Concrete laying works*—see Fig. 3
Deterministic model—likelihood of failure of machines 0.01

No. of variant	No. of units	Utilization of machines (–)	Actual labour consumption (*MTU/MU*)	Cost of *MU* (Kčs/*MU*)	Output (*MU/TU*)
1	20	0.54	43.65	56.08	0.42
2	18	0.60	38.84	50.13	0.47
3	16	0.58	36.33	47.37	0.38
4	14	0.60	36.43	46.83	0.43
5	12	0.53	38.17	49.91	0.33
6	10	0.73	27.53	36.07	0.43
7	8	0.61	32.03	43.25	0.26
8	6	0.61	32.43	43.91	0.23

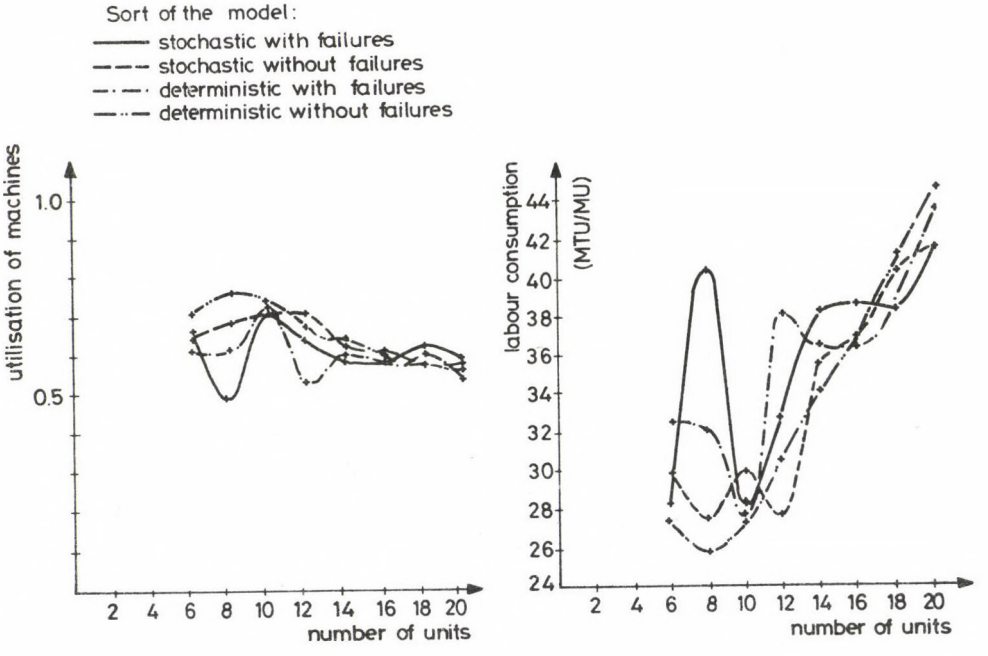

Fig. 7

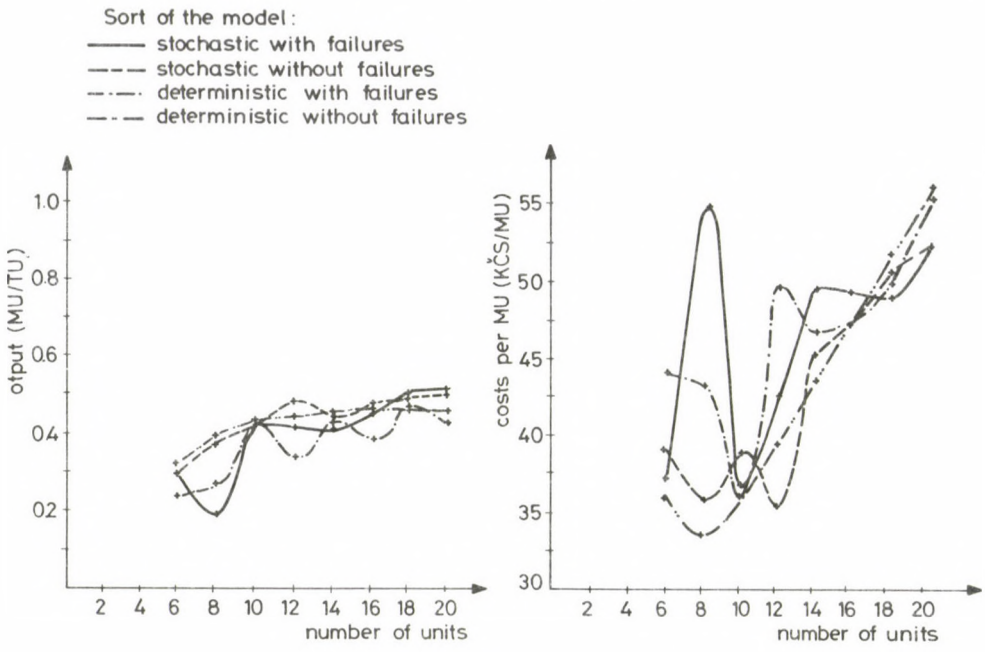

Fig. 8

6. Practical example—optimization of loading and transport of gravel at Gabčíkovo—Nagymaros

The model was recently used for the optimization of loading and transport of gravel for the embankments of the waterworks Gabčíkovo—Nagymaros on the river Danube. The scheme of this process responds to Fig. 1 with the exception of the 3rd phase, where no queue was created. The scheme of the situation of the building site is on Fig. 9. There were 3 different resources of gravel on site (A, B, C) and 17 places of consumption—17 sections of the embankments having the length of 1 km each. Many different variants of the process were simulated on the computer using different kinds and number of machines, see report [10]. The optimum according to the costs and fuel consumption was to use the *UNC-200* loaders and *Tatra T148 S1* dumptrucks, in certain numbers, for different sections, quoted in Table VI. In this table the basic characteristics (cost and fuel consumption per measure unit m^3 of gravel) of the process are compared in case of a case-free course of the process, and in the course of the process with random failures of machinery. The likelihood of failure for the loaders was 0.01, for dumptrucks 0.02. The average quantities were calculated according to the amount of gravel to be transported from the resources to the sections of the waterwork.

It is to be seen that the influence of failures of the machines on the quality parameters of the process is surprisingly high, the costs being increased by 66% and the

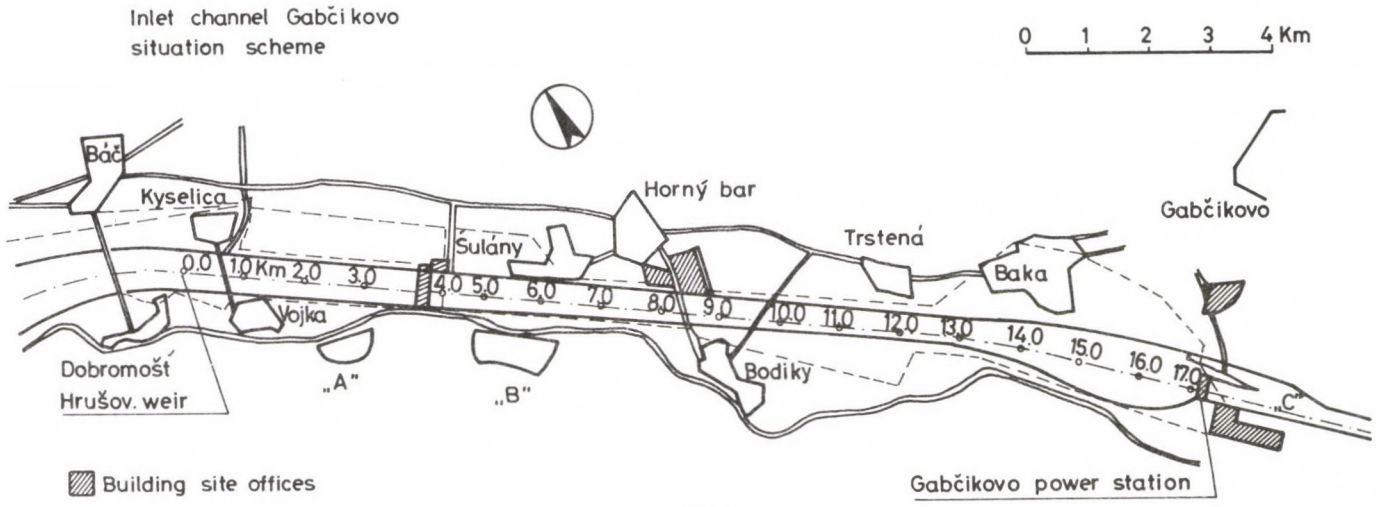
Inlet channel Gabčikovo
situation scheme
0 1 2 3 4 Km
Báč
Kyselica
Šulány
Horný bar
Trstená
Baka
Gabčikovo
0.0 1.0 Km 2.0 3.0 4.0 5.0 6.0 7.0 8.0 9.0 10.0 11.0 12.0 13.0 14.0 15.0 16.0 17.0
Vojka
Dobromošt
Hrušov. weir
„A"
„B"
Bodiky
„C"
Building site offices
Gabčikovo power station

Fig. 9

Table VI

	Machinery used	Case smooth course		Course with failures	
	No. of loaders	costs	fuel consumption	costs	fuel consumption
	No. of trucks	Kčs/m³	l/m³	Kčs/m³	l/m³
1	1 10	3.46	0.80	10.44	1.72
4	1 6	2.28	0.45	2.26	0.44
6	1 8	2.95	0.64	3.82	0.64
7	2 8	2.25	0.39	2.91	0.41
9	2 16	3.17	0.69	5.54	0.86
11	2 30	4.15	1.0	6.72	1.52
12	2 42	5.33	1.35	8.54	1.98
15	2 28	3.80	0.90	4.95	1.04
17	2 14	2.61	0.53	6.09	0.49
Average		3.40	0.77	5.64	1.00
Increase %				65.88	29.87

energy consumption by 30%. It is to be considered from this fact that it is worth to have at least one dumptruck on the site more which can be used in case of failure of a machine. Thus, a smooth course of the process can be ensured with a minimum increase of cost and fuel consumption.

7. Conclusions

Mathematical stochastic models have gained more and more significance in the building-process research, recently. The proposed model aims at bringing even more utilization of these methods in this specialization.

From the results which have been obtained so far it is to be seen that this model is suitable for the simulation of many types of construction processes. The results obtained by the proposed model provides a much better approach of the reality of the process than if calculated by using the traditional deterministic way or the queuing theory. The model is useful for the calculation of quality parameters having different variants of the process to gain the optimum. Those parameters should be judged at an extra of the quality parameters of the resulting product. It is capable of searching for the influence of different factors, on the quality indicators of the course of the process (e.g.

failures of machinery, number of means of production, etc.). The model contributes to more economic design of mechanized building processes and, therefore, for lowering the cost and energy consumption of those on site and to better utilizing the machinery to be used.

Further research in this field will be directed to obtaining more reliable statistical data for the input for the model (likelihood of failure of the machinery, time monitoring of the behaviour of similar systems, etc.) and the model itself is planned to be improved by competency of simulating construction processes which consist of more than one circular subsystem with certain points of contact among them.

References

1. Beková, N. N., Golenko, D. I.: Statisticheskyie metody optimizacii v ekonomicheskich issledovanyiach (Statistic methods of optimization in economical research). Statistika, Moskva 1971.
2. Buslenko, N. P., Shreyder, J. A.: Stochastické početní metody (Stochastic methods of calculation). SNTL, Praha 1965.
3. Hájek, V.: Matematické modely ve stavebnictví (Mathematical models in civil engineering). ČVUT, Praha 1966.
4. Hammersley, J. M., Hanscomb, D. C.: Monte Carlo Methods. Methuen and Co., London 1967.
5. Jarský, Č.: Průzkum matematických metod a modelů v oblasti technologie staveb (Survey of mathematical methods and models in technology of structures). ČVUT, Praha 1978.
6. Jarský, Č.: On Mathematical Stochastic Modelling of Mechanized Building Processes. Building Research Establishment Note 28/81, Garston, Watford 1981.
7. Jarský, Č.: Příspěvek k matematickému modelování mechanizovaných stavebních procesů (Contribution on mathematical modelling of mechanized building processes). ČVUT, Praha 1981.
8. Jarský, Č.: K matematickému stochastickému modelování stavebních procesů (On mathematical stochastic modelling of construction processes). Inženýrské stavby. 30, (1982) April.
9. Jarský, Č.: K simulaci stavebních procesů pomocí matematického stochastického modelu (On simulation of building processes with the help of a mathematical stochastic model). Pozemní stavby. 31, (1983) February.
10. Jarský, Č.: Optimalizace dopravy štěrkopísku do přívodního kanálu HC Gabčíkovo (Optimization of transport of gravel into the inlet channel of HC Gabčíkovo). Report of the state research task S 12-526-056/01.1, VUIS Bratislava, 1983.
11. Jarský, Č.: Quality assurance of construction processes. IABSE Reports 47, IABSE Zürich 1983.
12. Jurecka, W., Zimmermann, H.-J.: Operations Research im Bauwesen. Springer Verlag, Berlin 1972.
13. Saaty, L.: Elements of the Queuing Theory. McGraw-Hill, New York 1961.
14. Walter, J.: Stochastické modely v ekonomii (Stochastic models in economy). SNTL, Praha 1970.

Acta Technica Academiae Scientiarum Hungaricae, 97 (1—4), pp. 197—214 (1984)

PERCOLATION AROUND DAMS

J. JUHÁSZ

[Received: 4 October 1983]

A simple procedure easy to treat is presented for determining with adequate accuracy the plane percolation under, and spatial percolation around dams which is to be applied also to pocket calculators. The boundary conditions might be largely diversified. By using it, a single or several layers, projects with surface or subsurface foundation and different confining beds at different sections might be taken into account.

In the author's papers published earlier [1], [2], [3] a simple and easily treatable procedure has been presented for the evaluation with proper exactitude of the discharge of the plane percolation under a dam built on the surface, the pressures applied on the footing, the entrance and exit gradients, for the case of a system consisting of two and three water-bearing strata covered with a thick confining bed.

The problem may be continued to develop by laying the footing of the dam below the soil surface or by building a sheet wall (cutoff wall) under the dam. Also the case of a system of permeable strata of number n, of different thicknesses and coefficients of permeability as well as instances designed with sheet walls are arranged under the project.

Eventually, a relationship of close approximation is established which also describes the spatial percolation.

A percolation discharge along the unit width under the project built into a thick water-bearing formation might be determined (Fig. 1) by making use of the method of angled stream tube worked out by the author, as follows.

In a stream tube, the discharge of the water percolating through the confining bed, is given by the equation

$$\mathrm{d}Q = \frac{k_{f-2}}{\lambda_{f-2}} \frac{h_1}{M_{f-2}} \alpha_f \, \mathrm{d}m \tag{1}$$

with

$$\alpha_f = \frac{T_f}{M_1}$$

J. Juhász, H-1148 Budapest, Felsőbüki Nagy Pál u. 4, Hungary

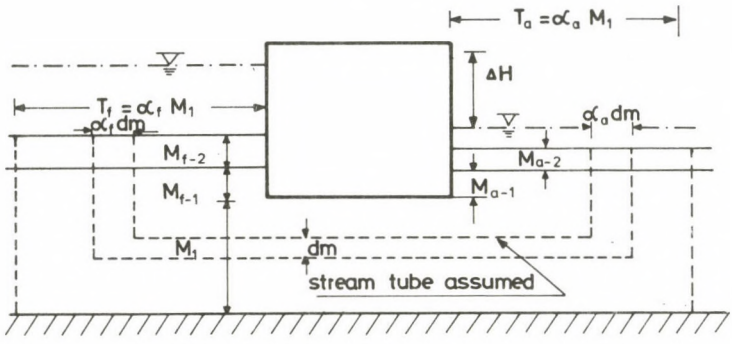

Fig. 1

and

$$dQ = \frac{k_{a-2}}{\lambda_{a-2}} \frac{h_2}{M_{a-2}} \alpha_a \, dm \tag{2}$$

$$\alpha_a = \frac{T_a}{M_1};$$

h_1 — part of total loss ΔH falling to the section investigated, is so far unknown;
λ_f — values of anisotropy at rock sections as designated.

At the vertical creep sections, in the waterbearing stratum up to the level of the lower edge of the project:

$$dQ = k_1 \frac{1}{\lambda_1} \frac{h_{v11}}{M_{f-1}} \alpha_f \, dm \tag{3}$$

and

$$dQ = k_1 \frac{1}{\lambda_1} \frac{h_{v21}}{M_{a-1}} \alpha_a \, dm \tag{4}$$

The discharge at the vertical percolation along the section of the water-bearing stratum under the foundation is as follows:

$$dQ = \frac{k_1}{\lambda_1} \frac{h_{v12}}{m} \alpha_f \, dm \tag{5}$$

and

$$dQ = \frac{k_1}{\lambda_1} \frac{h_{v22}}{m} \alpha_a \, dm \, . \tag{6}$$

Along the horizontal section of the water-bearing stratum:

$$dQ = k_1 \frac{\Delta H - (h_1 + h_2 + h_{v11} + h_{v21} + h_{v12} + h_{v22})}{(\alpha_f + \alpha_a)m + L_0} dm \, , \tag{7}$$

from (1)

$$h_1 = \frac{M_{f-2} \lambda_{f-2}}{\alpha_f k_{f-2}} \frac{dQ}{dm} , \tag{8}$$

from (2)
$$h_2 = \frac{M_{a-2}\lambda_{a-2}}{\alpha_a k_{a-2}} \frac{\mathrm{d}Q}{\mathrm{d}m}, \tag{9}$$

from (3)
$$h_{v11} = \frac{\lambda_1 M_{f-1}}{k_1 \alpha_f} \frac{\mathrm{d}Q}{\mathrm{d}m}, \tag{10}$$

from (4)
$$h_{v21} \frac{\lambda_1 M_{a-1}}{k_1 \alpha_a} \frac{\mathrm{d}Q}{\mathrm{d}m}, \tag{11}$$

from (5)
$$h_{v12} = \frac{\lambda_1 m}{k_1 \alpha_f} \frac{\mathrm{d}Q}{\mathrm{d}m}, \tag{12}$$

from (6)
$$h_{v22} = \frac{\lambda_1 m}{k_1 \alpha_a} \frac{\mathrm{d}Q}{\mathrm{d}m}. \tag{13}$$

Substitution of Eqs (8) to (13) into (7) yields

$$\frac{1}{k_1}[(\alpha_f + \alpha_a)m + L_0]\frac{\mathrm{d}Q}{\mathrm{d}m} = \Delta H - \left[\frac{M_{f-2}\lambda_{f-2}}{\alpha_f k_{f-2}} + \right.$$

$$\left. + \frac{M_{a-2}\lambda_{a-2}}{\alpha_a k_{a-2}} + \frac{\lambda_1}{k_1}\left(\frac{M_{f-1}}{\alpha_f} + \frac{M_{a-1}}{\alpha_a}\right) + \frac{\lambda_1}{k_1}\left(\frac{1}{\alpha_f} + \frac{1}{\alpha_a}\right)m\right]\frac{\mathrm{d}Q}{\mathrm{d}m},$$

or after rearrangement

$$\frac{\mathrm{d}Q}{\mathrm{d}m} = \frac{k_1 \Delta H}{Y},$$

where

$$Y = L_0 + \frac{k_1 M_{f-2}\lambda_{f-2}}{\alpha_f k_{f-2}} + \frac{k_1 M_{a-2}\lambda_{a-2}}{\alpha_a k_{a-2}} + \lambda_1\left(\frac{M_{f-1}}{\alpha_f} + \frac{M_{a-1}}{\alpha_a}\right) +$$

$$+ \left[\alpha_f + \alpha_a + \lambda_1\left(\frac{1}{\alpha_f} + \frac{1}{\alpha_a}\right)\right]m.$$

Notation

$$B_1 = L_0 + k_1\left(\frac{M_{f-2}\lambda_{f-2}}{\alpha_f k_{f-2}} + \frac{M_{a-2}\lambda_{a-2}}{\alpha_a k_{a-2}}\right) + \lambda_1\left(\frac{M_{f-1}}{\alpha_f} + \frac{M_{a-1}}{\alpha_a}\right), \tag{14}$$

$$C_1 = \lambda_1\left(\frac{1}{\alpha_f} + \frac{1}{\alpha_a}\right) + \alpha_f + \alpha_a. \tag{15}$$

Therefore

$$\mathrm{d}Q = \frac{k_1 \Delta H}{B + C_1 m}\mathrm{d}m.$$

Integration between the limits 0 and m gives

$$Q_1 = \frac{k_1 \Delta H}{C_1} \ln \frac{B_1 + C_1 m}{B_1}. \tag{16}$$

The discharge percolating through the whole thickness of the stratum M_1 is

$$Q_1 = \frac{k_1 \Delta H}{C_1} \ln \frac{B_1 + C_1 M_1}{B_1} \tag{17}$$

L. Újfaludi [4] confirmed by tests carried out on models of electric analogy that, compared with a sheet piling located at the middle of the project, a sheet piling arranged at the downstream or upstream end of the project at the same depth as that above, yields the same discharge with an approximation within 11 per cent. Therefore, also in case of the application of a sheet piling deepened to the depth of the footing of the project, to be seen in the figure, a comparable percolation discharge is yielded.

By using the data given, the calculation method consists in defining the maximum value of Q with the aid of Eq. (17) by varying the values of α_f and α_a. The values $\alpha_{f\,\mathrm{opt}}$ and $\alpha_{a\,\mathrm{opt}}$ multiplied with M_1 give the influent and the effluent percolation widths $T_{f\,\mathrm{opt}}$ and $T_{a\,\mathrm{opt}}$ where the phenomenon takes place. The successive approximation might be carried out with the use of a simple pocket calculator.

Should the percolation discharge be drained by a drainage channel, so the calculation should be accomplished in two stages. First, the discharge of the percolation is to be evaluated by using the relationship (17) but, with the assumption that in the equation (14) the values M_{a-2}, k_{a-2} and λ_{a-2} are equal to zero, i.e., the confining bed under the project no longer affects the flow. The equation $\alpha_{f\,\mathrm{opt}} \cdot M_1 = T_f$ gives the width of the influent percolation yielded by successive approximation at the storage side, and $\alpha_{a\,\mathrm{opt}} \cdot M_1 = T_a$ the width of the effluent percolation at the protected side. With the channel the discharge in this width of the percolation should be collected and drained according to Fig. 2. The depression S_0 related to the water table developed (or permitted) at the downstream face might be found with the aid of the familiar relationship

$$S_0 = \frac{2Q_1 \varphi}{k_1 \pi^2} \ln \frac{T_a}{D}. \tag{18}$$

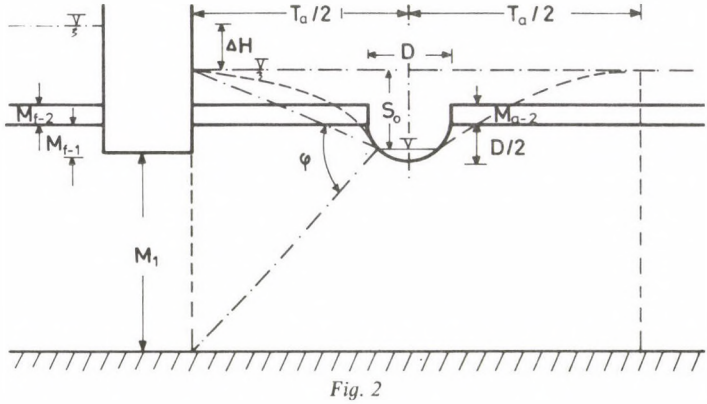

Fig. 2

In case of drainage by a fully-penetrating well (i.e., ideal well) Eq. (14) takes the following form

$$B_1 = L_0 + k_1 \frac{M_{f-2}\lambda_{f-2}}{\alpha_f k_{f-2}} + \frac{\lambda_1 M_{f-1}}{\alpha_f} \tag{19}$$

and

$$C = \frac{\lambda}{\alpha_f} + \alpha_f . \tag{20}$$

The discharge arriving in a well of r_0 radius in a series of wells located at a distance 2ρ, is $Q_k = 2\rho Q_1$. The depression $S_0 = H - h_0$ may be calculated from the relationship (Fig. 3):

$$H^2 - h_0^2 = \frac{\rho Q_1}{k_1 \pi} \ln \frac{\rho}{r_0} . \tag{19/a}$$

In case of several water-bearing strata to be found under the footing of the project, the discharge of the percolation might be evaluated by making use of the familiar assumption in accordance with which the possible movement may be separated no matter along which streamline, and the remaining part of the flow pattern remains unchanged. It is also evident that the maximum of the percolation discharge will develop by all means.

In view of the above assumptions, with respective application of the deduction presented in the foregoing, in accordance with Fig. 4, in case of a project with its footing laid on the bottom plane of the upper confining bed or above it, under the footing n

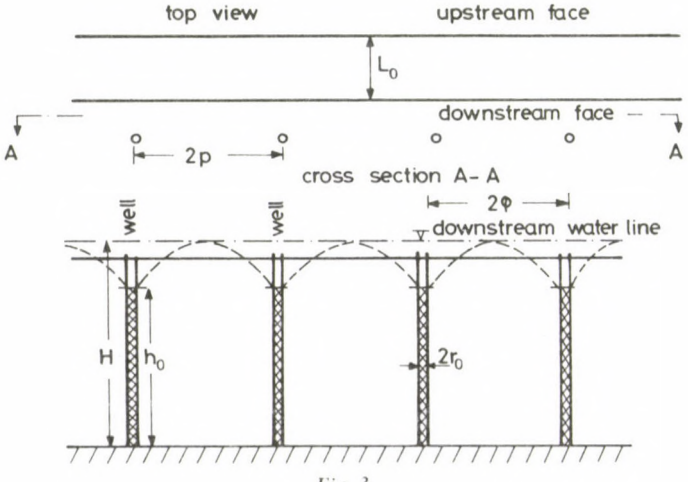

Fig. 3

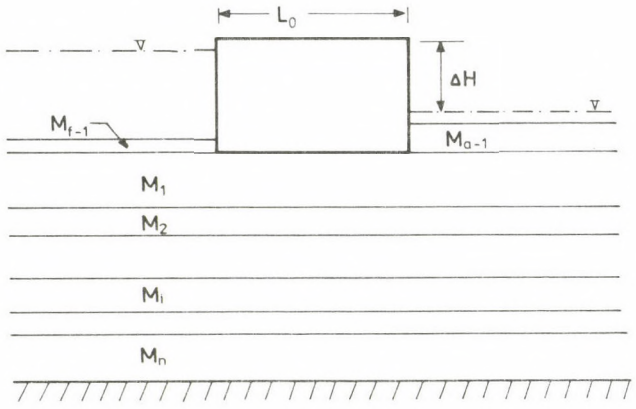

Fig. 4

permeable strata having been developed, in whichever *i*the layer, the discharge of percolation may be calculated as follows

$$Q_i = \Delta H k_{hi} \left[\frac{1}{C_i} \ln \frac{C_i \sum_1^{i-1} M_i + B_i}{B_i} - \frac{1}{C_i^*} \ln \frac{C_i^* \sum_1^{i} M_i + B_i^*}{B_i^*} \right] \tag{21}$$

wherein

$$C_i = \left(\frac{1}{\alpha_{fi}} + \frac{1}{\alpha_{ai}} \right) \lambda_i + \alpha_{fi} + \alpha_{ai}\,, \tag{22}$$

$$B_i = L_0 + \left(\frac{M_f \lambda_f}{k_f} \right)_i \frac{k_i}{\alpha_{fi}} + \left(\frac{M_a \lambda_a}{k_a} \right)_i \frac{k_i}{\alpha_{ai}}\,, \tag{23}$$

$$C_i^* = \left(\frac{1}{\alpha_{fi-1}} + \frac{1}{\alpha_{ai-1}} \right) \lambda_i + \alpha_{fi-1} + \alpha_{ai-1}\,, \tag{24}$$

$$B_i^* = L_0 + \left(\frac{M_f \lambda_f}{k_f} \right)_i \frac{k_i}{\alpha_{fi-1}} + \left(\frac{M_a \lambda_a}{k_a} \right)_i \frac{k_i}{\alpha_{ai-1}} \tag{25}$$

with product

$$\left(\frac{M_f \lambda_f}{k_f} \right)_i$$

characterizing an upper confining bed at upstream side of the project along section where water percolating through *i*-th layer passes through the confining bed.

Thus, with the above calculation method several kinds of confining beds could be considered, both at the upstream and downstream sides.

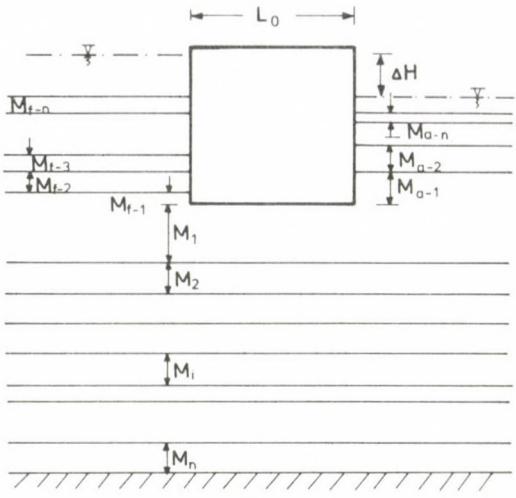

Fig. 5

Should the project be constructed with a deep foundation, as is to be seen, in Fig. 5 so the percolation discharge in the i-th layer as well as the values C_i and C_i^* satisfy the relationships (21), (22) and (24), however,

$$B_i = L_0 + \lambda_i \left(\frac{M_{f-1}}{\alpha_{fi}} + \frac{M_{a-1}}{\alpha_{ai}} \right) + \\ + k_i \left[\frac{1}{\alpha_{fi}} \left(\sum_{e=-2}^{-n} \frac{M_{fe} \lambda_{fe}}{k_{fe}} \right)_i + \frac{1}{\alpha_{ai}} \left(\sum_{e=-2}^{-n} \frac{M_{ae} \lambda_{ae}}{k_{ae}} \right)_i \right] \tag{26}$$

and

$$B_i^* = L_0 + \lambda_i \left(\frac{M_{f-1}}{\alpha_{fi-1}} + \frac{M_{a-1}}{\alpha_{ai-1}} \right) + \\ + k_i \left[\frac{1}{\alpha_{fi}} \left(\sum_{e=-2}^{-n} \frac{M_{fe} \lambda_{fe}}{k_{fe}} \right)_i + \frac{1}{\alpha_{ai}} \left(\sum_{e=-2}^{-n} \frac{M_{ae} \lambda_{ae}}{k_{ae}} \right)_i \right] \tag{27}$$

It is desirable to know the distribution pattern of the percolation discharge within each of the layers, so the thicknesses M_i of the layers should be replaced by the variable value $M_i > m$.

A significant objective of the analyses is the determination of the exit gradient at the downstream face of the dam as well as the values of the pressures developing under the dam.

In the instance of the existence of an upper confining bed, the exit gradient is given by the formula

$$I_k = \frac{h_a}{M_{fa}} . \tag{28}$$

In the case represented in Fig. 4, the pressure loss occurring at the downstream face of the project, immediately at its edge, might be obtained by using the equation

$$h_a = \frac{M_{fa}}{\alpha_a k_{fa}} \left[\frac{dQ_1}{dm}\right]_{m=0}, \tag{29}$$

wherein

$$\left[\frac{dQ_1}{dm}\right]_{m=0} = -\frac{k_{1h}\Delta H}{B_1},$$

wherefore

$$I_k = \frac{k_{1h}\Delta H}{k_{fa}\alpha_a B_1}; \qquad h_a = \frac{M_{fa} k_{1h}\Delta H}{k_{fa}\alpha_a B_1}. \tag{30}$$

The value of B_1 can be taken from the relationship (26), i.e., for the first layer from the relationship (14). With a project built without sheet piling or deep foundation, the value of b is equal to zero.

In evaluating the water discharge the streamlines are approximated by angular ones. Therefore, for making the value of the water discharge more exact, one uses a coefficient of correction.

In determining the coefficient of correction one should start from the fact that the rectilinear streamline assumed is actually an ellipse (Fig. 6). Should—with a certain safety—only the extreme streamlines be transformed into ellipses, and the reduction so obtained applied, one can obtain the following value for the coefficient of correction:

$$\vartheta = \frac{4.64(M_1 + L_0^*)}{L_0^* + 4\sqrt{M_1^2 + \frac{3L_0^{*2}}{4}}}.$$

Good approximate values are indicated as the function of L_0^* in Table 1. This coefficient of correction is, at the same time, the difference between the exact and approximate method suggested. It is to be seen that actually the difference hardly exceeds 1 or 2 per cent, even in case where there is no upper confining bed.

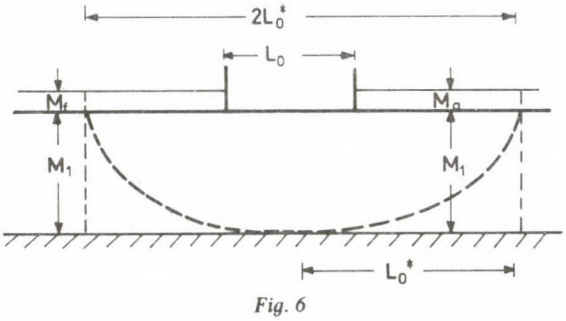

Fig. 6

Table 1

$\frac{\sum_1^i M_i}{L_0^* + \sum_1^i (T_{ia} + T_{if})}$	0.01	0.02	0.05	0.1	0.2	0.3	0.5	1.0
ϑ	1.005	1.01	1.02	1.05	1.09	1.13	1.18	1.27

The coefficient of correction can be applied to each of the water-bearing stratum by making use of the equation

$$\vartheta_i = \frac{4.64\left[\sum_1^i M_i + L_0^* + \sum_1^i (T_{if} + T_{ia})\right]}{L_0^* + \sum_1^i (T_{if} + T_{ia}) + 4\sqrt{\sum_1^i M_i + \frac{3}{4}\left[L_0^* + \sum_1^i (T_{if} + T_{ia})\right]^2}} \tag{31}$$

Thus, the corrected value of the water discharge is

$$Q_j = \vartheta Q\,. \tag{33}$$

The phenomena of percolation do not take place, in general, in the plane but in the space. Therefore, the analysis of the percolation is very important. The analysis of the spatial percolation is not so easy to perform, as that of the plane. Therefore, certain cases which can be resolved are presented and, on the basis of these approximate generalization will be concluded.

The analyses are carried out in several ways of approximation. In certain cases the confining beds are taken into account while in others, are not.

In case of percolation in space the distribution shown in Fig. 7 might be used as a good approximation. The percolation down below in its one-third part in the middle (region I) might be regarded as planar. Then follows the percolation in space in region

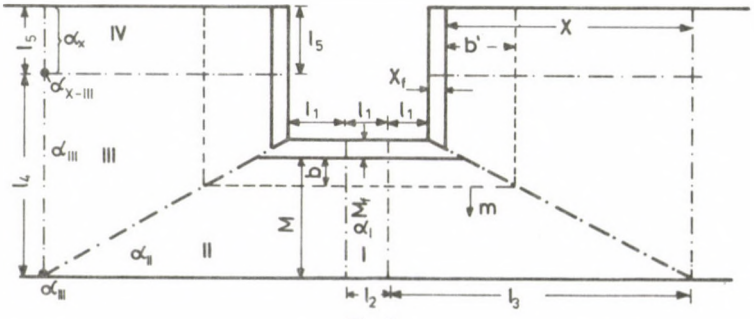

Fig. 7

II, and that along the side below in region III while at the upper half side again a kind of percolation which also may be considered to be planar (region IV).

The discharge of the plane percolation down below and at the side (regions I and IV) can be evaluated by making use of Eq. (17) after practical transformation:

$$Q_{\mathrm{I}} = \frac{k_1 \Delta H l_1}{C_{\mathrm{I}}} \ln \frac{B_{\mathrm{I}} + C_{\mathrm{I}}(M_1 - b)}{B_{\mathrm{I}}}, \tag{34}$$

wherein

$$B_{\mathrm{I}} = L_0 + \frac{2k_1 M_f}{k_f \alpha} + \frac{2\lambda b}{\alpha},$$

$$C_{\mathrm{I}} = \frac{2\lambda}{\alpha} + 2\alpha,$$

$$Q_{\mathrm{IV}} = \frac{k_1 \Delta H l_5}{C_{\mathrm{IV}}} \ln \frac{B_{\mathrm{IV}} + C_{\mathrm{IV}} X_1}{B_{\mathrm{IV}}}, \tag{35}$$

with

$$B_{\mathrm{IV}} = L_0 + \frac{2k_1 X_f}{k_x \alpha_x} + \frac{2b'}{\alpha_x}, \tag{36}$$

$$C_{\mathrm{IV}} = \frac{2\lambda}{\alpha_x} + 2\alpha_x. \tag{37}$$

First, Q is calculated in the known way. Thus, its values are obtained for region I. Thereafter, with the knowledge of X_1 the values of α_x will be evaluated for region IV, trying to find the maximum value of Q_{IV} for the X direction. In general $\alpha \neq \alpha_x$. The values of α_{II} and α_{III} needed for the calculation of the other parts of space may be found from the values α and α_x as follows:

$$\alpha_5 = \alpha + \frac{\alpha_x - \alpha}{l_1 + l_5} l_1,$$

whence

$$\alpha_{\mathrm{II}} = \frac{\alpha_5 + \alpha}{2}$$

and

$$\alpha_{\mathrm{III}} = \frac{\alpha_5 + \alpha_x}{2}.$$

With these quantities known, water discharges of space parts II and III may be obtained without further using the method of successive approximation.

Should the area not be determined horizontally, i.e., the value of X is not known, so its maximum empirical value to be considered is

$$X = \frac{T_a + T_f + L_0}{\lambda},$$

$$l_3 = X_1 + X_f + l_1. \tag{38}$$

In Fig. 7 the cross section of the headrace canal in front of the project is depicted from which water is percolating outwards. (The cross section of the downstream channel as that in Fig. 7. By way of information also the natural confining bed is indicated in the figure, however, it has no significance in the case of the present investigation.)

For the evaluation of the percolation round the corner, this is to be divided into two parts, i.e., a vertical section of height l_5 (region III) and a horizontal one of width l_1 (region II), and the evaluation is to be accomplished separately.

Along the lower section of width l_1 (region II), due to the change of the space of percolation in the vertical direction, the water discharge can be obtained by two consecutive integrations as follows.

The discharge percolating vertically through the confining bed is

$$\mathrm{d}Q = k_f \frac{\mathrm{d}h_1}{\mathrm{d}m_f} X_f \, \mathrm{d}y \,, \tag{39}$$

wherein

$$X_f = l_1 + am_f \,,$$

with

$$a = \frac{l_3 - l_1}{M + M_f} \,,$$

whence

$$\mathrm{d}Q = k_f \frac{\mathrm{d}h_1}{\mathrm{d}m_f} (l_1 + am_f) \, \mathrm{d}y \,,$$

therefore,

$$\mathrm{d}h_1 = \frac{\mathrm{d}Q}{\mathrm{d}y} \frac{1}{k_f} \frac{\mathrm{d}m_f}{l_1 + am_f} \,. \tag{40}$$

After integration, the replacement of the limits yields

$$h_1 = \frac{\mathrm{d}Q}{\mathrm{d}y} \frac{1}{k_f a} \ln \frac{l_1 + aM_f}{l_1} \,, \tag{41}$$

with designations to be seen in Fig. 7.

Should the confining bed at the downstream side be the same as that at the upstream side, so

$$h_2 = h_1 \tag{42}$$

In the water-bearing stratum, if the impervious curtain wall of depth b sinks into the water-bearing stratum, the discharge of the vertical percolation is as follows:

$$\mathrm{d}Q = \frac{k_1}{\sqrt{\lambda}} \frac{\mathrm{d}h_{vf}}{\mathrm{d}m} (l_1 + am) \, \mathrm{d}y \,,$$

whence, by integration between the limits and 0 one obtains

$$h_{vf} = \frac{\mathrm{d}Q}{\mathrm{d}y}\frac{\sqrt{\lambda}}{ak_1}\ln\frac{l_1+am}{l_1}. \tag{43}$$

Considering that "confining" beds of the very same resistance are assumed both at the downstream and upstream faces in agreement with the practice, at the downstream face the resistance of the water arising in the water-bearing stratum is given by the equation (43), i.e.,

$$h_{vf} = h_{va}. \tag{44}$$

The discharge percolating horizontally in the water bearing stratum is

$$\mathrm{d}Q = k_1 \frac{\Delta H - (h_1 + h_2 + h_{vf} + h_{va})}{2y + L_0}(l_1 + am)\,\mathrm{d}m \tag{45}$$

because of $y = \alpha m$ and $\mathrm{d}y = \alpha\,\mathrm{d}m$, replacement of (41), (42), (43) and (44) into Eq. (45) after rearrangement yields

$$\frac{\mathrm{d}Q}{\mathrm{d}m}\left[\frac{2\alpha m + L_0}{k_1(l_1+am)} + \frac{2}{a\alpha k_f}\ln\frac{l_1+aM_f}{l_1} + \frac{2\sqrt{\lambda}}{\alpha a k_1}\ln\frac{l_1+am}{l_1}\right] = \Delta H, \tag{46}$$

whence

$$\mathrm{d}Q = \frac{k_1 \Delta H\,\mathrm{d}m}{\frac{2\alpha m + L_0}{l_1+am} + \frac{2k_1}{a\alpha k_f}\ln\frac{l_1+aM_f}{l_1} + \frac{2\sqrt{\lambda}}{a\alpha}\ln\frac{l_1+am}{l_1}} \tag{47}$$

after rearrangement, carrying out the division expressed by the first term of the denominator and introducing the designation $l_1 + am = x$ from which $\mathrm{d}x = a\,\mathrm{d}m$, $am = x - l_1$, the equation appears in the form:

$$\frac{\mathrm{d}Q}{0.5\,k_1\Delta H} = \frac{\mathrm{d}x}{\frac{\alpha(x-l_1)+\frac{aL_0}{2}}{x} + \frac{k_1}{\alpha k_f}\ln\frac{l_1+aM_f}{l_1} - \frac{\sqrt{\lambda}}{\alpha}\ln(l_1) + \frac{\sqrt{\lambda}}{\alpha}\ln(l_1+am)}. \tag{48}$$

By introducing the designations

$$A = \frac{k_1}{\alpha k_{f-2}}\ln\frac{l_1+aM_{f-2}}{l_1} - \frac{\sqrt{\lambda}}{\alpha}\ln l_1 + \alpha,$$

$$C=\frac{aL_0}{2}-\alpha l_1\,,$$

$$D=\frac{\sqrt{\lambda}}{\alpha}\,,$$

Equation (48) may be written in the form

$$\frac{\mathrm{d}Q}{0.5\,k_1\,\Delta H}=\frac{\mathrm{d}x}{A+\dfrac{C}{x}+D\ln x}\,. \tag{49}$$

In the course of the investigations, the value of x changes between two and 10. Along this section the logarithmic function can well be approximated by the function

$$\ln x\simeq 2.8\left(\frac{x-1}{x}\right)^2.$$

Therewith, one obtains

$$\frac{\mathrm{d}Q}{0.5\,k_1\,\Delta H}=\frac{\mathrm{d}x}{A+\dfrac{C}{x}+2.8\left(\dfrac{x-1}{x}\right)^2}\,. \tag{50}$$

Performing the squaring and the rearrangement of the denominator in accordance with x then, multiplying both the numerator and the denominator with x^2, the equation reads as follows

$$\frac{\mathrm{d}Q}{0.5\,k\Delta H}=\frac{x^2\,\mathrm{d}x}{(A+2.8\,D)x^2+(C-5.6\,D)x+2.8\,D}\,. \tag{51}$$

By using the designations

$$A+2.8\,D=p\,, \tag{52}$$

$$C-5.6\,D=r\,, \tag{53}$$

$$2.8\,D=v \tag{54}$$

one obtains

$$\frac{\mathrm{d}Q}{0.5\,k_1\,\Delta H}=\frac{x^2\,\mathrm{d}x}{px^2+rx+v}\,. \tag{55}$$

Performing the division of the numerator with the denominator results

$$\frac{\mathrm{d}Q}{0.5\,k_1\,\Delta H}=$$

$$=\left[\frac{1}{p}-\frac{r}{p^2}\frac{1}{x}+\left(\frac{r^2}{p^3}-\frac{v}{p^2}\right)\frac{1}{x^2}-\frac{r^3}{p^4}\frac{1}{x^3}+\left(\frac{r^5}{p^5}-\frac{r^2v}{p^4}+\frac{v^2}{p^3}\right)\frac{1}{x^4}\right]\mathrm{d}x\,. \tag{56}$$

By the integration of each term separately, and using the following limiting values

$$\text{if} \quad m = M - b, \qquad \text{so} \quad x = l_1 + a(M-b) \qquad \text{and}$$

$$\text{if} \quad m = 0, \qquad \text{so} \quad x = l_1,$$

yields the discharge

$$Q = 0.5\, k_{ah}\, \Delta H \left\{ \frac{a(M-b)}{p} - \frac{r}{p^2} \ln \frac{l_1 a(M-b)}{l_1} - \right.$$

$$- \frac{r - pv}{p^3} \left(\frac{1}{l_1 + a(M_1 - b)} - \frac{1}{l_1} \right) + \frac{r^3}{2p^4} \left[\frac{1}{l_1 + a(M-b)^2} - \frac{1}{(l_1)^2} \right] -$$

$$\left. - \frac{r^4 - pr^2 v + p^2 v^2}{3p^5} \left[\frac{1}{l_1 + a(M-b)^3} - \frac{1}{(l_1)^3} \right] \right\}, \tag{57}$$

wherein

$$p = \frac{k_1}{\alpha k_f} \ln \frac{l_1 + aM_f}{l_1} - \frac{\sqrt{\lambda}}{\alpha} \ln (l_1) + \frac{2.8\sqrt{\lambda}}{\alpha} + \alpha, \tag{58}$$

$$r = \frac{aL_0}{2} - \alpha_f l_1 - \frac{5.6\sqrt{\lambda}}{\alpha}, \tag{59}$$

$$v = \frac{2.8\sqrt{\lambda}}{\alpha}, \tag{60}$$

$$a = \frac{l_3 - l_1}{M + M_f} = \frac{X + X_f}{M + M_f}. \tag{61}$$

According to the experiences obtained, it is sufficient practically to consider only the first two terms of the equation which results in the following relationship

$$Q_{II} = 0.5\, k_1\, \Delta H \left[\frac{a(M-b)}{p} - \frac{r}{p^2} \ln \frac{l_1 + a(M-b)}{l_1} \right]. \tag{62}$$

Under such geological conditions the maximum of the function (62) should be sought by changing the values of α and a.

Should the geological structure be as shown in Fig. 7, so the component of the percolation around the corner directed downwards is to be calculted by making use of the relationship (62).

The water discharge in region III can be evaluated with the aid of the relationship (62) transformed in accordance with the notation to be seen in Fig. 7.

$$Q_{III} = 0.5\, k_1\, \Delta H \left[\frac{\acute{a}(X-b')}{p'} - \frac{r'}{p'^2} \ln \frac{l_5 + \acute{a}(X-b')}{l_5} \right], \tag{63}$$

wherein

$$p' = \frac{k_1}{\alpha_X k_x} \ln \frac{l_5 + \acute{a} X_f}{l_5} - \frac{\sqrt{\lambda}}{\alpha_x} \ln l_5 + \alpha_x \frac{2.8\sqrt{\lambda}}{\alpha_x}, \tag{64}$$

$$r' = \frac{\acute{a} L_0}{2} - \alpha_x l_5 - \frac{5.6\sqrt{\lambda}}{\alpha_x}, \tag{65}$$

$$\acute{a} = \frac{l_4 - l_5}{X + X_f} = \frac{M + M_f}{X + X_f} = \frac{1}{a}. \tag{66}$$

Thus, the total of the percolation discharge around the project is given by the following summation of the values of discharges found by using the relationships (62), (63), (64) and (65)

$$Q = Q_{\mathrm{I}} + 2Q_{\mathrm{II}} + 2Q_{\mathrm{III}} + 2Q_{\mathrm{IV}}. \tag{67}$$

In case of a narrow project where the value of $3l_1$ is lower or only a little higher than that of $2l_5$, the region I of the lower percolation should be omitted whereby, the regions II of both sides join with each other, i.e., l_1 means the half width of the project; should the value of $2l_5$ be lower than that of l_1, so, by omitting region IV, the value of l_5 will mean the total height. Also in the case of this calculation the value of α_{opt} should be evaluated from the maximum value of Q_5, or Q_{IV} is to be omitted but the values of α_{II} and α_{III} should be calculated from the values of α_{opt}.

Obviously, if no such surfaces occur in the channel which would significantly reduce the rate of percolation (for example, covering or colmated layer) then $M_f = 0$, $X_f = 0$ and the equations will be somewhat simpler.

The pressures applied to the elements of the boundary surfaces (sides, underside) at certain preferred points can be evaluated with the use of relations (41) and (43); at the underside of the colmated layer and at any point of the water bearing stratum at a

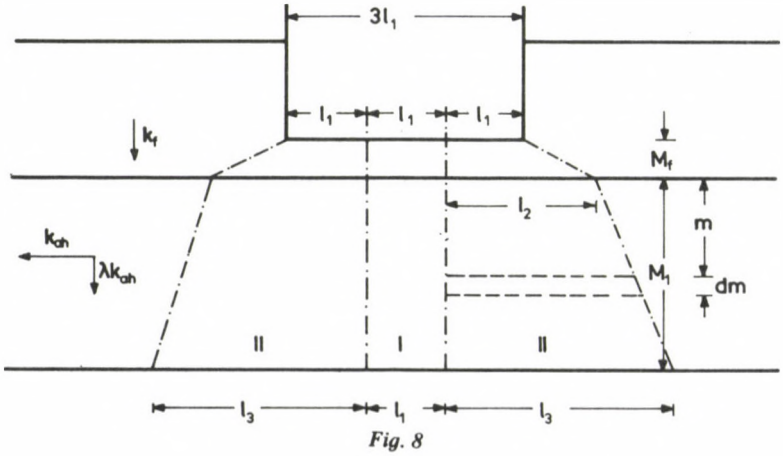

Fig. 8

depth designated with m. Owing to the assumed symmetry of the stratification the values at the upstream and the downstream sides are symmetrical. At the upstream side h_1, i.e., h_{v1} is to be subtracted, whereas at the downstream side h_2, i.e., is to be added to H.

In case where the geological structure corresponds to that depicted in Fig. 8, the percolation rate at the side of the project has no significance. The percolation discharge below the underside slab might be calculated as follows.

First, by assuming the discharge percolating vertically under the project to be plane percolation in the middle 3rd of the underside, one evaluates the discharge by using Eq. (34). At the same time, besides $Q_{\mathrm{I\,max}}$ also the optimum value of α is obtained.

In the second part of space, the calculation of the percolation discharge is to be performed in the following way.

The loss in discharge percolating through the upper confining bed agrees with that expressed by the relationship (41).

$$h_1 = \frac{\mathrm{d}Q}{\mathrm{d}y}\frac{1}{a_f k_f}\ln\frac{l_1 + a_f M_f}{l_1} \tag{68}$$

with

$$a_f = \frac{l_2 - l_1}{M_f}. \tag{69}$$

The height of loss in discharge of the vertical percolation through the water-bearing stratum is given by the equation

$$h_{vf} = \frac{\mathrm{d}Q}{\mathrm{d}y}\frac{\lambda}{a_1 k_1}\ln\frac{l_2 + a_1 m}{l_2} \tag{70}$$

with

$$a_1 = \frac{l_3 - l_2}{M_1}. \tag{71}$$

The discharge percolating horizontally through water bearing stratum may be found by the relationship

$$\mathrm{d}Q = k_h \frac{\Delta H - 2h_1 - 2_{h_{v1}}}{2y + L_0}(l_2 + a_1 m)\,\mathrm{d}m. \tag{72}$$

Substitution of Eqs (68) and (70) into Eq. (72) and factoring out dQ, yields

$$\mathrm{d}Q = \frac{k_1 \Delta H\,\mathrm{d}m}{\dfrac{2\alpha m + L_0}{l_2 + a_1 m} + \dfrac{2k_1}{a_f k_f \alpha}\ln\dfrac{l_1 + a_f M_f}{l_1} + \dfrac{2\lambda}{a_1 \alpha}\ln\dfrac{l_2 + a_1 m}{l_2}} \tag{73}$$

By determining the value of Q on the analogy with the relationships (47) to (72) one obtains

$$Q_{\mathrm{II}} = 0.5\, k_1 \Delta H\left[\frac{a_1 M_1}{p^0} - \frac{r^0}{p^{02}}\ln\frac{l_2 + a_1 M_1}{l_2}\right], \tag{74}$$

wherein

$$p^0 = \frac{a_1 k_1}{\alpha_{a_f k_f}} \ln \frac{l_1 + a_f M_f}{l_1} - \frac{\lambda}{\alpha} \ln l_2 \frac{2.8\,\lambda}{\alpha} + \alpha\,, \tag{75}$$

$$r^0 = \frac{a_1 L_0}{2} - \alpha l_2 \frac{5.6\,\lambda}{\alpha}\,. \tag{76}$$

The maximum discharge may be found by varying the value of l_2 in Eq. (74) while one assumes the value of l_3

$$l_3 = \left(3\frac{\lambda k_1}{k_f} - 0.5\right) l_1$$

to be constant.

The total of the percolation discharge is

$$Q = Q_I + 2Q_{II}\,.$$

Should the value of the coefficient of percolation not be lower by an order of magnitude than that of the lower layer, so by considering the side percolation to be of plane character, also the discharge of region IV might be determined. However, this might be, in general, omitted.

In case of the type of geological environment represented in Fig. 9 which frequently occurs in river valleys, as a first step of the calculation, the side percolation in region IV is to be determined. Should the maximum discharge be developed at a width larger than the distance X, so the discharge percolating through region IV should be evaluated by calculating with the actual X distance. As a matter of course, also the geometrical assumptions of regions II and III will be fitted into this condition.

The flow space represented in Fig. 8 will present itself also in that case where the sheet walls are introduced into the slopes of the valley. In such cases, the water discharge in the middle third (region I) should be evaluated in accordance with the

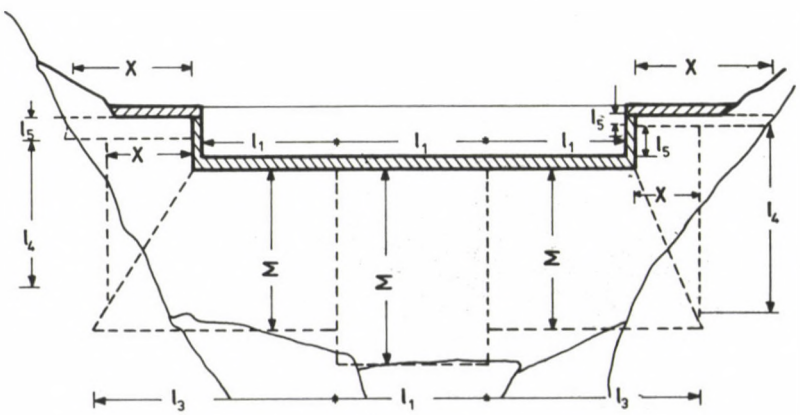

Fig. 9

notation used for the profile and the cross section shown in Fig. 1 and Fig. 8 respectively, by making use of Eq. (34). The water discharge in region II is expressed by the formula

$$Q_{II} = 0.5\, k_h \Delta H \frac{a_1 M_1}{p^0} - \frac{r^0}{p^{02}} \ln \frac{l_2 + a_1(M_1 - b)}{l_2}$$

where the values of p^0 and r^0 can be taken from the relationships (75) and (76) respectively.

References

1. Juhász, J.: Analysis of percolation under dams in case of thick water-bearing stratum. (in Hungarian). Hidrológiai Közlöny (1968), No. 8.
2. Juhász, J.: Certain instances of percolation under dams. (in Hungarian). Hidrológiai Közlöny, (1969), No. 8.
3. Juhász, J.: Hidrogeológia. Akadémiai Kiadó, Budapest 1976.
4. Ujfaludi, L.: Evaluation of percolation discharge in case of hydraulic structures founded on double-layer ground. (in Hungarian). Hidrológiai Közlöny (1981), No. 7.
5. Haszpra, O.: Evaluation by successive approximation of unconfined percolation in space with the aid of conductive-liquid analogue. (in Hungarian). Hidrológiai Közlöny (1978), No. 12.
6. Galli, L.: Evaluation of percolation under hydraulic projects in stratified grounds by the method of successive approximation. (in Hungarian). Vízügyi Közlemények (1959), No. 3.
7. Ujfaludi, L.: Evaluation of percolation discharge in base of hydraulic structures founded on double-layer ground. (in Hungarian). Vízügyi Közlemények, (1981), No. 12.
8. Ujfaludi, L.: Three-dimensional percolation in the ambiance of hydraulic projects. (in Hungarian). Hidrológiai Közlöny (1982), No. 8.

Acta Technica Academiae Scientiarum Hungaricae, 97 (1—4), pp. 215—225 (1984)

CHARACTERIZATION OF ELLIPTICALLY POLARIZED ANTENNA BY COMPLEX EFFECTIVE LENGTH

J. KAPOR*

[Received: 19 April 1983]

In this paper the interaction of elliptically polarized electromagnetic field and generalized receiving antenna is described by means of complex effective lengths. In the analysis the effective ellipse, similar to the polarization ellipse, is introduced, which gives physical interpretation of complex effective length. The complex effective length—having close relation to the polarization of the antenna—is used for describing the characteristics of elliptically polarised antennas. Based on this analysis it can be stated that the complex effective length is a universal characteristic of antennas and from it all the important antenna parameters can be derived. The complex effective length gives a suitable description of the receiving features of the antenna.

Introduction

The antenna is a transducer which radiates with high efficiency the power conducted on the waveguide or receives electromagnetic waves from the ambient space and converts it into conducted waves. The antenna may be considered as a passive, reciprocal four-pole which is terminated by the waveguide and the specific impedance of free space on the connecting points. In modern technology the antennas frequently contain preamplifier, capacitance diodes or ferrite devices, etc., to meet special requirements, thus creating the active, nonreciprocal class of antennas for which the theory of reciprocity is no longer applicable.

In our case it is assumed, that the antenna does not contain active or nonreciprocal elements and the incident plane wave at the point of reception is originated from a monochromatic source and the monochromatic feature is maintained through the propagation.

The antenna as a four-pole may be characterized by transfer parameters (effective length, effective area), input (input impedance) and output (radiating) parameters. In this paper our attention is focused on the effective area and complex effective length with the aid of which all the important antenna parameters may be expressed.

* J. Kapor, H-1133 Budapest Váci u. 88/a, Hungary

Complex effective length of an elliptically polarized antenna

Looking from the waveguide, the receiving antenna may be considered as an active two-pole (Fig. 1) where the electromotive force of generator V_{emf} and maximally available power P_{max} can be given with the aid of effective length and effective area, respectively. This clear equivalent circuit, which enables the use of simple and effective mathematical description, is valid till the physical processes in the near field of antenna are independent of the incident field strength amplitude.

The effective length (h_{eff}) of a linear, straight receiving antenna according to the equivalent circuit of Fig. 1 is:

$$h_{eff} = \frac{V_{emf}}{E_0} \tag{1}$$

where:

V_{emf} is the source voltage of unloaded antenna
E_0 is the field strength vector component of incident wave parallel to the antenna.

The effective length may be calculated based on the reciprocity theory, as well [1], from the current distribution of transmitting antenna:

$$h_{eff} = \frac{1}{I_0} \int_0^l I(z) \mathrm{d}z \tag{2}$$

where:

I_0 is the amplitude of current
$I(z)$ is the current distribution of antenna placed along the z axis
l is the geometric length of antenna.

In the case of linear, straight antenna the field strength produced by the excitation at an "r" displacement is proportional to this effective length [2]:

$$E_t = \frac{Z_0}{2\lambda r} I h_{eff} \sin \vartheta e^{j(\omega t - \beta r)} \tag{3}$$

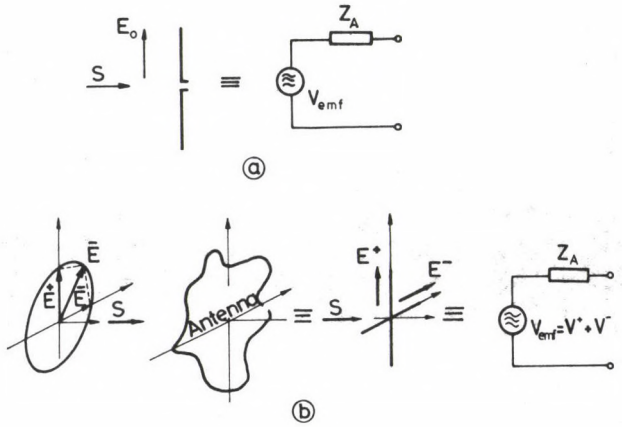

Fig. 1

where

h_{eff} is a scalar value
λ is the wave length
I is the amplitude of the excitation current
ω is the frequency
t is the time
$\beta = \frac{2\pi}{\lambda}$
$Z_0 = 120\ \pi$ Ohm
r; ϑ; φ are polar coordinates.

The receiving properties of a general antenna for an elliptically polarized wave with an optional direction of incident, similar to the linear straight antenna, may be characterized by the effective length. Here the general antenna means an optional kind of elliptically polarized antenna and consequently its effective length will have a complex value. In this case the effective length is not as plausible as with a linear straight antenna, but the unumbiguous relation of incident field strength vector to source voltage of antenna is maintained. Similar to (1), the expression for the general antenna is:

$$V_{\text{emf}} = \bar{E}_{i0} \cdot \bar{h}_r \tag{4}$$

where

$\bar{E}_{i0}$ is the amplitude vector of incident field strength
$\bar{h}_r$ is the complex effective length of receiving antenna.

Based on the reciprocity theory this effective length may be expressed from the radiation parameters in a form similar to (3):

$$\bar{E}_t(\vartheta; \varphi; r; t) = \frac{Z_0}{2\lambda r} I \bar{h}_t(\vartheta; \varphi) e^{j(\omega t - \beta r)} = \frac{\bar{E}_{t0}}{r} e^{j(\omega t - \beta r)}. \tag{5}$$

Using the same antenna for transmission and reception, naturally the complex effective length is the same. This is proved also by the empirical fact, that changing the receiving and transmitting function of an antenna, its polarization remains unchanged. As will be shown later, the effective length of an antenna is proportional to the polarization.

The complex effective length, as well as the polarization, is related to the current distribution along the antenna. The current distribution is determined by the input excitation and the ambient electromagnetic field in the case of transmitting and receiving antenna, respectively. However, we have a clear relation between the geometric features and effective length only in the case of linear straight antennas, as is shown by (2).

In general, the complex effective length ($\bar{h}$) is a function of the polar coordinates (ϑ; φ):

$$\bar{h}(\vartheta; \varphi) = \hat{h}_\vartheta(\vartheta; \varphi)\bar{e}_\vartheta + \hat{h}_\varphi(\vartheta; \varphi)\bar{e}_\varphi \tag{6}$$

where $\hat{h}_\vartheta$ and $\hat{h}_\varphi$ are complex amplitudes independent of time.

$$\hat{h}_\vartheta = |\hat{h}_\vartheta| e^{j\delta_\vartheta},$$

$$\hat{h}_\varphi = |\hat{h}_\varphi| e^{j\delta_\varphi}$$

where

δ_ϑ and δ_φ are optional phases

$\bar{e}_\vartheta$; $\bar{e}_\varphi$ orthogonal unity vectors in the plane of polarization (perpendicular to the vector of propagation)

Relation of effective length and polarization

Comparing the two sides of equation (5), it is evident, that:

$$\bar{E}_{t0}(\vartheta;\varphi)=c\cdot\bar{h}_t(\vartheta;\varphi) \tag{7}$$

where c is constant.

Considering an elliptically polarized wave, propagating forward in a $(\vartheta;\varphi)$ direction and generated by a general antenna, it may be concluded that the ratio of $\bar{E}_0$ amplitude vector and complex effective length of antenna is constant.

Further it means that the polarization properties of a generated field are related (or determined by) the complex effective length, too. Similar to the polarization ellipse, which describes the polarization properties of plane waves, we may define the effective ellipse to describe the complex effective length of source (Fig. 2).

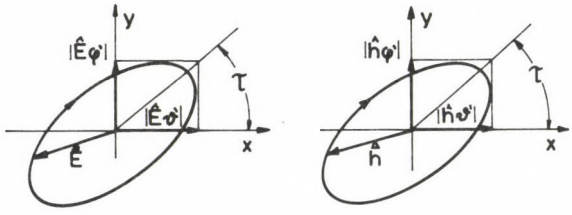

Fig. 2

The effective ellipse can be introduced as follows: Using the complex effective length of the antenna, the $\bar{E}_{t0}$ amplitude at an optional $(\vartheta';\varphi')$ point of space in a plane perpendicular to the propagation, may be written as follows (based on equation (7)):

$$\begin{aligned}\hat{\bar{E}}_{t0}(\vartheta';\varphi')&=c\{|\hat{h}_{\vartheta'}|e^{j\delta_{\vartheta'}}\bar{e}_x+|\hat{h}_{\varphi'}|e^{j\delta_{\varphi'}}\bar{e}_y\},\\ \hat{E}_{\vartheta'}&=c|\hat{h}_{\vartheta'}|e^{j\delta_{\vartheta'}}=|\hat{E}_{\vartheta'}|e^{j\delta_{\vartheta'}}\\ \hat{E}_{\varphi'}&=c|\hat{h}_{\varphi'}|e^{j\delta_{\varphi'}}=|\hat{E}_{\varphi'}|e^{j\delta_{\varphi'}}.\end{aligned} \tag{8}$$

In the plane of the antenna ($z=0$), taking into account the time dependence and omitting the c constant, the component expressions are:

$$\begin{aligned}h_x&=|\hat{h}_{\vartheta'}|\cos(\omega t+\delta_{\vartheta'}),\\ h_y&=|\hat{h}_{\varphi'}|\cos(\omega t+\delta_{\varphi'}).\end{aligned} \tag{9}$$

Eliminating the time variable from (9), an equation similar to the polari ion ellipse can be derived:

$$\frac{h_x^2}{|\hat{h}_{\vartheta'}|^2}+\frac{h_y^2}{|\hat{h}_{\varphi'}|^2}-2\frac{h_x h_y}{|\hat{h}_{\varphi'}||\hat{h}_{\varphi'}|}\cos\delta=\sin^2\delta. \tag{10}$$

$$\delta=\delta_{\vartheta'}-\delta_{\varphi'}.$$

The angle between the great axis of ellipse and the $\bar{e}_x$ unit vector is:

$$\tau=\frac{1}{2}\operatorname{arctg}\frac{2|\hat{h}_{\vartheta'}||\hat{h}_{\varphi'}|\cos\delta}{|\hat{h}_{\vartheta'}|^2-|\hat{h}_{\varphi'}|^2}. \tag{11}$$

For the sake of comparison the equation describing the polarization ellipse of E_{t0} vector [3] is

$$\frac{E_x^2}{|\hat{E}_{\vartheta'}|^2}+\frac{E_y^2}{|\hat{E}_{\varphi'}|^2}-2\frac{E_x E_y}{|\hat{E}_{\vartheta'}||\hat{E}_{\varphi'}|}\cos\delta=\sin^2\delta \tag{12}$$

and the τ angle is:

$$\tau=\frac{1}{2}\operatorname{arctg}\frac{2|\hat{E}_{\vartheta'}||\hat{E}_{\varphi'}|\cos\delta}{|\hat{E}_{\vartheta'}|^2-|\hat{E}_{\varphi'}|^2}. \tag{13}$$

Consequently, we have proved that the polarization of the antenna can be characterized by the effective length and their use are equivalent.

The physical interpretation of complex effective length

The elliptically polarized antenna may be substituted by two orthogonally placed straight antennas of different length in order to give a clear description of the complex effective length. The dipols are considered here to have a geometric length varying with time between $|\hat{h}_\vartheta|$ and "0" and $|\hat{h}_\varphi|$ and "0", respectively. In general, the length variation of two antennas have a δ phase offset. Based on this model, in the case of reception, the V_{emf} source voltage may be characterized by the sum of the voltages of two orthogonally placed antennas:

$$V_{emf}=V'+V''=\hat{E}_{i0\vartheta}\hat{h}_\vartheta+\hat{E}_{i0\varphi}\cdot\hat{h}_\varphi. \tag{14}$$

The maximum of source voltage is obtained, when the polarization of the incident wave is elliptical, the effective ellipses for the receiving antenna are similar, at the same time the great and small axes have the same direction and the describing vectors of the ellipses rotate in the opposite direction. There is no output power from the antenna, if the great axes of polarization and effective ellipses (which are similar) are orthogonal, and the rotating direction of the ellipses are the same. The rotating direction of the ellipses is determined as if looked at from the back of the receiving antenna from the side of the incident wave.

Connection of complex effective length and antenna characteristics

It has been shown that the polarization properties of the antenna at any direction are unambiguously determined by the complex effective length. Now we will prove that the complex effective length, being the transfer parameter of the passive and reciprocal equivalent four-pole of antenna, is suitable for the description of all the important parameters of the antenna.

The most important parameters of antenna (their definitions and basic equations are known [4], [5]):

$-D(\vartheta; \varphi)$ directivity.

The directivity of the antenna at a certain $(\vartheta; \varphi)$ direction:

$$D(\vartheta; \varphi) = \frac{S(\vartheta; \varphi)}{S_a} = \frac{S}{\frac{1}{4\pi}\oint_{4\pi} S \mathrm{d}\Omega} \tag{15}$$

where

$$S(\vartheta; \varphi) = \frac{\bar{E}_{t0}(\vartheta; \varphi)\bar{E}^*_{t0}(\vartheta; \varphi)}{240\pi} \tag{16}$$

is the pointing vector induced by the antenna at a $(\vartheta; \varphi)$ direction.
S_a: is the average of pointing vector on a sphere of radius r; and

$$\mathrm{d}\Omega = \sin\vartheta \mathrm{d}\vartheta \mathrm{d}\varphi$$

In an other form of definition (15) may be obtained by $\bar{E}_{t0}(\vartheta; \varphi) = c \cdot \bar{h}_t(\vartheta; \varphi)$ substitution:

$$D = \frac{\bar{h} \cdot \bar{h}^*}{\frac{1}{4\pi}\oint_{4\pi} \bar{h} \cdot \bar{h}^* \mathrm{d}\Omega}. \tag{17}$$

In the equation (17) there are no indices, since as it has been previously shown the complex effective length of the antenna is the same in both transmitting and receiving.

$-g(\vartheta; \varphi)$ and $f(\vartheta; \varphi)$ power and voltage antenna patterns, respectively.

The right side of equation (17) is multiplied by

$$\frac{\bar{h}_{\max} \cdot \bar{h}^*_{\max}}{\bar{h}_{\max} \cdot \bar{h}^*_{\max}} = 1$$

where $\bar{h}_{\max}$ denotes the complex effective length in the direction of maximum reception.

By rearranging the equation, we obtain

$$D = D_{\max} \frac{\bar{h} \cdot \bar{h}^*}{\bar{h}_{\max} \cdot \bar{h}^*_{\max}}. \tag{18}$$

By comparing Eq. (18) and the well-known expression

$$D = D_{\max} \cdot g(\vartheta; \varphi), \tag{19}$$

one can obtain the power antenna pattern:

$$g(\vartheta; \varphi) = \frac{\bar{h} \cdot \bar{h}^*}{\bar{h}_{\max} \cdot \bar{h}^*_{\max}} = \frac{|\bar{h}|^2}{|\bar{h}_{\max}|^2}. \tag{20}$$

According to this, the voltage antenna pattern is:

$$f(\vartheta; \varphi) = \sqrt{g(\vartheta; \varphi)} = \frac{|\bar{h}|}{|\bar{h}_{\max}|} \tag{21}$$

– R_r radiating resistance.

The maximum of power obtained from a matched antenna is:

$$P_{\max} = \frac{V_{\text{emf}} \cdot V^*_{\text{emf}}}{8R_r}. \tag{22}$$

From the relation of $P_{\max}$ and effective area (A_e) of antenna:

$$P_{\max} = A_e \cdot S = \frac{\lambda^2}{4\pi} D \cdot S. \tag{23}$$

From Eqs (22) and (23) one can obtain:

$$R_r = \frac{\pi}{2\lambda^2} \frac{V_{\text{emf}} V^*_{\text{emf}}}{S \cdot D}. \tag{24}$$

Substituting (4), (16) and (17) into (24) the radiating resistance is:

$$R_r = \frac{30\pi}{\lambda^2} \oint_{4\pi} \bar{h} \cdot \bar{h}^* \mathrm{d}\Omega. \tag{25}$$

Another form of (25) may be obtained by substituting the double integral from the expression of directivity (Eq. 17):

$$R_r = 30 \left(\frac{2\pi}{\lambda}\right)^2 \frac{|\bar{h}|^2}{D}. \tag{26}$$

In the case of an antenna loss without this equals the real part of its input impedance.

– T_A noise temperature.

A receiving antenna placed in the free space inherently receives—besides the waves of a wanted source—the fields of different noise sources. The effect

of noise sources can be taken into account by the T_A noise temperature of antenna:

$$T_A = \frac{1}{4\pi} \oint_{4\pi} D(\vartheta; \varphi) T(\vartheta; \varphi) \mathrm{d}\Omega \tag{27}$$

where $T(\vartheta; \varphi)$ is the noise temperature distribution in the ambiente of the antenna.

The definition of T_A by using the complex effective length:

$$T_A = \frac{1}{4\pi} \frac{D_{\max}}{|\bar{h}_{\max}|^2} \oint_{4\pi} \bar{h} \cdot \bar{h}^* \cdot T \mathrm{d}\Omega. \tag{28}$$

Effective area of elliptically polarized antenna

The most important antenna parameters have been previously determined based on the complex effective length of antenna, however the effective area, the other transfer parameter, is equally suitable for this purpose. In the description of the interaction of the antenna and electromagnetic field both parameters give simple and clear expressions. In the followings the effective area of elliptically polarized antenna is given. In the derivation the matching conditions of antenna and load as well as polarization of incident wave is taken into account:

The definition of effective area (A_e) of antenna is:

$$A_e = \frac{P_{\max}}{S_0} = \frac{V_{\mathrm{emf}} V_{\mathrm{emf}}^*}{8 R_r S} \tag{29}$$

where $P_{\max}$ is the maximum output power obtained from the matched antenna

S_0 is the power density in the direction of main lobe of antenna.

The relation of effective area and gain is well known:

$$A_e = \frac{\lambda^2}{4\pi} G_{\max} = \frac{\lambda^2}{4\pi} D_{\max} \cdot \eta_R \tag{30}$$

where $G_{\max}$ and $D_{\max}$ are the gain and directivity toward the main lobe

η_R is a coefficient describing the dissipative loss.

In the case of an antenna without loss:

$$G = D \qquad \text{and} \qquad A_e = A_{e\max}.$$

Equation (30) refers to a hypothetic, perfectly matched antenna receiving a plane wave in the direction of a main lobe, providing that the complex effective length is matched to the polarization of the incoming signal. In real life conditions—in general—these assumptions are not valid and the effective area is a function of—besides $(\vartheta; \varphi)$ coordinates—the matching to the load and to the polarization of incident wave.

These factors may be taken into account in a generalised version of Eq. (30), [6], [7]:

$$A_e(\vartheta; \varphi) = \frac{\lambda^2}{4\pi} D \eta_R \eta_\Gamma \eta_P, \tag{31}$$

or by using the complex effective length of receiving antenna Eq. (17):

$$A_e = \lambda^2 \eta_R \eta_\Gamma \eta_P \frac{\bar{h}_r \bar{h}_r^*}{\oint_{4\pi} \bar{h}_r \cdot \bar{h}_r^*}$$

– η_P coefficient.

Assuming that the impedance of antenna and load are $Z_A = R_A + jX_A$ and $Z_L = R_L + jX_L$. respectively, the η_Γ coefficient—describing the matching properties of antenna—is:

$$\eta_\Gamma = \frac{4R_A R_L}{(R_A + R_L)^2 + (X_A + X_L)^2}. \tag{32}$$

We may introduce the Γ reflexion coefficient:

$$\eta_\Gamma = 1 - |\Gamma|^2$$

where

$$\Gamma = \frac{Z_A - Z_L^*}{Z_A + Z_L}.$$

The extreme values of η_Γ refer to the matched antenna ($Z_A = Z_L^*$; $\eta_\Gamma = 1$) and to extreme loads ($Z_L = 0$ or $Z_L = \infty$; $\eta_\Gamma = 0$).

— η_P coefficient

The η_P coefficient characterizes the matching between the polarization of incident wave and complex effective length of antenna. Assuming an antenna without loss and a matched load, the effective area is:

$$A_e = \frac{V_{emf} \cdot V_{emf}^*}{8R_r \cdot S}. \tag{33}$$

Equation (33) may be simplified by using (4), (16) and (26)

$$A_e = \frac{\lambda^2}{4\pi} D \cdot \frac{|\bar{E}_{i0} \cdot \bar{h}_r|^2}{|\bar{E}_{i0}|^2 |\bar{h}_r|^2}. \tag{34}$$

The η_P coefficient is:

$$\eta_P = \frac{|\bar{E}_{i0} \cdot \bar{h}_r|^2}{|E_{i0}|^2 |\bar{h}_r|^2} . \tag{35}$$

The η_P coefficient can be obtained by using the complex effective length of transmitting and receiving antenna ($\bar{h}_t$ and $\bar{h}_r$) and substituting $\bar{E}_{i0}$ by $c \cdot \bar{h}_t$:

$$\eta_P = \frac{|\bar{h}_t \cdot \bar{h}_r|^2}{|\bar{h}_t|^2 |\bar{h}_r|^2} . \tag{36}$$

Eq. (36) clearly shows that using one of the two identical elliptically polarized antennas for reception and the other for transmission, the polarization matching in the transmission route is not optimal. The maximum of matching polarization can be achieved if the antennas of complex conjugated effective lengths are used. In this case the corresponding effective ellipses are images of each other or there is a certain coefficient by the help of which they become images of each other. This is shown in Fig. 3, where the effective ellipses are drawn in the same plane. The axes of ellipses are complex conjugate of each other and the direction of rotation of $\bar{h}_t$ and $\bar{h}_r$ vectors are the same.

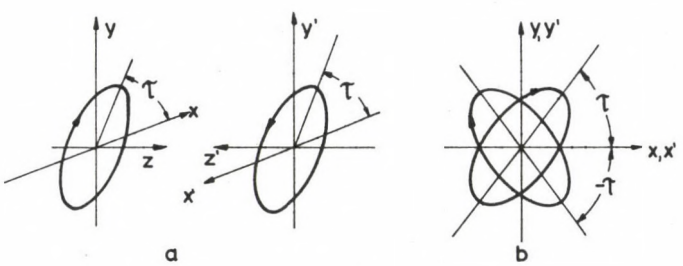

Fig. 3

In reality, a polarized wave originated from a monochromatic source propagates through a non-ideal, noisy environment. The statistically independent, randomly varying noise field which generally originates from the dispersion of waves and the thermic noise of environment, superimposes onto the wanted field and results in a partially polarized wave [7]. In order to take into account this side effect of polarization which becomes a stochastic time variable, Eq. (31) should be generalized [8]. At the same time the effective area, as defined by Eq. (31) and starting assumptions, has a general validity.

Conclusions

In this paper the interaction of elliptically polarized field and a general receiving antenna has been examined according to the model of the antenna shown in Fig. 1. The effective ellipse, which is similar to the polarization ellipse, has been introduced and it

gave a clear interpretation of complex effective length. The use of complex effective length has been generalized for the description of elliptically polarized antennas. According to the analysis given earlier, we can conclude:

— the effective length is characteristic and provides full description;
— with the help of the effective length and according to the given preconditions, a unified way of description can be obtained;
— the calculated (or measured) results obtained in conventional ways and by using the complex effective length show a good correspondance. The complex effective length can be used even for sophisticated situations;
— it is advisable to use the complex effective length in descriptions based on the effective area, as well.

Acknowledgements

I thank Mr. Béla Szekeres, assistant professor, my previous tutor for allowing me inspect his manuscripts about this field. Special thanks go to Dr. Csaba Ferencz who greatly helped with his consultations, in writing this paper.

References

1. Simonyi, K.: Theoretical Electricity. (in Hungarian). Tankönyvkiadó, Budapest 1967.
2. Istvánffy, E.: Waveguides, Antennas and Propagation. (in Hungarian). Tankönyvkiadó, Budapest 1979.
3. Born, Wolf: Principles of Optics. Pergamon Press, Oxford 1975.
4. Almássy, Gy.: Microwave Manual. (in Hungarian). Műszaki Könyvkiadó, Budapest 1973.
5. Kraus, J. D.: Antennas. McGraw-Hill, New York 1950.
6. Kapor, J.: Thesis (in Hungarian). Technical University of Budapest, 1975.
7. Ko, H. C.: On the reception of quasi-monochromatic, partially polarized radio waves. Proc. IRE (1962), 1950.
8. Hansen, R. C.: Microwave Scanning Antennas. Vol. I. Academic Press, New York 1964.

Acta Technica Academiae Scientiarum Hungaricae, 97 (4), pp. 227—239 (1984)

EFFECT OF REAL ROAD PROFILE SPECTRA DISTORTED BY TRAVEL SPEED PROCESSES ON DYNAMIC STRESSES OF TOWN BUSES

MICHELBERGER, P.*, KERESZTES, A., PÉTER, T.

[Received: 12 July 1983]

Our tests showed vehicles in urban traffic to be excited by road profile processes of spectral densities but differing from spectra known from publications but steady-state of second order. In the dynamic design of the high number of urban vehicles the spectrum distorsion should not be neglected. Road profile spectra recorded for fixed trapezoidal run curves exhibit important fluctuations.—Distorted road profile spectra computed from a high number of—even identical—trapezoidal run curves do not, however, fluctuate any longer. For short-distance ($L \leqq 400$ m) run curves individually examined, input and output statistics cease to be Gaussian but for stop spacings $L \leqq 800$ m or under long-time observed urban traffic conditions, linearized vehicle vibrating systems may be expected to undergo Gaussian input-output processes.—Thus, under urban traffic conditions, road profile spectra may be handled as second-order steady-state and Gaussian processes. Real excitational spectra needed for vehicle dynamic design may be produced by the method presented in this paper.

Introduction

Autobuses operating in towns, under normal traffic conditions, travel between two stops accelerating to some 14 to 30 sec then 20 to 40 sec at about constant speed, and 7 to 14 sec slowing down. Bus run curves recorded under real conditions are to be seen in [1].

Neglecting minor speed fluctuations and stop times, the recorded speed-time run curves may be closely approximated by a series of idealized, so-called trapezoidal run curves, where acceleration a_i, constant speed maxima $V_{\max_i}$, decelerations b_i and stop distances L_i are random variables ($i = 1, 2, \ldots, n$).

The high number of vehicles traveling in this mode of operation, describable by idealized run curves, justifies the examination of this special stochastic dynamic stress. The vehicle is examined as a vibrating system. In connection with dynamic stresses in the car body and the carriage, the following questions arise:

1. How real road profile excitation spectra at constant travel speed are distorted by the urban mode of operation?
2. According to measurements at constant travel speeds and statistical analyses, stochastic road profile excitations may be considered as Gaussian processes. Does

* Prof. Dr. P. Michelberger, H-1111 Budapest, Egry József u. 19–21, Hungary

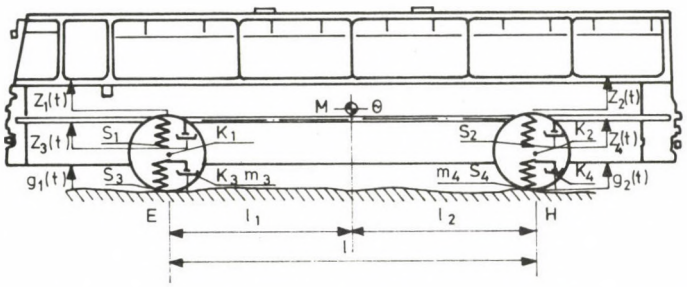

$M = 7580(kg)$; $\nu^2 = \frac{\Theta}{M} = 79709(cm^2)$; $m_3 = 870(kg)$; $m_4 = 1550(kg)$

$l_1 = 274.3(cm)$; $l_2 = 265.7(cm)$

$S_1 = 3740(N/cm)$; $S_2 = 8700(N/cm)$; $S_3 = 28000(N/cm)$; $S_4 = 56000(N/cm)$

$K = 128.5(N/cm/s)$; $K = 128.5(N/cm/s)$; $K = 35(N/cm/s)$; $K = 70(N/cm/s)$

Fig. 1

the special urban mode of operation significantly distort the normality of the process?

3. Can standard deviations of processes at vibrating system outputs in urban mode of operation be delimited by standard deviations obtained from the mean speed and the maximum speed of the run curve?

Computations involved parameters of a town bus type IKARUS. Suspension characteristics of the examined bus have been linearized [2]. The vibrating system has been described by a plane model of four degrees of freedom, considering the car body as a rigid mass (Fig. 1).

To examine the vibration phenomena in the time domain, digital simulation has been applied [2], [3], [4]. Exciting road profile functions have been produced according to [2] and [3], in the knowledge of spectral density functions in [5] and of the variable travel speed. The road profile has been considered as of average quality, and its standard deviation as $D_g = 1$ cm.

1. Theory of road profile spectrum distorsions

Theoretical analysis of road profile spectra suitable for the simulation of urban traffic conditions has been concerned with in [6]. Nodding vibrations due to accelerations and decelerations will not be considered here [8].

The processes of road profile excitation $g(s)$ depending on road length s, and time t-dependent travel speed $v(t)$ are assumed to be independent of steady-state processes.

Considering the urban traffic process in a time interval $[0, T]$, at an instant t the vehicle is at

$$s(t) = \int_0^t v(u)\mathrm{d}u \tag{1}$$

where $s(t)$ is a stochastic process having a steady increment.

Not, at an instant t, a given wheel of the vehicle is acted upon by excitation

$$\tilde{g}(t) = g\{s(t)\} = g\{\int_0^t v(u)\mathrm{d}u\}. \tag{2}$$

Distorted road profile excitation $\tilde{g}(t)$ is demonstrated in [6] to be of steady-state, and an integral transformation method is given to produce autocorrelation function $R_{\tilde{g}\tilde{g}}(\tau)$ and spectral density function $S_{\tilde{g}\tilde{g}}(\omega)$ of this process.

Be $R_{gg}(l)$ the autocorrelation function of process $g(s)$ depending on road length l, where:

$$R_{gg}(l) = M[g(s) \cdot g(s+l)], \tag{3}$$

and $S_{gg}(\Omega)$ the spectral density function of $g(s)$ where:

$$S_{gg}(\Omega) = \int_{-\infty}^{\infty} R_{gg}(l)e^{-i\Omega l}\mathrm{d}l. \tag{4}$$

Now, autocorrelation function of distorted process $\tilde{g}(t)$ becomes:

$$M[\tilde{g}(t) \cdot \tilde{g}(t+\tau)] = M[g\{s(t)\} \cdot g\{s(t+\tau)\}] =$$

$$= M[M[g\{s(t)\} \cdot g\{s(t+\tau)\} \,|\, s(t),\ s(t+\tau)]]. \tag{5}$$

If $s(t) = r$ and $s(t+\tau) = r+l$ then (5) becomes:

$$M\{M[g(r) \cdot g(r+l)|r,\ r+l]\} = M[R_{gg}(r+l-r)] = M[R_{gg}(l)]. \tag{6}$$

Thus, the complex process $\tilde{g}(t)$ is in fact a steady-state one.

Let continuous distribution function $F(\tau, l)$ yield the probability of a vehicle travel shorter than l for a running time τ recorded anywhere according to the run curve $v(t)$:

$$F(\tau, l) = P(s(t+\tau) - s(t) < l). \tag{7}$$

Now, according to (5), (6) and (7), the distorted road profile excitation process is a autocorrelation function of $R_{\tilde{g}\tilde{g}}(\tau)$:

$$R_{\tilde{g}\tilde{g}}(\tau) = M[\tilde{g}(t) \cdot \tilde{g}(t+\tau)] = \int_0^{\infty} R_{gg}(l) \cdot F(\tau, \mathrm{d}l) =$$

$$= \int_0^{\infty} R_{gg}(l) \cdot f(\tau, l)\mathrm{d}l, \tag{8}$$

where $f(\tau, l)$ is a density function for condition τ.

Distorted spectral density function $S_{\tilde{g}\tilde{g}}(\omega)$ is simply:

$$S_{\tilde{g}\tilde{g}}(\omega) = \int_{-\infty}^{\infty} R_{\tilde{g}\tilde{g}}(\tau) \cdot e^{-i\omega\tau} d\tau = 2\mathrm{Re} \int_{0}^{\infty} R_{\tilde{g}\tilde{g}}(\tau) e^{-i\omega\tau} d\tau. \tag{9}$$

Utilizing (8):

$$S_{\tilde{g}\tilde{g}}(\omega) = 2\mathrm{Re} \int_{0}^{\infty} \int_{0}^{\infty} R_{gg}(l) f(\tau, l) \cdot e^{-i\omega\tau} dl d\tau, \tag{10}$$

taking inverse transform of (4):

$$R_{gg}(L) = \frac{1}{2\pi} \int_{-\infty}^{\infty} S_{gg}(\Omega) e^{i\Omega l} d\Omega \tag{11}$$

yields the distorted spectrum:

$$S_{\tilde{g}\tilde{g}}(\omega) = \frac{1}{\pi} \mathrm{Re} \int_{0}^{\infty} \int_{0}^{\infty} \int_{-\infty}^{\infty} S_{gg}(\Omega) e^{i\Omega l} \cdot f(\tau, l) \cdot e^{-i\omega\tau} d\Omega dl d\tau =$$

$$= \frac{1}{\pi} \int_{-\infty}^{\infty} \mathrm{Re} \left[\int_{0}^{\infty} \int_{0}^{\infty} e^{i\Omega l - i\omega\tau} \cdot f(\tau, l) dl d\tau \right] S_{gg}(\Omega) d\Omega. \tag{12}$$

The inner kernel function is independent of spectrum $S_{gg}(\Omega)$ hence for further simplifications it is advisably produced separately:

$$\hat{F}(\Omega, \omega) = \mathrm{Re} \int_{0}^{\infty} \int_{0}^{\infty} e^{(\Omega l - \omega\tau)i} f(\tau, l) dl d\tau. \tag{13}$$

Finally, the distorted spectrum is obtained in a simpler form by using kernel function $\hat{F}(\Omega, \omega)$:

$$S_{\tilde{g}\tilde{g}}(\omega) = \frac{1}{\pi} \int_{-\infty}^{\infty} \hat{F}(\Omega, \omega) \cdot S_{gg}(\Omega) d\Omega. \tag{14}$$

The kernel function has been deduced in (7) for a special case, assuming the vehicle to travel only at either of the two speeds v_1 and v_2, neglecting changeover processes.

Furthermore, the times spent under either of the speed conditions are assumed to be independent of random variables but of identical exponential distribution.

In this case the kernel function is a rational fractional function of frequencies.

2. Distorsions of some real road profile spectra

Let us now consider distorsions of some real road profile spectra. Asphalt road profile spectra are seen in Fig. 2. Spectra traced in heavy line belong to constant travel speeds. Line $V_{\max}$ refers to a spectrum at maximum speed of 60 km/h, while V_a to a spectrum at 34 km/h mean velocity for a single trapezoidal run curve.

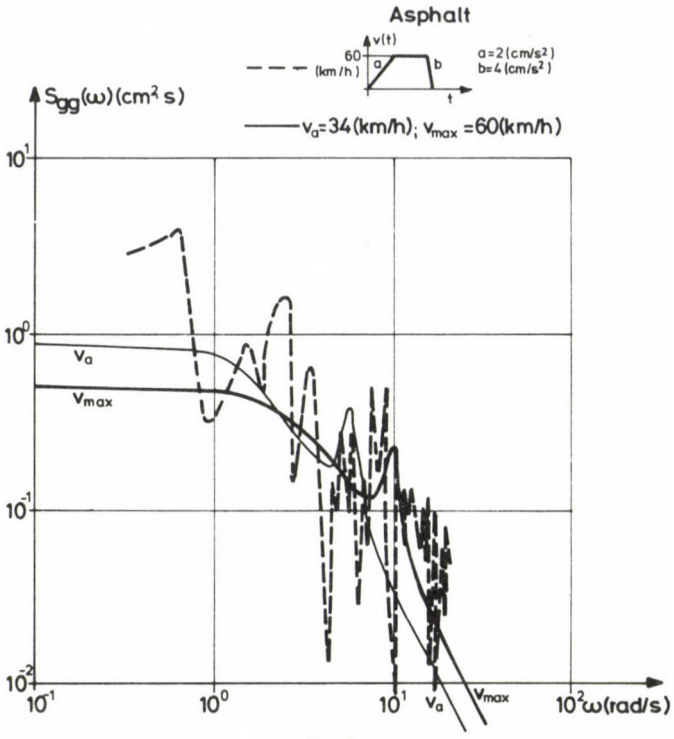
Asphalt
v(t)
60
(km/h)
a
b
t
a=2 (cm/s²)
b=4 (cm/s²)
$S_{gg}(\omega)$ (cm² s)
v_a=34 (km/h); v_{max} =60(km/h)
10^1
10^0
10^{-1}
10^{-2}
v_a
v_{max}
10^{-1}
10^0
10^1
v_a
v_{max}
10^2ω (rad/s)

Fig. 2

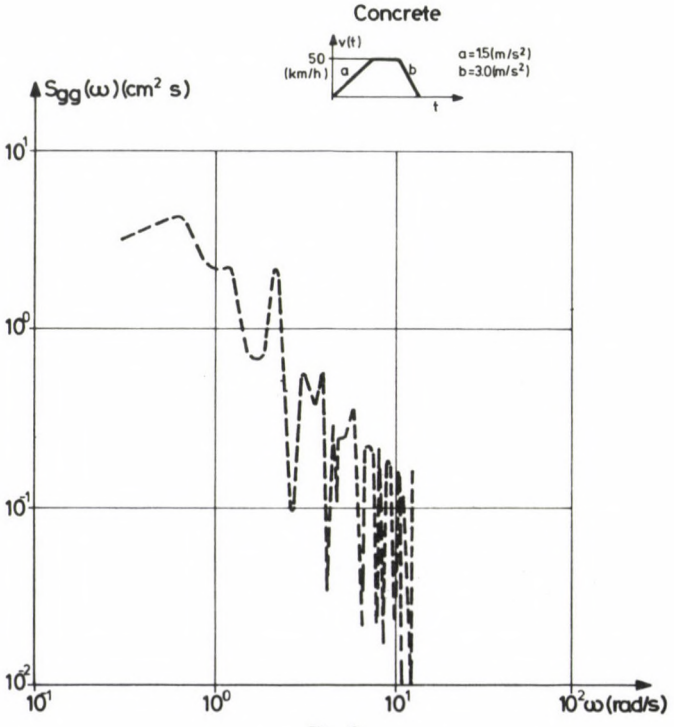
Concrete
v(t)
50
(km/h)
a
b
t
a=15(m/s²)
b=3.0(m/s²)
$S_{gg}(\omega)$ (cm² s)
10^1
10^0
10^{-1}
10^{-2}
10^{-1}
10^0
10^1
10^2ω (rad/s)

Fig. 3

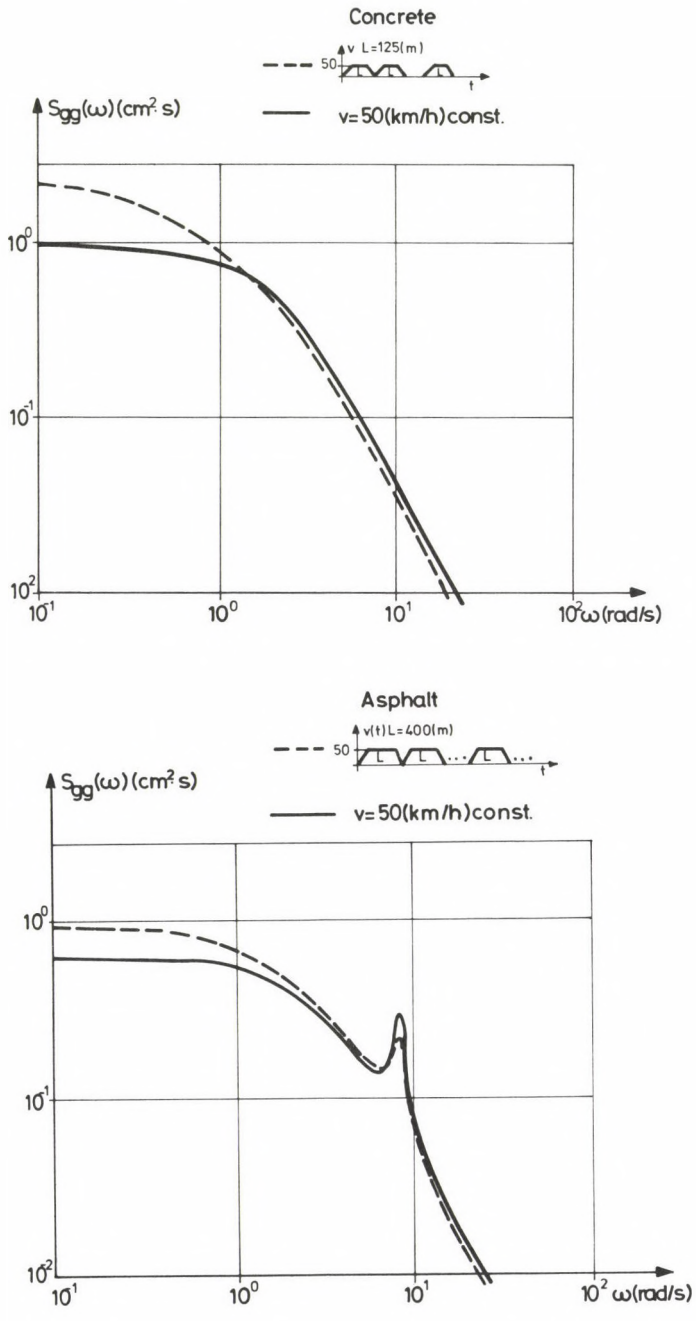
Concrete
v L=125(m)
50
t
$S_{gg}(\omega)$ (cm² s)
v=50(km/h)const.
10^0
10^{-1}
10^2
10^1
10^0
10^1
10^2 ω(rad/s)
Asphalt
v(t) L=400(m)
50
L
L
L
t
$S_{gg}(\omega)$ (cm² s)
v=50(km/h)const.
10^0
10^1
10^2
10^1
10^0
10^1
10^2 ω(rad/s)

Fig. 4

The spectrum curve for a single trapezoidal run curve is seen to be rather fluctuating because of the short record. But even then, the spectral density function is seen to increase for low frequencies. A similar examination of the spectrum of a real concrete road profile, again for a single trapezoidal run curve, is seen in Fig. 3.

The subsequent Fig. 4 presents real distorted road profile spectra obtained by integral transformation (14), for a theoretically infinite number of quite identical trapezoidal run curves.

Distorsions of concrete, and of asphalt, road profile spectra are seen in Figs 4a and b, respectively. Distorted spectrum curves have been traced in dash lines, and those for fixed speeds $V_{max} = 50$ km/h in unbroken lines.

Empirical distribution functions $F(\tau, l)$ have been produced by a digital computer for each $\Delta\tau = 0.02$ sec, at interval $\tau \in [0, 8]$. Now, fluctuations of the distorted spectrum are smoothed out. The rate of shifting to lower frequency ranges of road profile frequency components exciting the vehicle for a single trapezoidal run curve set is clearly visible.

Distorted asphalt and concrete road profile spectra for a random trapezoidal run curve set corresponding to normal urban traffic statistics, are calculated according to [1] are seen in Fig. 5. Increase of low frequency components has to increase vehicle vibration amplitudes compared to travel at normal urban traffic mean velocity. In this frequency range the signal-energy increase is negligible from the aspect of dynamic stresses, while the worsening of subjective vibrational stresses is manifest.

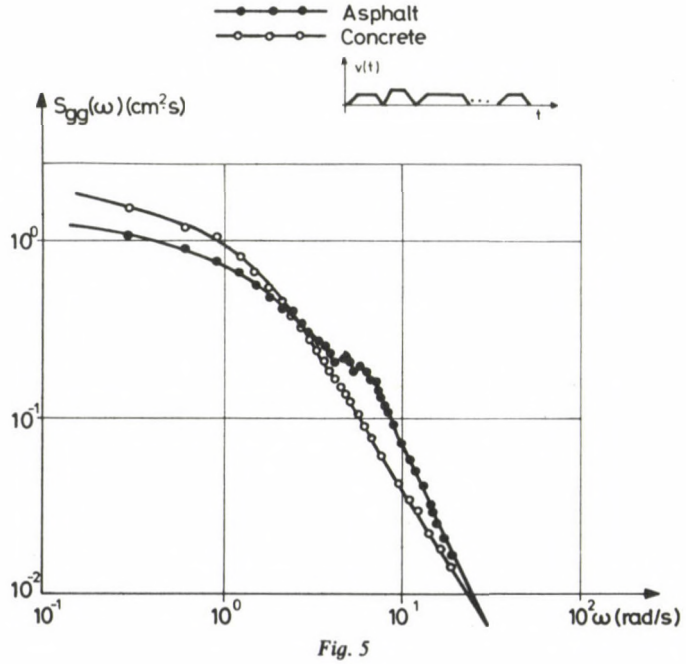

Fig. 5

In the urban traffic speed range also the spread of asphalt road profile spectra across the 4 to 8 rad/sec circular frequency range may be observed.

Again, under urban traffic conditions, more of higher frequency components can be stated to be contained in asphalt than in concrete road profile excitation.

3. Examination of the Gaussian character of input and output processes

Now, computer runs involved trapezoidal run curve accelerations fixed at 1 m/sec^2, and decelerations at 2 m/sec^2. Stop spacings ranged from $L=400$ to 1600 m with $\Delta L=200$ m increments.

Tests concerned with bus runs on an asphalt road.

A rapid approximate method of normality analysis is the graphic method, actually applied for preliminary tests. Empirical distribution function of road excitation was plotted in a Gaussian grid (Fig. 6). Distribution function of expected value $N(m, \sigma)$ and standard deviation σ for arbitrary m and σ is known to be rectilinear on Gaussian paper. Distribution function (in unbroken line) of road excitation sampled at 0.02 sec intervals at a constant travel speed $V=50$ km/h is nearly rectilinear.

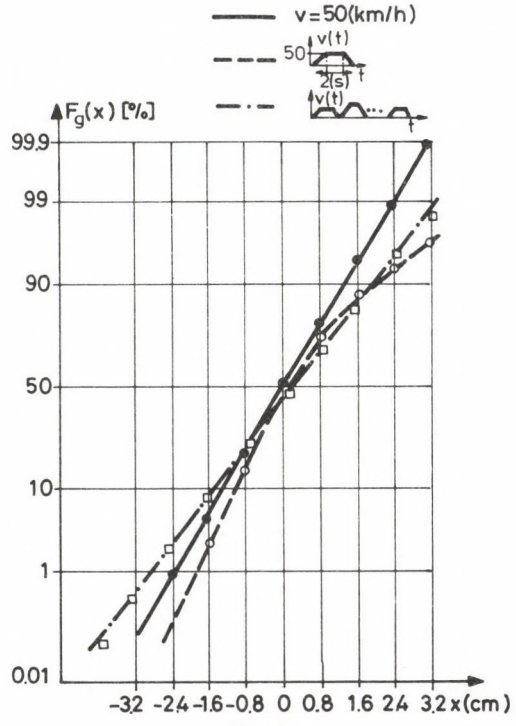

Fig. 6

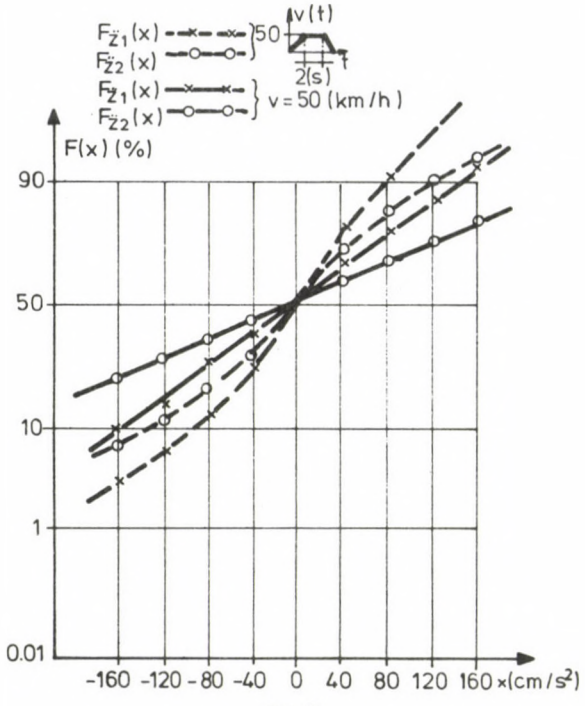

Fig. 7

Distribution function in the dashed line refers to road excitation samples recorded at 0.02 sec intervals with the shortest, single theoretical run curve. It is perspicuously non-rectilinear.

In this case the sampling spot spacings vary with speed variation along the road length. Road excitation samplings have been taken densely at the start of the vehicle, then increasingly farther, at last, at a constant speed, at even spacings. At braking—near stops—sampling spaces get condensed.

In case of a fixed, single trapezoidal speed-time run curve, this phenomenon distorts input statistics. There is no normality any longer if starts and stops are too close together. Distribution function computed from real urban traffic statistics has been plotted in dash-dot lines. This empirical distribution function plotted in Gaussian grid is, however, again rectilinear.

Actually, in addition to the road profile excitation, the vehicle is caused to vibrate also by speed variation along the path, a phenomenon superimposing so-called nodding vibrations on road excitational vibrations. Also this phenomenon argues for the examination of output normality.

The preliminary normality test for vibrational acceleration of the car body, plotted on Gaussian paper, is seen in Fig. 7. $\ddot{Z}_1$ and $\ddot{Z}_2$ are vertical vibrational accelerations above the front, and the rear axle, respectively. Vibrational acceleration

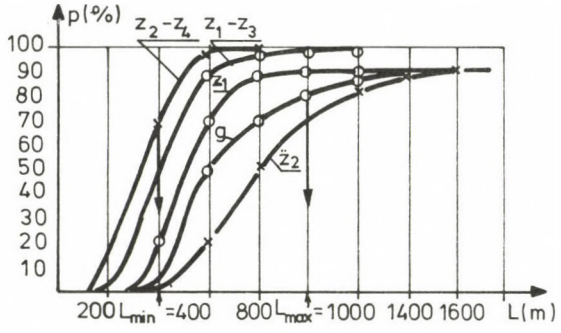

Fig. 8

functions in an unbroken line refer to constant speed $V = 50$ km/h, and in a dashed line to the shortest single theoretical trapezoidal run curve.

These preliminary examinations unambiguously showed the hypothesis of output normality to be acceptable for uniform speeds, while for short (some hundred m) stop spacings it has to be rejected.

Normality has also been checked by the χ^2 test. Input and output samples belonging to trapezoidal run curves for different stop spacing lengths L have been taken and relevant χ^2 values needed for normality tests calculated.

Percentages of probabilities p determined from the χ^2 table compiling computation results have been plotted in ordinate. Conform to expectations, the probability of normality increases with increasing stop spacing lengths.

Sample elements always numbered more than 800, and the degrees of freedom 30. In view of the high element number, the hypothesis has been accepted above $p = 70\%$.

Curve g belongs to the input (road excitation) normality testing.

$Z_1 - Z_3$ and $Z_2 - Z_4$ indicate χ^2 test results for relative displacements of car body and front and rear axle, respectively, of importance for the calculation of suspension spring stresses.

Probabilities of different output terminal signal normalities are seen to increase differently with increasing stop lengths.

On the other hand, for a single fixed trapezoidal run curve and less than 400 m stop spacing, input and output processes are not Gaussian any longer.

From 400 to 800 m, certain outputs may be considered as Gaussian, while for more than 800 m stop spacings, practically all inputs and outputs may be handled as Gaussian processes.

4. Standard deviations of vibrating system output signals

Making use of the trapezoidal run curves described above, standard deviations of output signals of the urban bus model for different stop spacings L have been calculated and plotted in Figs 9, 10, 11 and 12.

Standard deviation values for trapezoidal run curves have been plotted in unbroken line. Standard deviations obtained from mean speeds of various trapezoidal run curves are in a dashed line, while standard deviations for speed $V_{max} = 50$ km/h are in a dash-and-dot line. Standard deviations of mass point displacements are indicated by small circles, those of velocities by small squares, and of accelerations by small triangles.

Diagrams show standard deviations of mass point displacements for trapezoidal run curves to exceed those for speed V_{max}, standard deviation of any other output signal for trapezoidal run curves is less than that for speed V_{max}. This phenomenon is fully confirmed by the road profile spectrum distorsion discussed in Chapter 2.

With increasing stop lengths, standard deviations for trapezoidal run curves approximate those for speed V_{max}. This convergence is, however, rather slow, prohibiting neglect of differences for real urban stop lengths.

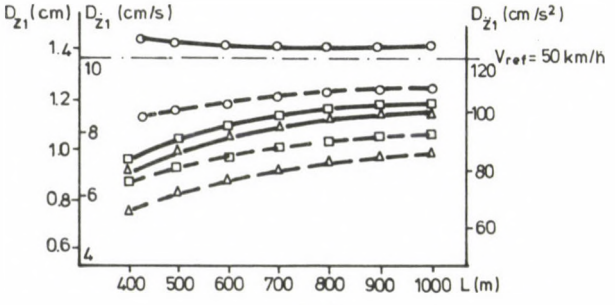

Fig. 9

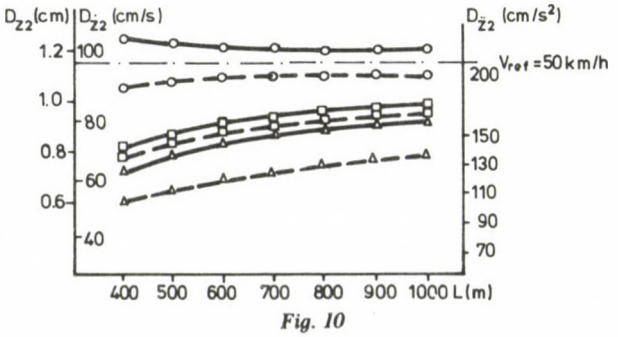

Fig. 10

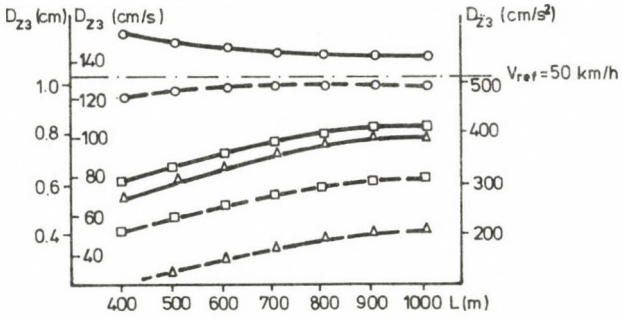

Fig. 11

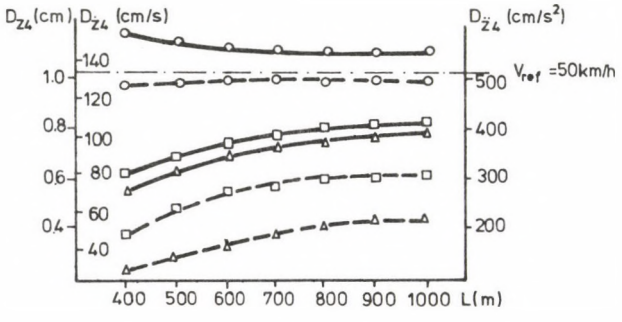

Fig. 12

Standard deviations for trapezoidal run curve mean speeds are, however, less for any output than the corresponding standard deviations for the trapezoidal run curve. Irrespective of displacement standard deviations, lower bound of standard deviations $D_T(Z)$ of trapezoidal run curves is that $D_{Va}(Z)$ obtained for mean speed V_a, and upper bound $D_{V_{max}}(Z)$ obtained with maximum speed V_{max}:

$$D_{Va}(Z) < D_T(Z) < D_{V_{max}}(Z).$$

Finally, since road profile processes distorted in urban traffic are steady-state processes in conformity with self-intended assumptions in Chapter 1, and since according to our investigations, in the case of a prolonged urban traffic, also features of a Gaussian process prevail, the Rice formula applied in fatigue design of materials may be written also under urban traffic conditions:

$$N(Z) = N_0 e^{-\frac{Z^2}{2D_{\tilde{Z}}}},$$

$$N_0 = \frac{1}{\pi} \frac{D_{\dot{\tilde{Z}}}}{D_{\tilde{Z}}},$$

where

$N(Z)$ — number of intersections of signal level Z in unit time;
$\tilde{Z}(t)$ — realization of some output process for the distorted spectrum;
$D_{\tilde{Z}}$ — standard deviation of the realization above;
$D_{\dot{\tilde{Z}}}$ — standard deviation of the derived process $\dot{\tilde{Z}}(t)$.

For linear time-invariant systems the standard deviations above are easy to calculate in the knowledge of the distorted road profile spectrum, spectrum of the derived process of the travel speed, and their cross spectra.

Cross spectra may be produced according to statements in Chapters 1 and 2, but here they are not concerned with.

References

1. Tóth, Gy. J.: Digital simulation of the operation mode of buses. (In Hungarian). Doctor Techn. Thesis, Budapest, 1977.
2. Péter, T.: Examination of the linearizability of car vibration models described by nonlinear stochastic differential equation systems. (In Hungarian). Doct. Techn. Thesis, Budapest 1977.
3. Ilosvai, L., Keresztes, A., Michelberger, P., Péter, T.: Mathematical vibration analysis of buses operating in towns. Periodica Polytechn. Transp. Eng. 7 (1979), 139–148.
4. Michelberger, P., Ilovai, L., Keresztes, A., Péter, T.: Normality analysis of dynamic stresses in buses depending on stop lengths. Periodica Polytechn. Transp. Eng. 10 (1982), 53–59.
5. Pevzner, J. M., Tikhonov, A. A.: An investigation into the statistical properties of the microprofile of the main types of motor road. Avtom. Prom. 1 (1964), 15–18.
6. Farkas, M., Fritz, J., Michelberger, P.: On the effect of stochastic road profiles on vehicles travelling with varying speed. Acta Techn. Hung. 91 (1980), 303–319.
7. Bellay, Á.: Differential equations for the transformation kernel of energy spectrum in case of random transformations of time. Periodica Polytechnica, Mech. Eng. (1983) (In press).
8. Rajbman, N. S. (ed.): Dispersional System Identification. Nauka Publisher, Moscow (1981).

Acta Technica Academiae Scientiarum Hungaricae, 97 (1—4), pp. 241—258 (1984)

CHANGE OF VIBRATION CHARACTERISTICS OF A SIMPLIFIED VEHICLE MODEL AS A FUNCTION OF EXTERNAL PARAMETERS

MICHELBERGER, P.,* SZŐKE, D.

[Received: 20 June 1984]

The stochastic vibration characteristics (such as ride comfort, road holding capacity, dynamic stresses) of a vehicle are determined by a combination of parameters varying continually or as discrete values. A plane rigid-body model of a city bus was used to investigate the quality characteristics as a function of speed of advance, condition of load of the vehicle, and type of road. In the knowledge of output informations, conclusions can be drawn to the predominant stresses acting upon dynamic models of high degree of freedom in first approach, and by comparison with the output informations of elastic-chassis models better simulating the practical conditions but not discussed in this paper, the changes resulting from the elastic chassis can be filtered out.

1. Introduction

The dynamic dimensioning of the chassis of vehicles (autobus) is a complex problem requiring considerable computer time. Recently, the finite element method has usually been used for static dimensioning while a suitably reduced model of less degree of freedom for determination of the dynamic stresses. By retransformation, the stresses in any arbitrary point of the chassis can be relatively simply calculated.

In general, the reduced model is a suitably linearized model (of a degree of freedom of $15 \div 30$) where the variance of vibration acceleration of the different points of the body is determined for given stochastic road excitation. Practical calculations showed that computation of the reduced model was laboursome, as well. Therefore, a still more simplified model shall reasonably be investigated in the course of preliminary design.

In first approach, the dynamic behaviour of the body is fundamentally determined by motion as a rigid body on which the vibration of the body ('elastic beam') is superimposed.

The vibration characteristics of a vehicle (such as ride comfort, road-holding capacity, dynamic stresses) are determined by a combination of parameters varying continuously or as discrete values in case of a simple model.

The model of a city bus is used to investigate the quality characteristics as a function of speed of advance and load condition of the vehicle, and of type or road as parameters.

* Prof. Dr. P. Michelberger H-1111 Budapest, Egry József u. 19–21, Hungary

The rigid body model supplies useful information on the expectable behaviour of the vehicle, and, on the other hand, changes brought about by the elastic chassis can be filtered out from the information obtained on stresses acting upon dynamic models of high degree of freedom in the knowledge of output informations.

In this work, dynamic studies are limited to some vibration characteristics of a linear plane model set up of the simple rigid body and of mass points characteristic of running gears, the behaviour of the elastic body as well as the differences between both models being discussed in another study to be presented later.

2. Model and dynamic description of the vehicle

Vibration of the plane vehicle linear model illustrated in Fig. 1 is described by equation (1).

$$\mathbf{M}\ddot{\mathbf{x}} + \mathbf{K}\dot{\mathbf{x}} + \mathbf{S}\mathbf{x} = \mathbf{G}(\mathbf{z}, \dot{\mathbf{z}}, v) \tag{1}$$

where

M	mass matrix
K	damping matrix
S	stiffness matrix
x_1, x_2	vertical deflection of front and rear axle, respectively
$x_y (0 \leq y \leq L_H)$	vertical deflection along length of the body
z, **ż**	deflection and/or derivative of road profile in the appropriate axial points at time $t (0 \leq t \leq T)$
$\mathbf{G}(\mathbf{z}, \dot{\mathbf{z}}, v)$	forces calculated from road excitation
L	wheel base
v	speed of advance of the vehicle.

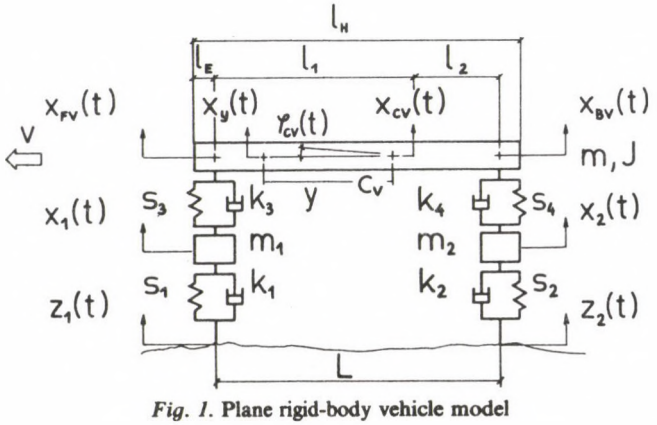

Fig. 1. Plane rigid-body vehicle model

The deflection of the points of the body modelled as a rigid body can be simply calculated as x_y is a linear combination of centre-of-mass motion x_c and rocking φ_c (assuming small deflections):

$$x_y = x_c + \varphi_c \cdot y, \qquad y \in [0 : L_H]. \tag{2}$$

Assuming that both the fore wheel and rear wheel run on the same road profile, transfer functions $W_x(i\omega)$ of the two-input system can be calculated on the basis of (3):

$$W_x(i\omega) = W_{xg_1}(i\omega) + e^{-i\omega\frac{L}{v}} \cdot W_{xg_2}, \tag{3}$$

where

$i^2 = -1$

$W_{xg_1}(i\omega)$ and $W_{xg_2}(i\omega)$ complex transfer functions of deflection of point x for excitation g_1 and g_2, respectively.

In the knowledge of power density spectrum $S_z(\omega)$ of the stochastic road profile, in case of

$$\mathbf{M}\{\mathbf{z}(t)\} = 0, \tag{4}$$

the variance of deflection of point x_k is given by the following integral:

$$D_{x_k}^2 = \frac{1}{\pi}\int_0^\infty |W_{x_k}(i\omega)|^2 \cdot S_z(\omega)\mathrm{d}\omega. \tag{5}$$

(In calculating for relative displacement, speed, and variance of acceleration, the appropriate transfer function shall be substituted in [5]).

Spectra $S_z(\omega)$ for different road types are determined by measurement where e.g. rational fraction functions are a good approach [1]:

$$S_z\left(\frac{1}{L}\right) = 2D_z^2 \left\{ \frac{c_1 A}{A^2 + \left(\frac{1}{L}\right)^2} + \frac{c_2 B\left[B^2 + \gamma^2 + \left(\frac{1}{L}\right)^2\right]}{\left[B^2 + \left(\frac{1}{L} - \gamma\right)^2\right]\left[B^2 + \left(\frac{1}{L} + \gamma\right)^2\right]} \right\} \tag{6}$$

where

$\frac{1}{L}$ wave number

D_z variance of road profile

A, B, C_1, C_2, γ empirical characteristic parameters obtained by measurements.

Should the vehicle advance at speed v, then frequency ω[rad/s] of road excitation will be obtained as

$$\omega = v \cdot 2\pi \cdot \frac{1}{L} \tag{7}$$

and thus the ω-dependent spectrum

$$S_z(\omega) \sim v \cdot S_z\left(\frac{1}{L}\right) \tag{8}$$

will be of a type similar to (6) over the range of $v \in [0 : v_{max}]$.

As is well known, the change of vibration characteristic as a function of length of body is given in the knowledge of the vibration characteristics (variance) by

$$D_x(y) = \sqrt{Ay^2 + By + C}, \qquad y \in [0 : L_H], \tag{9}$$

where

A, B, C constants depending on place and variance of the measured values.

By the use of (9), the average quality characteristics (variance) of the body can be simply determined:

$$M\{\sigma^2_{x_{L_H}}\} = \frac{1}{L_H} \int_0^{L_H} D_y^2 \mathrm{d}y = \frac{A \cdot L_H^2}{3} + \frac{B \cdot L_H}{2} + C \tag{10}$$

The maximum value of dynamically distributed load superimposed on static load in an arbitrary point of the body can be calculated on the basis of (9) [2] (Fig. 2):

$$f(y) = m^*(y) \cdot D_x^*(y) \mathrm{d}y \tag{11}$$

where

$m^*(y)$ specific mass [kg/m]

$D_x^*(y)$ maximum value of acceleration varying linearly due to rigid-body motion, calculated from the characteristic of end cross section.

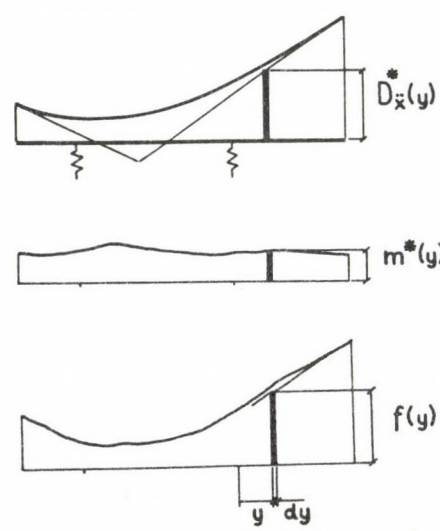

Fig. 2. Dynamic load distribution

From (11), the bending stress due to dynamic load can be determined as effective stress for the point of the body above the shaft by double integration, and approximate dimensions for the body can be calculated. In dimensioning, the sum of static bending moment and triple dispersion of dynamic bending moment shall be taken as a basis, assuming a stochastic process of normal distribution.

3. Parameter test

Spectrum analysis was used to determine the following quality characteristics (variances) of vehicle vibration:

$D_{\ddot{x}_{FV}}$	acceleration of point of body above fore-axle
$D_{\ddot{x}_{cv}}$	acceleration of centre of gravity of body
$D_{\ddot{x}_{BV}}$	acceleration of point of body above rear axle
$M\{\sigma^2_{\ddot{x}_L}\}$	average acceleration of body on the basis of (10)
$D_{\ddot{x}_L}$	acceleration of point L of body on the basis of (9)
$Stability_{FV}$	relative displacement of fore-axle and ground as compared with static indentation (high numerical values expressing inferior quality characteristics i.e. road holding capacity)
$Stability_{BV}$	stability index calculated for rear axle
P_{FV}, P_{BV}	energy dissipated per unit time on front and rear damper, respectively
M_{FV}	maximum bending stress in body cross section above fore-axle
M_{BV}	maximum bending stress in body cross section above rear axle

The dynamic characteristics have been calculated for a normalized road profile of an expected value of $D_z^2=1$, $M\{z(t)\}=0$. A threefold value has been taken into consideration for the stability index as in case of a road profile that can be characterized by normal distribution, the road holding capacity (braking, cornering) can be estimated with a probability of $p=99.7\%$. The energy converted into heat on the dampers has been determined from the variance of relative speed because

$$P(t)=F(t)\cdot\dot{x}_r=K\cdot\dot{x}_r^2\rightarrow M\{P(t)\}=K\cdot D^2_{\dot{x}_r}. \tag{12}$$

The quality characteristics specified above have been calculated as a function of speed at increments of

$$\Delta v=1\ \text{km/h} \quad \text{over the range of} \quad v\in[10:50]\ \text{km/h},$$

$$\Delta v=2\ \text{km/h} \quad \text{over the range of} \quad v\in[50:130]\ \text{km/h}$$

for two road types such as

A—bituminous road
B—concrete road,

and for three different conditions of load such as

1—empty vehicle
2—half-loaded vehicle
3—vehicle with rated load.

Data of the city bus model investigated:

$K_1 = 2000$ N/m/s; $K_2 = 4000$ N/m/s;

$K_3 = 20\,000$ N/m/s; $K_4 = 40\,000$ N/m/s;

$S_1 = 2\,800\,000$ N/m; $S_2 = 5\,600\,000$ N/m;

$m_1 = 870$ kg; $m_2 = 1550$ kg;

$L_H = 9.10$ m; $L = 5.40$ m; $l_e = 1.00$ m

Conditions of load:	*1*	*2*	*3*
S_3(N/m)	260 000	300 000	375 000
S_4(N/m)	300 000	500 000	750 000
m(kg)	6580	10 080	13 580
J(kg m^2)	60 419	86 060	110 930
l_1(m)	2.74	3.02	3.16
l_2(m)	2.65	2.38	2.24

A computer of type ODRA 1204 was used for calculations where the machine time amounted to ~2 minutes for each parameter triad (road, speed, load).

4. Test results

4.1 General experience

Predominant in the quality characteristics of the tested model of a degree of freedom of four are the known properties of a model of a degree of freedom of two (the condition for simple disintegration into real partial models of a degree of freedom of 2 each being realized with a relative error for the three conditions of load:

$$\mathrm{J} = m \cdot l_1 \cdot l_2$$

$$\Delta h_{\mathrm{rel}}(\%) = 1 - m \cdot l_1 \cdot l_2 / \mathrm{J} \tag{13}$$

$$\Delta h_1 = -20.6; \qquad \Delta h_2 = -15.8; \qquad \Delta h_3 = 13.3)$$

The variance of vibration acceleration in the points of the body and the stability indices increase at given speed with the reduction of mass and moment of inertia of the body while the energy converted into heat on the dampers (that is the relative speed of axle and corresponding point of the body) remains unaffected due to the fact that, in case of given mass ratio, the movement of the axle is hindered or braked by the body only insignificantly as shown by the signal flow diagram of the model of a degree of freedom of two (Fig. 3).

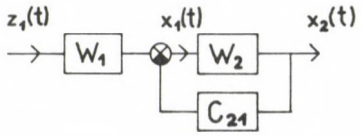

Fig. 3. Signal flow diagram of vehicle model of a degree of freedom of two

W_1 and W_2 are the transfer functions of independent subsystems of a degree of freedom of one

$$W_i = \frac{s_i + pk_i}{p^2 m_i + pk_i + s_i} \qquad i = 1, 2 \tag{14}$$

C_{21} feedback term

$$C_{21} = \frac{m_2 p^2}{p^2 m_1 + pk_1 + s_1} \tag{15}$$

On the basis of relationships (5) and (8), the quality characteristics—as if the two-input excitation resulting from wheel base shift were of one input—vary as a function of speed in accordance with a square root function or on the basis of (12) lineary.

What has been said above applies to concrete roads only. In case of bituminous roads, the second term in relationship (6) is non-zero with 'disturbances' occurring over the range of $v \in [30-60]$ [km/h]. At given speed v, the values of quality characteristics calculated for bituminous roads are always higher then the value of indices calculated for concrete roads.

4.2 Detailed discussion

Illustrated as a function of speed, type of road, and condition of load (*a*—bituminous road, *c*—concrete road, *u*—empty, *h*—half-loaded, *l*—rated load) in Figs 4, 5, 6, and 7 are the variance of vibration acceleration for centre of gravity, point above fore-axle, and point above rear axle, of the body and the average variance of vibration acceleration for the body, respectively.

$\ddot{x}_{cv}$ as a function of v changes fundamentally in accordance with 4.1 on which a harmonic oscillation prolonged as a function of v is superimposed with increasing amplitude. This is brought about by the second excitation shifted to a different extent in time. Time lag

$$\tau = \frac{L}{v} \tag{16}$$

results in a secondary excitation of frequency

$$f = \frac{v}{L} \tag{17}$$

with a resonance complying with, or counteracting, the inherent frequency of the model.

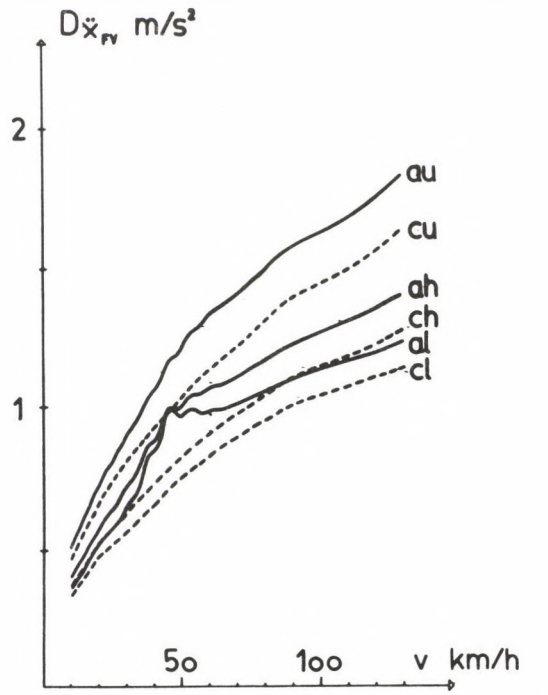

Fig. 4. Variance of vibration acceleration of centre of gravity of body as a function of speed

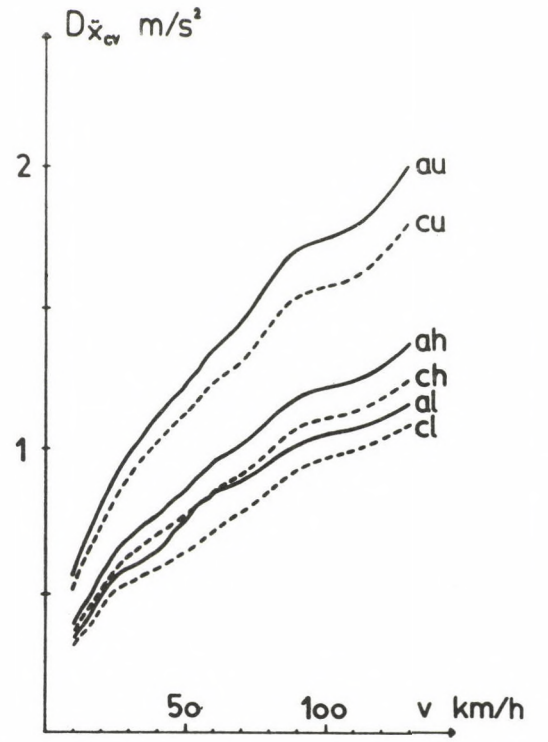

Fig. 5. Variance of vibration acceleration of point of body above fore-axle as a function of speed

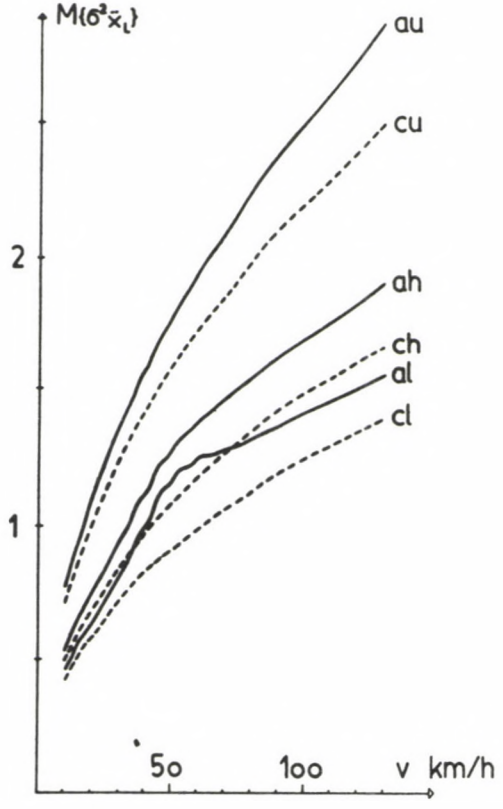

Fig. 6. Variance of vibration acceleration of point of body above rear axle as a function of speed

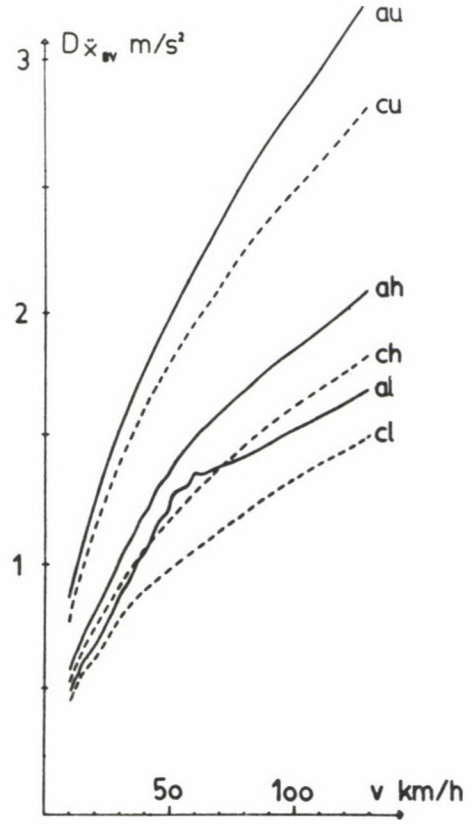

Fig. 7. Average variance of vibration acceleration of body as a function of speed

If the empty vehicle runs on a concrete road, local maxima of function $\ddot{x}_{cv}$ will occur at

$$v_1 = 125 \quad [\text{km/h}]$$
$$v_2 = 90$$
$$v_3 = 65$$
$$v_4 = 48$$

with associated frequency and ratio of

$$f_1 = 6.43 \text{ Hz}$$
$$f_2 = 4.63 \qquad \lambda_1 = 1.38$$
$$f_3 = 3.34 \qquad \lambda_2 = 1.38$$
$$f_4 = 2.47 \qquad \lambda_3 = 1.35 \tag{18}$$
$$\lambda_i = \frac{f_i}{f_{i+1}} \qquad (i = 1, 2, 3)$$

respectively.

Since the inherent frequencies of the body resting on the mainsprings fall within the range of

$$\alpha_{1,2} = [1.0, 1.2] \quad [\text{Hz}],$$

a secondary periodic signal of frequency $\bar{\lambda}$ higher than $\alpha_{1,2}$ will occur in the acceleration transfer functions, that is spectrum

$$S_{XS} \sim \delta(\omega - \bar{\lambda}) \cdot \cos\left(\omega \frac{L}{v}\right) \tag{19}$$

is superimposed on the one-input spectrum. In case of other conditions of load, inherent frequencies $\alpha_{1,2}$ slightly increase and thus also the maxima of $\ddot{x}_{cv}$ are shifted towards higher speeds. On the basis of (8) and (9), the amplitude of the signal superimposed on 'base' $\ddot{x}_{cv}$ changes as a function of v according to a square root function.

The inherent frequency of rocking around the centre of gravity also falls within the range of [1.0 – 1.2] [Hz] and thus variance $\ddot{x}_L$ of the points of body are modified by the secondary excitation resulting from time lag τ in a different way as a function of place (2). It can be seen from Figs 4 and 6 that a secondary excitation of approximately opposite phase is brought about by rocking, independently of the change of the condition of load (and thus, of the change of l_1 and l_2) because the curves 'flatten'.

What has been said above applies to concrete roads as well. However, disturbances of different level take place over different speed ranges in the $\ddot{x}_c$ curve depending on the condition of load. Because of the known maximum of the spectrum of

the bituminous road, also the output spectrum of rocking becomes distorted and as a result, $\ddot{x}_{FV}$ is modified over the range of $v \in [30-65]$ km/h] while $\ddot{x}_{BV}$ over the range of $v \in [40-75]$ [km/h] to an extent decreasing with the reduction of load.

The centre-of-gravity motion is still more modified by rocking at both ends (2) of the vehicle, an explanation for the phenomenon that the values of variance are higher e.g. at the front of the vehicle when loaded (the stresses increasing still more) then in case of an empty vehicle.

The distortions found for bituminous road result from the resonance interaction taking place between inherent frequencies of [1.0 – 1.4] [Hz] of the body, as well as the input spectrum maximum associated with advance of a speed of $v \in [30-60]$ [km/h] and the secondary excitation brought about by $\frac{L}{v}$.

It can be seen from Fig. 7 that the average variance of the body calculated on the basis of (10) is fundamentally determined by $\ddot{x}_{BV}$ and thus the statements relating to $\ddot{x}_{BV}$ are true.

Figs. 8 and 9 contain the stability indices. As suggested by the quality characteristics calculated on the basis of threefold variance, the fore-wheel practically never parts from the road over the speed range investigated while the rear wheel may become detached from the road when advancing at a constant speed of $v = 45-50$ [km/h] in empty condition and of $v = 105$ [km/h] in half-loaded condition. Considering road holding capacity, excitation and/or secondary excitation shifted in time is not appreciable to the vehicle, and also the interfering effect of bituminous road is minimum.

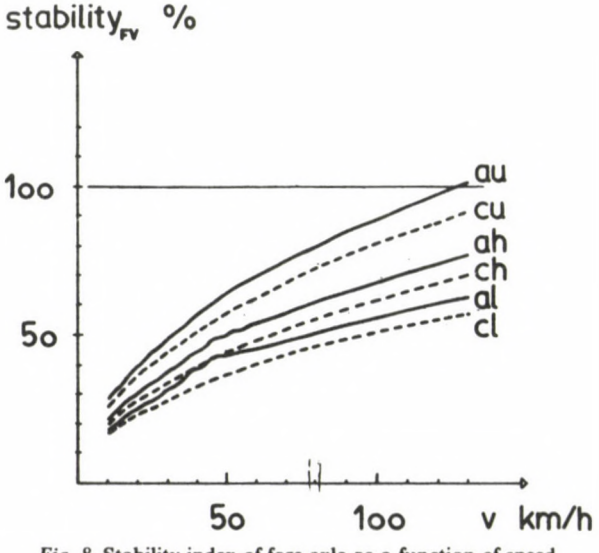

Fig. 8. Stability index of fore-axle as a function of speed

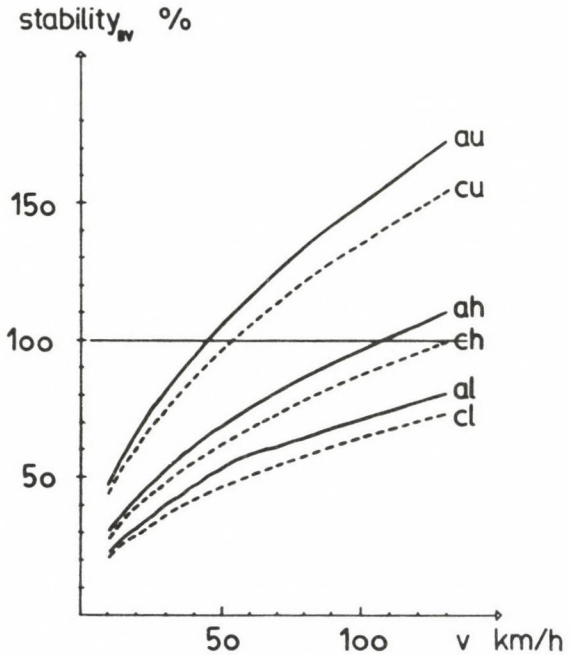

Fig. 9. Stability index of rear axle as a funtion of speed

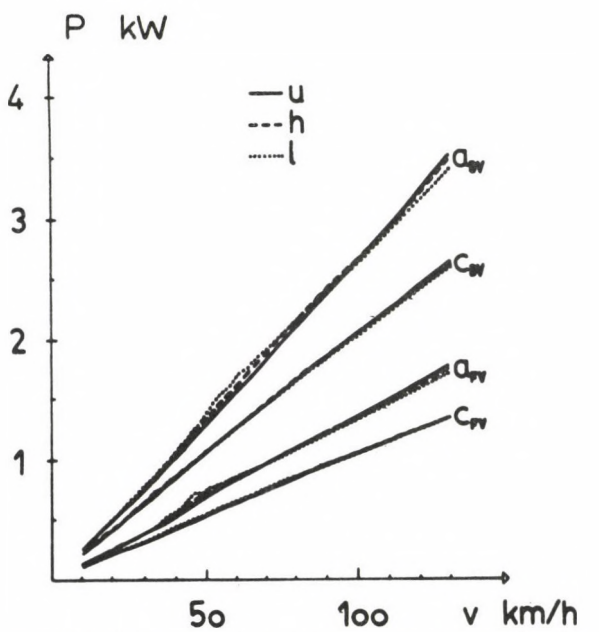

Fig. 10. Energy dissipated on built-in dampers per unit time as a function of speed

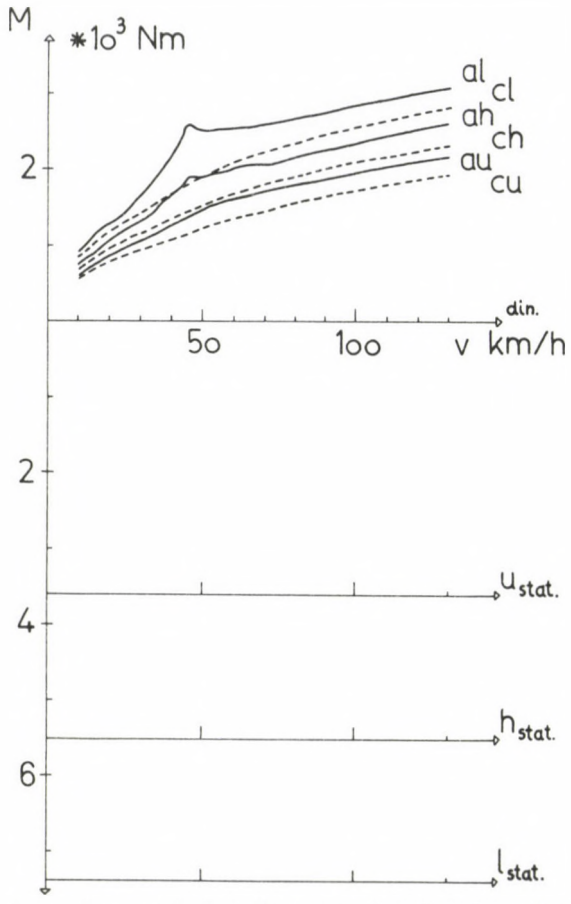

Fig. 11. Bending stress acting upon body in the cross section above fore-axle as a function of speed

The performance figures calculated on the basis of relationship (12) are given in Fig. 10. The minor disturbance of the bituminous road occurs in different speed ranges at the front and rear damper.

Figures 11 and 12 illustrate the sum of variance of static and threefold dynamic bending stress in the cross section of the body above the fore-axle and rear axle. What has been said in par. *4.1* is true here again, a difference being observable only in case of running on bituminous road, especially in the moment associated with the cross section above the fore-axle, over different speed ranges. This similarly to energy dissipation can be attributed to the fact that these quality characteristics are practically independent of excitation due to time lag (Figs 5 and 6) that is the vibration characteristics are determined by the corresponding characteristics of models simply disintegrating, having a degree of freedom of 2 each. In case of bituminous road, the output spectrum

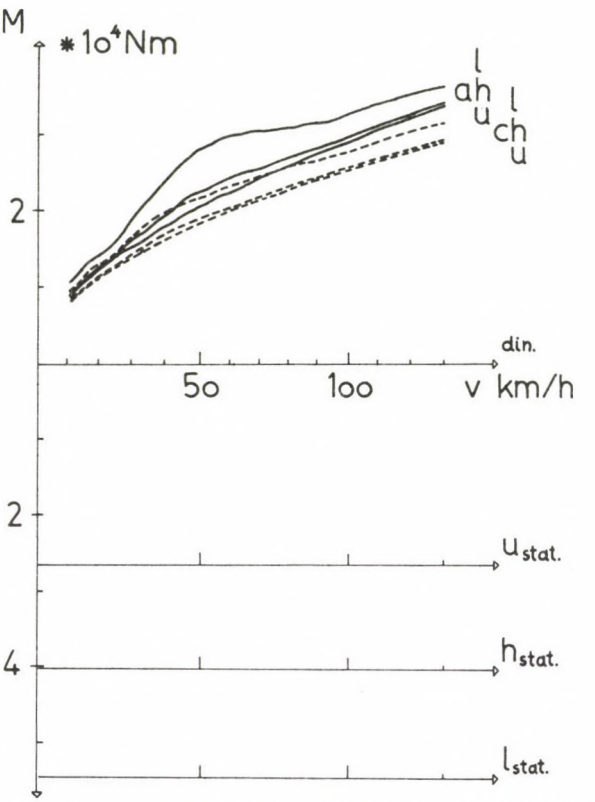

Fig. 12. Bending stress acting upon the body in the cross section above rear axle as a function of speed

and thus the value of variance is modified as a function of speed because of the known maximum of the input spectrum, depending on the condition of load (Fig. 3). On the basis of (2), this distortion occurs in different speed ranges in the quality characteristics associated with the fore-axle and rear axle as a result of the two-input excitation.

It can be seen from Fig. 12 that the dynamic stress acting upon the empty vehicle may exceed the static value even at speeds of $v = 80$ [~ 100] [km/h], a qualitative change in respect of dynamic stress (pulsating stress is taking place).

Figures 13 through 18 show the area of acceleration variance as a function of speed—length of body ($v - L_H$) for given road type and load condition.

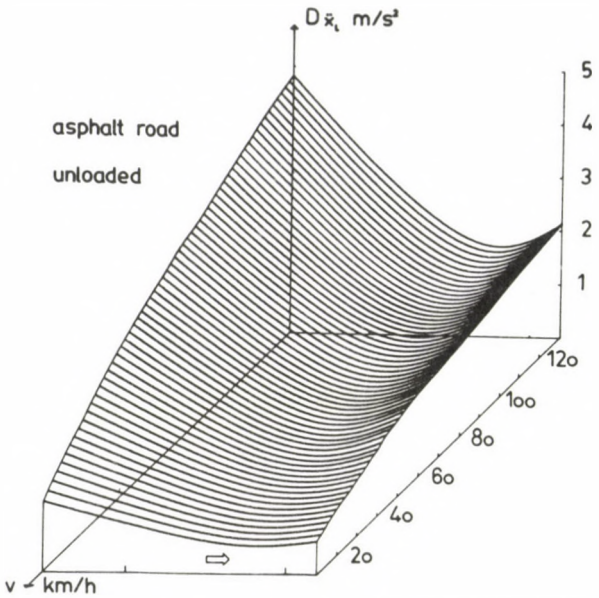

Fig. 13. Area of variance of acceleration as a function of length of body and speed for given type of road and condition of load

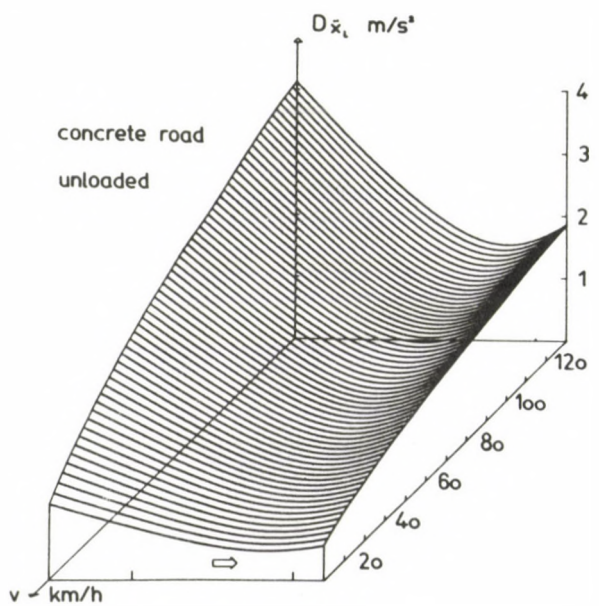

Fig. 14. Area of variance of acceleration as a function of length of body and speed for given type of road and condition of load

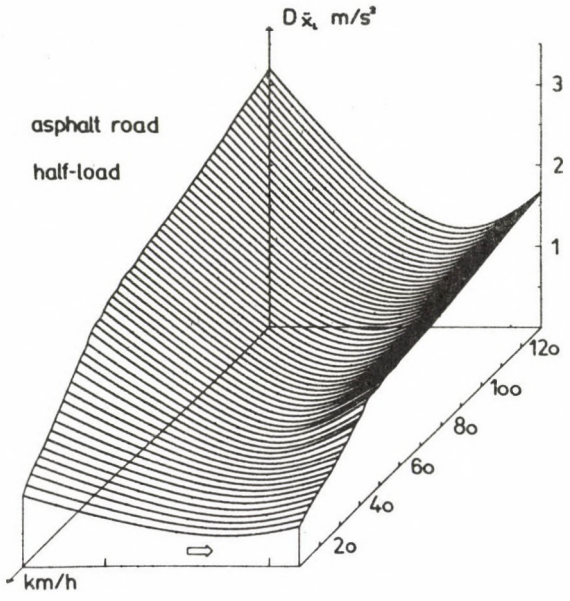

Fig. 15. Area of variance of acceleration as a function of length of body and speed for given type of road and condition of load

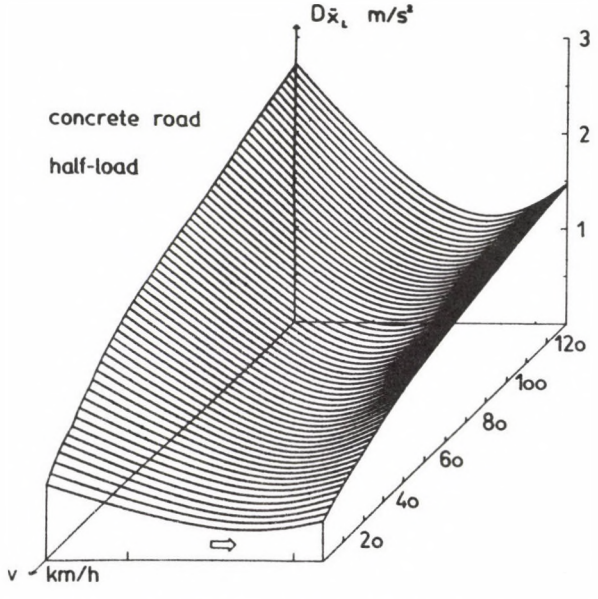

Fig. 16. Area of variance of acceleration as a function of length of body and speed for given type of road and condition of load

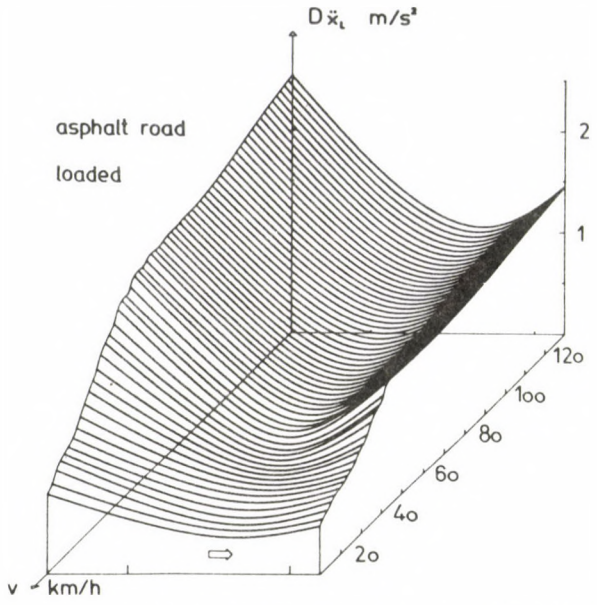

Fig. 17. Area of variance of acceleration as a function of length of body and speed for given type of road and condition of load

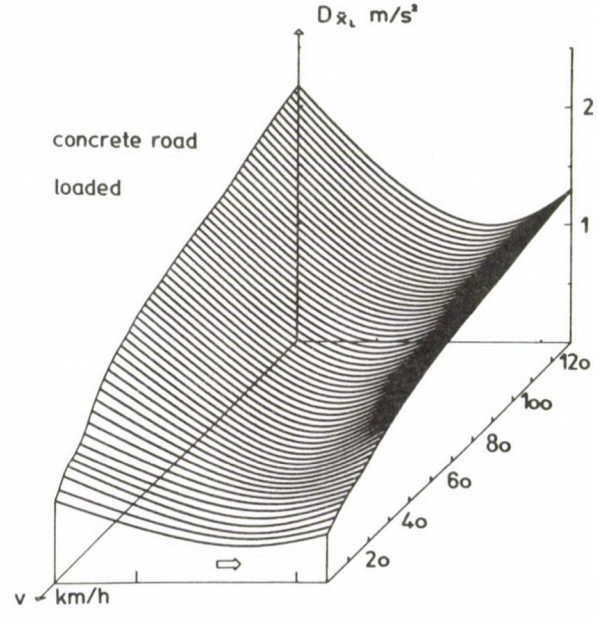

Fig. 18. Area of variance of acceleration as a function of length of body and speed for given type of road and condition of load

Summing up

In case of large buses (of a length of $9-11$ m), the wheel base varies in the range of $L\in[5-6.5]$ [m]. The parameters and/or relative parameters of a vehicle model of a degree of freedom of four differ only slightly from the parameters of the model investigated. That means that predominant in the vibration characteristics of vehicle models are the properties of structures of a degree of freedom of two and/or the statements in par. *4*. However, a heuristic disintegration of a model of a degree of freedom of four into models of a 2 degree of freedom of two each is not advisable because considerable disturbances may occur in the speed range of $v\in[30-60]$ [km/h] due to shifted excitation ($\tau=L/v$), depending on the type of road, and city buses are typically driven at speeds falling within the above range, and on bituminous or macadam roads.

References

1. Pevzner, J. M.–Tyihonov, A. A.: Issledovanie statisticheskih svojstisv mikroprofilya osnovnyh typov automibilnyh dorog. Automibilnaya Promyshlennosty (1974) N-4.
2. Rácz, E.: Light-weight constructions in vehicle and machine industry. (compiled by Rudnai, G.) (in Hungarian). Tankönyvkiadó, Budapest 1976.

Acta Technica Academiae Scientiarum Hungaricae, 97 (1—4), pp. 259—272 (1984)

A MATHEMACIAL MODEL FOR THE INVESTIGATION OF AGING PROCESSES WITH THE TWO-FLOW TURBOFAN JET-PLANTS

E. PÁSZTOR*

[Received: 28 February 1984]

The author determined the improvement of the parameters of two-flow turbofan jet-plants as a result of cleaning of flow-space boundary surfaces of jet-plants. It was found that cleaning affected the economy of the jet-plant favourably in every case. To determine the rate of improvement, a calculation method based on directly measurable parameters has been elaborated by the author to find that an improvement of around 1% of the basic parameters (thrust, fuel comsumption, etc.) of the jet-plant can be achieved under favourable cleaning conditions. Based on approximate economical considerations, the optimum number of cleanings between two general overhauls, and the optimum intervals at which cleaning shall be made within the service period of the jet-plant, has been determined, considering that the costs of cleaning are not negligible as the number of cleanings increase. According to the investigations, 2–3 cleanings shall be made in the period between two general overhauls.

1. Introduction

The main concern of the civil transport aviation companies lies in increasing the economy of passenger and freight transport. The considerable ratio of the operating costs can be ascribed to the fuel consumption, thus a reduction in these costs is of general importance.

Due to the roughening and fouling of the flow-space boundary surfaces of the jet-plants, the thrust (power) of jet-plants keeps decreasing with their fuel comsumption increasing. This reduction in thrust due to increasing flow-losses of jet-plants can be offset at least for some time by increasing the peak temperature of the working process (the temperature after the combustion chamber) to the limit specified for safe operation of turbine blades. Of course, this also involves increasing fuel consumption. In case the peak temperature of the work process cannot be increased any more, the thrust will certainly reduce as the flow-losses continue increasing.

The dust particles (grains of quartz) hitting against the flow-space boundary surfaces of the jet-plants in an air-flow of very high velocity (in this respect, the

* E. Pásztor, H-1221 Budapest, Honfoglalás u. 48/b. Hungary.

Acta Technica Academiae Scientiarum Hungaricae, 97, 1984
Akadémiai Kiadó, Budapest

compressor blade surfaces are especially sensitive) have a dual effect on the surfaces. On the one hand, the flow-space boundary surfaces of the jet-plants become worn and roughened, and on the other hand, the airborne dust particles adhere to the flow-space boundary surfaces. These effects give rise to increase in flow-losses, which in turn result in poor thermal-flow characteristics of jet-plants.

Due to cleaning of the flow-space boundary surfaces of jet-plants, their flow-resistance decreases and their thermal-flow characteristics improve. However, roughening of the flow-space boundary surfaces cannot be eliminated by cleaning and thus the original values of the thermal flow characteristics of jet-plants can be restored only partially. Nevertheless, cleaning of the flow-space boundary surfaces results in a remarkable improvement of the thermal flow characteristics and economy of jet-plants and therefore this method is widely used by the aviation transport companies [6].

2. Fouling process and cleaning possibilities of jet-plants

Air containing dust of different quality and in different quantities enters the jet-plants of aircrafts during their operation. The pollution of air is considerable, especially near the ground above cities. Air pollution is determined first of all by dust (grains of quartz), industrial smoke, as well as vanadium-oxide, sulphur and salt grains.

Airborne pollutants are deposited first of all on the compressor vanes, on the flow-space boundary surfaces of outer and inner circuits (two-flow jet-plants) and on the entry port of the jet-plants (in diffusor), especially if the flow-space boundary surfaces are stained also by gasoil-vapour leaking through the labyrinth-seal. In most cases, this can be removed by cleaning. However, coke formed as a result of dirt burned on the hot surfaces of the combustion chambers and turbines as well as on the nozzle of the inner circuit cannot be removed even by most thorough cleaning.

Two methods of cleaning of the flow-space boundary surfaces of jet-plants have been developed so far, (this paper investigating the methods of cleaning the jet-plants without disassembly). In the first method, coarsely ground rice or nutshell is added to inlet air of the jet-plant for a short time. Due to the abrasive effect of solid materials, fouling of the surfaces is reduced in most cases. The advantage of this method lies in the short time required for cleaning, but it is difficult to control the cleaning process so that also the protective coating of the surfaces may be damaged. In the second method, wash-liquid of different composition is injected at different intervals into the air entering the jet-plants. Essentially, this wash-liquid is similar to that used in household and industry. In this case, the jet-plant must be disassembled—although to the slightest possible extent—the pipes of some auxiliaries must be disconnected from the jet-plant as operational troubles may occur if the wash-liquid flowed to the wrong place.

In this paper, the liquid cleaning process developed for two-flow jet-plants NK-8-2U at the aviation transport company MALÉV is dealt with. Also, the author has developed a calculation method to determine the reduction in fuel consumption

attainable with the help of this process. The author is especially grateful to the management of MALÉV for making available the power characteristics of the jet-plants measured before and after cleaning, thus enabling and promoting the elaboration of the calculation method [3].

3. The process of improvement of thermal flow characteristics during cleaning of the jet-plant investigated

During cleaning of the jet-plant (the Schematic Drawing and the symbols used are shown in Fig. 1) the flow-resistance of the jet-plant reduces due to removal of the fouling from the flow-space boundary surfaces, first of all where air (not combustion products) is still flowing. The efficiency of ventilator (v), low-pressure compressor (k_1) and—to some extent—high-pressure compressor (k_2) stages improve, and the pressure reduction of the diffusor (d) and in duct of the outer circuit (ca) slightly reduce. According to the investigations, the increase in the efficiency of ventilator and low-pressure compressor is most significant; thus only these effects will be taken into account in the following.

The power input of the ventilator and low-pressure compressor rotating on the low-pressure shaft reduces due to improvement of the efficiency. Owing to the still unchanged power output of the low-pressure turbine (t_1), the new thermal-mechanical balance will occur at higher speeds (n_1) of the low-pressure shaft, and as a result, the speed of the hig-pressure shaft (n_2) increases accordingly.

Due to the control system and constructional features of this jet-plant, speed n_2 of the high-pressure shaft is constant, or it shall be controlled so as to rotate at speed n_2 = const. after cleaning. Speed n_2 of the shaft can be reduced only by reducing temperature T_5 after the combustion chamber, that is the mass of the fuel burned in the combustion chamber reduces. With given jet-plant, reduction in temperature T_5 can be observed as the reduction in temperature T_7 indicated by the thermometers after the turbine.

Hence, the efficiency of cleaning of the flow-space boundary surfaces of the jet-plant investigated can be checked through the change of two directly measurable characteristics, that is through the increase of speed n_1 of the low-pressure shaft and

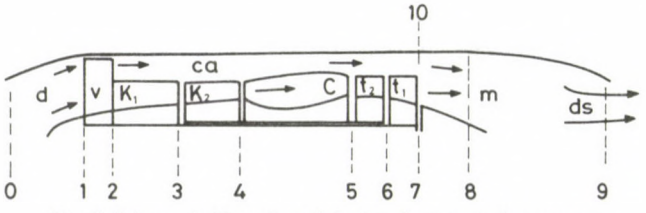

Fig. 1. Schematic Drawing of the jet-plant, notation system

decrease of temperature T_7 after the turbines. According to our theoretical investigations and measurement results, a change in both characteristics must occur as a result of cleaning except for cases when some part of the jet-plant, e.g. the outlet cross-section (A_9) of the nozzle has been modified.

In addition to the reduction in temperature T_7, an advantage not negligible indeed, the exploiter expects the cleaning to result also in increased thrust and reduced fuel comsumption. According to investigations carried out so far, the change of the latter two characteristics lies within 1% even in case of most thorough cleaning, so that their change cannot be determined by means of direct measurements. The inaccuraces of even most precise instruments suited for measurements lies usually above 1% and therefore the change of these characteristics can be determined by means of calculation, only. The calculation method developed for this purpose is described below.

4. Calculation method for the determination of increase in thrust and reduction in fuel comsumption as a result of cleaning

4.1 Principle of calculation, development of the mathematical model of the jet-plant tested

The calculation method has been elaborated on the assumption that the cleaning process results in a reduction of losses, and improvement of the efficiency, of ventilator v and low-pressure compressor k_1 only. Of course, we are free to assume that the efficiency of diffusor d, duct ca and high-pressure compressor k_2 improves as well. However, investigations suggested that changes in the latter case were so small (0.5 $\div$0.7%) that they would only complicate the calculation if taken into consideration with the results remaining essentially unchanged.

Starting from the above assumption, the calculation procedure can be split in two main parts. In the first part, we determine the changes in the efficiency of the ventilator and low-pressure compressure and in measurable characteristics after cleaning while in the second part, the parameters of the jet-plant after cleaning are determined on the basis of improved efficiency. This paper deals first of all with the first part of the calculation procedure, since the second part is built up of elements already known.

For the calculations, we need the mathematical model of the jet-plant in the operating conditions investigated.

This model represents an etalon jet-plant, the thermal-flow characteritics of which comply with the pre-cleaning characteristics of the jet-plant investigated. The percentual changes in the post-cleaning characteristics are then investigated in comparison with this etalon jet-plant. The jet-plant model presented below has been set up on the basis of results of our activities in this field so far, [1].

There we have no space to describe how the model was elaborated. *The most important thermal-flow characteristics of the jet-plant in start condition are given below.*

Coefficients of pressure loss:

$$\sigma_d = p_1/p_0 = 0.995\,; \quad \sigma_c = p_5/p_4 = 0.97\,; \quad \sigma_{ca} = p_7/p_2 = 0.99\,; \quad \sigma_m = p_8/p_7 = 0.99$$

Isentropic efficiency:

$$\eta_{isv} = 0.86\,; \quad \eta_{isk1} = 0.855\,; \quad \eta_{isk2} = 0.845\,; \quad \eta_{ist2} = 0.86\,; \quad \eta_{ist1} = 0.865\,;$$
$$\eta_{isds} = 0.95$$

Efficiency of combustion chamber:

$$\eta_c = 0.975$$

Two-flow coefficient of the jet-plant:

$$M = m_{ca}/m_{k1} = 1$$

Thermal-flow characteristics of the preferred cross-sections shown in Fig. 1 in an impact-type system:

$$p_0 = 0.104 \text{ M Pa}\,; \quad T_0 = 288 \text{ K}\,; \quad \pi_v = p_2/p_1 = 2.0515\,; \quad \pi_{k1} = p_3/p_2 = 1.7548\,;$$
$$\pi_{k2} = p_4/p_3 = 3\,; \quad T_5 = 1274.85 \text{ K}\,; \quad T_7 = 903 \text{ K}\,; \quad T_8 = 649.501 \text{ K}\,;$$
$$p_7 = 0.2054 \text{ M Pa}\,; \quad p_8 = 0.2034 \text{ M Pa}\,; \quad p_9 = p_0 = 0.104 \text{ M Pa}$$

The principal characteristics of the total jet-plant:

$F = 103.714$ KN: thrust of the jet-plant
$m_{ca} = m_{k1} = 108.816$ kg/s: air mass flowing through the outer and inner circuits
$B = 6292.52$ kg/h: fuel comsumption of the jet-plant per hour
$b = 0.06109$ kg/Nh: specific fuel consumption of the jet-plant

With the knowledge of the basic model of the jet-plant, calculations to determine the improvement of the jet-plant due to cleaning can be made.

4.2 Correction of measurement results

Before actual calculations, the data measured immediately before and after cleaning have to be related to exactly identical ambient conditions because any significant otherwise normal change in the ambient conditions during the period of cleaning may change the jet-plant characteristics more than the cleaning of the flow-space boundary surfaces [2].

Shown in Table I as an example are the measurable pre- and post-cleaning characteristics of the jet-plant involved, related to the identical ambient conditions (standard, $p_0 = 0.104$ MPa; $T_0 = 288$ K), for the case of start power.

Table I

	n_1	n_2	T_7
	%	%	K
Before cleaning	96.5	98.2	890
After cleaning	96.6	98.0	883

In case of maximum power $n_1 = n_2 = 100\%$.

As shown by the data, cleaning was successful because the value of T_7 reduced by 7 °C and n_1 increased by 0.1% in spite of the fact that at the time of post-cleaning control, the value of n_2 was not exactly the same before and after cleaning.

Now we came to the second, similarly important step of correction of the measurement results. With a view to determine the post-cleaning improvement of the jet-plant characteristics accurately by calculations, it is a *basic requirement that n_2 be exactly the same before and after cleaning.* If this requirement is not met, the inaccuracy of control may result in major changes n_2 before cleaning $\neq n_2$ after cleaning) in the jet-plant characteristics as compared with changes due to cleaning.

Since a mathematically accurate identity of the values of speed (n_2) before and after cleaning by means of control action, corrective relationships have been set up by means of the test-bench characteristics curves of the jet-plant. These relationships permit the pre- and post-cleaning operating conditions of the jet-plant to be compared at exactly the same speed n_2.

As an example, the corrective relationships applying to the condition of start are shown here.

$$t_{7\,\mathrm{cor}} = t_7 - (n_2 - 95.5) \cdot 13.333\,, \tag{1}$$

$$n_{1\,\mathrm{cor}} = n_1 - (n_2 - 95.5) \cdot 1.6\,. \tag{2}$$

In relationships (1) and (2) the values of temperatures t_7 and t_{cor} should be substituted in C° while the speed in percentage. The constant of a value of 95.5 is the percentage of speed n_2 specified for the condition of start.

Table II

	n_1	n_2	T_7
	%	%	K
Before cleaning	92.18	95.5	854
After cleaning	92.6	95.5	849

In Table II, the corrected values of Table I are shown. (The index "cor" has not been used here because only the corrected values will be taken into account in further calculations.)

As seen from the tabulated data (and as can be followed on the basis of thermal-flow considerations), *the corrected values differ from the non-corrected ones, indicating that correction was indispensable indeed.*

4.3 Description of the calculation method

After the corrective calculations have been accomplished, we have got the measured data, accurate in every respect, that can be taken as a basis for our calculations.

a. Considering that speed n_2 of the high-pressure shaft has not changed after cleaning, $n_2 = n_2^*$ (in the following the post-cleaning characteristics will be marked with asterisk:*), thus $\pi_{k2} = \pi_{k2}^*$ to a good approximation. The post-cleaning characteristics change by max. 1% as compared with those before cleaning. No calculable work-point shift is brought about in the compressor characteristics by this minimum change, and thus the error caused by the above approximation is negligible. According to our calculations, the mass of air flowing through the jet-plant has increased by about 0.5% due to cleaning, resulting in a reduction of about 1%, in the value of π_{k2} for $n_2 = \text{const.}$, a change rightly neglected.

b. Speed n_1 of the low-pressure shaft has increased as shown by the results in Table II, thus $\pi_v^* > \pi_v$ and $\pi_{k1}^* > \pi_{k1}$. Considering the extremely small changes (0.8 to 1%), the percentage increase in pressure can be calculated as follows.

As follows from the Euler impulse-moment equation:

$$\frac{\Delta T^*}{\Delta T} = \left(\frac{n_1^*}{n_1}\right)^2 \tag{3}$$

where ΔT^* and ΔT: the actual increase in the compressor temperature before and after cleaning, respectively.

A relation between actual temperature rise and pressure ratio is established by the Poisson's equation describing a polytropic change of state.

$$\left(\frac{1+\dfrac{\Delta T^*}{T}}{1+\dfrac{\Delta T}{T}}\right)^{\frac{n}{n-1}} = \frac{\pi^*}{\pi} \tag{4}$$

where T: temperature before the compressor investigated.

By the use of equations (3) and (4):

$$\pi^* = \pi \left[\frac{1 + \frac{\Delta T}{T}\left(\frac{n_1^*}{n_1}\right)^2}{1 + \frac{\Delta T}{T}} \right]^{\frac{n}{n-1}} \tag{5}$$

where: $n \approx 1.45 \div 1.5$: polytropic exponent of the actual change of state (losses). Its value can be exactly determined by means of the thermal-flow data contained in the mathematical model of the jet-plant in accordance with the following relationship applying equally to ventilator and low-pressure compressor:

$$\eta_{is} = \frac{\pi^{\frac{\kappa-1}{\kappa}} - 1}{\pi^{\frac{n-1}{n}} - 1} \tag{6}$$

where: $\kappa \approx 1.4 - 1.405$ is the isentropic coefficient of air.

c. The static pressure of the media (outer and inner circuits) entering the mixing chamber *m* should be identical to a good approximation as otherwise either of the media would undergo a throttle-type change of state at the inlet. The velocities of the media entering the mixing chamber should not differ considerably either as otherwise the losses resulting from impulse exchange during mixing would increase. It follows from what has been said above that the impact pressures (static + dynamic = total pressure) of the media entering the mixing chamber are also identical. It should be noted that this thesis was used when setting up the mathematical model of the jet-plant.

$$p_2 \cdot \sigma_{ca} = p_{10} = p_7 , \tag{7a}$$

$$p_2^* \cdot \sigma_{ca} = p_{10}^* = p_7^* . \tag{7b}$$

By means of conditions in (7a) and (7b), the total pressure-ratio of the turbines after cleaning ($\pi_{T\Sigma}^* = \pi_{T2}^* \pi_{T1}^*$) can be determined as follows.

Using the mathematical model:

$$p_5^* = p_0 \sigma_d \pi_v^* \pi_{k1}^* \pi_{k2}^* \sigma_c , \tag{8}$$

$$p_2^* = p_0 \sigma_d \pi_v^* . \tag{9}$$

By means of equations (7b) and (9):

$$p_7^* = p_0 \sigma_d \pi_v^* \sigma_{ca} . \tag{10}$$

The total pressure-ratio of the turbines by means of equations (8); (10):

$$\pi_{T\Sigma}^* = \frac{p_5^*}{p_7^*} = \frac{\pi_{k1}^* \pi_{k2}^* \sigma_c}{\sigma_{ca}} . \tag{11}$$

In the case investigated:

$$\pi_v^* = 2.0659\,; \quad \pi_{k1}^* = 1.7671\,; \quad \pi_{k2}^* = \pi_{k2} = 3\,; \quad \pi_{T\Sigma}^* = 5.1942\,.$$

d. According to our assumption, only the efficiency of the ventilator and low-pressure compressor stage improves after cleaning, the characteristics of the other units remaining unchanged:

$$(\eta_{isv}^* > \eta_{isv}\,; \quad \eta_{isk1}^* > \eta_{isk1})\,.$$

Considering that the units rotating on the low- and high-pressure shafts continue operating in the state of power equilibrium also after cleaning, this condition permits determining a post-cleaning efficiency of the ventilator and low-pressure compressor (η_{isv}^*; η_{isk1}^*) which complies with the characteristics measured after cleaning and corrected in the way described in this paper.

Post-cleaning efficiency η_{isv}^* and η_{isk1}^* can be determined by means of a linear iterative method. The use of linear iteration is justified here because of the extremely small (max. 1%) changes involved. In this method, different values are assumed for $\eta_{isv}^{*\prime}$ and $\eta_{isk1}^{*\prime}$ in the neighbourhood of the expected values of η_{isv}^* and η_{isk1}^* and the value of $\pi_{T\Sigma}^{*\prime}$ associated with them is determined.

For the values of $\eta_{isv}^{*\prime}$ and $\eta_{isk1}^{*\prime}$ where $\pi_{T\Sigma}^{*\prime} = \pi_{T\Sigma}^*$, i.e. the post-cleaning conditions have been satisfied, there $\eta_{isv}^{*\prime} = \eta_{isv}^*$, and $\eta_{isk1}^{*\prime} = \eta_{isk}^*$, i.e. the required post-cleaning efficiency has been determined.

In the second course of our calculations, the values of $\eta_{isv}^{*\prime}$ and $\eta_{isk1}^{*\prime}$ were varied proportionally to each other $\eta_{isv}^{*\prime} = f(\eta_{isk1}^{*\prime})$ since both of them were expected to improve. The functional relationship is shown in Fig. 2. Plotted in the Figure are the final efficiency values both before and after cleaning.

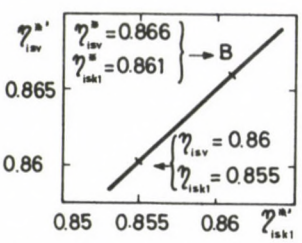

Fig. 2. Change in efficiency $\eta_{isv}^{*\prime}$ of the ventilator as a function of efficiency $\eta_{isk1}^{*\prime}$ of the low-pressure compressor. A = efficiency before cleaning, B = efficiency after cleaning

The basic relationships of the iterative calculations are as follows:

$$P_v^{*\prime} + P_{k1}^{*\prime} = P_{T1}^{*\prime}\,, \tag{12}$$

$$kP_{k2}^{*\prime} = P_{T2}^{*\prime} \tag{13}$$

where:

P = power of compressors and turbines

k = constant expressing the power-input of the auxiliary equipment.

With equations (12) and (13) developed, and taking into consideration the fact that the mass of air flowing through the ventilator is double, it can be written:

$$2m_{k1}c_{pl}T_1[(\pi_v^{*\prime})^{\frac{\kappa_l-1}{\kappa_l}}-1]\frac{1}{\eta_{isv}^{*\prime}}+c_{pl}m_{k1}T_1[(\pi_{k1}^{*\prime})^{\frac{\kappa_l-1}{\kappa_l}}-1]\frac{1}{\eta_{isk1}^{*\prime}}=$$

$$=c_{pg}m_gT_6^{*\prime}\left[1-\left(\frac{1}{\pi_{T1}^{*\prime}}\right)^{\frac{\kappa_g-1}{\kappa_g}}\right]\eta_{isT1}\,, \tag{12a}$$

$$kc_{pl}m_{k1}T_3^{*\prime}[(\pi_{k2})^{\frac{\kappa_l-1}{\kappa_l}}-1]\frac{1}{\eta_{isk2}}=c_{pg}m_gT_5^{*\prime}\left[1-\left(\frac{1}{\pi_{T2}^{*\prime}}\right)^{\frac{\kappa_g-1}{\kappa_g}}\right]\eta_{isT2}\,. \tag{13a}$$

The expressions still unknown in relationships (12a) and (13a) can be determined as follows, considering that T_7^* is already known from the results of the post-cleaning measurements:

$$T_6^{*\prime}=\frac{T_7^*}{1-\dfrac{\left[1-\left(\dfrac{1}{\pi_{T1}^{*\prime}}\right)^{\frac{\kappa_g-1}{\kappa_g}}\right]}{\eta_{isT1}}}\,. \tag{14}$$

On similar consideration $T_5^{*\prime}$:

$$T_5^{*\prime}=\frac{T_6^*}{1-\dfrac{\left[1-\left(\dfrac{1}{\pi_{T2}^{*\prime}}\right)^{\frac{\kappa_g-1}{\kappa_g}}\right]}{\eta_{isT2}}}\,. \tag{15}$$

Temperature $T_3^{*\prime}$ still unknown can be determined so as to start from the ventilator, considering that $T_0=T_1$:

$$T_3^{*\prime}=T_0\left[1+\frac{(\pi_v^*)^{\frac{\kappa_l-1}{\kappa_l}}-1}{\eta_{isv}^{*\prime}}\right]\cdot\left[1+\frac{(\pi_{k1}^*)^{\frac{\kappa_l-1}{\kappa_l}}-1}{\eta_{isk1}^{*\prime}}\right] \tag{16}$$

where: κ_l and κ_g isentropic exponents of air and combustion products, respectively.

C_{p1} and C_{pg} specific heat [J/kgK] of air and combustion products at a constant pressure, respectively.

m_g mass of combustion product (kg/s) flowing through the inner circuit of the jet-plant per unit time.

By means of equations (12a), (13a), (14), (15), (16), the values of $\pi_{T2}^{*\prime}$ and $\pi_{T1}^{*\prime}$ for each pair of values $\eta_{isv}^{*\prime}=f(\eta_{isk1}^{*\prime})$ previously assumed, i.e. the total pressure-ratio of the turbines $\pi_{T\Sigma}^{*\prime}=\pi_{T2}^{*\prime}\pi_{T1}^{*\prime}$ can be determined.

The results of calculations are shown in Fig. 3 where linear interpolation was used to satisfy basic equation $\pi_{T\Sigma}^{*\prime}=\pi_{T\Sigma}^{*}=5.1942$ and to determine the values for final

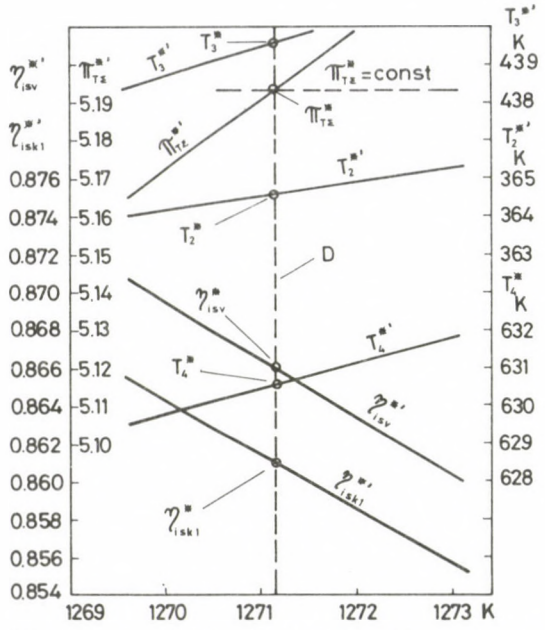

Fig. 3. Determination of the exact post-cleaning characteristics of the jet-plant by means of interpolation. ——— (*D*) = exact values of post-cleaning parameters

post-cleaning efficiency η_{isv}^* and η_{isk1}^*. The values of temperature for preferred section have also been plotted in Fig. 3 so that also temperatures are known by means of interpolation.

e. Then any post-cleaning characteristic of the jet-plant can be exactly determined on the basis of the thermal calculation method developed when the mathematical model of the jet-plant has been set up. (Essentially, no new elements are included in this method and therefore it is not presented here in detail.)

4.4 Numerical results of calculation

From Fig. 3 the values of increased post-cleaning efficiency $\eta_{isv}^* = 0.866$; $\eta_{isk1}^* = 0.861$ can be read from equation $\pi_{T\Sigma}^{*\prime} = \pi_{T\Sigma}^* = 5.1942$ in Fig. 3. Both efficiencies have improved more than a half % as a result of cleaning of the jet-plant. As shown in Fig. 3, the value of $T_7^* = 898$ K used for the calculation was obtained by subtracting temperature drop $\Delta T_7 = 5$ K observed during cleaning from temperature $T_7 = 903$ K associated with the start power of the model jet-plant. In the maximum temperature before the turbines a reduction of $\Delta T_5 = T_5 - T_5^* = 3.7$ K was observed. This had a favourable effect in that the fuel consumption decreased, and the service-life of the jet-plant increased.

Tabulated in Table III are the calculated values of the post-cleaning characteristics of the jet-plant.

Table III

After cleaning	Before cleaning	Absolute improvement	Percentual improvement
$F = 103\,714$ N	103 005 N	$\Delta F = 709$ N	0.688%
$B = 6282$ kg/h	6292.5 kg/h	$\Delta B = 10.5$ kg/h	0.167%
$m_{ca} = m_{k1} = 109.47$ kg/s	108.82 kg/s	$\Delta m_{ca} = \Delta m_{k1} = 0.65$ kg/s	0.597%
$b = 0.060\,57$ kg/Nh	0.061 09 kg/Nh	$\Delta b = 0.000\,52$ kg/Nh	0.851%

From among the improved jet-plant parameters it is the specific fuel consumption which deserves special attention: as the reduction of nearly 1% in fuel consumption fundamentally determines the economical advantages of cleaning of the flow-space boundary surfaces. If pre-cleaning thrust F has to be restored after cleaning, fuel consumption B will continue reducing due to reduction in the jet-plant load to reach a value of approximately $\Delta B = 53 \div 54$ kg/h.

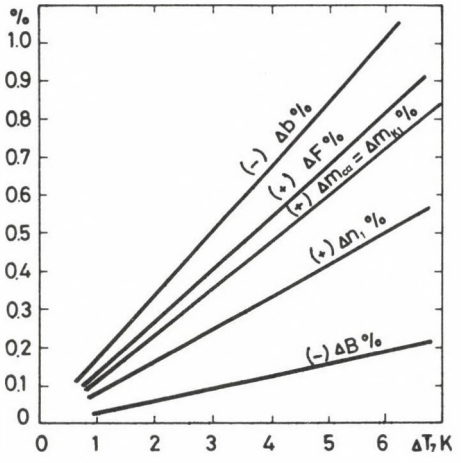

Fig. 4. Comprehensive presentation of the post-cleaning state characteristics of the jet-plant

The generalized results of the calculation are shown in Fig. 4 where the percentual improvement attainable for the different parameters is plotted versus temperature reduction $\Delta T_7 = T_7 \div T_7^*$ measured after the turbines. In compliance with our previous considerations, function $\Delta n_1 = f(\Delta T_7)$ can also be seen in Fig. 4. This relationship is valid only approximately as it has been obtained from measurement results.

5. Economical considerations associated with frequency of cleaning

On the basis of what has been said above, it can be stated that cleaning of the flow-space boundary surfaces of jet-plants is advantageous in every respect. In case of especially dirty jet-plants after an operation of about 5000 hours without cleaning, the reduction in temperature T_7 was as high as $8 \div 10$ °C while speed n_1 increased by nearly 1%. Due to the reduction in temperature T_7, the control reserve of the jet-plant increases, and increase in the service-time between two overhauls may reach 500 hours.

However, the jet-plant to be cleaned has to be put out of service at least for $6 \div 8$ hours, and at least four persons are required for the cleaning job, a fact to be taken into consideration in economic evaluation of the cleaning process. Moreover, the fuel consumption of the running test after cleaning amounts to about 500 kg.

The question arises how often should cleaning be performed between two overhauls of the jet-plant to obtain economically optimum results?

Increase B in fuel consumption due to fouling of the jet-plant in given duty can be written as a function of duty hours as follows [4], [5]:

$$\Delta B = \Delta B_{\max} \left(\frac{\tau}{T} \right)^m \tag{17}$$

where:

$\Delta B_{\max}$ = total increase between two overhauls

T = total duty hours of the jet-plant between two overhauls

τ = time lapsed since the beginning of the period investigated ($\tau_{\max} = T$)

m = constant depending on operation, construction, dust-content of air, quality of fouling.

The change of $(\Delta B/\Delta B_{\max})$ in equation (17) as a function of (τ/T) is shown in interval $0 \div 1$ of exponent m in Fig. 5. According to observations, fouling takes place first rapidly but slows down later because new dust particles are easily swept away from the layer of dust deposited on surfaces. Accordingly, $m = 0.8 \div 0.5$ approximately.

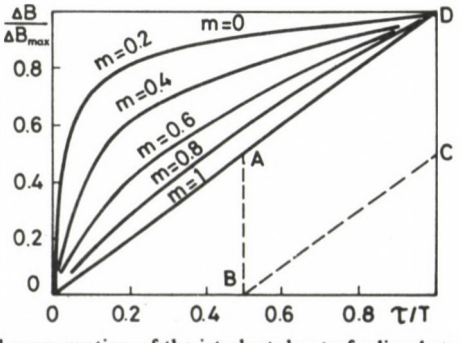

Fig. 5. Increase in fuel consumption of the jet-plant due to fouling between two overhauls.

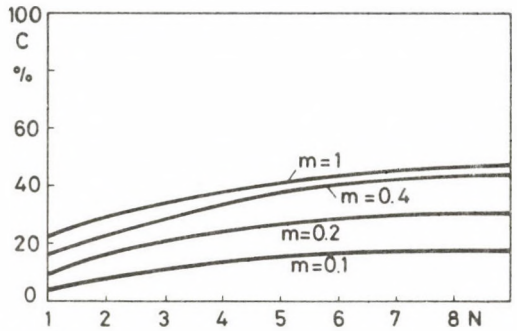

Fig. 6. Percentual value of maximum savings in fuel consumption attainable by cleaning of the jet-plant as a function of the number of cleanings in case of optimum cleaning intervals

The further economic considerations take $m = 1$ into consideration. It should be noted, however, that the situation will be essentially the same if $m = 0.8 \div 0.5$. Assume ($m = 1$) that pre-cleaning fuel consumption has been restored as a result of cleaning of the jet-plant. In this case, fuel savings over period T are proportional to area A – B – C – D – A. It is easy to prove that maximum savings in fuel will be achieved if cleaning is made at uniform intervals i.e. if $(\tau/T) = 0.5$ per cleaning.

This theorem is of general validity: even in case of more cleanings, maximum fuel consumption can be achieved if cleaning is made at uniform intervals.

Now the question arises: how often shall the cleaning process reasonably by repeated between two overhauls considering that the costs of cleaning cannot be neglected in evaluating the economy of the process. Information on this problem is given in Fig. 6 where the percentual value (C) of maximum attainable fuel savings is plotted against the number of cleanings. Obviously, in case $N > 8 \div 9$, the increase in the value of C is practically negligible, and maximum savings in fuel consumption at $C = 1$ will be achieved if $N = \infty$.

Consequently, $2 \div 3$ cleanings are recommended during the period between two overhauls, since the savings in fuel continuously reduce as the number of cleanings increases so that the savongs are no longer commensurate with the increase of operating cost rising linearly with the number of cleanings.

References

1. Thermal-flow analysis of jet-plant NK8-2U. Manuscript. Department for Aero-and Thermotechnics, Technical University, Budapest. 1978. Leader of the team: Prof. E. Pásztor. Commissioned by MALÉV.
2. Conversion of the parameters of the jet-plant NK8-2U into standard ambient characteristics.
3. Determination of the post-cleaning parameters of jet-plant NK8-2U by means of calculations. Leader of the team: Prof. E. Pásztor. Commissioned by MALÉV.
4. Dvigatyel szemeisztva NK-8 promüvka gazovozdusnavo trakta dvigatyelej i proverka parametrov dvigatyelej imejuschih bolsuju narabotku v ekspluatacii. Metodika N° MT-0053-78 Moskow.
5. Determination of cleaning frequency with the gas-turbine jet-plants used in civil transport aviation. Manuscript. MALÉV 1982.
6. Cleaning the compressors of aircraft engines. Aircraft engineering. January 1983.

Acta Technica Academiae Scientiarum Hungaricae, 97 (1—4), pp. 273—282 (1984)

APPLICATION OF HOLOGRAPHY TO THE STUDY OF COMBUSTION PROCESSES

K. REMÉNYI,* F. HORVÁTH

[Received: 27 September 1983]

Holography has created new possibilities for the investigation of combustion processes. The authors of the present paper utilized holography for gaining a new understandings of the processes taking place in the nearest environment of coal particles during combustion. Similar experiments, as well as investigations with hydrocarbon flames have also been reported on by other authors. The facilities used were of different types, but the pictures obtained clearly verified the similarity of these processes. The authors of the present paper for their experiments employed 5–10 MW ruby-laser with a double flash. The time interval between the two 20 nanosec pulses was 150–200 μsec. The photographs taken of the burning coal particles showed sphere symmetrical interference bands around the investigated particle. On the basis of the photographs and theoretical background, a conclusion has been reached, whereby in the course of combustion, in the environment of flat flames and particles, physico-chemical waves are developing.

Symbols

k — rate constant of the reaction; [1/s]
T — length of period; [s]
ν — wavefrequency; [1/s]
ω — angular frequency of wave; [1/s]
A — amplitude of wave
φ — phase of wave
r — radial-coordinate
c_r — velocity of wave
λ — wavelength
k_r — wavenumber
c — changing concentration
t — time; [s]

Introduction

Several articles deal with the applicability of holography to the investigation of combustion processes of gaseous, fluid and solid fuels; from these publications those referred to under numbers [1], [2], [3], [4] can be mentioned as the most significant ones. At the Institute for Electrical Power Research (VEIKI), we performed our investigations on the combustion of coal particles, roughly at the same time, when the results of reference [2] were demonstrated. In the following we report on the facilities

* Dr. K. Reményi, H-1014 Budapest, Uri u. 38, Hungary

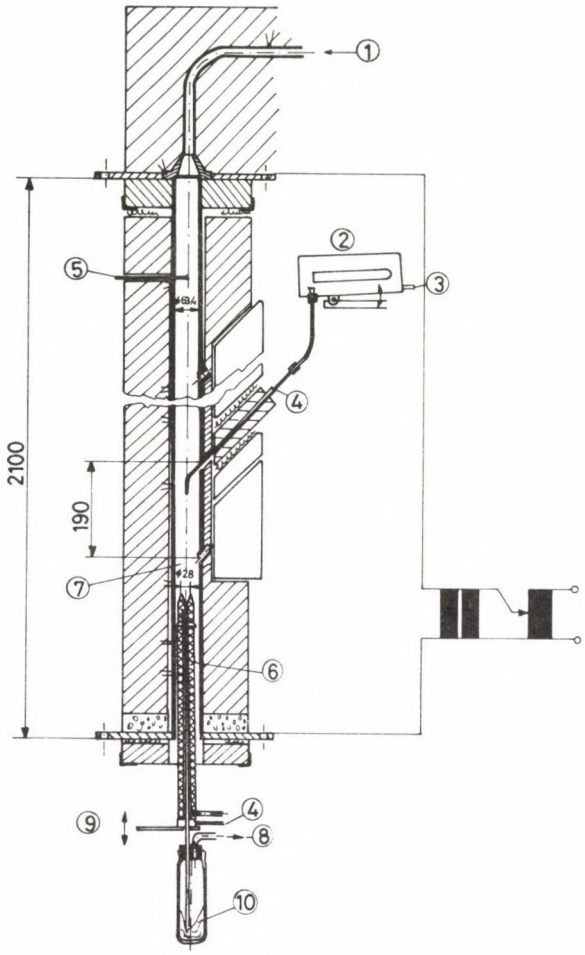

Fig. 1. Experimental apparatus

used, the conditions under which test series were performed, as well as on the results of combustion theory which may be generalized on the results obtained so far.

Before dealing with the application of holography, we will roughly outline our experimental fall-tube facility which is applicable to the investigation of combustion processes of coal particles (Fig. 1). The equipment is a proper tool for the versatile examination of combustion processes in time and space, at the same time readily applicable to the investigation of the individual coal particles during thermal decomposition, by means of holography.

In an electrically heated vertical tube (fall-tube) gas of predetermined composition flows downwards. Along the tube the temperature of the wall is practically constant, which is partly due to the fact, that the gas mixture is preheated to tube-temperature.

The average distance of the particles from each other is roughly 30 times the size of the particle diameter. Owing to this fact, the interactive effects of coal particles were disregarded in the course of the combustion.

In order to gain a valuable insight into the processes of pulverized coal combustion, during our fall-tube experiments holography was applied.

From this new technique, a better structural understanding of the thermal boundary layer surrounding the particle has been expected.

The holograms were made by the staff of the Holographic Laboratory of the Research Institute for Technical Chemistry of the Hungarian Academy of Sciences (MTA MÜKKI).

For the experiments various fractions of coal from Oroszlány and Balinka were employed. (Fractions $63 < d < 80$ μ and $125 < d < 160$ μ from Oroszlány; fractions $63 < d < 80$ μ from Balinka coal.) The temperatures of fall-tube were 1000 °C and 750 °C, respectively, during the experiments.

The holographic recording were taken in such a manner, that the laser beam was led through the opposite slots of the fall-tube and reference beam was bypassed around the apparatus.

The holographic method applied stems from the concept, that the burning particles while passing in front of the testing aperture, are transilluminated by the giant doublepulsed ruby laser of 5–10 MW, with flashing time of 20 nanoseconds, and then the particles are depicted on a highresolution film. At the instant of flash, the film is simultaneously exposed to a so-called "reference beam" bypassed from the laser light, and the former without touching the particles enters the emulsion and interferes with the "object wave" arriving from the particles. This interference scheme is called hologram.

It is characteristic of the hologram, that it includes all the necessary optical information on the object, thus the phase of illuminating waves and their intensity alike. Owing to this unique feature, the "object" can be reconstructed in three dimensions, if it is subjected to a permanently radiating gas laser.

The double-pulse phenomenon (time-delay of 150–200 nsec) simultaneously fixes two conditions on the same hologram, i.e. two states are superposed on each other. If the superposed conditions are completely identical, then after reconstruction the "object" will appear, as if the holographic recording had been taken only once, with a laser pulse at double length of time.

If either in the burning particle or in its environment some modification occurs between two pulses, it results in interference appearing on the surface of the object, or in its environment.

Taking into account all this possibilities, it was assumed that additional information could be gained from the holograms concerning the structure of the thermal boundary layer surrounding the particle.

The series of photographs (Fig. 2) presented as illustration were made after having reconstructed the holograms taken of coarse coal from Oroszlány at

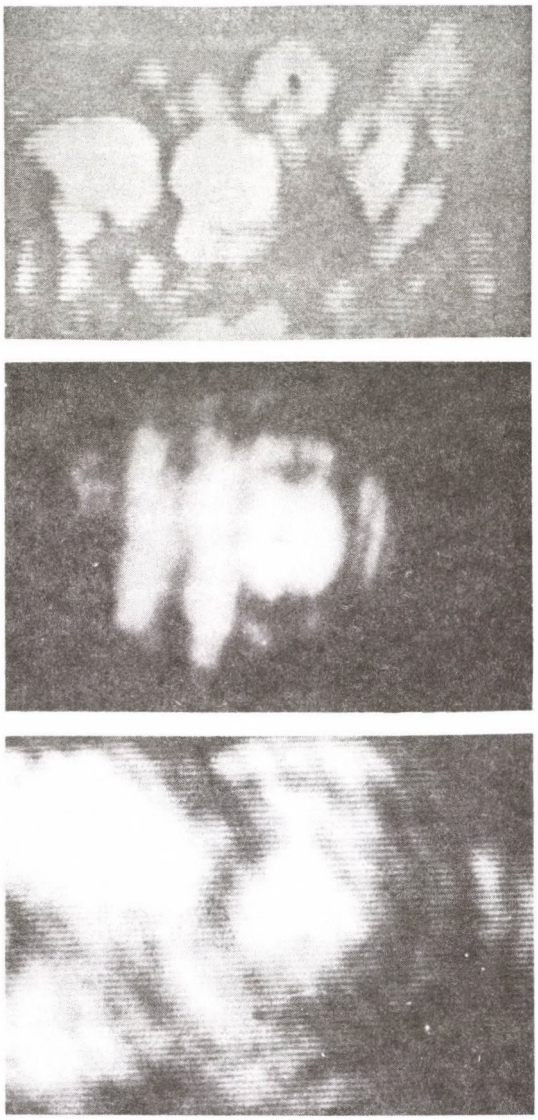

Fig. 2. Laser-holographic recordings of the burning cool particles from Oroszlány

temperature of 750 °C. The first picture of the series shows the pulverized coal injected directly into the opening provided for test purposes. The particles are not yet burning.

The coal particle illustrated in the second photo is burning now; a sphere can be seen around it. The photo was taken of the particle in the stage of volatile burning. Two diagonal bands shown in front of the particle examined are attributed to the effect of other particles. The sphere can be regarded as the zone or flame of volatile combustion.

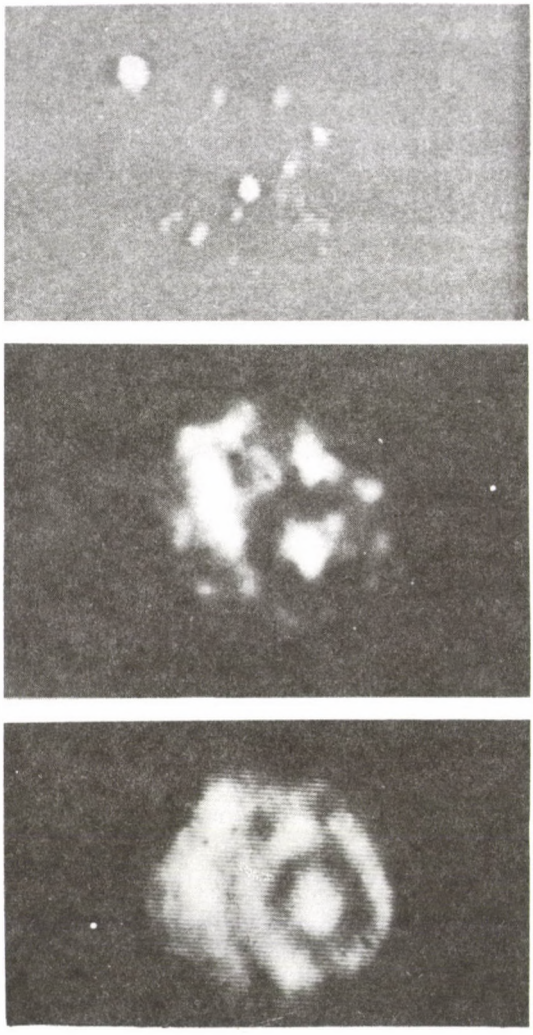

Fig. 3. Laser-holographic recordings of the burning cool particles from Balinka

In the third of the pictures the particle seems to be surrounded by a series of interference rings. The particle has reached the stage of coke combustion.

The same phenomenon can be observed in the second series of photographs (Fig. 3) which illustrates the boundary layer around the particles in case of pulverized coal combustion of Balinka.

The presented photographs taken of the holograms clearly prove, that by using this technique, a testing procedure can be attained applicable to calculations too, thus providing a new method in revealing the structure of the thermal boundary layer surrounding the particle.

The wave phenomena pertaining to the burning coal particle and the flame elements

The laser-holographic pictures taken of the coal particle, or of the flames of other combustibles clearly demonstrate, that out of the particle or from the flame elements, more or less uniform or slightly distorted spherewaves propagate ahead. For the sake of simplicity and for defining the numerical results, in the following we present our own photos to demonstrate the conception, on the other hand not excluding this its general applicability. The existence of this phenomenon is proved by the photos made by us, as well as by those presented in literature. This is fairly well proved by the fact, that in the photos taken in the precombustion stage, interference rings cannot be observed at all, while following the combustion they quickly appear. The interference rings also refer to the fact, that the application of diffusion equation for determining the circumstances of combustion is hardly appropriate, because the steady-state environment of the burning particle would not show any alteration between two laser pulses. According to the photographs taken of the burning particle, spherical interference bands are shaping around the particle, which provide a good reason to assume the occurrence of spherical-waves accompanying the combustion process. During combustion, the periodic feature of the chemical and thermal process can be attributed to the influence of combustion in time and space. In the environment of the particle, the motion of activated fuel fragments and the oxygen is of opposite direction. In the first semi-period combustible mixture fills up the space of reaction. After ignition and burn-out, the reaction product leaves the space of reaction in the second semi-period. Naturally the real process cannot be divided into sharply separable parts, but in the given part of the period the one or the other is dominating, and causes the periodic feature of combustion. Moreover, it was also taken into account, that in the space of reaction highly active intermedials are present and according to the measurements performed directly in the flames it was found, that in the space of reaction no equilibrium position was reached. The deviation from the state of equilibrium, the proceedings of combustion both in time and space, consequently the reaction itself brings about the excitation of physico-chemical wave-phenomenon in the combustion chamber and in its environment, which include the material transfer and the change of physical parameters, too. Owing to the rapid progression of chemical processes, the state of the system cannot be described by equilibrium-equations and the time-dependent character of the reactions and other processes must be allowed for.

The combustion of fuel can be outlined by the following process, when distinction is not made, whether solid material or flat burning flame element is dealt with.

The micro-element preliminarly heated up to the temperature of ignition and the oxidating substance are in direct contact with each other. Following the ignition, the highly rapid chemical reaction consumes the oxidating substance. Its continuous feeding (diffusion) despite the decreased concentration is hindered by the fact, that in

the space of reaction a large amount of high-temperature combustion product piled up, with an intense rise in temperature, and the intensity of reaction somewhat decreased. However, after a while the flow of oxidating substance commences in the direction of burning element and—the combustion product and the oxidant mostly exchanged—the process with less intense than the first blow-like start periodically recurred. The periodicity of cycles is first of all determined by the rate of reaction, i.e. the duration of reaction. The concept of periodic nature of combustion process described by us had already been dealt with for cold flames by Kondratiev, V. N. who cited different authors when defining the periodic recurrence of chemical processes [5]. This book also refers to the observations of Gervart and Frank–Kamenickij, according to which, under proper conditions the cold flames can be produced even as a sustained periodic process. In this case the periodicity is explained by the difference between the rate-constants of reactions of intermedials, i.e. attributed to the reaction mechanism. Since with previously performed experiments, the conclusions had to be drawn on the basis of pulsation of pressure, relatively slower processes could be observed. The laser holography is appropriate technique for the analysis of the rapid processes of the very small flame elements.

In course of the cited experiments, even the phenomenon was observed, that on the transition from cold into warm flame the interruption of cold flame ensues. The deceleration of the reaction at the end of the cold flame, and its prompt acceleration resulting in the warm flame, led to the theory of the so-called two-phase explosion, which denotes combustion, changing with time. As a result of experiments conducted with pulverized coal, Reményi [6] also described the theory of twofold and manifold ignition.

Summarizing the results of the literature concerning the laser holographic technique, it was found that for the evaluation of recordings performed by such a method, two ways were available. The first one is practically summarized, whereby assuming the combustion process in time and space, the periodicity is calculated by taking into account an average rate constant of the reaction.

The other way of assessment can be reckoned on the basis of assumed simple forms of reaction mechanism. According to this, the combustion takes place with the participation of intermedials. Following the ignition, after the appearence of CO_2 which is the first ultimate combustion product, the heterogeneous reaction

$$C + CO_2 \rightarrow 2\,CO$$

and the homogeneous reaction

$$CO + \frac{1}{2}\,O_2 \rightarrow CO$$

take place. In this case the periodic feature is determined by the harmonic oscillator brought about by the difference between the first k_1 and the second k_2 reaction rates.

In both cases the excitation of wave could be successfully accounted for the reactions taking place during the combustion, whereby its waveform nature could be

established and so the combustion could be dealt with by wave equations. In the periodic process the quantities characteristic of the process itself are assigned to values recurring at regular intervals. The characteristic length of time of the wave is the period of wave (T), during which a complete wave is recorded. The frequency of wave (ν) is the number of total oscillations allotted to the unit of time

$$\nu = \frac{1}{T}.$$

The angular frequency of wave is

$$\omega = \frac{2\pi}{T} = 2\pi\nu.$$

The significant value of the wavelength variation at t instant

$$x = A \sin(\omega \cdot t + \varphi_0),$$

where A is the maximum value of x which is called amplitude and φ_0 is the phase of wave at the initial ($t=0$) instant. By simplifying the examinations, considering longitudinal spherical-waves during combustion, for which the wave-equation is

$$\frac{1}{r^2} \cdot \frac{\partial}{\partial r}\left(r^2 \frac{\partial \varphi}{\partial r}\right) = \frac{1}{c^2} \cdot \frac{\partial^2 \varphi}{\partial t^2},$$

the general solution of which

$$\varphi = (ct - r)\frac{1}{r} f_1 + (ct + r)\frac{1}{r} f_2,$$

where f_1 and f_2 are arbitrary functions, $(ct-r)f_1/r$ is the potential of waves starting out from the centre, while $(ct+r)f_2/r$ denotes the potential arrival into the centre.

Let us consider the longitudinal wave as sinusoidal (harmonic), then we obtain

$$\varphi = a(x, y, z) \sin[\omega t - \alpha(x, y, z)].$$

The harmonic waves can also be characterized by the λ wavelength, i.e. by the spacing between the points with 2π phase-difference. If the c velocity of wave propagation is known, then the (k) wavenumber and the wavelength can be calculated on the basis of

$$k = \frac{\omega}{c}; \qquad \lambda = \frac{2\pi}{k} = cT = \frac{c}{\nu}.$$

The discussion of experiments

Assuming a simple first-order reaction for combustion, the rate of reaction

$$w = -\frac{\mathrm{d}c}{\mathrm{d}t} = kc$$

and the change of the concentration with time is

$$c = c_0 e^{-kt}.$$

If conclusions are to be drawn concerning the lifetime of molecules involved in the reaction, then an average lifetime can be a useful tool. Characterizing the quantity of molecules by the concentration at a "t" instant, during dt time interval, dc concentration-change would occur, and the amount of lifetimes of molecules characterized by dc concentration-change is tdc. Integrating this value, from $c = c_0$ to $c = 0$, and eliminating the details, we obtain c_0/k value for all of the molecules involved. If the average lifetime of molecules characterized by the co_0 concentration is denoted by T, then the amount of the lifetime-sum comes to $c_0 T$. From the equalities of the two values

$$\frac{c_0}{k} = cT, \quad \text{i.e.,} \quad T = \frac{1}{k}$$

is obtained.

In our case, however, the average lifetime of molecules informs us about the length of time of their staying in the combustion chamber, i.e. the duration is provided. Since the frequency of wave is the reciprocal of the period, thus

$$\nu = \frac{1}{T} = k,$$

i.e., equals to the reaction-kinetical rate constant, with dimension of 1/s.

On measuring the wavelength from the laser-holographic recordings obtained for the Oroszlány coal-particle, a value of 50 μm is given. Together with the calculated and measured data all qualities are available for the application of wavefunction.

With the second method of evaluation, by applying the theorem of periodicity of chemical processes, proper conclusions can be drawn concerning the wave phenomena of combustion. In this case, by simplifying reality, for the deviation from the stationary values of the products involved in the reaction (C, CO, CO_2, O_2, etc.) the equation of harmonic oscillator is obtained [5] in case of which, taking into account only two reactions, we receive for the frequency

$$\nu = \frac{a}{2\pi} \sqrt{k_1 \cdot k_2}.$$

Knowing the frequency and the λ wavelength obtained from the recordings, the wave equations are supposed to be adequate for the descriptions of combustion processes.

References

1. Palócz, M.: Holográfikus interferometria és fényképezés alkalmazása a tüzeléstechnikai kutatásban. (The application of the holographic interferometry and photography in the combustion technics). ETE (1977) Freiberg, GDR.

2. Trolinger, I. D.—Heap, M. P.: Coal particle combustion studied by halography. Applied Optics (1979), 1 June.
3. Reményi, K., Horváth, F.: Impulzushológráfia alkalmazása barna kőszénszemcsék égésfolyamatainak vizsgálatánál. (The application of pulse-holography for the examination of combustion processes of brown-coal particles). Energiagazdálkodás (1979), július.
4. Schönbücher, A.: Wärme-, Stoff- und Impulstransportvorgänge unter Berücksichtigung kohärenter Strukturen in Tankflammen organischer Flüssigkeiten. Brennstoff-Wärme-Kraft (1981), No. 9.
5. Kondratiev, V. N.: Kinetika himicheskih gazovih reaktsii. Izd. Akademii Nauk SSSR, Moskva 1958.
6. Reményi, K.: Combustion Stability. Akadémiai Kiadó, Budapest 1980.

Acta Technica Academiae Scientiarum Hungaricae, 97 (1—4), pp. 283—313 (1984)

FINITE ELEMENT METHOD FOR SOLVING ELASTO-PLASTIC AND ELASTO-VISCOPLASTIC PROBLEMS

L. SZABÓ*

[Received: 10 January 1983]

Finite element solution of elasto-plastic and elasto-viscoplastic problems is discussed. After a concise review of relevant publications, the elasto-plastic material matrix is presented according to the Prandtl–Reuss theory, in the case of anisotropic-kinematic hardening. Elasto-plastic deformations are described according to the Perzyna theory. Finite element equations and iterative computation methods are briefly outlined. Application of the elaborated computer program is illustrated on three problems.

1. Introduction

Design and stress analysis of shell structures and pressure vessels are increasingly ruled by the inelastic behaviour of materials.

Analyses starting from purely elastic material characteristics are generally inadequate, since often service loads may produce plastic deformations and creep processes. Load capacity design likely to lead to material saving constructions is only possible by plastic analysis. But calculations based on elasto-plastic material models are too complex to be analytically feasible in other than in quite simple cases, imposing a recourse to numerical methods.

Such an efficient computation method is that of finite elements permitting efficient plastic solution of complex structural design and load problems. This method offers simultaneous analysis of material and geometrical nonlinearities, and combined consideration of temperature and time factor, under arbitrary mechanical and thermal loads.

The finite element method started booming by the mid-'60s, and became generalized with the spreading of computers.

Earlier publications [1, 2] gave detailed accounts of the finite element solution of elasto-plastic problems with the validity of the Prandtl–Reuss theory, in case of isotropic hardening materials, assuming small deformations.

Here, hardening will be described by means of an anisotropic hardening model. Beside elasto-plastic deformations, finite element solution of elasto-viscoplastic problems [4] will be presented.

* L. Szabó, H-1015 Budapest, Csalogány u. 6–10, VI. 228, Hungary

In what follows, after reviewing the literature on the finite element solution of material and geometrical nonlinearity problems, finite element equations and computation procedure of elasto-plastic and elasto-viscoplastic problems will be detailed, and illustrated.

2. Review of publications

In the recent two decades, the finite element method has undergone important development, mainly attributable to the wide range of applicability of the method and to the development of computer technique.

Actually, the finite element method is a rather efficient, generalized method for solving different mechanical problems. Since the early'70s, in developed industrial countries high-capacity finite element program systems have been developed for the solution of a wide range of problems.

The finite element method had been applied by the early '60-s for solving material nonlinear problems. Several authors such as Gallagher [5], Swedlow [6], Argyris [8], Marcal [10, 12] Marcal–Pilgrim [11] Marcal–King [13] Argyris [30], Khojasteh–Bakht [28], Akyuz–Merwin [29], Yamada [21] were concerned with the finite element solution of elasto-plastic problems. Essentials of the theory have been developed, elasto-plastic material matrix relating stress increments and deformation increments have been written, solving simpler problems. These works are somewhat exceptionable from the point of view of correctness and theoretical supports, though they may be considered as significant achievements by including fundamentals and methods underlying subsequent research.

Later, computation methods were improved and new procedure developed, such as the method of initial stresses by Zienkiewicz & al. [15], the method of initial strain and tangential stiffness by Argyris and Scharpf [31].

Since the early '70-s, several publications were concerned with the finite element solution of plastic problems: Nayak–Zienkiewicz [17, 18], Richard–Blacklock [24], Yamada [22], Armen and al. [52], Landau and al. [41], Harkegard–Larsson [54], Popov and al. [25], Zudans [26], Khojasteh–Bakht–Popov [27]. Among theories of plastic deformation and yield, this latter has been preferred. Most of the authors made use of the Prandtl–Reuss theory, the Mises plastic conditions and isotropic strain hardening.

Recent publications make use, however, of the Hencky deformation theory, such as those by Tang [43], deLorenzi–Shih [44], Kim [45], Yamada and al. [23].

Also the applied numerical procedure has greatly developed. Nayak [16] published isoparametric finite element solution of elasto-plastic problems permitting the determination of the elasto-plastic zone inside the unit.

Besides refining computation methods, solutions for several problems have been described such as: the elasto-plactic analysis of shells by Backlung–Wennerström [23],

Landau and al. [41], cracks by Harkegard–Larsson [54], solution of three-dimensional problems by Owen–Salonen [19], Levy and al. [40].

Besides simpler material models, also more complex models have been applied. For instance, kinematic hardening was applied by Kalev Gluck [33], Zak–Craddock [48]; combined isotropic-kinematic hardening by Axelsson–Samuelsson [108], Haisler [127], Allen [136], Hunsaker [139].

Besides the finite element solution of time-independent elasto-plastic problems, several authors were concerned with time and temperature factors in plastic deformations, e.g. thermoplastic problems by Haug and al. [86], Basombrio–Sarmiento [109], Allen [110], Hsu–Too [111], Snyder–Bathe [140], Allen–Haisler [158], Hsu [160], Cry–Teter [87], Mcknight–Sobel [137], elasto-viscoplastic and creep problems by Sanders–Haisler [106, 161], Haisler–Sanders [107], Patterson [112], Levy–Pifko [134], Kawahara [120], Levy [85], Cormeau [144], Zienkiewicz–Cormeau [146], Greenbaum–Rubinstein [157].

In addition to elasto-plastic problems, much interest was spent on geometrical nonlinearity, already by the early '60-s. Finite element solution of geometrical nonlinear problems were first concerned with by Turner and al. [7], Argyris [8], Wilson and al. [9]. Initially, the application technique was rather intuitive. Later, significant development appeared in the field of geometrical nonlinearity. The incremental method was developed, applying loading step by step, in small increments, and several iterative procedures were suggested e.g. by Bergan [117], Kao [133], Zienkiewicz [131], Besseling [118]. By developing the increment technique, the nonlinear problem was reduced to linear problems by Yagmai [130], Horrigmoe–Bergan [129].

Besides the total Lagrangian discussion (Marcal [14], Hibbit–Marcal–Rice [129], Oden [60]) the updated Lagrangian way of description has been developed by Soreide [102], Gadala and al. [104], Horrigmoe and Bergan [129], Bathe–Oden–Wunderlich [59]. Argyris [90] soon pointed out the possibility of combined handling of material and geometrical nonlinearities, but significant results had not been achieved before the early '70-s.

Several research workers were successful in solving combined nonlinearities by the finite element method: Hofmeister and al. [114], Stricklin and al. [121], Dupuis and al. [122], Gunasekara–Alexander [103], Haisler [89], Key [113], Balmer [126], Hibbit and al. [123], with the detailed elaboration of various procedures, solving several problems of application.

Combined treatment of geometrical and material nonlinearities underwent abrupt development mainly in recent years: Argyris and al. [92–96], [115], Bathe and al. [97–100], McMeeking–Rice [124], Dodds and al. [132], Chen [141], Gortemaker–DePater [142], Nagtegal–De Jong [143], Yamada–Sakurai [34]. Various iterative methods were compared by Yamada [36], William [39], Mondkar–Powel [35], Crisfield [56], Powel–Simon [101], Mathies–Strang [128], Kao [133]. Important achievements in the last 15 years, various theories and numerical experiences were

published in comprehensive studies by Armen [49], Hodge [50], Snyder–Bathe [140], and in books by Zienkiewicz [57], Bathe–Wilson [58], Bathe and al. [59], Wunderlich and al. [61], Hinton–Owen [62–64], Irons [66], Whiteman [65], Seegerlind [80], Desai–Abel [81], Donea [83], Bathe [119].

Actually, an active research is going on concerning a finite element solution of geometrical and material nonlinear problems as seen from the multitude of publications: Nayak [20], Tracey–Freese [46], Zhang–Owen [47], Cheng and al. [53], Allen [88], Kleiber [138], Argyris [159] etc. and from recurrent congresses [163 to 167].

3. Recapitulation of the theory

3.1 Fundamental equations

Applying the Lagrangian discussion for describing the continuum displacement state, the strain and stress state is referred to the initial (non-load) condition.

With notations in Fig. 1 where C_0 is the initial (non-load) state of the continuum at instant $t=0$, C_1 and C_2 being states at instants t and $t+\Delta t$, locus coordinates of continuum point P for states C_1 and C_2 are:

$$^{t}x_i = {}^{0}X_i + {}^{t}u_i\,, \tag{1}$$

$$^{t+\Delta t}x_i = {}^{0}X_i + {}^{t+\Delta t}u_i = {}^{t}x_i + \Delta u_i \tag{2}$$

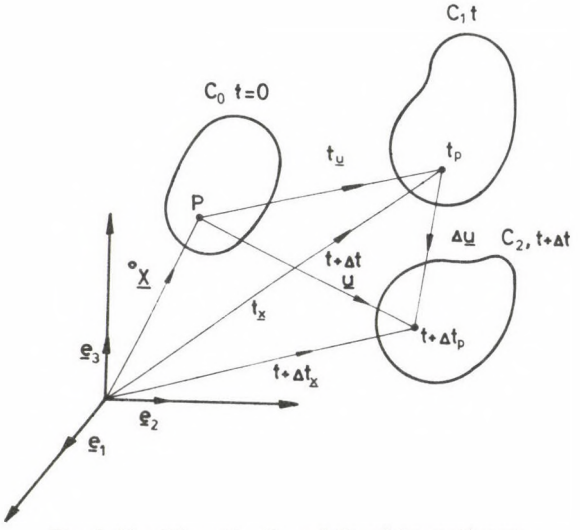

Fig. 1. Conditions C_0, C_1 and C_2 of the continuum

Introducing notation

$$ {}^{t}u_{i,j} = \frac{\partial {}^{t}u_i}{\partial {}^{0}X_j} . $$

Lagrangian strain tensor for state C_1 may be written as:

$$ {}^{t}e_{ij} = \frac{1}{2} ({}^{t}u_{i,j} + {}^{t}u_{j,i} + {}^{t}u_{k,i} {}^{t}u_{k,j}) \tag{3} $$

and its increment

$$ \Delta e_{ij} = \frac{1}{2} (\Delta u_{i,j} + \Delta u_{j,i} + {}^{t}u_{k,i} \Delta u_{k,j} + \Delta u_{k,j} {}^{t}u_{k,j} + \Delta u_{k,i} \Delta u_{k,j}) \tag{4} $$

Applying the principle of virtual work on state C_2, in conformity with [119, 162]—omitting deductions—we obtain:

$$ \int_V {}^{t+\Delta t}\sigma_{ij} \delta {}^{t+\Delta t}e_{ij} \, \mathrm{d}V = \delta {}^{t+\Delta t}W \tag{5} $$

where

${}^{t+\Delta t}\sigma_{ij}$ — second Piola–Kirchhoff stress tensor,

$\delta {}^{t+\Delta t}W$ —virtual work of external forces,

interpreted as:

$$ \delta {}^{t+\Delta t}W = \int_S {}^{t+\Delta t}t_k \delta \Delta u_k \, \mathrm{d}S + \int_V {}^{t+\Delta t}f_k \, \delta \Delta u_k \, \mathrm{d}V . \tag{6} $$

Stresses and strains at time $t + \Delta t$ may be expressed in terms of values at time t and their increments:

$$ {}^{t+\Delta t}\sigma_{ij} = {}^{t}\sigma_{ij} + \Delta \sigma_{ij} , \tag{7} $$

$$ {}^{t+\Delta t}e_{ij} = {}^{t}e_{ij} + \Delta e_{ij} . \tag{8} $$

In conformity with material law, stress increment $\Delta \sigma_{ij}$ may be expressed by the strain increment:

$$ \Delta \sigma_{ij} = D_{ijkl} \, \Delta e_{kl} . \tag{9} $$

Concerning displacement increments, strain increment Δe_{ij} may be decomposed to a linear and a nonlinear part:

$$ \Delta e_{ij} = \Delta \varepsilon_{ij} + \Delta \eta_{ij} , \tag{10} $$

$$ \Delta \varepsilon_{ij} = \frac{1}{2} (\Delta u_{i,j} + \Delta u_{j,i} + {}^{t}u_{k,i} \Delta u_{k,j} + \Delta u_{k,i} {}^{t}u_{k,j}) , \tag{11} $$

$$ \Delta \eta_{ij} = \Delta u_{k,i} \Delta u_{k,j} . \tag{12} $$

Substituting (7), (8), (9) and (10) into (5) and making use of:

$$ \delta {}^{t+\Delta t}e_{ij} = \delta \Delta e_{ij} \tag{13} $$

yields:

$$\int_V [D_{ijkl}\Delta e_{kl}\delta\Delta e_{ij} + {}^t\sigma_{ij}\delta\Delta\eta_{ij}]\,\mathrm{d}V = \delta\,{}^{t+\Delta t}W - \int_V {}^t\sigma_{ij}\delta\Delta\varepsilon_{ij}\,\mathrm{d}V. \tag{14}$$

Decomposing magnitude $\delta\,{}^{t+\Delta t}W$ to two parts:

$$\delta\,{}^{t+\Delta t}W = \delta\,{}^tW + \delta\Delta W$$

where $\delta\,{}^tW$ is negligible, since at time t the full load work of the solid in virtual displacement increments $\delta\Delta u_k$ is nearly zero.

Differential equation system (14) leads to the finite element algebraic equation system by introducing the known approximation for the field of displacements:

$$\Delta u_k = \sum_{\alpha=1}^{N} \psi_\alpha \Delta u_k^\alpha \tag{15}$$

where Δu_k^α is k-the component of displacement increment of node α of a finite element of N nodes.

Discretizing (15) yields strain increments

$$\Delta\varepsilon_{ij} = [B_{ij\alpha}^{(L_0)k} + B_{ij\alpha}^{(L_1)k}]\,\Delta u_k^\alpha = B_{ij\alpha}^{(L)k}\,\Delta u_k^\alpha, \tag{16}$$

$$\Delta\eta_{ij} = B_{ij\alpha\beta}^{(NL)}\,\Delta u_m^\alpha\,\Delta u_m^\beta \tag{17}$$

where

$$B_{ij\alpha}^{(L_0)k} = \psi_{\alpha,(j}\delta_{i)}^k,$$

$$B_{ij\alpha}^{(L_1)k} = \sum_{\beta=1}^{N} u_k^{(\beta}\psi_{\beta,i}\psi_{\alpha),j},$$

$$B_{ij\alpha\beta}^{(NL)} = \frac{1}{2}\psi_{\alpha,i}\psi_{\beta,j}.$$

Using these equations, (14) becomes:

$${}^{(1)}K_{\alpha\delta}^{pm}\,\Delta u_p^\alpha + {}^{(2)}K_{\alpha\beta\delta}^{prm}\,\Delta u_p^\alpha\Delta u_r^\beta + {}^{(3)}K_{\alpha\beta\gamma\delta}^{prsm}\,\Delta u_p^\alpha\,\Delta u_r^\beta\,\Delta u_s^\gamma = {}^{t+\Delta t}R_\delta^m - {}^tF_\delta^m \tag{18}$$

where

$${}^{(1)}K_{\alpha\delta}^{pm} = {}^{(0)}K_{\alpha\delta}^{pm} + {}^{(u)}K_{\alpha\delta}^{pm} + {}^{(\sigma)}K_{\alpha\delta}^{pm},$$

$${}^{(0)}K_{\alpha\delta}^{pm} = \int_V D_{ijkl}B_{ij\alpha}^{(L_0)p}B_{kl\delta}^{(L_0)m}\,\mathrm{d}V,$$

$${}^{(u)}K_{\alpha\delta}^{pm} = \int_V D_{ijkl}(B_{ij\delta}^{(L_0)m}B_{kl\alpha}^{(L_1)p} + B_{ij\delta}^{(L_1)m}B_{kl\alpha}^{(L_0)p} + B_{ij\delta}^{(L_1)m}\cdot B_{kl\alpha}^{(L_1)p})\,\mathrm{d}V,$$

$${}^{(\sigma)}K_{\alpha\delta}^{pm} = \int_V {}^t\sigma_{ij}B_{ij\delta\alpha}^{(NL)}\delta^{pm}\,\mathrm{d}V,$$

$$^{(2)}K^{prm}_{\alpha\beta\delta} = \int_V D_{ijkl}[2B^{(L)p}_{ij\alpha} B^{(NL)}_{kl\delta\beta}\delta^{mr} + B^{(NL)}_{ij\alpha\beta} B^{(L)m}_{kl\delta}\delta^{pr}]\,\mathrm{d}V,$$

$$^{(3)}K^{prsm}_{\alpha\beta\gamma\delta} = \int_V 2D_{ijkl} B^{(NL)}_{ij\alpha\beta} B^{(NL)}_{kl\delta\gamma}\delta^{pr}\delta^{sm}\,\mathrm{d}V,$$

$$^{t+\Delta t}R^m_\delta = \int_S {}^{t+\Delta t}t^m\psi_\delta\,\mathrm{d}S + \int_V {}^{t+\Delta t}f^m\psi_\delta\,\mathrm{d}V,$$

$${}^tF^m_\delta = \int_V {}^t\sigma_{ij} B^{(L)m}_{ij\delta}\,\mathrm{d}V.$$

Equation (18) is nonlinear in displacement increments, and it may be solved e.g. by the perturbation method [84].

But for engineering practice, linearized form of (18) obtained by neglecting second- and third-order terms is sufficient:

$$^{(1)}K^{pm}_{\alpha\delta}\,\Delta u^\alpha_p = \Delta R^m_\delta - J^m_\delta \tag{19}$$

where

$$\Delta R^m_\delta = {}^{t+\Delta t}R^m_\delta - {}^tR^m_\delta,$$

$$J^m_\delta = {}^tF^m_\delta - {}^tR^m_\delta$$

The usual denominations of previously defined matrices and vectors are:

$^{(0)}K^{pm}_{\alpha\delta}$ — elasto-plastic stiffness matrix;
$^{(u)}K^{pm}_{\alpha\delta}$ — initial displacement stiffness matrix;
$^{(\sigma)}K^{pm}_{\alpha\delta}$ — initial stress stiffness matrix;
ΔR^m_δ — nodal load increment vector;
J^m_δ — initial load vector.

Equation (19) may be solved by either of several iteration procedures (Newton–Raphson, modified Newton–Raphson, etc.).

The subsequent two chapters will present constitutive tangential stiffness matrix D_{ijkl} for elasto-plastic and elasto-viscoplastic deformations.

3.2 Elasto-plastic deformations

There are a great many publications on time-independent elasto-plastic deformations. Actually, several papers were concerned with the development of computational algorithms [46, 51, 53] and the finite element solution of various theories of plasticity [23, 43, 109]. For instance, a complete program for the finite element solution of two-dimensional and axisymmetric elasto-plastic problems is given by Owen–Hinton [64]. This program is, however, erroneous for the plane stress state, and the convergence of the iteration algorithm is insufficient.

A more precise and acceptable part of a program is that given by Dodds and al. [132] for determining elasto-plastic stress increments.

In what follows, fundamental relationships of the finite element program [1, 2] developed for solving two- and three-dimensional elasto-plastic problems will be presented, restricted to describe the stress increment strain increment relationship.

The complete strain increment tensor is divided into an elastic and a plastic part:

$$d\varepsilon_{ij} = d\varepsilon^e_{ij} + d\varepsilon^p_{ij} \tag{20}$$

Rearranging (20) and using Hooke's law, the stress increment is:

$$d\sigma_{ij} = D^e_{ijkl}(d\varepsilon_{kl} - d\varepsilon^p_{kl}) \tag{21}$$

where

$$D^e_{ijkl} = 2G \cdot T_{ijkl} + KL_{ijkl},$$

$$T_{ijkl} = I_{ijkl} - \frac{1}{3} L_{ijkl},$$

$$I_{ijkl} = \frac{1}{2}(\delta_{ik}\delta_{jl} + \delta_{il}\delta_{jk}),$$

$$L_{ijkl} = \delta_{ij}\delta_{kl},$$

$$G = \frac{E}{2(1+\nu)},$$

$$K = \frac{E}{3(1-2\nu)};$$

E — modulus of elasticity;
ν — Poisson's ratio.

Plastic strain increment $d\varepsilon^p_{ij}$ may be written according to the yield law:

$$d\varepsilon^p_{ij} = d\lambda \frac{\partial F}{\partial \sigma_{ij}} = d\lambda\, a_{ij} \tag{22}$$

where

$d\lambda$ — proportional scalar factor;
F — function for formulating the plasticity condition.

For a new anisotropic strain hardening model [3], function F is given in the form:

$$F = \left(\frac{3}{2} N_{ijkl}\bar{s}_{ij}\bar{s}_{kl}\right)^{1/2} - \sigma_y\left(\int d\varepsilon_p\right) = 0 \tag{23}$$

where

$$N_{ijkl} = I_{ijkl} + A(\varepsilon_p) \cdot M_{ijkl},$$
$$M_{ijkl} = \varepsilon^p_{ij}\varepsilon^p_{kl},$$
$$\bar{s}_{ij} = T_{ijkl}\bar{\sigma}_{kl},$$
$$\bar{\sigma}_{kl} = \sigma_{kl} - \alpha_{kl},$$

$$d\varepsilon_p = \left(\frac{2}{3} d\varepsilon_{ij}^p d\varepsilon_{ij}^p\right)^{1/2} \text{ — equivalent plastic strain;}$$

$$\bar{\sigma} = \left(\frac{3}{2} N_{ijkl} \bar{s}_{ij} \bar{s}_{kl}\right)^{1/2} \text{ — equivalent stress.}$$

As initial plasticity condition, yield function (23) delivers the Mises plasticity condition. In subsequent plastic deformations there is a hardening model where the loaded surface expands (or shrinks) in the stress space, performs translational motion and becomes distorted, as sketched in Fig. 2 in the two-dimensional principal stress space.

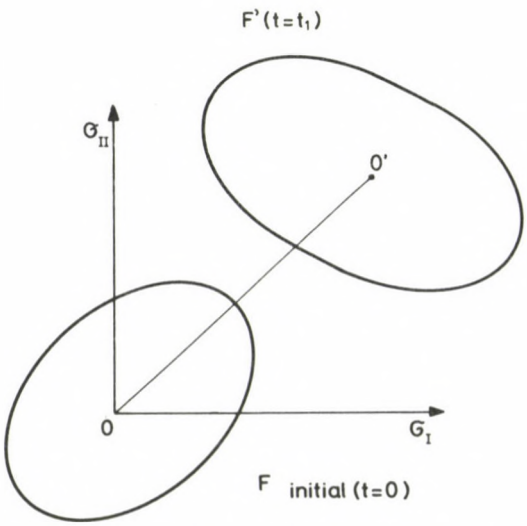

Fig. 2. Illustration of the anisotropic hardening model

Translation motion—kinematic hardening—is described by translation tensor $\alpha_{ij}(\varepsilon_{ij}^p)$. According to both classic kinematic hardening theories by Prager [116] and by Ziegler [135], the translation tensor increment is equally

$$d\alpha_{ij} = d\lambda(1-\beta) p t_{ij} . \tag{24}$$

Parameter $-1 < \beta \leq 1$ decomposes the plastic strain increment to an isotropic and a kinematic part ($d\varepsilon_{ij}^{p(i)}$ and $d\varepsilon_{ij}^{p(k)}$, respectively).

Definitions of p and t_{ij} in (24) according to Prager's theory:

$$p = \frac{2}{3} H . \tag{25}$$

$$t_{ij} = a_{ij} , \tag{26}$$

and to Ziegler's theory:

$$p = \frac{H}{\sigma}\left(\frac{2}{3} a_{ij} a_{ij}\right)^{1/2}, \tag{27}$$

$$t_{ij} = \bar{\sigma}_{ij}. \tag{28}$$

$\sigma_y(\varepsilon_p)$ and $A(\varepsilon_p)$ in function F (23) are material characteristic functions interpreting magnitudes:

$$H = \frac{\mathrm{d}\sigma_y}{\mathrm{d}\varepsilon_p} \tag{29}$$

and

$$\gamma = \frac{\mathrm{d}A}{\mathrm{d}\varepsilon_p}. \tag{30}$$

$\mathrm{d}\lambda$ is determined by the complete differential of function F:

$$dF = \frac{\partial F}{\partial \sigma_{ij}} \mathrm{d}\sigma_{ij} + \frac{\partial F}{\partial \alpha_{ij}} \mathrm{d}\alpha_{ij} + \frac{\partial F}{\partial \varepsilon^p_{ij}} \mathrm{d}\varepsilon^p_{ij} + \frac{\partial F}{\partial \varepsilon_p} \mathrm{d}\varepsilon_p. \tag{31}$$

Confrontation of (31) and of (21), (22) and (24) yields for $\mathrm{d}\lambda$:

$$\mathrm{d}\lambda = \frac{D^e_{ijkl} a_{ij} \mathrm{d}\varepsilon_{kl}}{D^e_{mn\,pq} - a_{mn} a_{pq} + (1-\beta) p t_{pq} a_{pq} - b_{pq} a_{pq} + (\beta H - \gamma h)\left(\frac{2}{3} a_{pq} a_{pq}\right)^{1/2}} \tag{32}$$

where:

$$a_{pq} = \frac{\partial F}{\partial \sigma_{ij}} = \frac{3}{2\bar{\sigma}} N_{pq\,mn} \bar{s}_{mn},$$

$$b_{pq} = \frac{\partial F}{\partial \varepsilon^p_{pq}} = \frac{3A}{2\bar{\sigma}} \bar{s}_{mn} \varepsilon^p_{mn} \bar{s}_{pq},$$

$$h = \frac{3}{4\sigma} M_{pq\,mn} \bar{s}_{pq} \bar{s}_{mn}.$$

Utilizing $\mathrm{d}\lambda$ in (32), (21) and (22) yields:

$$\mathrm{d}\sigma_{ij} = D_{ijkl} \mathrm{d}\varepsilon_{kl} \tag{33}$$

where:

$$D_{ijkl} = D^e_{ijkl} - \frac{D^e_{ij\,mn} a_{mn} a_{pq} D^e_{pq\,kl}}{D^e_{rs\,tv} a_{rs} a_{tv} + (1-\beta) p t_{rs} a_{rs} - b_{rs} a_{rs} + (\beta H - \gamma h)\left(\frac{2}{3} a_{rs} a_{rs}\right)^{1/2}}$$

Adequately selecting H, β and A, the equation above serves for computations based on different hardening model types. These cases are described in [3] and [55].

3.3 Elasto-viscoplastic deformations

Computation of elasto-viscoplastic deformations relies on Perzyna's theory [168, 169]. Finite element analyses, according to this theory, were made by e.g. Cormeau [144, 145, 155], Zienkiewicz [150], Owen–Hinton [64], Zienkiewicz [148], Zienkiewicz–Norris–Naylor [153], Nagarjan–Popov [170], Owen–Praksh–Zienkiewicz [147], Owen–Zienkiewicz–Cormeau [151], Pian–Lee [156], Nagarjan–Popov [170], Hughes–Taylor [171].

These publications give detailed finite element equations according to this theory. Several computational algorithms (explicit, explicit/implicit, implicit), are compared for different examples of application. A complete finite element program for two-dimensional elasto-viscoplastic problems was presented by Owen–Hinton [64].

Perzyna's elasto-viscoplastic equation combines creep and plastic strain, at the same time it permits the analysis of the pure creep phenomena.

In the program elaborated for solving elasto-viscoplastic problems, algorithms and programs developed by the mentioned authors have been made use of. Program in [64] has been developed for reckoning with geometrical nonlinearity.

In the following, relationships for stress increment determination will be outlined.

Stress increment during time Δt is obtained from:

$$\Delta\sigma_{ij} = D^{e}_{ijkl}(\Delta\varepsilon_{kl} - \Delta\varepsilon^{vp}_{kl}) . \tag{34}$$

Utilizing the time integration scheme, relying on the method of finite differences for determining the viscoplastic strain increment $\Delta\varepsilon^{vp}_{ij}$:

$$\Delta\varepsilon^{vp}_{ij} = \Delta t[(1-\alpha)^{t}\dot{\varepsilon}^{vp}_{ij} + \alpha^{t+\Delta t}\dot{\varepsilon}^{vp}_{ij}] \tag{35}$$

where $0 \leqq \alpha \leqq 1$ is the weighting factor.

Viscoplastic strain rate in (35) becomes in the Perzyna theory:

$$\dot{\varepsilon}^{vp}_{ij} = \gamma < \Phi(F/\sigma_y) > \frac{\partial F}{\partial \sigma_{ij}} \tag{36}$$

where γ is a fluidity parameter, Φ the yield function and F the plasticity condition, while brackets $\langle\ \rangle$ are interpreted as:

$$\langle \Phi(F/\sigma_y) \rangle = \begin{cases} 0 & \text{if} \quad F \leqq 0 \\ \Phi(F/\sigma_y) & \text{if} \quad F > 0 \end{cases}$$

In the developed program, F is given in terms of the Mises plasticity condition:

$$F = \left(\frac{3}{2} s_{ij} s_{ij}\right)^{1/2} - \sigma_y(\int \mathrm{d}\varepsilon_p) = 0 . \tag{37}$$

Magnitude ${}^{t+\Delta t}\dot{\varepsilon}_{ij}^{vp}$ in (35) is obtained by the Taylor series expansion of viscoplastic strain rate $\dot{\varepsilon}_{ij}^{vp}$ till the first term:

$$ {}^{t+\Delta t}\dot{\varepsilon}_{ij}^{vp} = {}^{t}\dot{\varepsilon}_{ij}^{vp} + {}^{t}\left(\frac{\partial \dot{\varepsilon}_{ij}^{vp}}{\partial \sigma_{kl}}\right) \Delta\sigma_{kl} = {}^{t}\dot{\varepsilon}_{ij}^{vp} + H_{ijkl}^{\sigma}\,\Delta\sigma_{kl}\,. \tag{38} $$

Utilizing (34), (35) and (38):

$$ \Delta\sigma_{ij} = \hat{D}_{ijkl}(\Delta\varepsilon_{kl} - \Delta t\, {}^{t}\dot{\varepsilon}_{kl}^{vp}) \tag{39} $$

where

$$ \hat{D}_{ijkl} = [D_{ijkl}^{(e)^{-1}} + \alpha\Delta\, {}^{t}H_{ijkl}^{\sigma}]^{-1}. $$

In case of a pure explicit time integration, ($\alpha = 0$) $\hat{D}_{ijkl}$ simplifies to D_{ijkl}^{e}. But for $\alpha > 0$, in producing $\hat{D}_{ijkl}$ in the computations, inversion is needed. For reducing running time, in producing $\hat{D}_{ijkl}$, inversion may be analytically made with the method in [82].

Omitting deductions, $\hat{D}_{ijkl}$ becomes:

$$ \hat{D}_{ijkl} = \frac{2G}{1+3G/\psi_S}\, T_{ijkl} + KL_{ijkl} - \frac{9G^2(\psi_S - \psi)s_{ij}s_{kl}}{\sigma^2(\psi + 3G)(\psi_S + 3G)} \tag{40} $$

where:

$$ \psi_S = \frac{1}{\alpha\Delta t\, \gamma\Phi/\sigma}, $$

$$ \psi = \frac{1}{\alpha\Delta t\, \gamma \dfrac{\mathrm{d}\Phi}{\mathrm{d}F}}. $$

4. The computation method

The incremental finite element basic equation (19) deduced under 3.1 will be applied for solving elasto-plastic and elasto-viscoplastic problems. In solving the nonlinear equation system, two cases have been distinguished.

The first case (a) refers to the solution of elasto-plastic problems and to a group of elasto-viscoplastic problems where the steady state for a timely constant external load is wanted.

The second case (b) involves solutions of elasto-viscoplastic problems for different loading rates. Time increments will be denoted as:

$$ t_{i+1} = t_i + \Delta t_i $$

where Δt_i is the time interval at step i.

Computation steps for either of the two cases (a, b) are the following:

a) External load R is applied in k steps. Steps involve external load increments

$$ \lambda_k R = \Delta R_k $$

each.

Iteration steps of the equilibrium solution for external load increment ΔR_k are:

1. Solution of

$$\mathbf{K}_k^i \Delta u^i = \Delta R_k^i - J^i \tag{41}$$

where

$$\mathbf{K}_k^i = \begin{cases} \mathbf{K}_k & - \text{ in the modified} \\ \mathbf{K}^i & - \text{ in the original} \end{cases} \text{ Newton–Raphson procedure}$$

$$\Delta R_k^i = \begin{cases} \Delta R_k & \text{for } i=1 \\ 0 & \text{for } i>1 \end{cases}$$

$$J^i = \begin{cases} J_k & \text{for } i=1 \\ F^i - R_k - V^i - J_k & \text{for } i>1 \end{cases}$$

where J_k is the residual load vector for the preceding external load increment, and

$$R_k = R_{k-1} + \Delta R_k$$

and

$$V^i = \begin{cases} 0 & - \text{ in elasto-plastic problems} \\ \int_V \mathbf{B}_i^T \hat{\mathbf{D}}_i \dot{\varepsilon}_i^{vp} \Delta t \, \mathrm{d}V & - \text{ in elasto-viscoplastic problems.} \end{cases}$$

2. Forming magnitudes

$$u^{i+1} = u^i + \Delta u^i,$$

$$\varepsilon^{i+1} = \varepsilon^i + \Delta \varepsilon^i,$$

$$\sigma^{i+1} = \sigma^i + \Delta \sigma^i$$

3. Producing magnitudes

$$J^{i+1} \quad \text{and} \quad \mathbf{K}^{i+1}.$$

4. The iteration is examined for convergence. Within the specific error criterion, the next external load increment is applied. Else, computation is started again from $i \to i+1$ and 1.

b) In the second case, elasto-viscoplastic deformations for the given load rate $\dot{R}$ is determined. In this case the computation involves:

1. Solution of

$$\mathbf{K}^i \Delta u^i = \Delta R^i - J^i \tag{42}$$

where

$$\Delta R^i = \Delta t_i \dot{R} \quad \text{and} \quad J^i = \begin{cases} 0 & \text{if } i=0 \\ F^i - R^i - V^i & \text{if } i>0 \end{cases}$$

2. Utilizing Δu^i from (42), determination of magnitudes

$$u^{i+1} = u^i + \Delta u^i,$$

$$R^{i+1} = R^i + \Delta R^i,$$

$$V^{i+1} = \int_V \mathbf{B}_{i+1}^T \hat{\mathbf{D}}_{i+1} \dot{\varepsilon}_{i+1}^{vp} \Delta t_{i+1} \, dV,$$

$$F^{i+1} = \int_V \mathbf{B}_{i+1}^T \sigma_{i+1} \, dV,$$

$$\mathbf{K}^{i+1} = \int \mathbf{B}_{i+1}^T \hat{\mathbf{D}}_{i+1} \mathbf{B}_{i+1} \, dV.$$

3. Application of external load increment for the next time interval:

$$\Delta R^{i+1} = \Delta t_{i+1} R$$

and repeating the computation from 1 for $i \to i+1$, until the predefined load level.

5. Examples of application

In addition to theoretical works, quoted authors present solutions of several problems, either by programs developed by themselves or by means of extended program systems. An important part of a great many problems may be considered as basic problems, with solutions suited for the testing of the developed program. Most of these problems may be solved analytically, or relevant measurements are available. Subsequently some of these kinds of problems will be presented.

Several authors determined elasto-plastic deformation of a plate weakened by a circular hole and exposed to tensile load:

For small elasto-plastic deformations: [10], [12], [45], [147], [109], [42], [54].

For elasto-viscoplastic deformations: [146], [142], [145], [148].

For large elasto-plastic deformations: [142].

Theokaris–Marketos [68] examined this problem by measurement. Elasto-plastic deformation of a plate weakened by a V notch exposed to a tensile load was examined in: [21], [18], [13], [57], [114].

The most frequent problems include elasto-plastic ([18], [64], [87]), elasto-viscoplastic ([154], [64], [146]), and creep deformations [14] of thick-walled tubes.

The most large elasto-plastic deformations of a clamped-edge shallowcap under concentrated load have many solutions: [122], [35], [39], [105], [138], [115], [78], [16], [64], [75], [133].

There are several elasto-plastic analyses of the cylinder to sphere connection, tested by measurement by Dino–Gill [67]: [151], [132], [122].

[11], [26], [27], and [25] describe elasto-plastic, [150] and [170] elasto-viscoplastic, [123], [122], [170], large elasto-plastic deformations of a torispherical pressure vessel. Elasto-plastic deformations combined with geometrical nonlinearity of shell structures and plates of different geometries were analyzed in [14], [16], [34], [93], [94], [97], [114], [115], [117], [121–125], [75], [78], [150].

In the following, application of the finite element program [4] developed on the theoretical fundamentals described above will be illustrated in some problems.

5.1 Elasto-plastic deformation of thick-walled tubes

Mathematical model of a thick-walled tube subject to internal pressure is seen in Fig. 3. The problem is treated as that of symmetry of revolution and solved by means of 8-node isoparameter elements, for a 3×3 Gaussian integration.

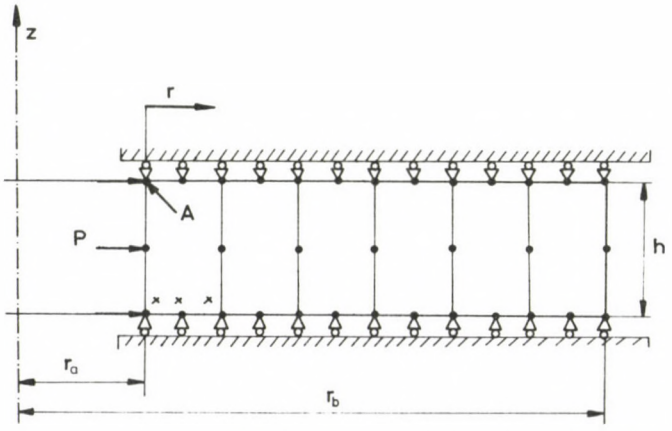

Fig. 3. Mathematical model and finite element division of the thick-walled tube

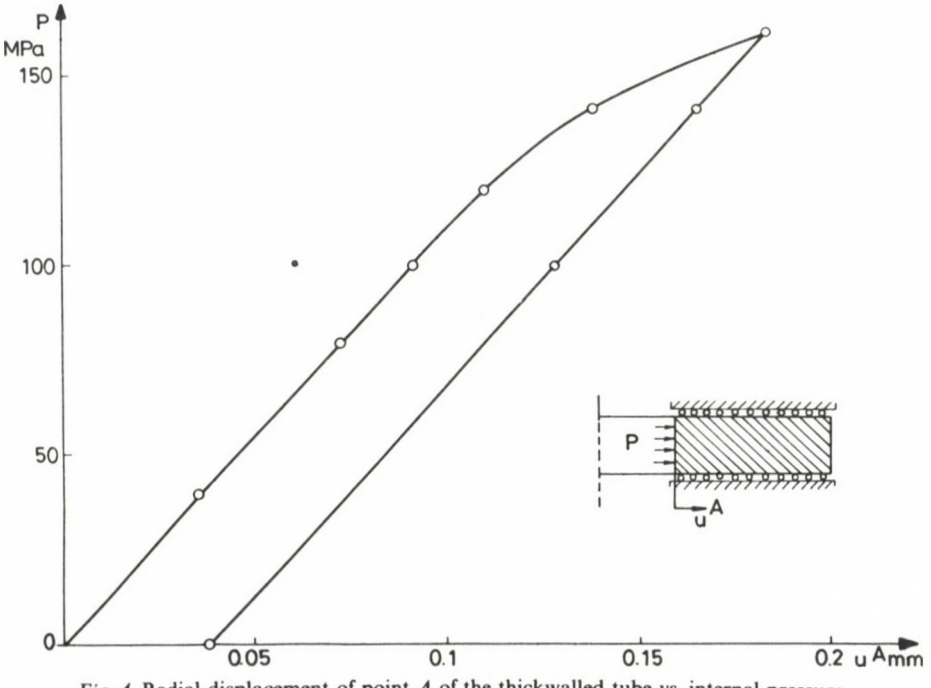

Fig. 4. Radial displacement of point *A* of the thickwalled tube vs. internal pressure

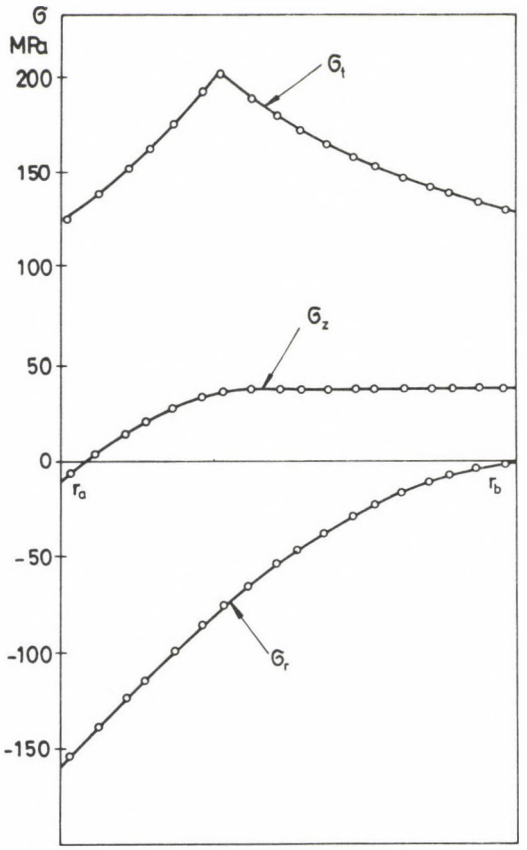

Fig. 5. Distribution of stresses σ_t, σ_r and σ_z across the wall thickness at pressure $p = 160$ MPa

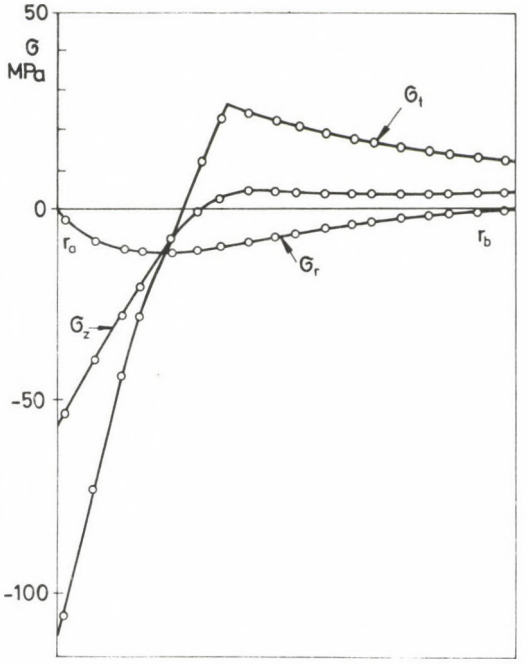

Fig. 6. Distribution of residual stresses across the wall thickness after unloading

Computation data:

$E = 2.1\ 10^5$ MPa
$\nu = 0.3$
$\sigma_{y0} = 240$ MPa
$H = 0.0$ elastic-perfectly plastic material model)
$r_b = 100$ mm
$r_k = 200$ mm
$h = 50$ mm.

Computation results have been plotted in Figs 4, 5, 6. Figure 4 shows displacement of tube inner surface vs. internal pressure. Tangential (σ_t), radial (σ_r) and axial (σ_z) stress distributions along the wall thickness for a pressure $p = 160$ MPa can be seen in Fig. 5. At this pressure the tube got to the plastic range up to radius $r_c = 166$ mm. The tube is unloaded from a pressure $p = 160$ MPa elastically, the residual stress distributions are seen in Fig. 6.

5.2 Creep of a pressure vessel with a spherical end closure

Next, creep of a pressure vessel with a spherical end closure lid was examined. The problem was solved by means of the elastic-viscoplastic program. Geometry and finite element division can be seen in Fig. 7. The problem was solved by means of 8-

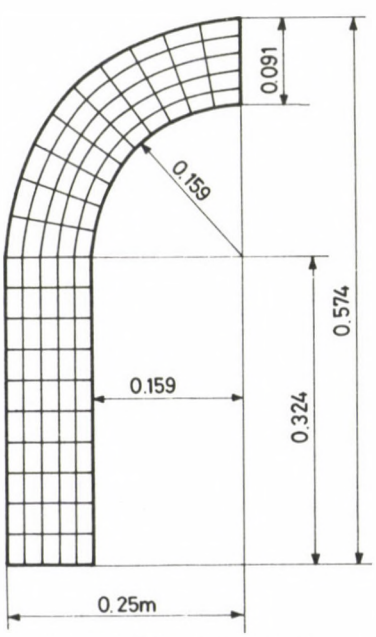

Fig. 7. Geometrical dimensions and finite element division of the cylinder with a lid

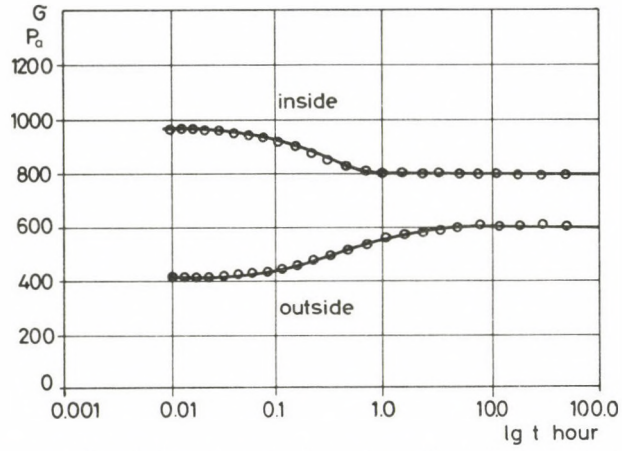

Fig. 8. Development of equivalent stresses inside and outside the lid to a cylinder connection

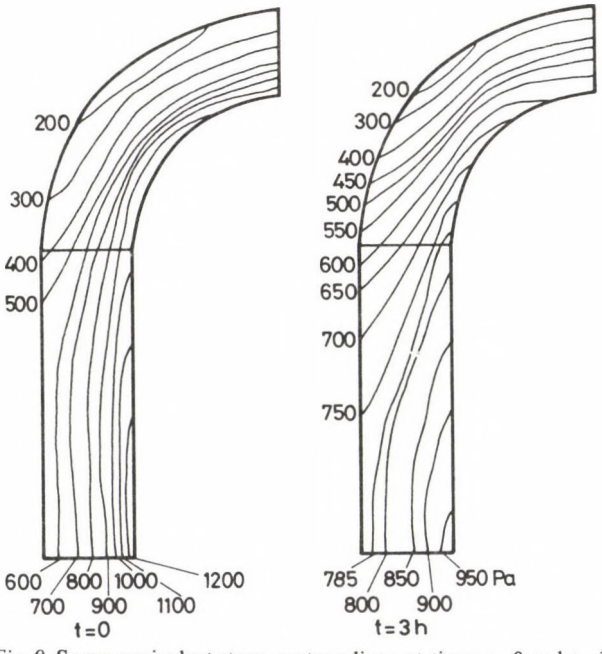

Fig. 9. Some equivalent stress contour lines at times $t=0$ and $t=3$ h

node, isoparametric elements of symmetry of revolution. The bin was exposed to a pressure $p=445$ Pa. Computation data:

$E = 20 \cdot 10^5$ Pa
$\nu = 0.3$
$\Phi(F/\sigma_y) = (F/\sigma_y)^{3.61}$
$\sigma_y = 1$ (creep)
$\gamma = 21.146 \cdot 10^{-16}$

Figure 8 shows equivalent stress relaxation at the outer and inner side of the cylinder-end closure junction. The steady state was found to be established after about 3 hours. Contour lines of some values of the equivalent stress at instants $t = 0$ and $t = 3$ h can be seen in Fig. 9.

5.3 Rectangular plate under a uniform load

The problem of a rectangular plate under a uniform load will be examined in accordance with two different geometric boundary conditions. In the first case, the plate is clamped, and in the second case supported along the edge. Both cases amply occur in publications. The problem was solved by Ang–Lopez [76] and Lin-Ho [77] with the method of finite differences. The lower and upper limits of load capacity was examined by Hodge–Belytschko [70], [79].

The problem was solved by Hodge–McMahon [72], Belytschko–Velebit [73], Backlund–Wennerström [32], Barnar–Sharman [71], Spilker–Munir [69] and Martins–Owen [125] with the finite element method. The problem will be solved under both boundary conditions, also taking large deformations into consideration, applying a linear elastic material model.

This plate problem was examined from the aspect of geometrical nonlinearity by Brebbia-Connor [74], Hughes–Liu [78], Martins–Owen [125], Javaherian and al. [75].

The finite element analysis applied to thick shell elements, applying 6-point Gaussian integration along the thickness. Because of symmetry, it is sufficient to examine one quarter of the plate. Finite element division is seen in Fig. 10 (16 elements, 65 nodes).

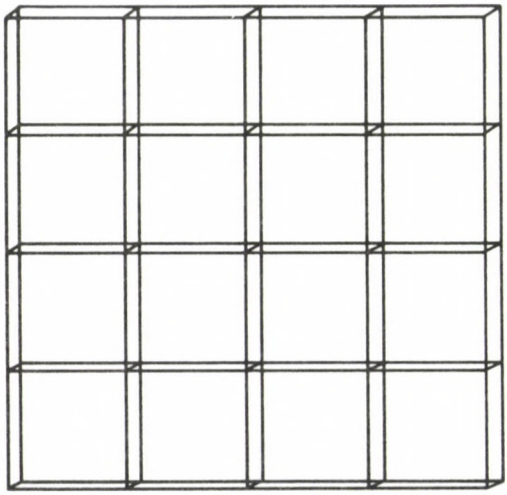

Fig. 10. Finite element division of the quarter plate

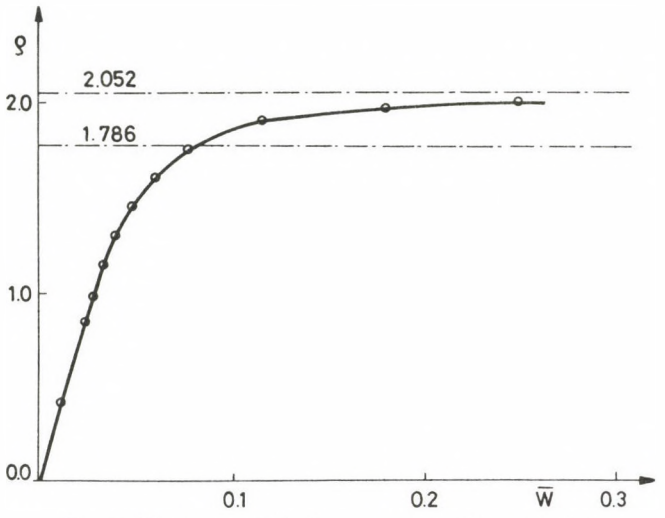

Fig. 11. Plate centre deflection vs. pressure (clamped edge)

Further computation data:

L = 500 mm
h = 20 mm
E = $2.1 \cdot 10^5$ MPa
σ_{y_0} = 300 MPa
ν = 0.3
H = 0.0 (elastic-perfectly plastic material model).

5.3.1 Clamped edge

Plate centre deflection vs. pressure is seen in Fig. 11. Dimensionless magnitudes plotted on axes are:

$$\rho = \frac{p \cdot L^2}{6 \cdot M_0}$$

$$\bar{W} = \frac{W \cdot D}{4 \cdot M_0 \cdot L^2}$$

where:

$$M_0 = \frac{1}{4} \sigma_{y_0} h^2$$

$$D = \frac{E \cdot h^3}{12(1 - \nu^2)}$$

Also lower and upper limits of load capacity are to be seen in the figure [70, 79]. Plastic zones for different load increments can be seen in Fig. 12.

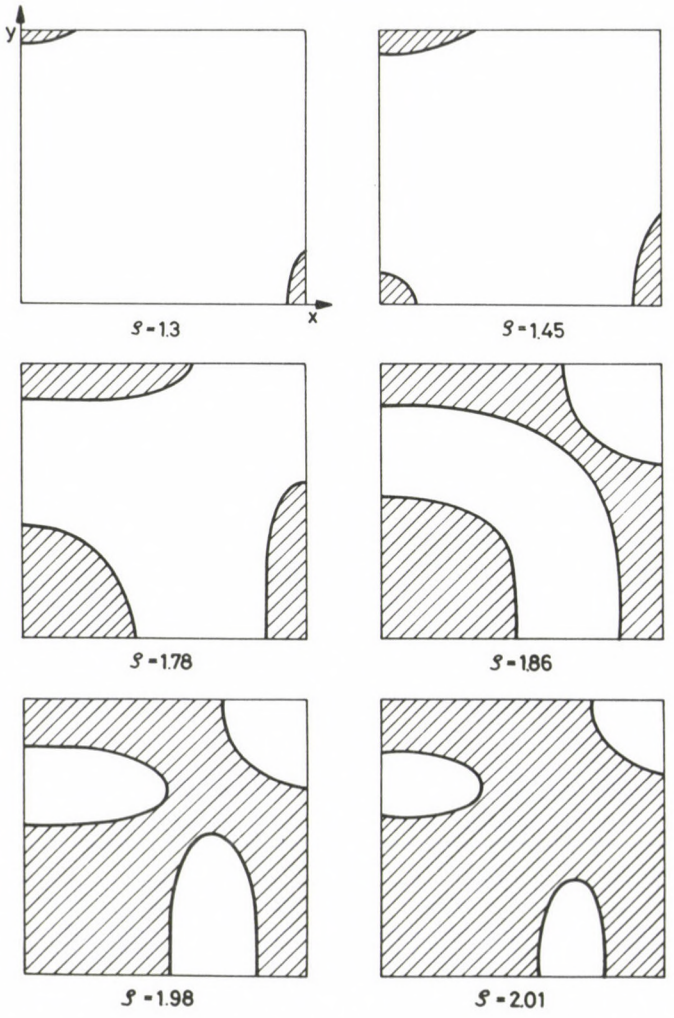

Fig. 12. Development of the plastic zone in the quarter plate with a clamped edge

The clamped-edge plate has also been solved as a problem of geometrical nonlinearity. In this case the plate material is linear elastic. Plate centre deflection vs. pressure is to be seen in Fig. 13.

In this case, non-dimensional parameters on axes are:

$$\gamma = \frac{p \cdot L^4}{D \cdot h}$$

$$W^* = \frac{Wc}{h}$$

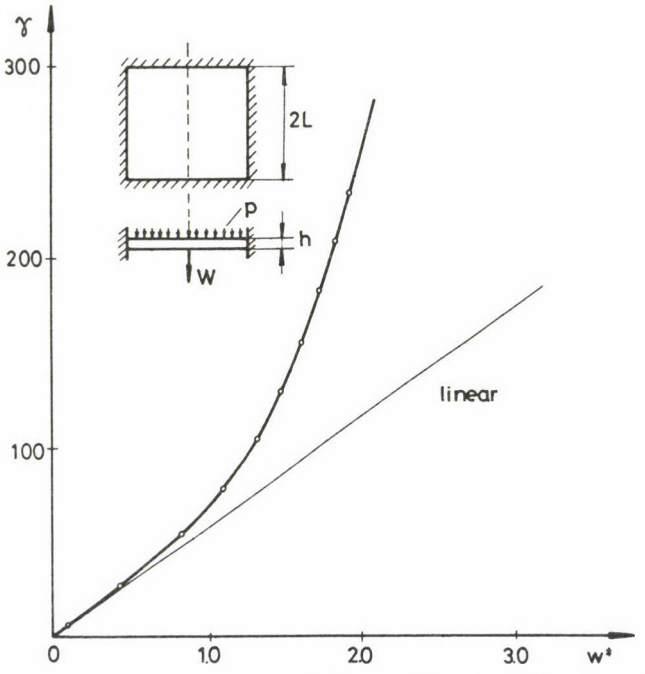

Fig. 13. Deflection of the plate centre vs. pressure in the case of geometrical nonlinearity (clamped edge)

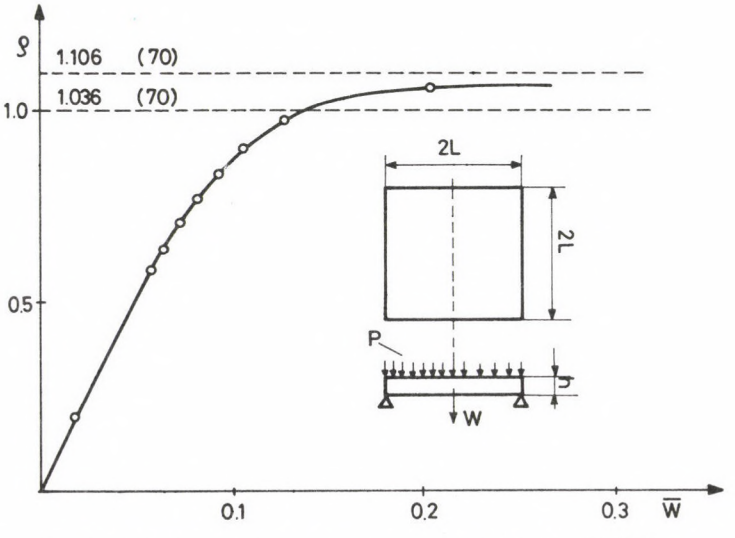

Fig. 14. Deflection of the plate centre vs. pressure (supported edge)

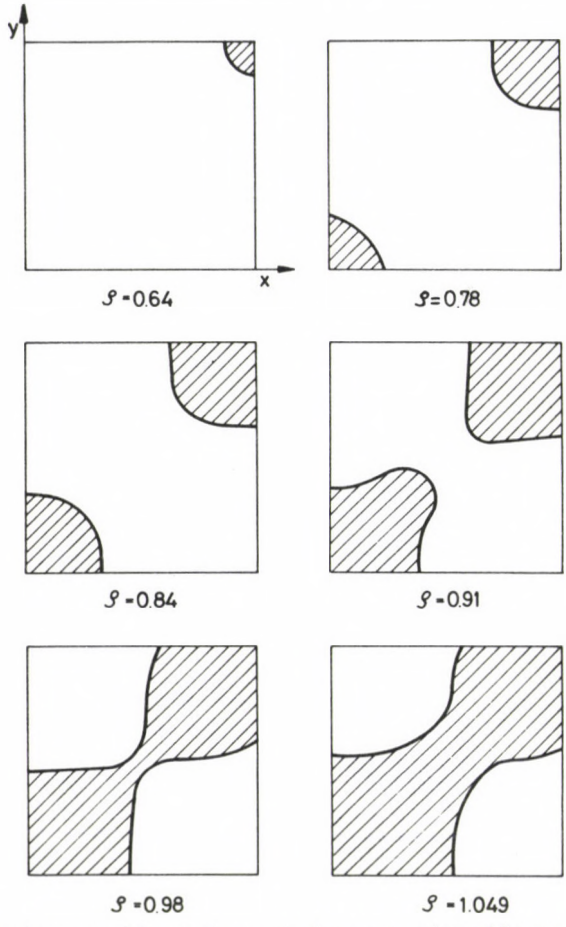

Fig. 15. Development of the plastic zone in the quarter plate with a supported edge

5.3.2 Supported edge

Deflection of the centre of a plate supported along its edge vs. pressure is to be seen in Fig. 14, also indicating lower and upper limits of load capacity. Development of the plastic zone can be seen in Fig. 15. Development of the plastic zone along the plate diagonal across the wall thickness under both boundary conditions has been plotted in Fig. 17.

Centre deflection of a supported-edge plate computed by reckoning with geometrical nonlinearity is to be seen in Fig. 16.

Definition of parameter λ:

$$\lambda = \frac{p \cdot L^4}{E \cdot h^4} .$$

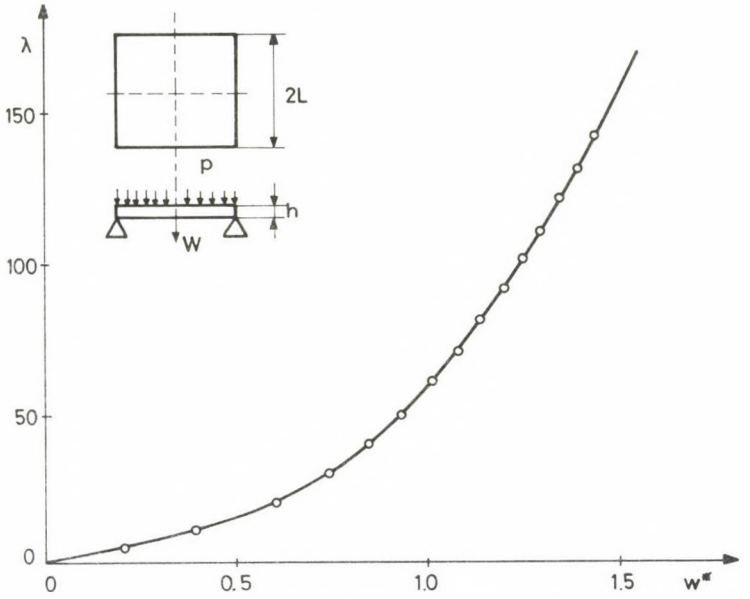

Fig. 16. Plate centre deflection vs. pressure in the case of geometrical nonlinearity (supported edge)

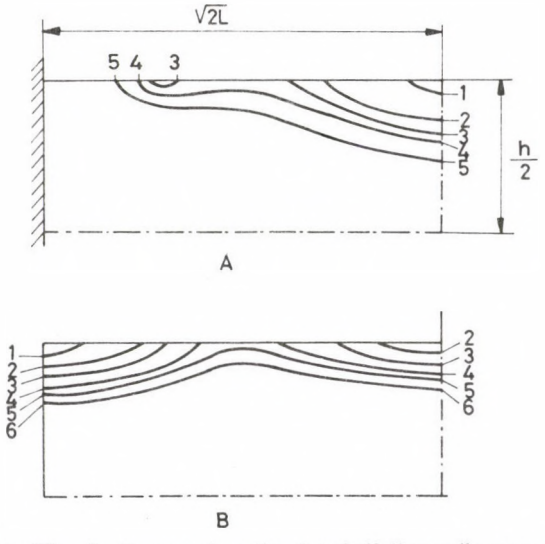

Fig. 17. Development of the plastic zone along the plate half diagonally across the wall thickness.
a) clamped edge b) supported edge

References

1. Szabó, L.: Rugalmas-képlékeny problémák megoldása végeselem módszer alkalmazásával. VEIKI Beszámoló Jelentés. (Solution of Elasto-Plastic Problems by the Finite Element Method. Report VEIKI). October 1982.
2. Szabó, L., Pammer, Z.: Háromdimenziós rugalmas-képlékeny feladatok megoldása végeselem módszerrel. (Finite element solution of three-dimensional elasto-plastic problems). Gép, 24 (1982), 361–369.
3. Szabó, L.: Comparison of some plasticity theories by means of finite element method. *Periodica Polytechnica Mech. Eng.* 27 (1983).
4. Szabó, L.: Rugalmas-képlékeny és kúszási feladatok megoldása végeselem módszerrel. VEIKI Kutatási Jelentés. (Finite element solution of elasto-plastic and creep problems. Research Report VEIKI). March 1983.
5. Gallagher, R. H., Padlog, J., Kamel, W. H.: Stress analysis of heated complex shapes. *ARS. Journal* (1962), 700–707.
6. Swedlow, J. L., Yang, W. H.: Stiffness analysis of elastoplastic plates. Graduate Aeronautical Lab., California Inst. of Techn. SM 65–10 (1965).
7. Turner, M. J., Dill, E. H., Martin, H. C., Melosh, R. J.: Large deflection of structures subjected to heating and external loads. J. Aero. Sciences. 27 (1960), 97–102.
8. Argyris, J. H.: Matrix methods of structural analysis—a precis of recent developments. in: Matrix Methods in Struct. Analysis. ed.: Fraeys, B., de Veubeke. Pergamon Press, Oxford, 1964, 1–64.
9. Wilson, E. L., Jones, L. R., Hsueh, T. M.: Large displacement analysis of axisymmetric shell. Report No. 69–13 Univ. California, Berkeley, 1969.
10. Marcal, P. V.: A stiffness method for elastic-plastic problems. Int. J. Mech. Sci. 7 (1965), 229–238.
11. Marcal, P. V., Pilgrim, W. R.: A stiffness method for elastic-plastic shells of revolution. J. Strain Analysis, 1 (1966), 339–350.
12. Marcal, P. V.: Finite element analysis with material nonlinearities-theory and practice. Brown University. Techn. Rep. No. 3. NOOO14-0007/3. August 1969.
13. Marcal, P. V., King, I. P.: Elastic-plastic analysis of two-dimensional stress systems by the finite element method. Int. J. Mech. Sci. 9 (1967), 143–155.
14. Marcal, P. V.: Large deflection analysis of elastic-plastic shells of revolution. AIAA J. 8 (1970), 1627–1633.
15. Zienkiewicz, O. C., Valliappan, S., King, I. P.: Elasto-plastic solutions of engineering problems 'initial stress', finite element approach. Int. J. Num. Meth. Eng. 1 (1969), 75–100.
16. Nayak, G. C.: Plasticity and large deformation problems by the finite element method. Ph. D. Thesis, Univ. of Wales, Swansea, 1971.
17. Nayak, G. C., Zienkiewicz, O. C.: Note on the 'alpha' constant stiffness method for the analysis of nonlinear problems. Int. J. Num. Meth. Eng. 4 (1972), 579–582.
18. Nayak, G. C., Zienkiewicz, O. C.: Elasto-plastic stress analysis. A generalization for various constitutive relations including strain softening. Int. J. Num. Meth. Eng. 5 (1972), 113–135.
19. Owen, D. R. J., Salonen, E. M.: Three-dimensional elasto-plastic finite element analysis. Int. J. Num. Meth. Eng. 9 (1975), 209–218.
20. Nayak, G. C.: Plasticity solution by finite element method. in: IUTAM Symposium eds: Hult, 3. Lemaitre, J. Senlis, 1980, 185–189.
21. Yamada, Y., Yoshimura, N., Sakurai, T.: Plastic stress strain matrix and its application for the solution of elastic-plastic problem by the finite element method. Int. J. Mech. Sci. 10 (1968), 343–354.
22. Yamada, Y.: Recent developments in matrix displacement method for elastic-plastic problems in Japan. — Recent Advances. in: Matrix Methods of Structural Analysis and Design. ed: Gallagher, R. H., Yamada, Y., Oden, J. T. Univ. Alabama Press, 1971, 283–316.
23. Yamada, Y., Huang, Y., Nishiguchi, I.: Deformation theory of plasticity and its installation in the finite element analysis routine. 2nd Number. Methods in Fract. Mech. 1980. Proc. of the Int. Conf. Swansea, July 7–11 (1980), 343–357.
24. Richard, R. M., Blacklock, J. R.: Finite element analysis of inelastic structure. AIAA J. 7 (1969), 432–438.
25. Popov, E. P., Khojasteh-Bakhi, M., Sharifi, P.: Elastic-plastic analysis of some pressure vessel heads. J. of Eng. for Industry (1970), 309–316.

26. Zudans, Z.: Finite element incremental elastic-plastic analysis of pressure vessels. J. of Eng. Industry. (1970), 293–302.
27. Khojasteh, Bakht, Popov, E. P.: Analysis of elastic-plastic shells of revolution. J. of the Eng. Mech. Div. EM. 3. 96 (1970), 327–340.
28. Khojasteh, Bakht, M.: Analysis of elastic-plastic shells of revolution under axisymmetric loading by finite element method. Report No. SESM 67–8, Univ. California, Berkeley, April 1967.
29. Akyuz, F. A., Merwin, J. E.: Solution of nonlinear problems of elastoplasticity by finite element method. AIAA J. 6 (1968), 1825–1831.
30. Argyris, J. H.: Elasto-plastic analysis of three dimensional media. Acta Techn. Hung. 54 (1966), 219–238.
31. Argyris, J. H., Scharp, D. W.: Methods of elastoplastic analysis. J. of Appl. Math. and Phys. 23 (1972), 517–552.
32. Backlund, J., Wennerström, H.: Finite element analysis of elasto-plastic shells. Int. J. Num. Meth. Eng. 8 (1974), 415–424.
33. Kalev, T., Gluck, J.: Elasto-plastic finite element analysis. Int. J. Num. Meth. Eng. 11 (1977), 875–881.
34. Yamada, Y., Sakurai, T.: Basic formulation and a computer program for inelastic large deformation analysis. Third Int. Conf. Pressure Vessel Technology Tokyo, (1977), 341–351.
35. Mondkar, D. P., Powell, G. H.: Evaluation of solution schemes for nonlinear structures. Comput. & Struct. 9 (1978), 223–236.
36. Yamada, Y.: Constitutive modelling of inelastic behavior and numerical solution of nonlinear problems by the finite element method. Comput. & Struct. 8 (1978), 533–543.
37. Cheng, S. Y., Hsu, T. R.: On an elasto-plastic stress-strain relationship for multi-axial stress states. Int. J. Num. Meth. Eng. 12 (1978), 1617–1622.
38. Rich, T. P.: Closed form elastic-plastic stiffness matrix for axisymmetric finite elements. Int. J. Num. Meth. Eng. 12 (1978), 59–65.
39. William, K. J.: Numerical solution of inelastic rate processes. Comput. & Struct. 8 (1978), 511–531.
40. Levy, A., Pifko, A., Armen, H.: Finite element elastic-plastic analysis of LMFBR components. Nucl. Eng. Des. 45 (1978), 411–418.
41. Landau, L., Wrobel, L. C., Ebecken, N. F. F.: Elastic-plastic analysis of shell structures. Comp. & Struct. 9 (1978), 351–358.
42. Yagawa, G., Nishioka, T., Ando, Y.: Elastic-plastic finite element analysis using superposition. Nucl. Eng. Des. 34 (1975), 247–254.
43. Tang, S. C.: Elasto-plastic and large deformation analysis of thin shells by the deformation theory of plasticity. Comp. & Struct. 6 (1976), 297–303.
44. de Lorenzi, H. G., Shih, C. F.: Finite element implementation of the deformation theory of plasticity. GE T IS Rep. 80CRD058 (1980).
45. Kim, O. H.: A finite element formulation based on Nadai's deformation theory for elasto-plastic analysis. Int. J. Num. Meth. Eng. 17 (1981), 1861–1876.
46. Tracey, D. M., Freese, C. E.: Adaptive load incrementation in elastic-plastic finite element analysis. Comput. & Struct. 13 (1981), 45–53.
47. Zhang, L., Owen, D. R. J.: A modified secant Newton method for non-linear problems. Comput. & Struct. 15 (1982), 543–547.
48. Zak, A. R., Craddock, J. N.: An elastic-plastic analysis of non-axisymmetric structures. Comput. & Struct. 10 (1979), 841–846.
49. Armen, H.: Assumptions, models, and computation methods for plasticity. Comput. & Struct. 10 (1979), 161–174.
50. Hodge, Ph. G.: Computer solutions of plasticity problems. Problems of Plasticity. Noordhoff, 1974, 261–286.
51. Hsu, T. R., Berteles, A. W. M.: An improved approximation of constitutive elasto-plastic stress-strain relations. AIAA J. 12 (1974), 1450–1452.
52. Armen, H., Levine, H. S., Pifko, A. B.: Plasticity theory and finite element applications. in: Advances in Computer Methods in Structural Mechanics and Design ed.: Oden, J. T., Univ. Alabama Press. 1972, 393–437.
53. Cheng, S. Y., Hsu, T. R., Too, J. J. M.: An integrated load increment method for finite elasto-plastic stress analysis. Int. J. Num. Meth. Eng. 15 (1980), 833–842.
54. Harkegard, G., Larsson, S. G.: On the finite element analysis of elastic-plastic structures under plane strain conditions. Inst. för Hallfasthetslare. Kungl. Tekniska Högskolan. Stockholm. Pub. Nr 77.

55. Szabó, L.: A képlékenységtan néhány keményedési elméletének összehasonlítása végeselem módszer segítségével. (Comparison of Some Hardening Theories in Plasticity by Means of the Finite Element Method). Gép 36 (1984), 98–105.
56. Crisfield, M.: Iterative solution procedure for linear and non-linear structural analysis. TRRL Lab. Report 900, Transport and Road Research Laboratory, Crowthorne, Berkshire, U. K. 1979.
57. Zienkiewicz, O. C.: The Finite Element Method. McGraw-Hill, New York 1976.
58. Bathe, K. J., Wilson, E. L.: Numerical Methods in Finite Element Analysis. Prentice-Hall, Englewod Cliffs. New Jersey 1976.
59. Bathe, K. J., Oden, J. T., Wunderlich, W.: Formulations and Computational Algorithms in Finite Element Analysis. M. I. T. Press, Massachusetts 1977.
60. Oden, J. T.: Finite Element of Nonlinear Continua. McGraw-Hill, New York 1972.
61. Wunderlich, W., Stein, E., Bathe, K. J.: Nonlinear finite element analysis in structural mechanics. Springer-Verlag, Berlin 1981.
62. Hinton, E., Owen, D. R. J.: An Introduction to Finite Element Computations. Pineridge Press, Swansea, U. K. 1979.
63. Hinton, E., Owen, D. R. J.: Finite Element Programming. Academic Press, London 1977.
64. Owen, D. R. J., Hinton, E.: Finite Elements in Plasticity: Theory and Practice. Pineridge Press Limited, Swansea, U. K. 1980.
65. Whiteman, J. K.: The mathematics of finite elements and applications. Academic Press, London 1978.
66. Irons, B. M., Ahmad, S.: Finite Element Techniques. Ellis Horwood, Chichester 1980.
67. Dinno, K. S., Gill, S. S.: An experimental investigation into the plastic behavior of flush mozzles in spherical pressure vessels. Int. J. Mech. Sci. 7 (1965), 817–839.
68. Theokaris, P. S., Marketos, E.: Elastic-plastic analysis of perforated thin strips of strain-hardening material. J. Mech. Phys. Sol. 12 (1964), 377–390.
69. Spilker, R. L., Munir, N. I.: Elastic-plastic analysis of plates by the hybrid-stress model and initial-stress approach. Int. J. Num. Meth. Eng. 17 (1981), 1791–1810.
70. Belytschko, T., Hodge, Ph. G.: Plane stress limit analysis by finite elements. J. Eng. Mech. Div. ASCE, EM 6 (1970), 931–944.
71. Barnard, A. J., Sharman, P. W.: The elasto-plastic analysis of plates using hybrid finite elements. Int. J. Num. Meth. Eng. 10 (1976), 1343–1356.
72. Hodge, Ph. G., McMahon, A. A.: A simple finite element model for elastic-plastic plate bending. Comput. & Struct. 2 (1972), 841–854.
73. Belytschko, T., Velebit, M.: Finite element method for elastic-plastic plates. J. Eng. Mech. Div. ASCE, EM 1 (1972), 227–242.
74. Brebbia, C., Connor, J.: Geometrically nonlinear finite element analysis. J. Eng. Mech. Div. ASCE 95 (1969), 463–483.
75. Javaherian, H., Dowling, P. J., Lyons, L. P. R.: Nonlinear finite element analysis of shell structures using the semi-loof element. Comput. & Struct. 12 (1980), 147–159.
76. Ang, A. H. S., Lopez, A. L.: Discrete model analysis of elastic-plastic plates. J. Eng. Mech. Div. ASCE EM 1. 94 (1968), 271–293.
77. Lin, T. H., Ho, E. Y.: Elasto-plastic bending of rectangular plates. J. Eng. Mech. Div. ASME EM 1 94 (1968), 199–210.
78. Hughes, T. J. R., Liu, W. K.: Nonlinear finite element analysis of shell: Part I. Three-dimensional shells. Comput. Meth. in Appl. Mech. Eng. 26 (1968), 331–362.
79. Hodge, Ph. G., Belytschko, T.: Numerical methods for the limit analysis of plates. J. of Appl. Mech. 35 (1968), 796–802.
80. Seegerlind, L. J.: Applied Finite Element Analysis. John Wiley, New York 1976.
81. Desai, C. S., Abel, J. F.: An Introduction to the Finite Element Method. van Nostrand Reinhold, New York 1972.
82. Szabó L.: Evaluation of elasto-viscoplastic tangent matrices without numerical inversion, Comput. & Struct. 22 (1985) 1235–1236.
83. Donea, J.: Advanced Structural Dynamics. Applied Science Publishers, London 1980.
84. Kleiber, M.: Perturbation approach to the incremental equations of large deformation elasto-plasticity. Bull. Acad. Polon. Sci. Ser. Sci. Techn. 28 (1980), 75–80.
85. Levy, A.: Finite element three-dimensional elastic-plastic creep analysis. 5th Int. Conf. Structural Mechanics in Reactor Technology. M. M. 1/2, 1979.

86. Haug, E., Locci, J. M., Arnaudeau, F. C.: PAM-NL: A general finite element program for the nonlinear thermomechanical analysis of structures. 5th Int. Conf. Structural Mechanics in Reactor Technology. M. M. 1/3, 1979.
87. Cyr, N. A., Teter, R. D.: Finite element elastic-plastic-creep analysis of two-dimensional continuum with temperature dependent material properties. Comp. & Struct. 3 (1973), 849–863.
88. Allen, D. H.: A survey of current temperature dependent elastic-plastic-creep constituve laws for applicability to finite element computer codes. 21st AIAA/ASCE/ASME/SDM Conference. Seattle 1980.
89. Haisler, W. E.: AGGIE I. A finite element program for nonlinear structural analysis. Office of Naval Research. No. 3275-77-1 (1977).
90. Argyris, J. H.: Matrix analysis of three-dimensional elastic media-small and large displacements. AIAA J. 3 (1965), 45–51.
91. Argyris, J. H., Chan, A. S. L.: Static and dynamic elasto-plastic analysis by finite elements in space and time. in: Symposium on Foundations of Plasticity. ed.: Sawczuk, A. Noordhoff, Leyden (1973), 147–163.
92. Argyris, J. H., Doltsinis, J. St.: On the large strain inelastic analysis in natural formulation, Part I: Quasistatic problems. Comput. Meth. in Appl. Mech. and Engng. 20 (1979), 213–251.
93. Argyris, J. H., Doltsinis, J. St.: On the large strain inelastic analysis in natural formulation Part II: Dynamic problems. Comput. Meth. in Appl. Mech. and Engng. 21 (1980), 91–126.
94. Argyris, J. H., Kleiber, M.: Incremental formulation in nonlinear mechanics and large strain elasto-plasticity — Natural approach. Part I. Comp. Meth. in Appl. Mech. and Eng. 11 (1977), 215–247.
95. Argyris, J. H., Doltsinis, J. St., Kleiber, M.: Incremental formulation in nonlinear mechanics and large strain elasto-plasticity — Natural approach. Part II. Comp. Meth. in Appl. Mech. and Eng. 14 (1978), 259–294.
96. Argyris, J. H., Doltsinis, J. St., Knudson, W. C., Szimmat, J., Wüstenberg, H., William, K. J.: Eulerian and Lagrangean techniques for elastic and inelastic large deformation processes. TICOM 2, March 26–29. Proceedings, ISD-Report No. 256. Stuttgart (1979).
97. Bathe, K. J., Bolourchi, S.: A geometric and material nonlinear plate and shell element. Comp. & Struct. 11 (1980), 23–48.
98. Bathe, K. J., Ramm, E., Wilson, E. L.: Finite element formulations for large deformation analysis. Int. J. Num. Meth. Engng. 9 (1975), 353–386.
99. Bathe, K. J., Ozdemir, H.: Elastic-plastic large deformation static and dynamic analysis. Comp. & Struct. 6 (1976), 81–92.
100. Bathe, K. H., Ozdemir, H., Wilson, E. L.: Static and dynamic geometric and material nonlinear analysis. Struct. Eng. Lab. University of California Berkeley. Rp. UCSESM 74–4 (1974).
101. Powell, G., Simon, J.: Improved iteration strategy for nonlinear structures. Int. J. Num. Meth. Eng. 17 (1981), 1455–1467.
102. Soreide, T. H.: Collapse behaviour of stiffened plates using alternative finite element formulation. Report No. 77–3. The Norwegian Inst. of Tech. Univ. Trondheim 1977.
103. Gunasekara, J. S., Alexander, J. M.: Matrix analysis of the large deformation of an elastic-plastic axially symmetric continuum. in: Symposium of Foundations of plasticity. ed.: Sawczuk, A. Noordhoff, Leyden 1973, 125–144.
104. Gadala, M. S., Dokainisch, M. A., Oravas, A. E.: Geometric and material nonlinearity problems "Lagrangian and updated Lagrangian formulations". Num. Meth. in Fracture Mechanics. Proc. of the Second Int. Conf., Swansea, 1980, 277–294.
105. Bathe, K. H., Ozdemir, H., Wilson, E. L.: Static and dynamic geometric and material nonlinear analysis. Struc. Eng. Lab. University of California Berkeley. Rp. UCSESM 74–4 (1974).
106. Sanders, D. R., Haisler, W. E.: An incremental form of the single-integral nonlinear viscoelastic theory for elastic-plastic-creep finite element analysis. Office of Naval Research. No. 3275-79-1 (1979).
107. Haisler, W. E., Sanders, D. R.: Elastic-plastic-creep large strain analysis at elevated temperature by the finite element method. Office of Naval Research, No. 2375-78-1 (1978), Comp. & Struct. 10 (1979), 375–381.
108. Axelsson, K., Samuelsson, A.: Finite element analysis of elastic-plastic materials displaying mixed hardening. Int. J. Num. Meth. Eng. 14 (1979), 211–225.
109. Basombrio, F. G., Sarmiento, G. S.: PLASTEF. A code for the numerical simulation of thermoelastoplastic behaviour of materials using the finite element method. Nucl. Eng. Des. 49 (1978), 231–241.

110. Allen, D. H.: Computational aspects of the nonisothermal classical plasticity. Comput. & Struct. 15 (1982), 589–599.
111. Hsu, T. R., Too, J. J. M.: Analysis of residual stresses/strain in pressure vessels due to cyclic thermomechanical loads. Third Int. Conf. Pressure Vessel Technology. Tokyo, (1977), 83–91.
112. Patterson, C.: Finite element analysis for plasticity and creep. Institute of Physics Conference Proceedings. Non-linear problems in stress analysis, Durham University 1977, 125–136.
113. Key, S. W.: Concepts underlying finite element methods for structural analysis. Nucl. Eng. Des. 46 (1978), 259–268.
114. Hofmeister, D. L., Greenbaum, G. A., Evensen, D. A.: Large strain, elasto-plastic finite element analysis. AIAA J. 9 (1971), 1248–1254.
115. Argyris, J. H., Balmer, H., Kleiber, M., Hindenlang, U.: Natural description of large inelastic deformations for shells of arbitrary shape — application of trump element. Comput. Meth. Appl. Mech. Eng. 22 (1980), 361–389.
116. Prager, W.: A new method of analysing stresses and strain in work hardening plastic solids. J. Appl. Mech. 23 (1956), 493–396.
117. Bergan, P. G.: Nonlinear analysis of plates considering geometric and material effects. Report No. SESM 71–7, Univ. California, Berkeley, April 1971.
118. Besseling, J. F.: Nonlinear analysis of structures by the finite element method as a supplement to a linear analysis. Comp. Meth. Appl. Mech. Eng. 3 (1974), 173–194.
119. Bathe, K. J.: Finite Element Procedures in Engineering Analysis. Prentice-Hall, Englewood Cliffs, New Jersey 1982.
120. Kawahara, M.: Large strain, viscoelastic and elastoviscoplastic numerical analysis by means of the finite element method. Nucl. Eng. Des. 34 (1975), 233–246.
121. Stricklin, J. A., Haisler, W. E., Riesemann, W.: Evaluation of solution procedures for material and/or geometrically nonlinear structural analysis. AIAA J. 11 (1973), 292–299.
122. Dupuis, G. A., Hibbitt, H. D., McNamara, S. F., Marcal, P. V.: Nonlinear material and geometric behavior of shell structures. Comput. & Struct. 1 (1971), 223–239.
123. Hibbit, H. D., Marcal, P. V., Rice, J. R.: A finite element formulation for problems of large strain and large displacement. Int. J. Solids Struct. 6 (1970), 1069–1086.
124. McMeeking, R. M., Rice, J. R.: Finite element formulation for problems of large elastic-plastic deformation. Int. J. Solids Struct. 11 (1975), 601–616.
125. Martins, R. A. F., Owen, D. R. J.: Elasto-plastic and geometrically nonlinear thin shell analysis by the semiloof element. Comput. & Struct. 13 (1981), 505–513.
126. Balmer, H. A., Doltsinis, J. St.: Extension to the elasto-plastic analysis with the ASKA program system. Comp. Meth. Appl. Mech. Eng. 13 (1978), 363–401.
127. Haisler, W. E.: Development and evaluation of solution procedures for nonlinear structural analysis. Ph. D. Thesis, Texas A & M Univ. 1970.
128. Mathies, H., Strang, G.: The solution of nonlinear finite element equations. Int. J. Num. Meth. Eng. 14 (1979), 1613–1626.
129. Horrigmoe, G., Bergan, P. G.: Incremental variational principles and finite element models for nonlinear problems. Comp. Meth. Appl. Mech. Eng. 7 (1976), 201–217.
130. Yaghmai, S.: Incremental analysis of large deformations in mechanics of solids with applications to axisymmetric shells of revolution. Report No. SESM68–17. Univ. California, Berkeley 1968.
131. Zienkiewicz, O. C.: Incremental displacement in nonlinear analysis. Int. J. Num. Meth. Eng. 3 (1971), 587–588.
132. Dodds, R. H., Lopez, L. A., Pecknold, D. A.: Numerical and software requirements for general nonlinear finite element analysis. University of Illinois. No. N00014-75-E0164 (1978).
133. Kao, R.: A comparison of Newton–Raphson methods and incremental procedures for geometrically nonlinear analysis. Comp. & Struct. 4 (1974), 1091–1097.
134. Levy, A., Pifko, A. B.: On computational strategies for problems involving plasticity and creep. Int. J. Num. Meth. Eng. 17 (1981), 747–771.
135. Ziegler, H.: A modification of Prager's hardening rule. Quart. Appl. Math., 17 (1959), 55–65.
136. Allen, D. H.: An investigation into the combined isotropic-kinematic workhardening rule. Office of Naval Research. No. 3275-79-2 (1979).
137. McKnight, R. L., Sobel, L. H.: Finite element cyclic thermoplasticity analysis by the method of subvolumes. Comput. & Struct. 7 (1977), 417–424.

138. Kleiber, M., König, J. A., Sawczuk, A.: Studies on plastic structures: stability, anisotropic hardening, cyclic loads. Comput. Meth. Appl. Mech. Eng.33 (1982), 487–556.
139. Hunsaker, B. Ir.: The application of combined kinematic-isotropic hardening and the mechanical sublayer modell to small strain inelastic structural analysis by the finite element method. Thesis, Texas A & M University 1976.
140. Snyder, M. D., Bathe, K. J.: Formulation and numerical solution of thermo-elastic-plastic and creep problems. NTIS (1977), No 82448-3.
141. Chen, W. H.: Finite deformation, elastoplastic incremental finite element analysis of ductile metal structures. 5th Int. Conf. Structural Mech. in React. Techn. Vol. L3/5 (1979).
142. Gortemaker, P. C. M., de Pater, C.: Finite element formulation for large elastic-plastic deformations. 5th Int. Conf. Structural Mech. in React. Techn. Vol. L L4/6 (1979).
143. Nagtegaal, J. C., De Jong, J. E.: Some computational aspects of elastic-plastic large strain analysis. Int. J. Num. Meth. Eng. 17 (1981), 15–41.
144. Cormeau, I.: Elastoplastic thick shell analysis by viscoplastic solid finite elements. Int. J. Num. Meth. Eng. 12 (1978), 203–227.
145. Cormeau, I.: Numerical stability in quasistatic elasto/viscoplasticity. Int. J. Num. Meth. Eng. 9 (1975), 109–127.
146. Zienkiewicz, O. C., Cormeau, I.: Viscoplastity. Plasticity and creep in elastic solids. A unified numerical solution approach. Int. J. Num. Meth. Eng. 8 (1974), 821–845.
147. Owen, D. R. J., Praksh, A., Zienkiewicz, O. C.: Finite element analysis of nonlinear composite materials by use of overlay systems. Comput. & Struct. 4 (1974), 1351–1367.
148. Zienkiewicz, O. C.: Visco-plasticity, plasticity, creep and visco-plastic flow. in: Comput. Mechanics. ed.: J. T. Oden. Inst. Conf. Comput. Meth. in non-linear Mech., Austin, Texas, 1974, 297–328.
149. Pande, G. N., Owen, D. R. J., Zienkiewicz, O. C.: Overlay modells in time-dependent nonlinear analysis. Comput. & Struct. 7 (1977), 435–443.
150. Kanchi, M. B., Zienkiewicz, O. C., Owen, D. R. J.: The viscoplastic approach to problems of plasticity and creep involving geometric nonlinear effects. Int. J. Num. Meth. Eng. 12 (1981), 169–181.
151. Zienkiewicz, O. C., Owen, D. R. J., Cormeau, I. C.: Analysis of viscoplastic effects in pressure vessels by the finite element method. Nucl. Eng. Des. 28 (1974), 278–288.
152. Zienkiewicz, O. C., Cormeau, I.: Viscoplasticity and plasticity. An alternative for the finite elements solution of materials nonlinearities. Proc. Colloque sur les Methodes de Calcul Scientifique et Technique. IRIA. Rocquencourt 1973, 171–199.
153. Zienkiewicz, O. C., Norris, V., Naylor, D. J.: Plasticity and visco-plasticity in soil mechanics with special reference to cyclic loading problems. in: Int. Conf. Finite Elements in Nonlinear Solid and Struct. Mech. Geilo, Norway 1977, 455–485.
154. Zienkiewicz, O. C., Cormeau, I.: Visco-plasticity solution by the finite element process. Arch. Mech. 24 (1972), 873–888.
155. Cormeau, I. C.: Visco-plasticity and Plasticity in the finite element method Ph. D. Thesis, University of Wales 1976.
156. Pian, T. H. H., Lee, S. W.: Creep and visco-plastic analysis by assumed stress hybrid finite elements. in: Int. Conf. Finite Elements in Nonlinear Solid and Struct. Mech. Geilo, Norway 1977, 807–822.
157. Greenbaum, G. A., Rubinstein, M. F.: Creep analysis of axisymmetric bodies using finite elements. Nucl. Eng. Des. 7 (1968), 379–397.
158. Allen, D. H., Haisler, W. E.: Thermoplastic analysis using the finite element code AGGIE I. Office of Naval Research, No. 3275-79-4 (1979).
159. Argyris, J. H., Doltsinis, J. St., Pimenta, P. M., Wüstenberg, H.: Thermomechanical response of solids at high strans—natural approach. Comput. Meth. Appl. Mech. Eng. 32 (1982), 3–57.
160. Hsu. T. R.: On behaviour of fuel elements subject to combined cyclic thermomechanical loads. Nucl. Eng. Des. 56 (1980), 279–287.
161. Sanders, D. R., Haisler, W. E.: An incremental form of the single-integral nonlinear viscoelastic theory for elastic-plastic-creep finite element analysis.Pressure Vessels and Piping Conf. ASME (1979).
162. Kleiber, M.: Large elasto-plastic deformations. Theory and numerical analysis of structures. in Polish, Rept. No. 13/78 Inst. of Fundamental Techn. Research, Warsaw, 1978.
163. Int. Conf. Finite Elements in Nonlinear Solid and Structural Mechanics. Geilo, Norway 1977.
164. Symposium on Computational Methods in Nonlinear Structural and Solid Mechanics. Washington, D. C. 1980.

165. Symposium on Advances and Trends in Structural and Solid Mechanics. Washington, D. S. 1982.
166. FENOMECH '81. Proc. of the 2nd Int. Conf. on Finite Elements in Nonlinear Mechanics. Stuttgart 1981.
167. Proc. Int. Conf. Numerical Methods for Nonlinear Problems. Swansea, U. K. 1980.
168. Perzyna, P.: Fundamental problems in visco-plasticity, in: Recent Advances in Applied Mechanics. Academic Press, New York 1966.
169. Perzyna, P.: The constitutive equations for rate sensitive plastic-independence. Quart. App. Math. 20 (1963), 321–332.
170. Nagarajan, S., Popov, E. P.: Plastic and viscoplastic analysis of axisymmetric shells. Int. J. Solids Structures 11 (1975), 1–19.
171. Hughes, T. J. R., Taylor, R. L.: Unconditionally stable algorithms for quasi-static elasto/viscoplastic finite element analysis. Comput. & Struct. 8 (1978), 169–173.

Acta Technica Academiae Scientiarum Hungaricae, 97 (1—4), pp. 315—322 (1984)

FINITE ELEMENT ANALYSIS OF ANISOTROPIC PLASTIC HARDENING

L. SZABÓ*

[Received: 9 May 1984]

The theory of anisotropic hardening discussed in this paper can be applied in the determination of elastic-plastic deformations under non-proportional loads. However, the numerical example presented in the paper cannot be regarded as a correct solution, because a function is to be determined by trial-and-error and not by measurements. The elaboration of a measurement procedure and the comparison of computed and experimental results for different load paths require further studies and investigations.

Introduction

In recent years many authors discussed the combined isotropic-kinematic hardening [1, 2, 3, 5].

This law of hardening describes in a relatively adequate manner the behaviour of the material under cyclic loads, which is confirmed by a number of finite element applications [1, 3, 6], as well.

The model will be further refined by taking the anisotropic hardening phenomena also into account. Zyczkowsky [7] gives a very good summary of the various theories of anisotropic hardening. Beside the large number of theoretical works, relatively few papers discuss the numerical application of the theory.

This paper describes a theory of anisotropic hardening elaborated on the basis of works by Axelsson [2] and Tanaka et al. [4]. The basic relationships are presented in matrix form, which facilitates the direct finite element applications. The numerical application of the theory discussed is presented in the example of a non-proportional loading of a thin-wall tube.

2. Basic equations

The yield function may be given as follows:

$$F=\left(\frac{3}{2}\bar{\sigma}^T T N T \bar{\sigma}\right)^{1/2}-\sigma_y\left(\int \mathrm{d}\varepsilon_p\right)=0\,, \tag{1}$$

* Szabó, L. H-1015, Budapest, Csalogány u. 6–10, VI. 248, Hungary

where

$$\bar{\sigma} = \sigma - \alpha$$

$\sigma^T = [\sigma_{11}, \sigma_{22}, \sigma_{33}, \tau_{12}, \tau_{23}, \tau_{31}]$

(the stress vector)

$\alpha^T = [\alpha_{11}, \alpha_{22}, \alpha_{33}, \alpha_{12}, \alpha_{23}, \alpha_{31}]$

(the translation vector of the centre point of the yield surface)

$$T = I_6 - \frac{1}{3} ii^T$$

$I_6 = 6 \times 6$ unit matrix

$i^T = [1, 1, 1, 0, 0, 0]$

$N = G + A(\varepsilon_p) M$

$$G = \begin{bmatrix} I_3 & 0 \\ 0 & 2 \cdot I_3 \end{bmatrix}$$

$I_3 = 3 \times 3$ unit matrix

$M = \varepsilon^p \varepsilon^{pT}$

$\varepsilon^{pT} = [\varepsilon^p_{11}, \varepsilon^p_{22}, \varepsilon^p_{33}, \gamma^p_{12}, \gamma^p_{23}, \gamma^p_{31}]$ (the plastic strain vector)

$$\mathrm{d}\varepsilon_p = \left(\frac{2}{3} \mathrm{d}\varepsilon^{pT} L \mathrm{d}\varepsilon^p \right)^{1/2}$$ (the equivalent plastic strain increment)

$$L = \begin{bmatrix} I_3 & 0 \\ 0 & \frac{1}{2} I_3 \end{bmatrix}$$

The yield function represented by equation (1) differs from the one proposed by Axelsson [2] only in parameter A. In this paper A is regarded as a function of ε_p, while by Axelsson it has a constant value. The yield function is given by Tanaka et al [4] in a similar form. By Tanaka parameter A is similarly interpreted as the function of ε_p, but matrix M has a different interpretation.

To give the relationship between the increments in stress and strain, by applying the conventional deduction, the plastic deformation as a whole may be divided into an elastic and a plastic component:

$$\mathrm{d}\varepsilon = \mathrm{d}\varepsilon^e + \mathrm{d}\varepsilon^p . \tag{2}$$

Equation (2) can be further re-formed according to Hooke's law:

$$\mathrm{d}\sigma = D(\mathrm{d}\varepsilon - \mathrm{d}\varepsilon^p) . \tag{3}$$

The plastic strain increment can be resolved into an isotropic and a kinematic component:

$$d\varepsilon^{p(i)} = \beta \, d\varepsilon^p , \tag{4a}$$

$$d\varepsilon^{p(k)} = (1-\beta) \, d\varepsilon^p \tag{4b}$$

where $-1 < \beta \leqq 1$ is a parameter depending on the material.

Furthermore, based on the normality condition the increment in plastic strain may be given as follows:

$$d\varepsilon^p = d\lambda \frac{\partial F}{\partial \sigma} \tag{5}$$

with special condition, as follows

$$\text{if} \quad F=0 \quad \text{and} \quad dF=0 \quad \text{then} \quad d\lambda \neq 0$$

$$\text{if} \quad F \leqq 0 \quad \text{and} \quad dF<0 \quad \text{then} \quad d\lambda = 0$$

The total differential of the yield function (1)

$$dF = \frac{\partial F}{\partial \sigma} d\sigma + \frac{\partial F}{\partial \alpha} d\alpha + \frac{\partial F}{\partial \varepsilon^p} d\varepsilon^p + \frac{\partial F}{\partial \varepsilon_p} d\varepsilon_p = 0 \tag{6}$$

is to be solved for $d\lambda$. Based on Prager's and Ziegler's theory, the kinematic hardening can be uniformly discussed because

$$d\alpha = d\lambda (1-\beta) pt \tag{7}$$

where in case of Prager's theory

$$p = \frac{2}{3} H ,$$

$$t = L \frac{\partial F}{\partial \sigma} , \tag{7a}$$

$$H = \frac{d\sigma_y}{d\varepsilon_p}$$

and, in the case of Ziegler's theory

$$p = \frac{H}{\sigma_y} \left(\frac{2}{3} \frac{\partial F^T}{\partial \sigma} L \frac{\partial F}{\partial \sigma} \right)^{1/2} ,$$

$$t = \bar{\sigma} . \tag{7b}$$

Using equations (3), (4), (5), (6), (7) $d\lambda$ may be given as

$$d\lambda = \frac{a^T D \, d\varepsilon}{a^T D a + (1-\beta) p t^T a - e^T a + (\beta H - \gamma h) \left(\frac{2}{3} a^T L a \right)^{1/2}}$$

where:

$$a = \frac{\partial F}{\partial \sigma} = \frac{3}{2\sigma_y} N T \bar{\sigma},$$

$$e = \frac{\partial F}{\partial \varepsilon^p} = \frac{2A}{2\sigma_y} \bar{\sigma}^T T \varepsilon^p T \bar{\sigma},$$

$$h = \frac{3}{4\sigma_y} \bar{\sigma}^T T M T \bar{\sigma},$$

$$\gamma = \frac{\mathrm{d}A}{\mathrm{d}\varepsilon_p}.$$

By use of equations (3), (5) and (8), the relationship between the increments in stress and strain is given by

$$\mathrm{d}\sigma = D^{ep}\,\mathrm{d}\varepsilon \tag{9}$$

where:

$$D^{ep} = D - \frac{dd^T}{d^T a + (1-\beta) p t^T a - e^T a + (\beta H - \gamma h)\left(\frac{2}{3} a^T L a\right)^{1/2}}$$

and

$$d = Da.$$

Equation (9) can be incorporated conveniently into the computer program published by Owen-Hinton [8]. In this way, the program can be used for computing combined isotropic-kinematic and anisotropic hardening.

3. Numerical application

The theory of anisotropic hardening discussed above is applied to the non-proportional tension and torsion of a thin-wall tube. The results of the computation are compared with Liu's[9] experimental results.

The finite element computation is based on the assumption of a plane stress state, applying an 8-node isoparametric rectangular element and 3×3 Gaussian integration (Fig. 1). The computation was made for two load paths shown in Fig. 2. The load coordinates are contained in Table I.

Table I. Coordinates of load paths D_1 and C_3.

	D_1 (MPa)		C_3 (MPa)	
	σ_{11}	τ_{12}	σ_{11}	τ_{12}
A	151.2	93.08	133.34	79.77
B	257.2	33.09	166.3	62.53
C	259.3	0.	166.3	0.
D	–	–	69.49	41.36
E	–	–	108.25	62.53

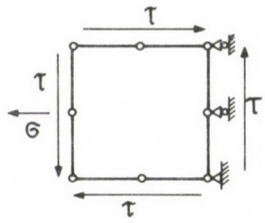

Fig. 1. Finite element model for the analysis of the thin-walled tube

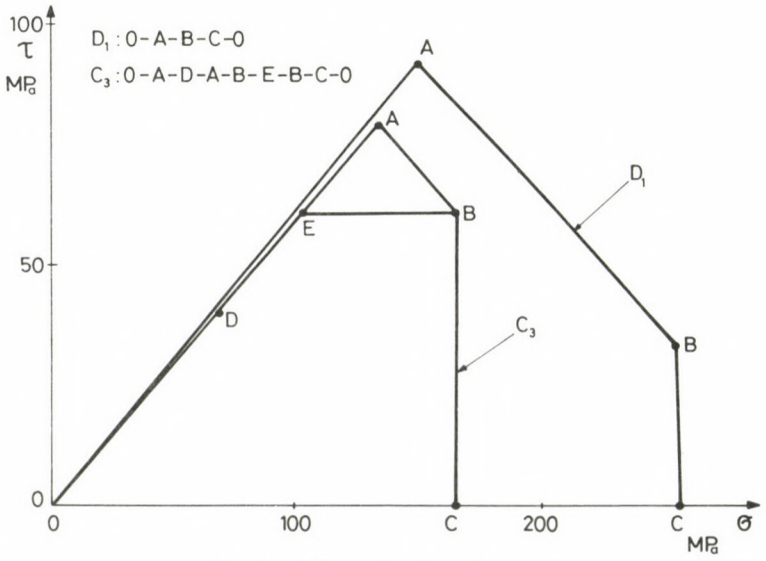

Fig. 2. Loading paths D_1 and C_3

Parameters of the tube material are:

$\sigma_y = 181.0$ MPa
$E = 19.5 \cdot 10^4$ MPa
$\nu = 0.3$
$H = 0.194\,93 \cdot 10^4$ MPa (bilinear stress-strain curve)

The experimental results compared with those of the computation are shown in Figs 3, 4, 5 and 6.

For load path D_1 Figs 3 and 4 show the axial stress-strain curves and the shear stress vs. strain, respectively. The results of the computation obtained for anisotropic-kinematic hardening are represented by circles. Function A is expressed by

$$A = 16\,000 \exp(-674.59 \cdot \varepsilon_p) - 220 \qquad \text{for} \quad D_1,$$

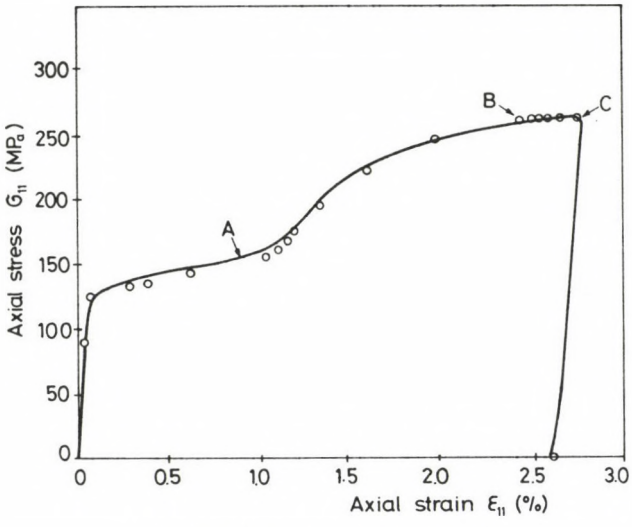

Fig. 3. Axial stress-strain curve for D_1
---- experiment
0FEM

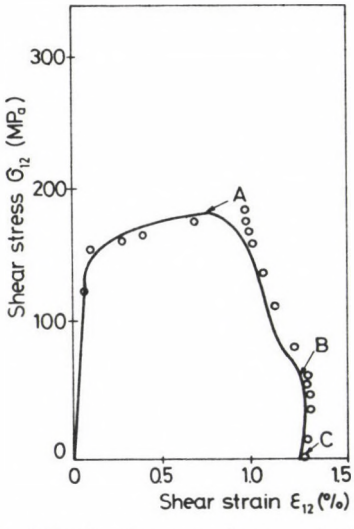

Fig. 4. Torsional stress-strain curve for D_1
---- experiment
0FEM

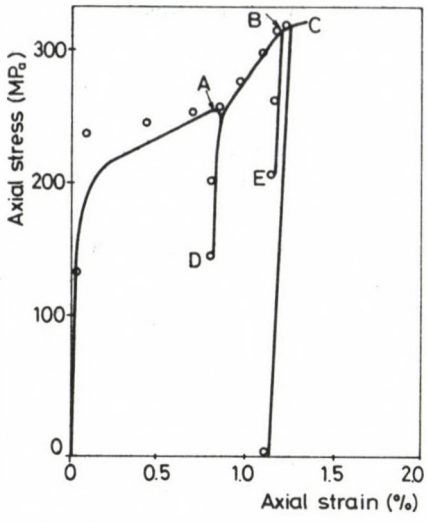

Fig. 5. Axial stress-strain curve for C_3
– – – –experiment
0FEM

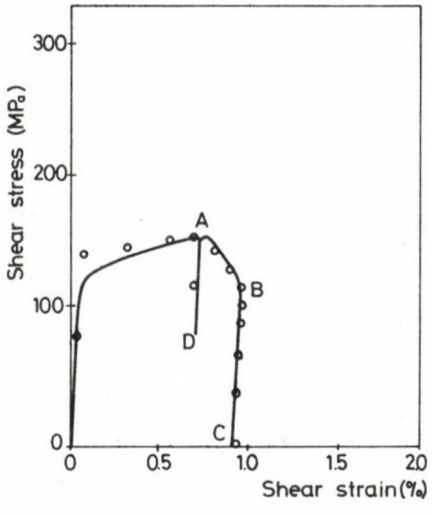

Fig. 6. Torsional stress-strain curve for C_3
– – – –experiment
0FEM

and

$$A = 16\,000 \exp(-380.258 \cdot \varepsilon_p) + 350 \qquad \text{for} \quad C_3 .$$

For load path C_3 the results are shown in Figs 5 and 6.

4. Conclusions

The theory of anisotropic hardening discussed in this paper can be applied for the determination of elastic-plastic deformations under non-proportional loads. However, the numerical example presented cannot be regarded as a correct solution, because function A was determined by trial-and-error and not by measurements.

The elaboration of a measurement procedure for the determination of function A, and the comparison of computed and experimental results for other load paths require further studies and investigations.

References

1. Axelsson, K., Samuelsson, A.: Finite element analysis of elastic-plastic materials displaying mixed hardening. Int. J. Num. Meth. Engng. 14 (1979), 211–225.
2. Axelsson, K.: Finite element application of mixed and distortional plastic hardening Int. Conf. Finite Elements in Nonlinear Solid and Structural Mechanics. Geilo, Norway 1977, pp 191–209.
3. Tanaka, M.: Large deflection analysis of elastic-plastic circular plates with combined isotropic and kinematic hardening Ingenieur-Archiv 41 1972 342–356.
4. Tanaka, M., Miyagawa, Y.: On generalized kinematic hardening theory of plasticity Ingenieur-Archiv 44, 1975, 255–268.
5. Allen, D. H.: A note on the combined isotropic-kinematic work hardening rule Int. J. Num. Meth. Engng. 15 1980, 1724–1728.
6. Haisler, W. E.: Numerical and experimental comparison of plastic work-hardening rules Trans. of the 4th Int. Conf. on Struct. Mech in Reactor Techn., San Francisco L 4/7, 1977 1–16.
7. Zyczkowski, M.: Combined Loading in the Theory of Plasticity. PWN-Polish Scientific Publishers, Warsaw 1981.
8. Owen, J. R. J., Hinton, E.: Finite Elements in Plasticity: Theory and Practice. Tineridge Press Limited, Swansea 1960.
9. Liu, E. C.: Room temperature elastic-plastic response of thin-walled tubes subjected to nonradial combinations of axial and torsional loadings. in: Inelastic Behavior of Pressure Vessel and Piping Components. eds.: T. Y. Chang, E. Krempl. PVP-PB-028, 1978, pp. 1–12.

Acta Technica Academiae Scientiarum Hungaricae, 97 (1—4), pp. 323—340 (1984)

APPLICATION OF THE HOPF BIFURCATION THEORY FOR THE DYNAMICAL MODEL OF THE NOSE-GEAR

Dr. Á. S. VANCSA

[Received: 31 January 1984]

These results show that stability investigations of the linearized dynamical system are not enough for technical designing of such structures. Nonlinearities must be taken into consideration, too. — The method of Hopf bifurcation theory proved that unstable periodic solutions may occur around the stable equilibrium position of the draw-bar in comparison with the moving coordinate system of speed (later on, for the sake of terminological simplicity, it will be called the equilibrium position of the system). This situation is very dangerous from the technical point of view. — On the other hand it is very useful to know the size of the radius of the stable periodic orbits around an unstable equilibrium position when one is in the unstable region. And what may be more important than this, occurring stable vibrations warn us that the equilibrium position of the system has lost its stability and has become unstable, so we have to change the parameters of the system to restabilize the equilibrium position.

1. Introduction

It is very important to investigate the behaviour of wheels of drawn axes. This is interesting because with certain masses and speed these wheels begin to dance i.e. they lose their stability. That is why a designer has to know what kind of vibration occurs in the case of the first wheel of an aeroplane or in the case of jointed buses or trucks with trailers.

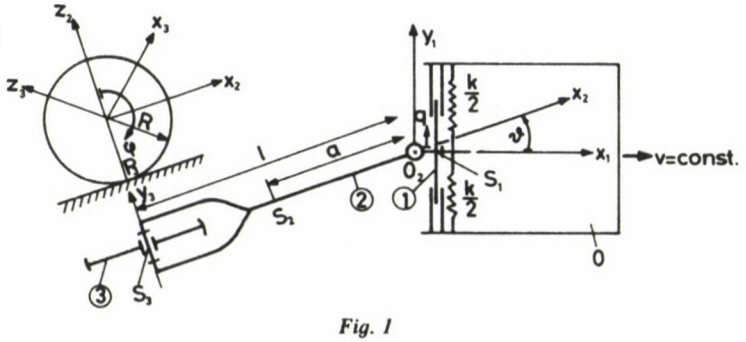

Fig. 1

* Mrs. Ágnes S. Vancsa, H-1131 Budapest Vőlegény u. 2., Hungary

This phenomenon can be dealt with by the application of modern bifurcation theory [1].

A simple mechanical model of the wheel of drawn axis is shown in Fig. 1 [2].

The motion of this system can be described by the Appell equations.

Notations:

body	mass	moment of inertia
1	M_1	0
2	M_2	$\boldsymbol{\theta}_{S_2}=\begin{bmatrix} A_2 & -F_2 & -E_2 \\ -F_2 & B_2 & -D_2 \\ -E_2 & -D_2 & C_2 \end{bmatrix} R_2$
3	M_3	$\boldsymbol{\theta}_{O_3}=\boldsymbol{\theta}_{S_3}=\begin{bmatrix} A_3 & 0 & 0 \\ 0 & B_3 & 0 \\ 0 & 0 & A_3 \end{bmatrix} R_3$

R — the radius of the wheel,
v — the speed of drawing,
R_1: (x_1, y_1, z_1), R_2: (x_2, y_2, z_2), R_3: (x_3, y_3, z_3)-coordinate systems,
S_1, S_2, S_3-centers of gravity,
a, l — lengths,
k — stiffness of the spring.

The chosen general coordinates are q, ϑ, φ.

There is a kinematical constraint because we assume that the wheel rolls without slipping. This gives us two scalar equations:

$$\mathbf{v}_{P_3}=\begin{bmatrix} v+l\dot{\vartheta}\sin\vartheta-R\dot{\varphi}\cos\vartheta \\ \dot{q}-l\dot{\vartheta}\cos\vartheta-R\dot{\varphi}\sin\vartheta \\ 0 \end{bmatrix}=0 \tag{1}$$

From the first equation we have

$$\dot{\varphi}=\frac{v+l\dot{\vartheta}\sin\vartheta}{R\cos\vartheta}.$$

This can be substituted into the second one so that:

$$\dot{q}=\frac{1}{\cos\vartheta}(v\sin\vartheta+l\dot{\vartheta}).$$

Let us denote the quasi-speed of the system of one degree of freedom by $s=\dot{\vartheta}$.

The Appell equation is

$$\frac{\partial S}{\partial\dot{s}}=\pi_S. \tag{2}$$

Where $S(\dot{s}, s, \vartheta, q)$ means the so-called acceleration energy, π_s is the quasi-force.

Equation (2) in its details is as follows:

$$\dot{s}\left[M_1\frac{l^2}{\cos^2\vartheta}+M_2\left(a^2+\frac{l^2}{\cos^2\vartheta}-2al\right)+M_3l^2\tan^2\vartheta+C_2+A_3+B_3\frac{l^2}{R^2}\tan^2\vartheta\right]+$$

$$+s\left[M_1\left(v\frac{l}{\cos^3\vartheta}+s\frac{l^2\sin\vartheta}{\cos^3\vartheta}\right)+M_2\left(\frac{v}{\cos\vartheta}\left(\frac{l}{\cos^2\vartheta}-a\right)+sl^2\frac{\tan\vartheta}{\cos^2\vartheta}\right)+\right.$$

$$\left.+M_3l\tan\vartheta\left(v\frac{\tan\vartheta}{\cos\vartheta}+\frac{sl}{\cos^2\vartheta}\right)+B_3\frac{l\sin\vartheta}{R^2\cos^3\vartheta}(ls+v\sin\vartheta)\right]=$$

$$=-kq\frac{l}{\cos\vartheta}.$$

The whole system of differential equations is:

$$\begin{aligned}\dot{\vartheta}&=s\\ \dot{s}&=\frac{G}{H},\\ \dot{q}&=v\tan\vartheta+\frac{l}{\cos\vartheta}S,\end{aligned}\tag{3}$$

where

$$G=-\left[\left(M_1\frac{v}{\cos^2\vartheta}+M_2v\left(\frac{1}{\cos^2\vartheta}-\frac{a}{l}\right)+M_3v\frac{\sin^2\vartheta}{\cos^2\vartheta}+B_3\frac{v}{R^2}\frac{\sin^2\vartheta}{\cos^2\vartheta}\right)s+kq+\right.$$

$$\left.+\left(M_1+M_2+M_3+\frac{B_3}{R^2}\right)l\frac{\sin^2\vartheta}{\cos^2\vartheta}s^2\right],$$

$$H=M_1\frac{l}{\cos\vartheta}+M_2\left(\frac{a^2}{l}\cos\vartheta+\frac{l}{\cos\vartheta}-2a\cos\vartheta\right)+M_3l\frac{\sin^2\vartheta}{\cos\vartheta}+$$

$$+(A_3+C_2)\frac{\cos\vartheta}{l}+B_3\frac{l}{R^2}\frac{\sin^2\vartheta}{\cos\vartheta}.$$

2. Investigation of the linearized system

If one wants to determine the critical values of the system, where it loses its stability, one has to investigate the linearized system. The linearized system is:

$$\begin{bmatrix}\dot{\vartheta}\\ \dot{s}\\ \dot{q}\end{bmatrix}=\begin{bmatrix}0 & 1 & 0\\ 0 & -\tilde{a}_{22}/N & -k/N\\ v & l & 0\end{bmatrix}\begin{bmatrix}\vartheta\\ s\\ q\end{bmatrix}+\mathbf{0}(\vartheta^2+s^2+q^2),\tag{4}$$

where

$$\tilde{a}_{22}=v\left(M_1+M_2\left(1-\frac{a}{l}\right)\right),$$

$$N=M_1 l+M_2\frac{(l-a)^2}{l}+\frac{A_3+C_2}{l}.$$

The characteristic equation is

$$D(\lambda)=\begin{vmatrix}-\lambda & 1 & 0\\ 0 & -\tilde{a}_{22}/N-\lambda & -k/N\\ v & l & -\lambda\end{vmatrix}=-\lambda\left(\lambda^2+\frac{\tilde{a}_{22}}{N}\lambda+\frac{kl}{N}\right)-\frac{kv}{N}=0,$$

$$D(\lambda)=\lambda^3+\frac{\tilde{a}_{22}}{N}\lambda^2+\frac{kl}{N}\lambda+\frac{kv}{N}=0. \tag{5}$$

The condition of stability is given by the Routh–Hurwitz criterion,

1. all coefficients are positive as $a<l$ (see Fig. 1), so
2. the determinant $\begin{vmatrix}\frac{\tilde{a}_{22}}{N} & 1\\ \frac{kv}{N} & \frac{kl}{N}\end{vmatrix}$ has to be positive.

That is

$$\tilde{a}_{22}\frac{kl}{N^2}-\frac{kv}{N}>0,$$

$$\tilde{a}_{22}l>Nv.$$

Thus, the condition of stability is

$$l\left(M_1+M_2\frac{l-a}{l}\right)>M_1 l+M_2\frac{(l-a)^2}{l}+\frac{A_3+C_2}{l}.$$

Introducing the notation $\theta=A_3+C_2$ we put the inequality into the form

$$M_2(l-a)a>\theta. \tag{6}$$

Now we have the critical value of M_2 which is

$$M_{2\,\mathrm{crit}}=\frac{\theta}{a(l-a)}.$$

If the inequality (6) is satisfied, then all eigenvalues of (4) have negative real parts i.e. the equilibrium point of the linearized system is asymptotically stable.

We may assume that M_2 consists of two parts, namely

$$M_2 = M_{2S} + M_{2O}.$$

M_{2S} is in the centre of gravity of body 2, thus it produces no moment of inertia. M_{2O} is that part of M_2 which brings about the moment of inertia

$$C_2 = M_{2O}\rho^2,$$

where ρ is the radius of inertia with respect to the gravity center S_2. According to this assumption the moment of inertia C_2 can be considered to be independent of the mass M_{2S}. Introducing the notation $b = l - a > 0$ we can arrange expression (6) into the form

$$(M_{2S} + M_{2O})ab > A_3 + M_{2O}\rho^2,$$

or

$$M_{2S} > \frac{1}{ab}(A_3 - M_{2O}(ab - \rho^2)) = \frac{M_{2O}}{ab}\rho^2 + \frac{A_3}{ab} - M_{2O}. \tag{7}$$

This expression (7) serves as basis for the demonstration of the so-called stability charts.

If the parameters a, b and A_3 are considered to be constants we can determine the regions of stability (denoted by S), and regions of instability (denoted by U in the figures).

There are three varying parameters in this interpretation

$$M_{2S}, \rho \quad \text{and} \quad M_{2O}.$$

It seems reasonable to separate two basic cases and three special ones.

1. $$M_{2O} < \frac{A_3}{ab}.$$

In this case, the system would be unstable if there were no mass M_{2S} but with a properly chosen M_{2S} it becomes stable. The regions of stability and instability can be seen in Fig. 2/a. The equation of the dividing line is

$$M_{2S} = \frac{M_{2O}}{ab}\rho^2 + \frac{A_3}{ab} - M_{2O},$$

2. $$M_{2O} > \frac{A_3}{ab}.$$

In this case the stability region grows considerably. See Fig. 2/b. The equation of the dividing line is

$$M_{2S} = \frac{M_{2O}}{ab}\rho^2 + \frac{A_3}{ab} - M_{2O}.$$

And now the special cases:

3. $$M_{2O} = 0.$$

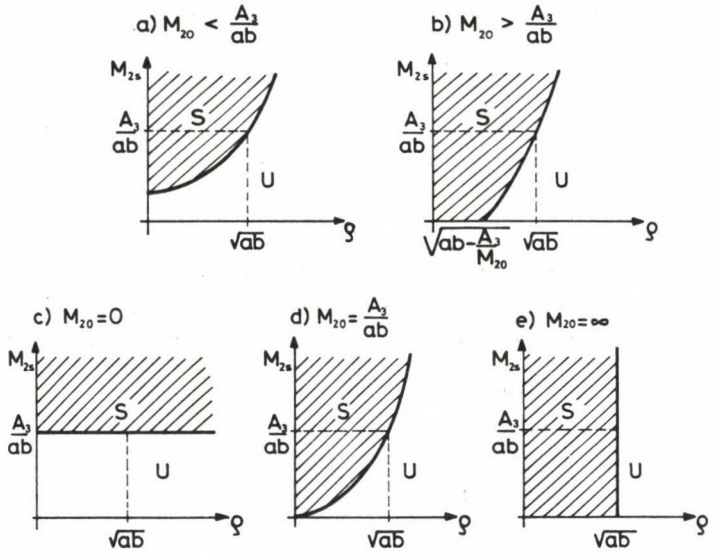

Fig. 2

This means that the mass of drawing body 2 is much smaller than the mass of body 1 or the wheel. The equation of the dividing line is

$$M_{2S}=\frac{A_3}{ab}.$$

The regions can be seen in Fig. 2/c.

4. $$M_{20}=\frac{A_3}{ab}.$$

In fact, this value of M_{20} is between the values of the general cases **1** and **2**. The equation of the dividing line is

$$M_{2S}=\frac{A_3}{a^2b^2}\rho^2.$$

The stability chart is to be found in Fig. 2/d.

5. $$M_{20}=\infty.$$

Contrary to case **3**, the mass of drawing body 2 is much bigger than that of the others. In this case, the critical value $\sqrt{ab}$ of the radius of inertia ρ separates the stability and instability regions. The equation of the dividing line is

$$\lim_{M_{20}\to\infty}\frac{M_{2S}}{M_{20}}=\lim_{M_{20}\to\infty}\left(\frac{\rho^2}{ab}-\frac{A_3}{M_{20}ab}-1\right),$$

$$0=\frac{\rho^2}{ab}-1, \qquad \text{i.e.}$$

$$\rho=\sqrt{ab}$$

This stability chart is to be found in Fig. 2/e.

If $\lambda_{1,2}=\pm i\omega$ are the roots of the characteristic equation (5) then ω is the frequency of the periodic solution of the linear system. Clearly, ω is the common root of the following equations at the critical point.

$$\mathrm{Re}\,(D(i\omega))=-\frac{\tilde{a}_{22}}{N}\omega^2+\frac{kv}{N}=0\Rightarrow\omega^2=\frac{kv}{\tilde{a}_{22}}\bigg|_{M_{2\,\mathrm{crit}}}=\frac{kal}{M_1al+\theta},$$

$$\frac{1}{\omega}\,\mathrm{Im}\,(D(i\omega))=-\omega^2+\frac{kl}{N}=0 \qquad \Rightarrow\omega^2=\frac{kl}{N}\bigg|_{M_{2\,\mathrm{crit}}}=\frac{kal}{M_1al+\theta}.$$

Thus, we can say that the frequency of the periodic solution of the linear system is

$$\omega=\sqrt{\frac{kal}{M_1al+\theta}}. \tag{8}$$

Let us consider M_2 the varying bifurcation parameter. According to Hopf's theorem [3, 5] bifurcation occurs if

$$\mathrm{Re}\,\frac{\mathrm{d}\lambda}{\mathrm{d}M_2}\bigg|_{\substack{\lambda=i\omega\\ M_2=M_{2\mathrm{crit}}}}\neq 0.$$

Now we have to calculate this derivative at the critical point. If we differentiate the characteristic equation (5) we get the following:

$$3\lambda^2\frac{\mathrm{d}\lambda}{\mathrm{d}M_2}+\frac{\tilde{a}'_{22}N-\tilde{a}_{22}N'}{N^2}\lambda^2+2\lambda\frac{\tilde{a}_{22}}{N}\frac{\mathrm{d}\lambda}{\mathrm{d}M_2}-\frac{klN'}{N^2}\lambda+\frac{kl}{N}\frac{\mathrm{d}\lambda}{\mathrm{d}M_2}-\frac{kvN'}{N^2}=0,$$

where

$$\tilde{a}'_{22}=\frac{\mathrm{d}\tilde{a}_{22}}{\mathrm{d}M_2} \qquad \text{and} \qquad N'=\frac{\mathrm{d}N}{\mathrm{d}M_2}.$$

$$\frac{\mathrm{d}\lambda}{\mathrm{d}M_2}\left(3\lambda^2+2\lambda\frac{\tilde{a}_{22}}{N}+\frac{kl}{N}\right)=\frac{1}{N^2}((\tilde{a}_{22}N'-\tilde{a}'_{22}N)\lambda^2+k(v+l\lambda)N'). \tag{9}$$

At the critical point

$$\tilde{a}_{22}=\frac{v}{al}(M_1al+\theta)=\frac{kv}{\omega^2},$$

$$N=\frac{M_1al+\theta}{a}=\frac{kl}{\omega^2},$$

$$\tilde{a}'_{22} = v\frac{l-a}{l},$$

$$N' = \frac{(l-a)^2}{l}.$$

Substituting these values into (9):

$$\left.\frac{\mathrm{d}\lambda}{\mathrm{d}M_2}\right|_{\substack{\lambda=i\omega \\ M_2=M_{2\mathrm{crit}}}} = \frac{-\omega^2\left(v\frac{l-a}{l}\frac{kl}{\omega^2} - \frac{kv}{\omega^2}\frac{(l-a)^2}{l}\right) + \frac{k(l-a)^2}{l}(li\omega+v)}{\frac{k^2l^2}{\omega^4}\left(-3\omega^2+2i\omega\frac{v}{l}+\omega^2\right)} =$$

$$= -\frac{\omega^4[vl(l-a)+(l-a)^2li\omega]\left(\omega^2+i\omega\frac{v}{l}\right)}{2kl^3\omega^2\left(\omega^2+\frac{v^2}{l^2}\right)},$$

$$\mathrm{Re}\left.\frac{\mathrm{d}\lambda}{\mathrm{d}M_2}\right|_{\substack{\lambda=i\omega \\ M_2=M_{2\mathrm{crit}}}} = -\frac{v\omega^4 a(l-a)}{2kl(\omega^2l^2+v^2)} < 0. \tag{10}$$

Thus, there are bifurcating periodic orbits.

Further on we should like to find out whether the occurring periodic solutions are stable or unstable according to the supercritical or subcritical cases when $M_2 \lessgtr M_{2\,\mathrm{crit}}$, respectively.

3. Higher order terms in the system of differential equations

For this investigation, we have to calculate the nonlinearities up to the third order. Omitting the quotation of all the tiresome calculations, we just wish to show the end-result.

$$\begin{bmatrix} \dot{\vartheta} \\ \dot{s} \\ \dot{q} \end{bmatrix} = \begin{bmatrix} 0 & 1 & 0 \\ 0 & -v/l & -\omega^2/l \\ v & l & 0 \end{bmatrix} \begin{bmatrix} \vartheta \\ s \\ q \end{bmatrix} + \begin{bmatrix} 0 \\ k_{12}\vartheta^2 s + k_{13}\vartheta^2 q + k_{21}\vartheta s^2 \\ l_{11}\vartheta^3 + l_{12}\vartheta^2 s \end{bmatrix} \tag{11}$$

where the coefficients are as follows:

$$k_{12} = -\frac{v}{2l},$$

$$k_{13} = \frac{\omega^4}{2kl}\left(M_1 + 2M_3 + \frac{2B_3}{R^2} + \theta\frac{l+a}{al(l-a)}\right),$$

$$k_{21} = -\frac{\omega^2}{k}\left(M_1 + M_3 + \frac{\theta}{a(l-a)} + \frac{B_3}{R^2}\right),$$

$$l_{11} = -\frac{v}{3},$$

$$l_{12} = \frac{l}{2}.$$

Note that there is no term of second order.

4. Poincaré normal form

The next step is to calculate the Poincaré normal form of this system (11). For this, we determine the right and left hand side eigenvectors of the coefficient matrix **A** of the linearized system.

The right hand side eigenvectors of **A** belonging to the eigenvalue $\lambda = i\omega$ satisfy the following algebraic equations

$$\begin{bmatrix} \mathbf{A} & \omega\mathbf{E} \\ -\omega\mathbf{E} & \mathbf{A} \end{bmatrix} \begin{bmatrix} \mathbf{s}_1 \\ \mathbf{s}_2 \end{bmatrix} = \mathbf{0},$$

where

$$\mathbf{A} = \begin{bmatrix} 0 & 1 & 0 \\ 0 & -v/l & -\omega^2/l \\ v & l & 0 \end{bmatrix}, \qquad \mathbf{E} = \begin{bmatrix} 1 & 0 & 0 \\ 0 & 1 & 0 \\ 0 & 0 & 1 \end{bmatrix},$$

$\mathbf{s}_1$, $\mathbf{s}_2$ are the right hand side eigenvectors.

In this system of linear equations, we have two free variables. Solving this system, we get the eigenvectors:

$$\mathbf{s}_1 = \begin{bmatrix} \dfrac{\omega^2 l}{v^2 + \omega^2 l^2} \\ -\dfrac{\omega^2 v}{v^2 + \omega^2 l^2} \\ 1 \end{bmatrix}, \qquad \mathbf{s}_2 = \begin{bmatrix} \dfrac{\omega v}{v^2 + \omega^2 l^2} \\ \dfrac{\omega^3 l}{v^2 + \omega^2 l^2} \\ 0 \end{bmatrix}.$$

The left hand side eigenvectors of **A** satisfy the equations:

$$\begin{bmatrix} \mathbf{A}^T & \omega\mathbf{E} \\ -\omega\mathbf{E} & \mathbf{A}^T \end{bmatrix} \begin{bmatrix} \mathbf{n}_1 \\ \mathbf{n}_2 \end{bmatrix} = \mathbf{0},$$

where the superscript T denotes "transpose", i.e.

$$\mathbf{A}^T = \begin{bmatrix} 0 & 0 & v \\ 1 & -v/l & l \\ 0 & -\omega^2/l & 0 \end{bmatrix},$$

$\mathbf{n}_1$, $\mathbf{n}_2$ are the left hand side eigenvectors of $\mathbf{A}$.

By solving the equations, we get the two eigenvectors:

$$\mathbf{n}_1 = \begin{bmatrix} 0 \\ 0 \\ 1 \end{bmatrix}, \qquad \mathbf{n}_2 = \begin{bmatrix} -v/\omega \\ -l/\omega \\ 0 \end{bmatrix}.$$

With the help of $\mathbf{n}_1$ and $\mathbf{n}_2$ one can produce $\mathbf{s}_3$ which is orthogonal to the plane determined by $\mathbf{n}_1$ and $\mathbf{n}_2$:

$$\mathbf{s}_3 = \mathbf{n}_1 \times \mathbf{n}_2 = \begin{bmatrix} l/\omega \\ -v/\omega \\ 0 \end{bmatrix}.$$

Now, we have the transformation matrix $\mathbf{T}$:

$$\mathbf{T} = [\mathbf{s}_1, \mathbf{s}_2, \mathbf{s}_3] = \begin{bmatrix} \dfrac{\omega^2 l}{v^2+\omega^2 l^2} & \dfrac{\omega v}{v^2+l^2\omega^2} & \dfrac{l}{\omega} \\ -\dfrac{\omega^2 v}{v^2+\omega^2 l^2} & \dfrac{\omega^3 l}{v^2+l^2\omega^2} & -\dfrac{v}{\omega} \\ 1 & 0 & 0 \end{bmatrix}, \tag{12}$$

$$\det \mathbf{T} = -1.$$

The inverse of $\mathbf{T}$ is

$$\mathbf{T}^{-1} = \begin{bmatrix} 0 & 0 & 1 \\ v/\omega & l/\omega & 0 \\ \dfrac{\omega^3 l}{v^2+l^2\omega^2} & -\dfrac{\omega v}{v^2+l^2\omega^2} & -\dfrac{\omega^3}{v^2+l^2\omega^2} \end{bmatrix}.$$

If we denote

$$\mathbf{y} = \begin{bmatrix} \vartheta \\ s \\ q \end{bmatrix}, \qquad \dot{\mathbf{y}} = \begin{bmatrix} \dot{\vartheta} \\ \dot{s} \\ \dot{q} \end{bmatrix}$$

then equation (11) will be

$$\dot{\mathbf{y}} = \mathbf{A}\mathbf{y} + \mathbf{f}(\mathbf{y}), \tag{13}$$

where $\mathbf{f}(\mathbf{y})$ contains the nonlinearities of order three. If one introduces the new vector variables

$$\mathbf{x} = \begin{bmatrix} x_1 \\ x_2 \\ x_3 \end{bmatrix}, \qquad \dot{\mathbf{x}} = \begin{bmatrix} \dot{x}_1 \\ \dot{x}_2 \\ \dot{x}_3 \end{bmatrix}$$

one can say that

$$\mathbf{y} = \mathbf{T}\mathbf{x} \qquad \text{i.e.} \qquad \mathbf{x} = \mathbf{T}^{-1}\mathbf{y},$$

and the transformation of equation (11) is the following:

$$\dot{\mathbf{x}} = \mathbf{T}^{-1}\mathbf{A}\mathbf{T}\mathbf{x} + \mathbf{T}^{-1}\mathbf{f}(\mathbf{T}\mathbf{x}) \tag{14}$$

where the matrix of the linear part has the Poincaré form:

$$\mathbf{T}^{-1}\mathbf{A}\mathbf{T} = \begin{bmatrix} 0 & \omega & 0 \\ -\omega & 0 & 0 \\ 0 & 0 & -v/l \end{bmatrix} = \mathbf{P} = [p_{ij}].$$

From this matrix one can learn that the third eigenvalue of $\mathbf{A}$ is $\lambda_3 = -\dfrac{v}{l}$ which is a negative real number.

5. Restriction to the center manifold

Before transforming the nonlinearities in each of the three equations we can prove that it is not necessary to do this with the third one because there are no terms of second order so we are now on the center manifold.

Lemma: Let the investigated system be like (11) in which there are no terms of second order. If it is so, then the equation of the center manifold is

$$x_3 = h(x_1, x_2)$$

where

$$h(x_1, x_2) = O((x_1^2 + x_2^2)^{3/2}),$$

i.e. it does not contain second order terms either.

Proof: We should like to have the equation of the center manifold in the following form

$$x_3 = \frac{1}{2}(h_{11}x_1^2 + 2h_{12}x_1x_2 + h_{22}x_2^2) + O((x_1^2 + x_2^2)^{3/2}).$$

Because of the invariance of the center manifold,

$$x_3(t) = h(x_1(t), x_2(t)),$$

where the solution $x_1(t)$, $x_2(t)$, $x_3(t)$ is on the manifold, and h_{11}, h_{12}, h_{22} are the coefficients of the second order terms in $h(x_1, x_2)$.

If we use the differential equation (14) we obtain

$$\dot{x}_3 = (h_{11}x_1 + h_{12}x_2)\dot{x}_1 + (h_{12}x_1 + h_{22}x_2)\dot{x}_2 + O((x_1^2 + x_2^2)^{3/2})$$

i.e.

$$\dot{x}_3 = \omega x_2(h_{11}x_1 + h_{12}x_2) - \omega x_1(h_{12}x_1 + h_{22}x_2) + O((x_1^2 + x_2^2)^{3/2}).$$

And of course, we have the third equation of (14)

$$\dot{x}_3 = p_{33}x_3 + O((x_1^2 + x_2^2 + x_3^2)^{3/2}), \quad \text{as well.}$$

To get the unknown coefficients h_{11}, h_{12}, h_{22} one has to solve the equation

$$-\omega x_1(h_{12}x_1 + h_{22}x_2) + \omega x_2(h_{11}x_1 + h_{12}x_2) =$$

$$= \frac{1}{2}p_{33}(h_{11}x_1^2 + 2h_{12}x_1x_2 + h_{22}x_2^2).$$

As the corresponding coefficients are equal, we will have a homogeneous system of linear equations

$$\begin{bmatrix} \frac{1}{2}p_{33} & \omega & 0 \\ -\omega & p_{33} & \omega \\ 0 & -\omega & \frac{1}{2}p_{33} \end{bmatrix} \begin{bmatrix} h_{11} \\ h_{12} \\ h_{22} \end{bmatrix} = \mathbf{0}.$$

This system of linear equations has only the trivial solution if and only if the determinant of its coefficient matrix is not equal to zero.

$$\begin{vmatrix} \frac{1}{2}p_{33} & \omega & 0 \\ -\omega & p_{33} & \omega \\ 0 & -\omega & \frac{1}{2}p_{33} \end{vmatrix} = \frac{1}{2}p_{33}\left(\frac{1}{2}p_{33}^2 + 2\omega^2\right) < 0,$$

and not equal to zero, so the required coefficients $h_{11}=h_{12}=h_{22}=0$, and the equation of the center manifold is

$$x_3=O((x_1^2+x_2^2)^{3/2}). \tag{15}$$

Thus, we have to transform only the first two equations of (11). If we do this we get a form which is suitable for the stability investigation of bifurcating orbits.

$$\begin{bmatrix}\dot{x}\\ \dot{x}_2\\ \dot{x}_3\end{bmatrix}=\begin{bmatrix}0 & \omega & 0\\ -\omega & 0 & 0\\ 0 & 0 & -v/l\end{bmatrix}\begin{bmatrix}x_1\\ x_2\\ x_3\end{bmatrix}+$$

$$+\begin{bmatrix}b_{30}x_1^3+b_{21}x_1^2x_2+b_{12}x_1x_2^2+b_{03}x_2^3\\ d_{30}x_1^3+d_{21}x_1^2x_2+d_{12}x_1x_2^2+d_{03}x_2^3\\ \ldots x_1^3+\ldots x_1^2x_2+\ldots x_1x_2^2+\ldots x_2^3\end{bmatrix}+\mathbf{0}(|x|^4) \tag{16}$$

where the coefficients are as follows:

$$b_{30}=t_{13}^{-1}t_{11}^2(t_{11}l_{11}+t_{21}l_{12}),$$

$$b_{21}=t_{13}^{-1}t_{11}(3t_{11}t_{12}l_{11}+(2t_{12}t_{21}+t_{11}t_{22})l_{12}),$$

$$b_{12}=t_{13}^{-1}t_{12}(3t_{11}t_{12}l_{11}+(t_{12}t_{21}+2t_{11}t_{22})l_{12}),$$

$$b_{03}=t_{13}^{-1}t_{12}^2(t_{12}l_{11}+t_{22}l_{12}),$$

$$d_{30}=t_{22}^{-1}t_{11}(t_{21}^2k_{21}+t_{11}t_{21}k_{12}+t_{11}t_{31}k_{13}),$$

$$d_{21}=t_{22}^{-1}[t_{21}(2t_{11}t_{22}+t_{12}t_{21})k_{21}+t_{11}(2t_{12}t_{21}+t_{11}t_{22})k_{12}+$$
$$+2t_{11}t_{12}t_{31}k_{13}],$$

$$d_{12}=t_{22}^{-1}[t_{22}(t_{11}t_{22}+2t_{12}t_{21})k_{21}+t_{12}(t_{12}t_{21}+2t_{11}t_{22})k_{12}+$$
$$+t_{12}^2t_{31}k_{13}],$$

$$d_{03}=t_{22}^{-1}t_{12}(t_{22}^2k_{21}+t_{12}t_{22}k_{12}),$$

and t_{13}^{-1}, t_{22}^{-1} and t_{ij}, $i,j=1,2,3$ are the elements of matrices $\mathbf{T}^{-1}$ and $\mathbf{T}$ respectively.

6. Stability investigation of bifurcating periodic solutions

If we apply the *Lemma*, system (16) reduced onto the center manifold thus will consist of the first two equations of (16) on account of equation (15) of the center manifold. According to the 8th step of the algorithm published in [1, 90 pp.] the

question of stability may be decided with the help of the sign of

$$\delta = \frac{1}{8}(3b_{30} + b_{12} + d_{21} + 3d_{03}) \tag{17}$$

as it is proved in that book.

Now it is easy to see that there is no need to calculate each of the eight coefficients of equation (16) just the four in (17).

$$3b_{30} + b_{12} = 3\frac{\omega^2 l}{v^2 + l^2\omega^2}\left[\frac{\omega^2 l}{v^2 + l^2\omega^2}\left(-\frac{\omega^2 l}{v^2 + l^2\omega^2}\frac{v}{3} - \frac{\omega^3 v}{v^2 + l^2\omega^2}\frac{l}{2}\right) - \frac{\omega^2 v^2}{(v^2 + l^2\omega^2)^2}\frac{v}{3}\right] +$$

$$+ \frac{\omega v}{v^2 + l^2\omega^2}\left(-\frac{\omega^3 v^2}{(v^2 + l^2\omega^2)^2} + 2\frac{\omega^5 l^2}{(v^2 + l^2\omega^2)^2}\right)\frac{l}{2} = -\frac{3}{2}\frac{\omega^4 v l}{(v^2 + l^2\omega^2)^2},$$

$$d_{21} + 3d_{03} = \frac{l}{\omega}\left[k_{21}\left(-\frac{\omega^2 v}{v^2 + l^2\omega^2}\left(2\frac{\omega^5 l^2}{(v^2 + l^2\omega^2)^2} - \frac{\omega^3 v^2}{(v^2 + l^2\omega^2)^2}\right) +\right.\right.$$

$$\left. + 3\frac{\omega^4 v l}{(v^2 + l^2\omega^2)^2}\frac{\omega^3 l}{v^2 + l^2\omega^2}\right) +$$

$$+ k_{12}\left(\frac{\omega^2 l}{v^2 + l^2\omega^2}\left(-2\frac{\omega^3 v^2}{v^2 + l^2\omega^2} + \frac{\omega^5 l^2}{v^2 + l^2\omega^2}\right) + 3\frac{\omega^5 v^2 l}{(v^2 + l^2\omega^2)^3}\right) +$$

$$\left. + k_{13} 2\frac{\omega^3 l v}{(v^2 + l^2\omega^2)^2}\right] =$$

$$= \frac{\omega^2 l}{(v^2 + l^2\omega^2)^2}\left[\omega^2 v k_{21} + \omega^2 l k_{12} + 2lvk_{13}\right] =$$

$$= \frac{\omega^4 v l}{k(v^2 + l^2\omega^2)^2}\left[\omega^2\left(M_3 + \frac{B_3}{R^2} - \frac{\theta}{l(l-a)}\right) - \frac{k}{2}\right].$$

Thus,

$$\delta = \frac{1}{8}\frac{\omega^4 v l}{(v^2 + l^2\omega^2)^2}\left[\frac{\omega^2}{k}\left(M_3 + \frac{B_3}{R^2} - \frac{\theta}{l(l-a)}\right) - 2\right] \tag{18}$$

We know from [1, 3, 4, 5] that according to Hopf's theorem the periodic solutions occur for $M_{2\,\mathrm{crit}} - \varepsilon < M_2 < M_{2\,\mathrm{crit}}$ with some sufficiently small $\varepsilon > 0$ are orbitally asymptotically stable with asymptotic phase if $\delta < 0$ but those occurring for $M_2 > M_{2\,\mathrm{crit}}$ are unstable if $\delta > 0$.

The cases are called

1. $\delta < 0$ and $\mathrm{Re}\dfrac{\mathrm{d}\lambda}{\mathrm{d}\mu} > 0$ and $\mu > \mu_{\mathrm{crit}}$,
2. $\delta < 0$ and $\mathrm{Re}\dfrac{\mathrm{d}\lambda}{\mathrm{d}\mu} < 0$ and $\mu < \mu_{\mathrm{crit}}$

supercritical and the cases

3. $\delta>0$ and $\mathrm{Re}\dfrac{\mathrm{d}\lambda}{\mathrm{d}\mu}>0$ and $\mu<\mu_{\mathrm{crit}}$,

4. $\delta>0$ and $\mathrm{Re}\dfrac{\mathrm{d}\lambda}{\mathrm{d}\mu}<0$ and $\mu>\mu_{\mathrm{crit}}$

subcritical, where μ denotes the bifurcation parameter.

In our system

$$\mathrm{Re}\frac{\mathrm{d}\lambda}{\mathrm{d}\mu}<0$$

is at the critical point. Our δ in (18) is interesting because it can, in fact, assume negative and positive values, thus, there are parameter constellations which imply supercritical (orbitally asymptotically stable) vibrations and there are such that imply subcritical (unstable) ones.

First we are interested in the supercritical case, i.e.

$$\delta<0,\ \mathrm{Re}\frac{\mathrm{d}\lambda}{\mathrm{d}M_2}<0 \qquad \text{and} \qquad M_2<M_{2\,\mathrm{crit}} \tag{19}$$

By using (18) and knowing that

$$\begin{aligned}
\omega^2&=\frac{kal}{M_1al+\theta},\\
\theta&=A_3+C_2,\\
A_3&=\frac{1}{4}M_3R^2,\\
C_2&=M_{20}\rho^2,\\
B_3&=\frac{1}{2}M_3R^2,
\end{aligned} \tag{20}$$

we get the following:

$$\frac{al}{M_1al+\theta}\left(M_3+\frac{B_3}{R^2}-\frac{\theta}{l(l-a)}\right)-2<0,$$

$$M_3+\frac{B_3}{R^2}-\frac{A_3+C_2}{l(l-a)}<2\left(M_1+\frac{A_3+C_2}{al}\right),$$

$$M_3\left(1+\frac{1}{2}-\frac{1}{4}\frac{R^2}{l(l-a)}\right)-\frac{C_2}{l(l-a)}<2M_1+\frac{2}{4}\frac{M_3R^2}{al}+\frac{2C_2}{al},$$

$$M_3\left(\frac{3}{2}-\frac{1}{4}\frac{R^2(2l-a)}{al(l-a)}\right)<2M_1+C_2\frac{2l-a}{al(l-a)}.$$

We can use the notation $b=l-a$ again and we get

$$\frac{1}{4}M_3\frac{6abl-R^2(l+b)}{alb}<2M_1+C_2\frac{l+b}{alb}, \tag{21}$$

and

$$C_2>\frac{1}{4}M_3\frac{6abl-R^2(l+b)}{l+b}-2M_1\frac{alb}{l+b},$$

with expressions (20)

$$M_{20}\rho^2>A_3\left(\frac{6abl}{R^2(l+b)}-1\right)-2M_1\frac{abl}{l+b},$$

$$\rho^2>\frac{A_3}{M_{20}}\left(\frac{6abl}{R^2(l+b)}-1\right)-2\frac{M_1}{M_{20}}\frac{abl}{l+b}. \tag{22}$$

This inequality is trivially fulfilled if the term noted by K is less than or equal to zero

$$K=\frac{6abl}{R^2(l+b)}-1\leqq 0 \qquad \left(\Rightarrow R^2\geqq\frac{6abl}{l+b}\right).$$

In this case all the periodic solutions near the equilibrium occur for $M_{2\,\mathrm{crit}}-\varepsilon<M<M_{2\,\mathrm{crit}}$ are orbitally asymptotically stable. Note that this is a geometrical condition for the supercritical bifurcation.

If $K>0$ and we assume that the mass of body 1 is small i.e. $M_1\approx 0$ then condition (22) becomes:

$$\rho>\sqrt{\frac{A_3}{M_{20}}\cdot K}=\rho_0. \tag{23}$$

Conversely, if $\rho<\rho_0$ then $\delta>0$ i.e. subcritical bifurcation occurs.

Figure 3 shows the stability regions and the strips of the stable and unstable periodic orbits for different values of M_{20} and $0<K<1$. The figures are very similar to those which we get if $K\geqq 1$.

The amplitudes of the periodic orbits can be computed according to [1]:

$$r\approx\sqrt{-\frac{\mathrm{Re}\dfrac{\mathrm{d}\lambda}{\mathrm{d}M_2}(M_{2\,\mathrm{crit}})}{\delta}(M_2-M_{2\,\mathrm{crit}})}=$$

$$=\sqrt{-\frac{v\omega^4ab}{2kl(v^2+l^2\omega^2)}\frac{8(v^2+l^2\omega^2)^2}{\omega^4vl}\frac{M_2-\theta/ab}{\omega^2/k(3/2M_3-\theta/lb)-2}}=$$

$$=\sqrt{-\frac{4ab}{kl^2}\left(v^2+\frac{kal^3}{M_1al+\theta}\right)\frac{M_2-\theta/ab}{\dfrac{al}{M_1al+\theta}(3/2M_3-\theta/lb)-2}}=$$

$$=\sqrt{-\frac{4(v^2M_1al+v^2\theta+kal^3)(M_2ab-\theta)}{kl^2(3/2M_3al-\theta a/b-2M_1al-2\theta)}}=$$

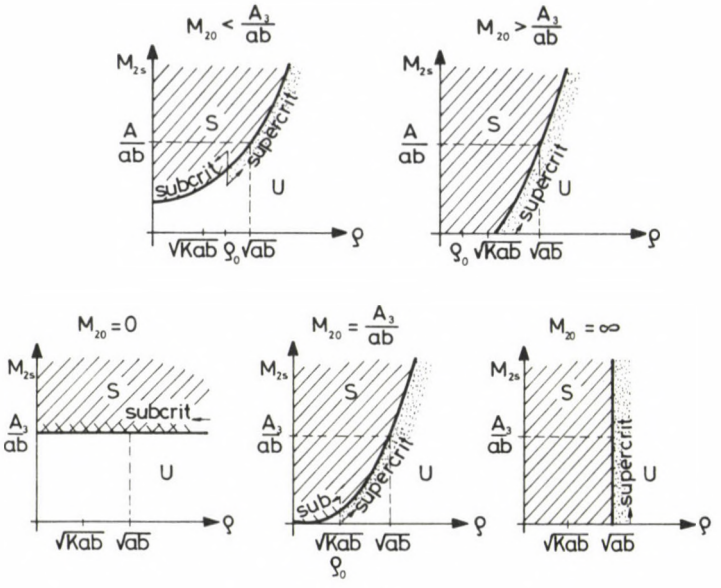

Fig. 3

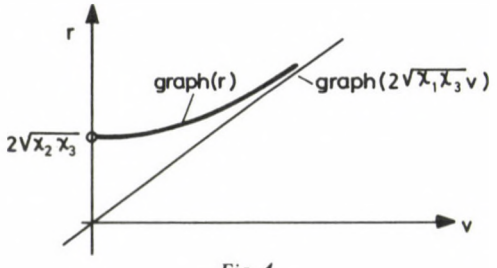

Fig. 4

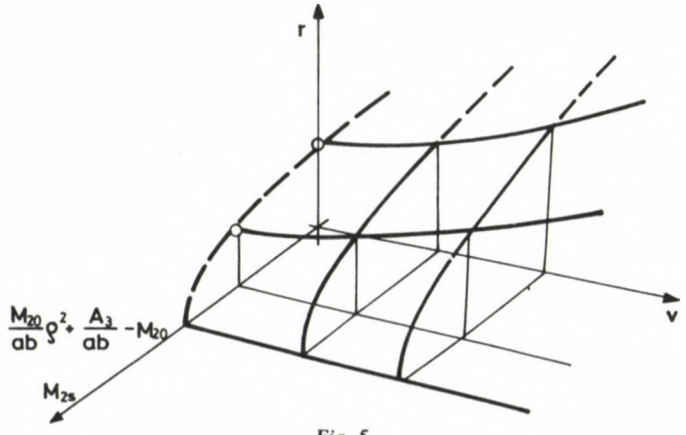

Fig. 5

Thus,

$$r \approx 2\sqrt{(v^2\chi_1 + \chi_2)\chi_3}, \tag{24}$$

$$\chi_1 = M_1 al + \frac{1}{4} M_3 R^2 + M_{20}\rho^2 > 0,$$

$$\chi_2 = kal^3 > 0,$$

$$\chi_3 = \frac{1/4 M_3 R^2 + M_{20}(\rho^2 - ab) - M_{2S}ab}{kl^2(M_3(3/2al - 1/4R^2(l+b)/b) - M_{20}\rho^2(l+b)/b - 2M_1 al)} > 0.$$

Note that the speed v has neither a role in the stability investigation nor in the bifurcation. But (25) shows that the amplitude of the vibration strongly depends on v. The correspondence between r and v is hyperbolic. (See Figs 4, 5.)

This result responds to our technical common sense.

References

1. Hassard, B. D., Kazarinoff, N. D., Wan, Y. H.: Theory and Applications of Hopf Bifurcation. London Mathematical Society Lecture Note Series. 41. Cambridge 1981.
2. Brossard, J. P.: Mécanique générale, I. N. S. A. Lyon 1972.
3. Chow, S. N., Hale, J. K.: Methods of Bifurcation Theory. Springer Verlag, New York 1982.
4. Andronoff, A. A., Leontowich, E. A., Gordon, I. I., Mayer, A. G.: Bifurcation Theory of Dynamical Systems on the Plane. Nauka, Moscow 1967 (in Russian).
5. Marsden, J. E., McCracken, M.: The Hopf Bifurcation and Its Applications. Springer Verlag, New York 1976.

Acta Technica Academiae Scientiarum Hungaricae, 97 (1—4), pp. 341—345 (1984)

BOOK REVIEWS

MIKLÓS HERPY–JEAN-CLAUDE BERKA: *Aktive RC-Filter. Ein Lehrbuch für aktive Filterschaltungen zu entwerfen.* Akadémiai Kiadó, Budapest 1984, 326 pages

Dr.–Ing. M. Herpy, author of the successful book "Analog Integrated Circuits" has now undertaken to sum up the design of active filter networks with a co-author. Using their ten year industrial and educational experiences they had written a book that is useful for both the students in higher education and practical experts.

The book begins with a summary of network theory (1. Introduction, 2. Description of filternetworks). It is followed by a survey of the approximation of amplitude characteristics and group-delay characteristics (3. Approximation). The active RC filter networks are discussed comprehensively in the 4th chapter (4. Synthesis of active RC filters). The 5th chapter discusses sensitivity and tolerances in detail. The most useful circuits of the vast family of biquadratic sections are evaluated on a common basis in the 6th chapter. A summary of the steps of the design procedure, with a view to the most important practical issues, such as dynamic range, measurements and tuning, follows. Actual filter design is demonstrated by 6 carefully worked out examples. Design formulas for 16 different second order sections and 2 different third order sections are discussed in a separate chapter. Diagrams and tables offer easy access to the most important catalogue data of filter design. The book ends with a rich bibliography and subject index.

The present edition is a revised version of a book originally published in Hungarian, in 1981. This explains some strong references to results obtained in Hungary.

In short, the book "Active RC Filters" discusses the cascade synthesis of RC filters in a remarkably concise and systematic way. It can warmly be recommended as a very good reference book to a wide circle of research, design and production specialists.

K. Géher

L. KOLLÁR–E. DULÁCSKA: *Buckling of Shells for Engineers.* Akadémiai Kiadó, Budapest–John Wiley, Chichester–New York, etc., 1984, 303 pages

This book is an essentially enlarged version of the Hungarian "Héjak horpadása" (Buckling of Shells), or of the German version "Schalenbeulung" by the same authors. Its aim is to present a clear explanation of the rather intricate buckling process in shells, offering simple methods for deciding over the adequate safety against buckling of shell structures.

Detailed discussion is presented on inherent buckling conditions of various shell types, in particular, on stability problems of cylindrical and conical shells under loads of radial and of generatrix directions, as well as of cylindrical shells under hydrostatic loads or in torsion. The effects of various factors on the critical load and on post-critical phenomena are shown in several diagrams. A thorough analysis is made on the buckling of spherical shells, and in general, on spherical caps, including problems of post-critical behaviour. Many figures illustrate the effect of factors influencing buckling. Also the buckling phenomena of spherical caps under point loads, and in general, of elliptic shells are considered, including the possibility of snap-through. Much attention is paid to the rather popular various hyperbolic shell types and also to cases of uniformly loaded hypar shells, saddle-shaped shells and shells of hyperboloid of revolution. These latter are discussed from the aspect of different possibilities of buckling. Interesting statements are made on the behaviour of different types of free-edged shells, arch shells and orthotropic shells. Separate treatment is given to stability problems of sandwich shells, rib-stiffened shells and reticulated shells. The effect of plasticity and creep of the shell material on the critical force, and peculiarities in the behaviour of shells made of different materials are examined. Special consideration is due to the practical application of achievements of the theory of stability, in particular, to effects of factors affecting shell buckling. In conclusion, two numerical examples are given for

the sake of illustration, concerning the stability analysis of a cylindrical lattice made of steel, and of a reinforced concrete spherical cap.

This publication is to supply important contribution to engineering practice. Although buckling of shells has been concerned with in many international publications, it is quite difficult for practicing engineers to cover the problem partly because of the complexity of the applied mathematical methods. Another difficulty is that studies concerned with the problem of shell buckling generally affect certain particular problems, without directly helping practicing engineers. Moreover, experimental results are regionally scattered, and experimental or empirical critical values are much lower than those expected from theoretical analyses.

In conformity with general views, the authors attribute the deviations to an irrealistic, idealized assumption of the shell shape and supporting conditions. Even if inevitable initial imperfections are accounted for in the theory by an other than regular shape, deviations are assumed to be of regular arrangement. Another error is due to reckoning with only a limited number of possibilities from among the infinity of buckling forms realizable, and to applying different neglects in computations. Deviations can also result from the idealized assumption of the material properties of shells and from the omission in theoretical analyses of chemical, physical and dynamical effects on the shell during its service life.

All these deviations may lead to eccentric stresses in the shell wall, responsible for shells buckling at much lower than theoretically calculated critical loads. In this book, each possible initial imperfection is taken into account separately, with the resulting, and otherwise arisen eccentric stresses in the shell wall, special material properties of the shell wall, and all these are simultaneously pondered in making a suggestion for the reasonable assumption of the safety factor.

The discussion is interwoven with the concept of linear critical load, a value obtained—rather than by lengthy deductions—in a quite ingenious manner, relying on the theory of shallow shells. This ideation is based on the experimental observation that the buckling of shells involves a wave (or waves) generally affecting a small area, and within the wave range, the shell can be considered to be shallow. This simplification yields the same value for the linear critical load as the more exact theory by the ulterior omission of nonlinear terms.

As a general statement, this book meets the intention of its authors to give a comprehensive, clear-cut explanation of the complex phenomenon of the buckling of shells. A detailed presentation is given of results in publications on the buckling of shells, including several valuable studies by the authors themselves. The list of over 300 references is a helpful tool for further research.

This book is an interesting treatise on shell stability problems for professionals, and an indispensable assistance to those concerned with the design and construction of shell structures.

P. Csonka

G. FRANZ (Editor): *Beton-Kalender 1984*. Taschenbuch für Beton, Stahlbeton und Spannbeton, sowie die verwandten Fächer. W. Ernst u. Sohn Verlag für Architektur und technische Wissenschaften, Berlin, Vol. 73. Part I: p. 974; Part II: p. 1095.

The first part of this book is concerned with concrete and mortar material properties, reinforcement types, structural engineering problems and designing rules of reinforced concrete structural members, including those of prestressed concrete.

The second part comprehensively discusses standard specifications for the design of reinforced concrete structures, theoretical and practical knowledge on shell structures, stress pattern in silos, rules of constructing reinforced concrete structures, knowledge on insulating and dampproofing of constructions, and limit design theory of reinforced concrete structures.

This work has been edited by Dr.–Ing., Dr.–Ing. E. h. Gotthard Franz Professor Emeritus of the University of Karlsruhe, a world renown scientist. Chapters have been written by authorities in reinforced concrete, elaborating their respective subjects with deepgoing competency. A special attention should be called to the fact that among the authors a foreigner—the Hungarian Lajos Kollár,—author of the chapter on shell structures is also to be found. This chapter is a concise, clear-cut recapitulation of knowledge on design, computation and construction of shell structures, relying in part on the theoretical and practical achievements of its authors. It is concluded by a profuse list of references of nearly 150 items.

As an overall statement, this Volume 73 of Beton-Kalender follows the age-old tradition to be a valuable, indispensable manual comprising the wide scope of reinforced concrete construction. It offers useful knowledge to those interested in theoretical and practical problems of reinforced concrete construction, desirous of designing and constructing their structures reasonably and economically, utilizing the latest achievements of recent knowledge.

The valuable contents of this work make it worth reading and it is of universal interest not only

in German-speaking countries but also beyond, since the contained knowledge matter is of universal use throughout the domain of reinforced concrete construction.

P. Csonka

J. SZABÓ–L. KOLLÁR: *Structural design of cable-suspended roofs.* Akadémiai Kiadó, Budapest and Ellis Horwood Limited, Chichester 1984, 243 pages

This book is published in the "Ellis Horwood Series in Engineering Science". It presents a comprehensive account of the general analysis of cable-suspended roofs in a form suitable for practical use.

The first chapter gives a general discussion of suspended roofs, showing the types of same, the most important concepts and effects, and it gives a brief survey of the calculation methods.

The second chapter is an illustrative example for the approximative calculations of suspended roofs. It is shown how to calculate the effects of dead weight, pretensioning, the different types of the wind load, the snow load, the temperature change. Also the effect of the deformation of the edge ring is considered.

To check the accuracy of the approximate method a comparative numerical example is shown in the third chapter.

Cable-net systems are often kinematically indeterminate (statically overdeterminate) ones, so it can be a serious task to determine an equilibrium position of a prestressed net. In the fourth chapter the equilibrium equations are analysed both in the general and special (parallel forces, rectangular cable net) cases. Detailed algorithms are given for the calculation of the net shape at different edge conditions (mast, arbitrary rigid edge, flexible edge cable) and for the construction of the net of the principal curvatures or of the geodetic net.

The fifth chapter gives algorithms for the exact calculation of the state change (the change of the form and the tensile forces) of the net both in the case of rigid edges and in that when the net is connected to an elastic bar structure. Some method of limited accuracy are shown, too.

The sixth chapter deals with particular problems: buckling of the edge ring, the optimum shape, the local flutter and vibration of cable net.

In the appendix there is a brief survay of matrix algebra, and the equilibrium and displacement equations of a bar with space curved axis are given.

The work presents valuable information to structural designers and engineers, and it could also be excellently used as a text book for university and post-graduate students.

Zs. Gáspár

M. MAJOR: *Építészettörténeti és építészetelméleti értelmező szótár.* (Explanatory Dictionary for History and Theory of Architecture). Akadémiai Kiadó, Budapest 1983, 431 pages

A pioneering feat has been to compile—under the guidance and with the active specialist contribution of Máté Major, academician—this explanatory dictionary coping with manyfold functions. It unambiguously defines concepts in its scope, often misused—according to the Preface by the Editor—even by specialists. Explanations of difficult wording are assisted by appropriate architectural sketches.

This is at the same time a technical dictionary in six languages; all concepts are given also in English, French, German, Italian and Russian. By the end of the volume, indices for all the six languages refer to page numbers where technical terms may be retrieved for translation into the other languages. In the matter of explanations, the dictionary is intended for Hungarian readers, but as a dictionary in five world-wide languages, it has an—also geographically—much wider domain of application.

Delimitation of concepts in history and theory of architecture from those in other fields of architecture might have been difficult. For instance, as concerns building structures, purlin is an entry, stirrup is not. Garden architecture is one, landscape architecture is not. Understandably, purlins had been applied in historical architecture, and gardens belong to buildings more than does landscape. These two examples illustrate timely and spatial delimitations, at the same time point to the urgence of processing the overall technical language of architecture.

Value of this exemplary initiative is enhanced by both its being the first in this scope, and its ampleness. In fact, two thousand terms are a wealth, exceeding the full vocabulary of ancient, simple people. Fourteen contributors from the Institute of History and Theory of Architecture, Technical University, Budapest, did comprehensive work, offering wide-range information to both specialists and public, and a valuable assistance to technical translators.

M. Kubinszky

F. CSÁKI, K. GANSZKY, I. IPSITS, S. MARTI: *Power Electronics.* Akadémiai Kiadó, Budapest 1983, 708 pages

This is the second, revised edition of the well-known university textbook. Since the advent of semiconductor electronics, power electronics under-

went enormous change and development; this new aspect is already reflected in this book.

After the introduction, convertor circuits, their calculation for different practical applications, and their components have been comprehensively dealt with, and so have been DC and AC choppers, as well as different single- and multiphase inverters. A chapter each is spent on principal tools of power electronics: magnetic components, vacuum valves, gas-filled elements—of rather historical interest—and of course, an extensive one with a special accent, on semiconductor units. A special chapter discusses design and construction of equipment containing semiconductor devices. Finally, unique equipment descriptions are offered. The list of references enumerates relevant books and papers published until recently, in addition to references pertaining to each heading.

I. P. Valkó

Zement-Taschenbuch (Cement pocket-book) Bauverlag GmbH, Wiesbaden–Berlin (FRG), 48th Edition (1984)

One of the world-renowned, internationally wide spread and used German technical handbook series is the Zement-Taschenbuch (Cement Pocketbook). It is regularly published since 1911. It appeared in the first period yearly as Zementkalender (Cement Calendar). Since the year 1950 the handbook has been published more rarely, in intervals of several years as Zement-Taschenbuch.

According to the increasing interest in this handbook, it grew up to a volume of several hundred pages dealing with the continuous development of cement production and concrete technology, also with the achieved new—up-to-date—experimental and practical results of public utility in these fields.

The, in 1984 published—until now the last—volume is already the 48. edition. The previous one appeared in 1980.

The 1984 volume contains in the same arrangement as the former editions all necessary knowledges, the newest theoretical and practical achievements on cement and concrete for experts working in building industry especially with cement and concrete. Separate chapters discuss the cement production technologies inclusive those of heterogeneous cements, also dealing with hydraulic admixtures; cement chemistry and hydration process of cement; the structure and properties of cement stone; the cement's main technical features important for the building industry, the aggregates and required characteristics of them also treating lightweight aggregates; many kinds of chemical admixtures; up-to-date concrete mixing technologies, the hardening process of concrete and the factors of influence, the technical features of concrete. The content of the volume and the manner of handling the subjects serve principally the practice.

Each new edition of the Zement-Taschenbuch contains since 1964. a chapter, which gives more detailed informations on some, selected, special part-problems about using cement for special purposes and preparing special concretes. These informations are based on results of the latest development. The volume 48. contains three such themes, as follows:

Increasing the long-term durability of open air concrete building-objects exposed to weather effects. It discusses the factors causing deteriorations, general directions to prevent deterioration, gives directives to chose the proper materials, to design the building, to apply the corresponding concrete technology by which the durability might be raised.

Impregnation, coating and painting of free concrete surfaces. Gives informations about possibilities, methods to do it and the acquireable efficiency of protection.

Making heavily stressed, high load bearing wearing-layers of concrete roads of hydraulic binding agent and highstrength aggregate. Deals with the special technical features of the concrete securing the requirements, the mix design of concrete and its quality control.

The following chapter contains the list of the titles of special themes discussed in former volumes with the ordinal number of edition in which the detailed information is to be found.

The last chapter enumerates the most important, respective German standards and regulations.

Finally, there is a list in the volume of the cement works in operation in the Federal Republic of Germany.

The Zement-Taschenbuch as a handbook dealing with the up-to-date state of cement and concrete techniques, and which gives very useful instructions, directives for the building practice is very precious for those working in the building industry. The book is applicable entirely in the Hungarian building practice, because the principals and the technologies contained in the book also correspond to the Hungarian prescriptions.

T. Gyengő

H. NEUMANN–K. STECKER: *Temperaturmessung.* (Thermometry) Akademie-Verlag, Berlin, 1983. 160 pages

This book deals with thermometry. According to the international system of weights and measures (absolute) temperature is a fundamental magnitude, of unit 1 K. The problem lies in the fact that temperature, sensorially more or less perceptible, is a directly non-measurable, intensive state characteristic. Countless empirical temperature scales can be made on the basis of measurable characteristics varying with the thermal condition of materials (e.g. volume, electric resistance, etc.). There are several possibilities to define the absolute temperature scale, e.g. as ratio of heat introduced to, or leaving, a Carnot cycle, or as integrating factor of the quantity of heat, or, on the basis of the fact that absolute temperature is proportional to the product of pressure by molar volume if pressure tends to zero.

After definition of the temperature scale, gas thermometers, instruments relying on thermal expansion, vapour pressure measurement, temperature dependence of electric resistance, thermal stresses and radiation are presented in detail while thermometers on other bases (e.g. sound propagation velocity or capacitance variation) only in general. Finally, allusion is made on the correlation between heat transfer and thermometry.

This book has been intended for physicists and engineers. For each instrument type, operational fundamentals, construction types in use, and sources of error in application are presented.

A more exact definition of the temperature scale and determination of fixed points of the practically applied temperature scale would be desirable, since the basis of statements in the book thermometry as a whole seems somewhat unfounded.

Again, a more precise description of knowledge in measurement would be welcome. Namely, for instance, the way of introducing virial equations in discussing gas thermometers can hardly be followed. Also, it would have been preferable to start from equation $w=(\partial P/\partial \rho)_s^{1/2}$ and virial equations in giving relationships for evaluation of the measurement results instead of presenting a relationship valid in case of ideal gases alone, then, irrespective of that, a relationship containing acoustic virial coefficients. In the same place, the statement that the adiabatic exponent for ideal gases is 5/3 is quite erroneous; it applies to monatomic gases only (p. 130).

In discussing the fundamentals of thermometers based on volume change, it is rather unusual to indicate mean cubic expansion coefficient for interval (T_0, T_1) in the form of $\gamma(T_1 - T_0)$, and then to include it in an equation containing multiplier $(T_1 - T_0)$ as well (p. 35). Although "stem correction" is mentioned in the book (p. 39), no method for estimating mean stem temperature is presented.

In the chapter on the effect of heat transfer, the thermal conductivity equation should have been reasonably written as a partial differential equation as usual. On the basis of what has been said here, the differential equation seems as if it could be solved without boundary conditions!

On the basis of these examples selected at random, the book seems to be of little use in its present form. However, it still gives a survey of problems and roughly outlines the solution to these problems, and the references given in the book are a valuable source of solutions to the problems discussed.

Thus, although the book is by far not ranging among the bests in the recensionist's opinion, it was perhaps not quite unnecessary to write it.

I. Szabó

Acta Physica Hungarica

(Formerly: Acta Physica
Academiae Scientiarum Hungaricae)

Editor in Chief:
I. Kovács

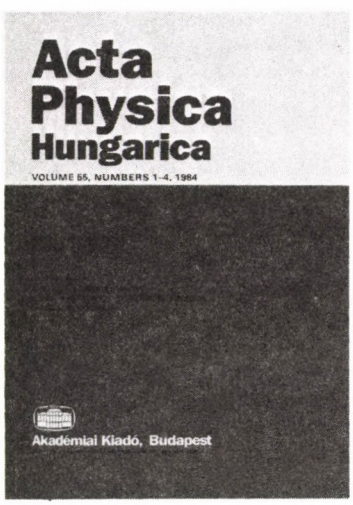

Acta Physica Hungarica publishes original papers (articles with abstracts and short communications) in the sphere of theoretical and experimental physics, including the fundamental problems and applications of classical and quantum physics, elementary particles and fields, nuclear physics, atomic and molecular physics, optics, acoustics, thermodynamics, fluids and plasmas, the properties of condensed matter, etc. It also publishes reviews on recent physical literature.

Founded 1951
Papers in English, French, German and Russian
Publication: two volumes annually — one volume contains four issues
Price per volume: $44.00; DM 99,—
Size: 17 × 25 cm
ISSN 0231–4428

Order form
to be returned to
KULTURA
Hungarian Foreign Trading Company
P.O. Box 149, H-1389 Budapest, Hungary
☐ Please enter my/our subscription for
ACTA PHYSICA HUNGARICA for one year
☐ Please enter my/our standing order for
ACTA PHYSICA HUNGARICA starting with

Name: _____

Address: _____

Date and signature: _____

ACTA PHYSICA HUNGARICA

Contents of Volume 54. Numbers 3–4

1828

Akadémiai Kiadó

Publishing House
of the Hungarian Academy of Sciences
Budapest

Invitation for papers
Manuscripts should be sent to
Prof. I. Kovács, Editor
Department of Atomic Physics
Technical University
1521 Budapest
Budafoki út 8.
Hungary

PRINTED IN HUNGARY
Akadémiai Kiadó és Nyomda, Budapest

NOTICE TO CONTRIBUTORS

Papers in English* are accepted to the condition that they have not been previously published or accepted for publication.

Manuscripts in two copies (the original type-written copy plus a clear duplicate one) complete with figures, tables, and references should be sent to the

Acta Technica
Münnich F. u. 7. I. 111A
Budapest, Hungary
H-1051

Although every effort will be made to guard against loss, it is advised that authors retain copies of all material which they submit. The editorial board reserves the right to make editorial changes.

Manuscripts should be typed double-spaced on one side of good quality paper with proper margins and bear the title of the paper and the name(s) of the author(s). The full postal address(es) of the author(s) should be given in a footnote on the first page. An abstract of 50 to 100 words should precede the text of the paper. The paper should not exceed 25 pages including tables and references. The approximate locations of the tables and figures should be indicated on the margin. An additional copy of the abstract is needed. Russian words and names should be transliterated into English.

References. Only papers closely related to the author's work should be referred to. The citations should include the name of the author and/or the reference number in brackets. A list of numbered references should follow the end of the manuscript.

References to periodicals should mention: (1) name(s) and initials of the author(s); (2) title of the paper; (3) name of the periodical; (4) volume; (5) year of publication in parentheses; (6) number of the first page. Thus: 5. Winokur, A., Gluck, J.: Ultimate strength analysis of coupled shear walls. American Concrete Institute Journal 65 (1968), 1029.

References to books should include: (1) author(s) name; (2) title; (3) publisher; (4) place and year of publication. Thus: Timoshenko, S., Gere, J.: Theory of Elastic Stability. McGraw-Hill Company, New York, London 1961.

Illustrations should be selected carefully and only up to the necessary quantity. Black-and-white photographs should be in the form of glossy prints. The author's name and the title of the paper together with the serial number of the figure should be written on the back of each print. Legends should be brief and attached on a separate sheet. Tables, each bearing a title, should be self-explanatory and numbered consecutively.

Authors will receive proofs must be sent back by return mail.

Authors are entitled to 50 reprints free of charge.

* Hungarian authors should submit their papers also in Hungarian.

Periodicals of the Hungarian Academy of Sciences are obtainable at the following addresses:

AUSTRALIA
C.B.D. LIBRARY AND SUBSCRIPTION SERVICE
Box 4886, G.P.O., *Sydney N.S.W. 2001*
COSMOS BOOKSHOP, 145 Ackland Street
St. Kilda (Melbourne), Victiria 3182

AUSTRIA
GLOBUS,Höchstädtplatz 3, *1206 Wien XX*

BELGIUM
OFFICE INTERNATIONAL DE LIBRAIRIE
30 A venue Marnix, *1050 Bruxelles*
LIBRAIRIE DU MONDE ENTIER
162 rue du Mindi, *1000 Bruxelles*

BULGARIA
HEMUS, Bulvar Ruszki 6, *Sofia*

CANADA
PANNONIA BOOKS, P.O. Box 1017
Postal Station "**B**", *Toronto, Ontario M5T 2T8*

CHINA
CNPICOR, Periodical Department, P.O. Box 50
Peking

CZECHOSLOVAKIA
MAD'ARSKÁ KULTURA, Národní třida 22
115. 66 Praha
PNS DOVOZ TISKU, Vinohradská 46, *Praha 2*
PNS DOVOZ TLAČE, *Bratislava 2*

DENMARK
EJNAR MUNKSGAARD, Norregade 6
1165 Copenhagen K

FEDERAL REPUBLIC OF GERMANY
KUNST UND WISSEN ERICH BIEBER
Postfach 46, *7000 Stuttgart 1*

FINLAND
AKATEEMINEN KIRJAKAUPPA, P.O. Box 128 *SF-00101*
Helsinki 10

FRANCE
DAWSON-FRANCE S. A., P. 40, *91121 Palaiseau*
EUROPÉRIODIQUES S. A., 31 Avenue de Versailles, *78170 La Celle St. Cloud*
OFFICE INTERNATIONAL DOCUMENTION ET
LIBRAIRIE,48 rue Gay-Lussac
75240 Paris Cedex 05

GERMAN DEMOCRATIC REPUBLIC
HAUS DER UNGARISCHEN KULTUR
Karl Liebknecht-Straße 9, *DDR-102 Berlin*
DEUTSCHE POST ZEITUNGSVERTRIEBSAMT Straße der
Pariser Kommüne 3 4, *DDR-104 Berlin*

GREAT BRITAIN
BLACKWELL'S PERIODICALS DIVISION
Hythe Bridge Street, Oxford OX1 2ET
BUMPUS, HALDANE AND MAXWELL LTD.
Cowper Works, *olney, Bucks MK46 4BN*
COLLET'S HOLDINGS LTD., Denington Estate *Wellingborough, Northants NN8 2QT*
WM. DAWSON AND SONS LTD., Cannon House *Folkstote, Kent CT19 5EE*
H. K. LEWIS AND CO., 136 Gower Street
London WC1E 6BS

GREECE
KOSTARAKIS BROTHERS INTERNATIONAL
BOOKSELLERS, 2 Hippokratous Street, *Athens-143*

HOLLAND
MEULENHOFF-BRUNA B. V., Beulingstraat 2,
Amsterdam
MARTINUS NIJHOFF B.V.
Lange Voorhout 9 11, *Den Haag*
SWETS SUBSCRIPTION SERVICE
347b Heereweg, *Lisse*

INDIA
ALLIED PUBLISHING PRIVATE LTD., 13/14
Asaf Ali Road,*New Delhi 110001*
150 B-6 Monunt Road, *Madras 600002*
INTERNATIONAL BOOK HOUSE PVT. LTD.
Madame Cama Road, *Bombay 400039*
THE STATE TRADING CORPORATION OF INDIA LTD.,
Books Import Division, Chanralok 36 Janpath, *New Delhi 110001*

ITALY
INTERSCIENTIA, Via Mazzé 28, *10149 Torino*
LIBRERIA COMMISSIONARIA SANSONI, Via Lamarmora 45,
50121 Firenze
SANTO VANASIA, Via M. Macchi 58
20124 Milano
D. E. A., Via Lima 28, *00198 Roma*

JAPAN
KINOKUNIYA BOOK-STORE CO. LTD.
17-7 Shinjuku 3 chome, Shinjuku-ku, *Tokyo 106-91*
MARUZEN COMPANY LTD., Book Department, P.O. Box
5050 Tokyo International, *Tokyo 100-31*
NAKUA LTD. IMPORT DEPARTMENT
2-30-19 Minami Ikebukuro, Toshima-ku, *Tokyo 171*

KOREA
CHULPANMUL, *Phenjan*

NORWAY
TANUM-TIDSKRIFT-SENTRALEN A.S., Karl Johansgatan
41 43, 1000 Oslo

POLAND
WEGIERSKI INSTYTUT KULTURY, Marszalkowska 80,
00-517 warsawa
CKP-I W, ul. Towarowa 28,*00-958 Warsawa*

ROUMANIA
D.E.P., *Bucuresti*
ILEXIM,Calea Grivitei 64-66, *Bucuresti*

SOVIET UNION
SOJUZPECHAT IMPORT, *Moscow*
and the post offices each town
MEZHDUNARODNAYA KNIGA, *Moscow G-200*

SPAIN
DIAZ DE SANTOS, Lagasca 95, *Madrid 6*

SWEDEN
GUMPERTS UNIVERSITETSBOKHANDEL AB
Box 346, *40125 Göteborg 1*

SWITTZERLAND
KARGER LIBRI AG, Petersgraben 31, *4011 Basel*

USA
EBSCO SUBSCRIPTION SERVICES
P.O. Box 1943, *Birmingham, Alabama 35201*
F.W. FAXON COMPANY, INC.
15 Soutwest Park, *Westwood Mass. 02090*
READ-MORE PUBLICATIONS, INC.
140 Cedar Street, *New York,N.Y. 10006*

YUGOSLAVIA
JUGOSLOVENSKA KNJIGA,Terazije 27, *Beograd*
FORUM,Vojvode Mišića 1, *21000 Novi Sad*

HU ISSN 0001-7035 Index: 26.025